

Diss. ETH No. 21138

Single-mode and Comb Operation of Broadband Quantum Cascade Lasers

A dissertation submitted to
ETH ZÜRICH

for the degree of
Doctor of Sciences

presented by
Andreas Hugi

Master of Science in Micro- and Nanotechnology
University of Neuchâtel
born on March 20, 1981
citizen of Grenchen, SO - Switzerland

accepted on the recommendation of

Prof. Dr. Jérôme Faist, examiner
Prof. Dr. Frank K. Tittel, co-examiner
Prof. Dr. Tobias Kippenberg, co-examiner

May 2013

Abstract

The quantum cascade laser is a unipolar semiconductor laser based on intersubband transitions in quantum wells. The realization of broadly tunable single-mode quantum cascade lasers and optical frequency-comb quantum cascade lasers in the mid-infrared is particularly interesting due to the fundamental roto-vibrational absorption bands present within this wavelength range. Nowadays, the quantum cascade laser operates in continuous-wave operation at room-temperature and features multi-watt optical output powers. The small footprint, the freedom in design and the tailorable emission wavelength make these lasers the ideal light sources for compact, field-deployable, robust and cost-efficient mid-infrared spectroscopic systems.

The presented work deals with the design and realization of broadband quantum cascade lasers in the mid-infrared spectral region. Broadband homogeneous and inhomogeneous gain can be engineered, nonlinearities can be tailored and the group-velocity dispersion can be controlled. In the course of this work, such broadband quantum cascade lasers are employed in different application scenarios. One being the use of these active regions as a gain element for broadband tuning an external-cavity configuration. New active region designs help to push tuning-ranges to new boundaries. We reach tuning-ranges around the center wavelength of 18 % in continuous-wave operation and 40 % in pulsed mode. The measured output power is 140 mW in continuous-wave, respectively 1 W peak power in pulsed mode. In collaboration with the Swiss Federal Laboratories for Material Science and Technology (EMPA) and BLOCK-engineering, we perform broadband spectroscopy covering 280 cm^{-1} on three different substances using an external-cavity quantum cascade laser.

These broadband laser sources can also be used to replace conventional glowbars in Fourier-transform interferometers. These high-brightness sources offer potentially better signal-to-noise ratios. Furthermore, due to the available high-power, they allow the measurement of highly-absorbing samples, such as liquids. Performed under comparable conditions, we benchmark a glowbar against a broadband quantum cascade

laser. The quantum cascade laser yields an increase in signal-to-noise ratio of roughly 15 dB.

In the last part of the presented work, optical frequency-comb operation of a broadband quantum cascade laser is demonstrated. Today's mid-infrared combs are mainly based on down-converted, mode-locked near-infrared lasers in nonlinear crystals. A novel and noteworthy comb generation scheme is based on the optical pumping of an ultra high-quality factor microresonator with a continuous-wave laser source. Such combs also start to penetrate the mid-infrared region. However, all these generation schemes depend on a chain of optical elements. A more direct, all electrical injection comb generation scheme based on a semiconductor laser is preferable. We demonstrate an optical frequency-comb at $7\text{ }\mu\text{m}$ featuring a bandwidth of 308 nm, which corresponds to a wavelength coverage of $\frac{\Delta\lambda}{\lambda} = 4.4\%$. We measure intermode beat stabilities of $\Delta\nu < 10\text{ Hz}$. Four-wave mixing mode-proliferation combined with gain provided by the broadband quantum cascade laser leads to a fixed phase relation similar to that of a frequency-modulated laser. A novel characterization technique for frequency-combs is presented and analyzed in this work, the so called intermode beat spectroscopy. This technique can be used to characterize combs featuring a frequency-modulated like output. We use the intermode beat spectroscopy to analyze the quantum-cascade-laser frequency-comb. These results are achieved in collaboration with Alpes Lasers and H.C. Liu from the Shanghai Jiao Tong University in Shanghai.

Zusammenfassung

Der Quantenkaskadenlaser ist ein unipolarer Halbleiterlaser, welcher auf optischen Übergängen in Quantentöpfen basiert. Die Herstellung von einerseits breit abstimmbaren einmodigen Lasersystemen, sowie andererseits optischen Frequenzkämmen im mittleren Infrarot Bereich, basierend auf Quantenkaskadenlasern, ist äusserst interessant, da sich die fundamentalen Absorptionsbänder der meisten leichten Moleküle in diesem Wellenlängenbereich befinden. Heutzutage kann der Quantenkaskadenlaser bei Raumtemperatur in Dauerstrich (CW) betrieben werden und verfügt über mehrere Watt optische Ausgangsleistung. Die geringe Grösse, die Freiheit im Design, sowie die Anpassung der Wellenlänge, macht diesen Laser zur idealen Lichtquelle für kompakte, im Feld einsetzbare und robuste Spektroskopie-Systeme.

Die hier präsentierte Arbeit handelt vom Design und der Herstellung von breitbandigen, im mittleren Infrarotbereich emittierenden Quantenkaskadenlasern. Breitbandige homogene und inhomogene Verstärkung kann entworfen, nichtlineare Prozesse können kontrolliert und die Gruppengeschwindigkeitsdispersion kann beeinflusst werden. Im Zuge dieser Arbeit werden solche Quantenkaskadenlaser in verschiedenen Szenarien eingesetzt. Zum einen werden sie als Verstärkungselement in einer externen Kavität eingesetzt. Das ermöglicht ihre breit abstimbare, einmodige Emission. Neue Designs der aktiven Region helfen die Grenzen der Abstimmbarkeit zu erweitern. Wir realisieren eine Abstimmbarkeit von 18 % im CW- und 40 % im gepulsten Betrieb. Die Ausgangsleistung beträgt 140 mW im CW- und 1 W maximale Leistung im gepulsten Betrieb. Des Weiteren präsentieren wir breitbandige Spektroskopie-Messungen über 280 cm^{-1} . Diese Messungen wurden in Kollaboration mit der eidgenössischen Materialprüfungs- und Forschungsanstalt (EMPA) und BLOCK-engineering durchgeführt.

Diese breitbandigen Quantenkaskadenlaser können auch als Ersatz zur gewöhnlichen Glühbirne in Fourier-transform Interferometern eingesetzt werden. Die starke Lichtdichte offeriert potenziell ein besseres Signal-zu-Rausch Verhältnis. Zusätzlich kann die Laserlichtquelle auch stark absorbierende Medien durchdringen. Ein Beispiel

hierfür sind wässrige Lösungen. Messungen, welche unter vergleichbaren Konditionen durchgeführt wurden, zeigen eine Verbesserung des Signal-zu-Rausch Verhältnisses um 15 dB.

Der letzte Teil der Arbeit präsentiert die Resultate von optischen Frequenzkamm Quantenkaskadenlaser. Heutzutage basieren optische Frequenzkämme meist auf herunterkonvertiertem, modengekoppeltem Laserlicht im nahen Infrarotbereich. Dies wird durch nichtlineare Interaktionen in Kristallen erreicht. Eine neue und beachtenswerte Art der Frequenzkammerzeugung basiert auf CW-Laserlicht gepumpten Mikroresonatoren mit sehr hohem Q-Faktor. Diese Frequenzkämme erreichen heutzutage auch den mittleren Infrarot-Bereich. All diese Frequenzkämme basieren jedoch auf der Aneinanderreihung von mehreren optischen Elementen. Ein direkter, nur elektrisch gepumpter Frequenzkammgenerator, basierend auf einem Halbleiterlaser ist wünschenswert. Wir präsentieren einen optischen Quantenkaskadenlaser-Frequenzkamm bei $7\text{ }\mu\text{m}$ Wellenlänge mit einer Bandbreite von 308 nm. Dies entspricht einer Wellenlängenabdeckung von 4.4 %. Wir messen eine Zwischenmoden-Stabilität von $< 10\text{ Hz}$. Modengenerierung basierend auf vier-Wellen Mischung, zusammen mit der vom breitbandigen Quantenkaskadenlaser gelieferten Verstärkung, sind dafür verantwortlich, dass der Laser eine Phasenverhältnis vorweist, welche einem Frequenzmodulierten Signal ähnlich ist. Ein neuartiges Analyseverfahren für Frequenzkämme, die Zwischenmodenschwebung-Spektroskopie, wird präsentiert. Dieses Verfahren kann auch auf Laser angewendet werden, welche eine Phasenverhältnis ähnlich einem Frequenzmodulierten Signal aufweisen. Wir benutzen die Zwischenmodenschwebung-Spektroskopie um unseren Quantenkaskadenlaser-Frequenzkamm zu charakterisieren. Diese Resultate wurden in Kooperation mit Alpes Lasers und H.C. Liu von der Shanghai Jiao Tong Universität in Shanghai realisiert.

Acknowledgments

First and foremost I would like to thank my supervisor Prof. Dr. Jérôme Faist. His guidance and inspiration is the source of this document. When working with Jérôme, one quickly starts to feel his passion for physics. I was particularly impressed by the deep understanding of physics he brings along. Though he has a very busy schedule, the door to his office is always open when one needs advice on a problem. When working in the lab, Jérôme routinely passes to see how things are evolving, giving the right tip at the right moment to solve a problem. This curiosity is one of the reasons he keeps track of all the projects, problems and achievements in the group, making him a truly exceptional boss.

I would like to thank Dr. Mattias Beck for the growth of the epi-layers and for the friend he is. To celebrate or recover from a set back, he is a sure bet to join for a beer or two. I am also grateful to Dr. Giacomo Scalari, Dr. Fabrizio Castellano, Dr. Yargo Bonetti and Dr. Laurent Nevou, whom I always could bother with my questions. Next I would like to thank my colleagues with whom I had the pleasure of sharing the office as well as many laughs: Dr. Milan Fischer, Dr. Maria Amanti, Dr. Richard Maulini, Dr. Romain Terazzi, Borislav Hinkov, Federico Valmorra, Johannes Riebling and Gustavo Villares. I also thank the entire mid-IR team, Dr. Tobias Gresch, Dr. Alfredo Bismuto, Borislav Hinkov, Dr. Pierre Jouy, Sabine Riedi, Gustavo Villares, Johanna Wolf, Dr. Yargo Bonetti, Dr. Andreas Wittmann and Dr. Romain Terazzi. And of course I would like to thank the entire group, past and present. I would like to thank Dr. Pierre Jouy, Gustavo Villares and Borislav Hinkov for proofreading parts of this thesis. Special thanks goes to Dr. Arun Mohan who was my supervisor for my master thesis. I would also like to mention Dr. Christoph Walther who became a good friend of mine, am looking forward to the windsurfing. I also want to thank here Markus Geiser for his funny jokes during the working hours, and thanks to him I know now that the bars in Altstetten are not the hippest place to go. Furthermore, I will always remember fondly the city trips we organized with the group. We spend some really good

times in Prague (mainly in cellars-restaurants) and Barcelona. Friday-beer, Werdinsel, Skidays, Jumbo-Jumbo cordonbleu, concerts, ...this list goes on, thanks again to the whole group.

During the course of this work, I had the opportunity to work together with many other groups and external companies. I would like to thank Alpes Lasers for their close collaboration, in particular Dr. Stéphane Blaser. Furthermore, I would like to thank Dr. Lukas Emmenegger, Dr. Bela Tuzson and Dr. Joachim Mohn from EMPA. I remember fondly the collaborative work to realize an absorption spectroscopy setup using the EC-QCL. Furthermore, without their help and knowledge, the project to replace a glowbar with a broadband QCL would not have succeeded. Furthermore, the knowledge of Bela helped a lot realizing a low noise setup for the QCL comb operation. I would like to thank Prof. Dr. M. Quack and his entire group to allow us to use the high-resolution FTIR. These measurements marked the beginning of the research on the QCL-comb. I particularly would like to thank Dr. Edouard Miloglyadov who supported me during the measurements and with whom I had interesting discussions about mid-IR combs. Since we were missing a lot of equipment for comb characterization at the beginning of the work, I would also like to thank Prof. Dr. U. Keller and her entire group. I could basically walk into Dr. Valentin Wittwer office and ask if it would be possible to rent a missing piece of equipment. I would also like to thank BLOCK engineering who gave me the opportunity to go to their company in Massachusetts USA at the beginning of my PhD to help with the realization of their first prototype EC-QCL. In particular I would like to thank Petros Kotidis and Bob Schildkraut.

I would also like to thank the competent team around the FIRST-clean room. Without their great work and passion this work would not have been possible. Many thanks also to the engineering bureau, Marcel Bär is the origin of many great setups running in the lab. And it goes without saying that those setups could not be realized without the professional and fast work we know from the mechanical workshops here on the campus on Höggerberg. In the course of this PhD I had the opportunity to move the lab twice. It was in those times that I really started appreciating the staff from the Betriebsgruppe, thank you for keeping the department running so smoothly.

Furthermore I would like to thank my whole family. It is thanks to their support that I am where I am now. I also want to thank the various members of the music groups I have/had the chance to play with.

I am truly indebted to my girlfriend Julia Vielle. She was on my side during the whole duration of the PhD. I know it was not always easy for her since this thesis demanded long working hours and it often kept my mind turning even when at home. In the end, coming home to Julia is the best medicine against all worries in life.

Abbreviation

Amplitude modulation	AM
Anti-reflection	AR
Carrier-envelope offset	CEO
Continuous-wave	CW
Cross-phase modulation	XPM
Deuterated Tri-Glycine Sulfate	DTGS
Difference frequency generation	DFG
Distributed-feedback	DFB
External-cavity	EC
Fabry-Pérot	FP
Fast-Fourier transform	FFT
Fourier-transform interferometry	FTIR
Frequency modulation	FM
Full-width at half maximum	FWHM
Group-velocity dispersion	GVD
High-reflectance	HR
Infrared	IR
Light-Current-Voltage	LIV
Master-oscillator power-amplifier	MOPA
Mercury cadmium telluride	MCT
Metalorganic vapour phase epitaxy	MOVPE
Micro-electro-mechanical systems	MEMS
Molecular beam epitaxy	MBE
Optical parametric oscillator	OPO
Periodically poled lithium niobate	PPLN
Quantum cascade laser	QCL
Quantum-well infrared photodetector	QWIP
Quartz-enhanced photoacoustic spectroscopy	QEPAS
Resolution bandwidth	RBW
Self-phase modulation	SPM

Side-mode suppression ratio	SMSR
Signal to noise ratio	SNR
Substack	ST
Terahertz	THz
Transverse-electric	TE
Transverse-magnetic	TM
Vertical-external-cavity surface-emitting-laser	VECSEL

Contents

Abstract	i
Zusammenfassung	iii
Acknowledgments	v
Abbreviation	vii
1 Introduction	1
1.1 Motivation	1
1.2 The mid-infrared range	2
1.3 Quantum cascade lasers	4
1.4 Laser spectroscopy	5
1.4.1 Long-path absorption spectroscopy	7
1.4.2 Photoacoustic spectroscopy	8
1.4.3 Comb spectroscopy	9
2 Quantum cascade laser	15
2.1 Fundamentals	15
2.1.1 Rate equations	16
2.2 QCL broadband design	18
2.2.1 Rate equations heterogeneous laser	26
2.3 QCL fabrication	27
2.3.1 Buried-heterostructure	28
2.4 GVD in quantum cascade lasers	30
2.4.1 Fabry-Pérot emission spectrum	31
2.4.2 Calculation of GVD in a QCL	33
2.4.3 Material dispersion	34
2.4.4 Modal dispersion	35
2.4.5 Dispersion due to the gain	37
2.5 Nonlinearities in QCLs	45
2.6 Parametric coupling	48
2.6.1 Theory	49
2.6.2 Wave mixing	51

2.6.3	Four-wave mixing in a QCL amplifier	56
3	Dielectric mid-IR AR- and HR coatings	57
3.1	Introduction	57
3.2	Thin film materials in the mid-IR	59
3.3	Theory	60
3.3.1	Single- and multi layer coatings	65
3.3.2	Design and optimization of coatings	66
3.4	Characterization of coatings	67
3.5	Coating examples	69
4	Broadband EC-QCL	73
4.1	Introduction	75
4.2	Theory	76
4.2.1	EC-setups	76
4.2.2	Lens and grating	77
4.2.3	EC-QCL rate-equations	79
4.2.4	EC-QCL pulsed- and cw-operation	82
4.2.5	EC-QCL tuning analysis	84
4.3	Room-temperature cw-operation of an EC-QCL	85
4.4	Heterogeneous rt cw-operation of an EC-QCL	87
4.5	EC-QCL based on multiple substack active region	89
4.6	Broadband EC-QCL absorption spectroscopy	95
4.7	EC-QCL activities	100
4.8	Broadband QCL as white light source	101
4.8.1	FTIR resolution limits	102
4.8.2	Characterization	103
5	Frequency-comb operation of QCLs	109
5.1	Introduction	110
5.1.1	Optical frequency combs	110
5.1.2	Prior work on QCL comb operation	111
5.2	Fundamental mode-locking	112
5.3	Frequency-modulation mode-locking	114
5.4	Mid-infrared comb sources	117
5.5	Mode-locked semiconductor lasers	119
5.6	Kerr-combs	120
5.7	Characterization	121
5.7.1	FTIR and second-order autocorrelation	121
5.7.2	Intermode beat spectroscopy	124
5.8	Frequency-comb operation of broadband QCLs	138
6	Conclusions and perspectives	153
	Bibliography	178
A	Curriculum vitae & List of publications	179

List of Figures

1.1	Near-IR to mid-IR line strength comparison of nitric oxide. The absorption bands of nitric oxide are orders of magnitude stronger in the mid-IR ($5.3\text{ }\mu\text{m}/2.6\text{ }\mu\text{m}$) region compared to the near-IR ($1.8\text{ }\mu\text{m}/1.6\text{ }\mu\text{m}$) region. Source: HITRAN 2008.	3
1.2	Atmospheric windows in the mid-IR region. The absorption line strength of H_2O shows two transmission windows between $3\text{-}5\text{ }\mu\text{m}$ and $8\text{-}12\text{ }\mu\text{m}$. Source: HITRAN 2008.	4
1.3	a Absorption spectroscopy with a broadband incoherent source and b with a tunable single-mode source. Figures adapted from [8].	6
1.4	a Quartz enhanced photoacoustic spectroscopy. Standard setup as described in Ref. [50]. b Time and frequency interpretation of the interaction of a series of pulses with an atomic system. The bandwidth of the first pulse is much broader than the resonance line. If in resonance, subsequent coherent pulses can then coherently accumulate from the ground state $ g\rangle$ to the excited state $ e\rangle$. Figure inspired by [51].	8
1.5	a Simple two-photon spectroscopy setup. b Two-photon spectroscopy with a cw-laser source. c Two-photon spectroscopy with an optical frequency comb. If the modes of a frequency comb are properly phased, a pairwise addition of comb modes in resonance provides an efficient two photon excitation.	11
1.6	a Dual-comb spectroscopy. Two optical combs are superimposed to generate a time-domain scanning interferogram. No moving parts are necessary. b Dual-comb spectroscopy explained in the frequency domain. Neighboring modes of the two combs with slightly different repetition frequencies of f_r and $f'_r = f_r - \Delta$ will generate a characteristic beating of frequency $n\Delta$ in the RF-domain.	14

2.1	Schematic conduction band diagram of a quantum cascade laser and gain clamping. a Cascading of the fundamental period in quantum cascade lasers. One period can be split into two parts, the active region and the relaxation/injection region. b Population inversion analysis in a quantum cascade laser transition by a simplified rate equation model. The most important non-radiative lifetimes are indicated. c Population inversion as a function of injection current density J assuming zero thermal population. Above threshold when the modal gain overcomes the total losses, the gain is clamped.	16
2.2	Bound-to-continuum design. a QCL active region based on the bound-to-continuum design emitting at 9.75 μm . Applied electrical field 35 kV/cm. b Simulated and measured electroluminescent spectra. Solid line: Measured luminescence spectrum at 300 K under a bias of 8 V. Dashed line: Sum of the computed oscillator strengths of the transitions from level 12, taking into account different linewidth broadenings arising from interface roughness scattering. Data published in [113, 115].	19
2.3	Alternative broadband designs. a Bandstructure of a dual-upper-state design. b Measured luminescence spectra. Reprinted with permission from Kazuue Fujita <i>et al.</i> , APL 98 231102 (June 2011). © 2011, American Institute of Physics. c Simulated bandstructure of a continuum-to-continuum design published in Ref. [122] using the software of our group. d Pulsed LIV characteristics of the structure published by Yao <i>et al.</i> in [122]. Pulsed operation, 100 ns pulse width, 100 kHz repetition rate. The data is corrected for 74% collection efficiency and the optical output power is multiplied by two to account for the two facets. Reprinted with permission from Yu Yao <i>et al.</i> , APL 97 081115 (August 2010). © 2010, American Institute of Physics.	21
2.4	Luminescence and LIV measurements of EV1470D, a redo from the broadband continuum-to-continuum design published in [127]. a Luminescence measurements at 20°C (201 ns, 200 kHz) at different applied biases of a 370 μm long ridge. The light is extracted perpendicular to the ridge. The FWHM of the measurement is indicated after the applied field. b LIV characteristics of a 3/ μm long device from EV1470D at different temperatures. The data is not corrected for the collection efficiency. . . .	22
2.5	Comparison between the data published in [127] and the redo EV1470D. Characteristic temperature T_0 of EV1470D, a redo from the broadband continuum-to-continuum design published in [127]. a Comparison of the threshold current density (J_{th}) and T_0 of the redo and the published data. b Calculation of the waveguide losses of EV1470D.	23
2.6	Principal characteristics of an intersubband transition in a quantum well.	24

2.7	Schematic conduction band diagram of a QCL. It illustrates the cascading principle of QCLs and the possibility to form a broadband emitter by taking advantage of the transparency of the intersubband transition. The broadband emitter is formed by adding different substacks emitting at different frequencies to form the active region. Inset a shows the simulated gain curve of two dissimilar substacks within a QCL as a function of transmission energy.	25
2.8	Buried-heterostructure processing steps.	28
2.9	Fabry-Pérot mode spacing in a dispersive medium. The mode spacing is given by the group velocity and the cavity length $\Delta\nu = \frac{v_g}{2L}$	32
2.10	GVD calculation in a QCL. The individual GVD contributions need to be multiplied by the respective modal overlap.	34
2.11	Refractive index and GVD of material systems used for mid-IR QCLs. a Refractive index of different binary III-V semiconductor compounds and of $\text{Al}_{0.3}\text{Ga}_{0.7}\text{As}$. b Group velocity of InP as a function of wavelength. c GVD of InP as a function of wavelength.	35
2.12	Waveguide design of QCLs. a Illustration of the TM-mode penetration in the cladding as a function of wavelength. b Refractive index as a function of wavelength of heavily doped InP and GaInAs forming a guiding plasmon layer in the QCL.	36
2.13	GVD due to the waveguide. a Lateral and vertical effective refractive index and group refractive index of a $4.5\mu\text{m}$ wide buried-heterostructure QCL. b GVD due to the plasmon doping concentrations. c Effect of the waveguide width on the GVD.	38
2.14	Kramer-Kronig relations. a Illustration of the relationship between real and imaginary part of the first order susceptibility χ . b Normalized GVD to illustrate the effect of the gain.	40
2.15	Iterative LIV simulation of all three substacks. The active region width was set to $8\mu\text{m}$, the number of periods to 17 and the facet reflectivity to 0.25. a LIV after the first iterative process. b LIV after the third iterative process.	43
2.16	Iterative GVD calculation for heterogeneous cascade. a GVD due to the gain after the first iterative process. b GVD due to the gain after the third iterative process.	43
2.17	GVD calculation in QCLs. GVD of due to a narrow-band active region (bound-to-continuum) and heterogeneous broadband active region. The total GVD including all different GVD terms for the broadband active region is shown as the solid black line.	45
2.18	$X^{(3)}$ and four-wave mixing in a two level system. a Four-wave mixing. b Energy level description of the four-wave mixing process under population inversion.	47
2.19	Four-wave mixing signal as a function of difference frequency. Reprint from [163].	48
2.20	Four wave mixing: a Phase matching condition and b interaction of four photons fulfilling the energy conservation $\hbar\omega_1 + \hbar\omega_2 = \hbar\omega_3 + \hbar\omega_4$	53

2.21	Coupled wave equations for non-degenerate and degenerate four wave mixing: a Non-degenerate four-wave mixing with $\omega_1 + \omega_2 = \omega_3 + \omega_4$. b Degenerate four-wave mixing with $\omega_4 = 2\omega_1 + \omega_2$. c FWM up- and down signal generated in a QCL amplifier. Reprint from [163].	54
3.1	Typical far-field measurement of a buried-heterostructure QCL. The ridge with is approximately 10 μm , the laser wavelength is $\lambda = 9 \mu\text{m}$	62
3.2	Propagation of electromagnetic radiation at dielectric boundaries. a TM-polarized output of the QCL. Two different possible propagation constants $\beta_{1/2}$. b Reflection and refraction of a TM-polarized wave with respect to the applied dielectric coating. The magnetic field vectors are chosen to give a positive power flow. c Reflection and refraction of a TE-polarized wave with respect to the applied dielectric coating. d Multilayer propagation of electromagnetic radiation.	63
3.3	HR and broadband AR coating measurements using the FTIR. a Simulation and measurement of dielectric HR-coating. b Simulation and measurement of broadband AR-coating taking the diffracted output beam of the laser into account.	69
4.1	Summary of EC-QCL tuning achieved using different active region designs. The results are compared to a standard distributed feedback (DFB)-QCL process to illustrate the increased tuning range of EC-QCLs. Different tuning curves are achieved either in pulsed or continuous-wave operation employing different active region designs. To date, the emission of a QCL is generally broadened by combining dissimilar substacks (ST) in one active region. The different tuning results are superimposed on HITRAN simulation of abortion spectra to illustrate the possibility to tune over entire absorption bands with one EC-QCL. Sources: (1) [36], (2) [175], (3), [176], (4) [177], (5) [178]. Reprint from [113].	74
4.2	EC-QCL configurations. a Littrow configuration. The first order diffracted beam is back coupled into the laser, the zeroth order beam is outcoupled through a mirror. b Littrow back-extraction setup. c Modified Littrow front extraction setup to prevent the walk-off of the outcoupled beam [195]	76
4.3	a Back-extraction setup used in the broadband spectroscopic measurements. The front- and back-extraction lens are both Ge f/0.8 lenses of 24mm diameter. b Redesign of the external cavity setup for the very broadband tuning of the five color active region. The miniaturization of the setup was necessary to limit constraints of tuning capability due to simple geometric reasons. The redesign features a very small yet high NA lens and a very small grating.	78
4.4	Measurement of the linewidth variations arising from Joule heating of an EC-QCL in pulsed mode operation. All the measurements were taken at a repetition rate of 198 kHz and measured using an FTIR Nicolet 800. Reprint from [113].	83

4.5	Comparison of EC-QCL with and without HR coating on the back facet. a Schematic illustration of the effect of an HR coating on the total mirror losses in the case of a FP chip and in the case of the external-cavity. b Simulation of the ratio of the chip mirror losses versus the EC mirror losses as a function of front and back reflection of the FP chip.	85
4.6	Room-temperature continuous-wave operation of an EC-QCL, showing the shortest and longest-wavelength single-mode spectra. Data published in [175]	86
4.7	Top: High resolution spectra at the extremes of tuning range of a continuous-wave heterogeneous EC-QCL with two different active region types. The chip could be tuned over 201 cm^{-1} (18 % of center frequency) with a SMSR >35 dB. Bottom: continuous-wave output power of the same laser as a function of frequency for three different sets of operation conditions. A tuning of 172 cm^{-1} with >20 mW of continuous-wave output power at 18°C was demonstrated. Reprint from [177].	88
4.8	Broadband design to avoid cross absorption. a Conduction band diagram of a short bound-to-continuum under an applied bias of 60 kV/cm. The wavelength is $11.5\text{ }\mu\text{m}$ designed to avoid cross-absorption at higher energies. b Simulation of the absorption of the longest respectively shortest wavelength stack in a five stack active region. The long wavelength (lwl) stack is optimized to have low absorption up to high energies, whereas the short wavelength (swl) stack is optimized to avoid cross-absorption at low energies.	89
4.9	Short bound-to-continuum design. a Simulated electroluminescent spectra under different applied bias. Due to the relatively large applied fields on these structures, the 8-7 and 8-6 transition are clearly distinguishable in the simulations. b Simulated net gain including resonant absorption losses of individual cascades. All cascades are simulated at approximately the same current density of 6.5 kAcm^{-2} . The total modal net gain, is the sum of all gains of the cascades times the modal overlap. Reprint [178]. .	90
4.10	a Modal intensity profile and symmetric cascade arrangement. Reprint [178]. b Luminescence measurement of a $300\text{ }\mu\text{m}\times 20\text{ }\mu\text{m}$ wide ridge. The traces are corrected for the spectral response of the detector. The FWHM is 480 cm^{-1} at the rollover current of 511 mA and 500 cm^{-1} at 117 mA. . . .	92
4.11	Broadband laser characteristic. a As cleaved light-current-voltage characteristic of a typical 3 mm long and $20\text{ }\mu\text{m}$ wide ridge at different temperatures. The power collected on one facet is doubled to account for the power of the back facet. b Laser spectra taken at currents of 2.3 A, 3.4 A, 5.1 A and 6.15 A at 273 K (50 kHz, 100 ns). Reprint [178].	93

4.12	Anti-reflection coating for broadband tuning in an external-cavity configuration. a Light-current-voltage characteristics of an as cleaved (red) and HR and AR coated (green) broadband 5-stack QCL. The light-current-voltage characteristic of the HR and AR coated chip in an external-cavity configuration at 15 °C is shown in solid blue. A peak output power of more than 1 W is measured. b Anti-reflection coating measurement on a reference sample using the FTIR. The deposited v-coating shows a reflection of < 10 % over the whole tuning range. Reprints from [178].	93
4.13	a Tuning behavior with corresponding peak optical output power of the EC-QCL at various wavelengths. Measurements were taken at 15 °C at a duty cycle of 1.5 % (15 ns, 1 MHz) at different currents. b Magnification of the spectra for linewidth comparison of the EC-QCL at 1080 cm ⁻¹ and 1180 cm ⁻¹ . Reprints from [178].	95
4.14	EC-QCL Setup Back-Extraction setup. a Schematic setup illustration. We employed a back-extraction EC-configuration to avoid walking of the beam. b Picture of the actual setup implementation.	97
4.15	Back-extraction EC-QCL characterization. a EC-QCL laser spectrum at the center of the gain curve featuring a FWHM of 0.5 cm ⁻¹ . Inset closeup of the single mode laser spectrum. b LIV at the center of the gain curve at 2 % duty cycle (200 ns, 100 kHz) at 20 °C. Inset: Output power over the whole tuning range.	98
4.16	Spectroscopy measurements comparing EC-QCL measurements with FTIR measurements. a 270 ppm DIMP. b 45 ppm TEP. c 500 ppm DMMP.	99
4.17	Resolution limits of an FTIR. a The finite path difference is responsible for a sinc profile in the acquired spectrum. b Resolution limit governed by the finite aperture with of the FTIR light-source. Figures inspired by [5]102	
4.18	Characterization of the Aerodyne laser box. The laser is fabricated and mounted at Alpes Lasers, the characterization is done at ETH. a Output power. b Pulse shape.	105
4.19	FTIR and laser synchronization during the acquisition of spectra.	105
4.20	SNR comparison between a glowbar and a broadband QCL in a FTIR. a SNR of the glowbar. b SNR of the broadband QCL.	106
4.21	Water absorption spectra measured using an FTIR using as a light source a conventional glowbar and a broadband QCL driven in continuous-wave operation.	107
5.1	Mode-locked laser output. a E-field and intensity of a mode-locked laser. b Optical spectrum and phase of a mode-locked laser.	111
5.2	Fast a and slow b saturable absorber. There is a short net-gain window smaller than the pulse width available to successively shorten the pulse.	113
5.3	Frequency comb laser output with perfect FM-phase and amplitude relations.	115

5.4	Locking of the beat frequencies. a Dispersed three mode operation at $\omega_{1,2,3}$ and generated beat frequencies at $\omega'_{1,2,3}$. Graph adapted from [253]. b Generation of optical frequency comb spectrum. The dispersed Fabry-Pérot resonator modes lock to the equally spaced modes generated by four-wave mixing processes. Reprint from [229].	116
5.5	a Mid-IR comb generation through difference-frequency generation (DFG) on a nonlinear crystal. b Mid-IR comb generation using the divide-and-conquer approach in a optical-parametric oscillator (OPO). Figure adapted from [95].	118
5.6	a Background-free intensity autocorrelation setup. The input pulse is split into two separate pulses, one of which is delayed by τ . The two pulses are then spatially overlapped on a nonlinear-medium, in this example a second-harmonic-generation crystal. b Fringe-resolved autocorrelation setup. Figures adapted from [302].	121
5.7	Simulated fringe-resolved interferometric autocorrelation trace of a a mode-locked laser emitting a train of pulses and (inset: spectra) b a laser featuring a perfectly FM-output (inset: spectra).	122
5.8	a 2-photon QWIP measurements from a buried heterostructure QCL ($\lambda = 8\mu\text{m}$). The inset shows the measure intermode beat at the round-trip frequency. Reprinted figure 16 with permission from Gordon <i>et al.</i> , Phys. Rev. A, 77, 053804 2008. © 2008 by the American Physical Society. b Intermode beat spectroscopy setup. Reprint from [229]	123
5.9	QWIP characteristics. a Transmission measurements and fit at room-temperature of a single-pass. b I-V in the dark at liquid nitrogen temperature. Data is provided by H.C. Liu.	125
5.10	Intermode beat spectroscopy measurement complex plane analysis. . . .	129
5.11	Intermode beat interferogram of a fundamentally mode-locked laser. a Simulation of a laser with 0.25 cm^{-1} mode spacing. Inset: Zoom at zero delay. b Measurement of fundamentally mode-locked fiber laser of TOP-TICA. Data published in [229].	132
5.12	Intermode beat interferogram and spectrum of a fundamentally mode-locked laser TOPTICA femto-second laser source corrected for the quadratic response. a Intermode beat interferogram. b Intermode beat spectrum. Data published in [229].	133
5.13	Intermode beat interferogram FM-output. a Simulation of a laser with 0.25 cm^{-1} mode spacing featuring a perfect FM-amplitude and phase configuration. b Generated photocurrent in a optical beam-splitter discriminator. c Characteristic discriminator efficiency as function of delay. Graph inspired by [308].	134
5.14	Intermode beat spectrum harmonic frequencies. a Intermode beat spectrum simulation of a FM-source. The quadratic dependence on the acquisition has been omitted in the simulation not to generate higher order terms. b Measured intermode beat spectrum of the TOPTICA femto-second laser over the whole range. The data has been corrected for the nonlinear response of the spectrum analyzer. Reprint from [229].	137

5.15	Intermode beat interferogram random varying phases. b and c Simulation of an intermode beat interferogram and intensity interferogram for a laser with varying phase configuration with time. The mode spacing is 0.25 cm^{-1} .	137
5.16	LIVs and intermode beat. a Light intensity - current - voltage characteristic at -20°C . The laser is delivered by Alpes Lasers. The measurements are carried out at ETH. Data published in [229]. b Light intensity - current - voltage at different temperatures of an epi-down mounted QCL on a diamond-submount. The laser chip is delivered by Alpes Lasers. The epi-down mounting and characterization is done at ETH. c Narrow intermode beat, with a full-width at half-maximum of $< 10\text{ Hz}$ at the onset of the multi-mode emission. The resolution bandwidth of the spectrum analyzer is set to 10 Hz .	138
5.17	High resolution (0.0026 cm^{-1}) Fourier transform infrared spectrometer spectra and measured mode spacing at a current of 740 mA at -20°C . Reprint from [229]	139
5.18	Narrow intermode beat measurements. a At twice the round-trip frequency. b At the round-trip frequency. The data was acquired over 1 hour with max hold on to illustrate the drift.	140
5.19	Intermode beat measurements and corresponding laser spectra at different currents at -20°C . Data published in [229].	141
5.20	Amplitude noise of the broadband quantum cascade laser at different bias currents at -20°C . a Amplitude noise for injection currents with intermode beat linewidths in the Hz range. b Amplitude noise for injection currents with increased intermode beat linewidths (kHz-MHz). Data published in [229]	142
5.21	Intermode beat spectroscopy. a Intensity interferogram and intermode beat interferograms measured in two successive scans separated by 90 min , at 490 mA . The resolution bandwidth is 100 kHz . b Comparison of the measured intermode beat interferogram at 480 mA with the intermode beat interferogram simulations of a perfectly frequency-modulated (FM) signal. Inset, magnified view of region at zero delay. Data published in [229].	143
5.22	Intermode beat spectroscopy. a Comparison of the intermode beat spectrum, $\mathcal{J}(\nu_{rt}, \omega)$, and the intensity spectrum, $\mathcal{J}(0, \omega)$, at an injection current of 500 mA . Data published in [229]. b Optical discriminator by a sheet of polyethylene that features a wavelength dependent absorption.	143
5.23	Polyethylene discriminator. a Intermode beat in the kHz range with and without optical discriminator. b Intermode beat in the Hz range after putting an optical discriminator.	144

5.24	Intermode beat spectroscopy. a Intermode beat interferogram at a injection current of ($I = 480$ mA). The radio-frequency (RF) span is 100 MHz with a resolution bandwidth of 2 MHz. b Corresponding intermode beat spectrum. c Intermode beat interferogram at a high injection current ($I = 679$ mA). The radio-frequency (RF) span is 100 MHz with a resolution bandwidth of 2 MHz. d Corresponding intermode beat spectrum. Data published in [229].	145
5.25	Intermode beat interferogram of a QCL comb featuring Hz intermode beat linewidths. a Full intermode beat interferogram. b Sample of the intermode beat at sampling position 12 of the intermode beat interferogram. c Comparison of the intermode beat and intensity interferogram.	146
5.26	Intensity and intermode beat spectrum in the Hz regime. a Intensity spectrum. b Intermode beat spectrum showing the whole acquired spectrum. c Intermode beat spectrum at the fundamental frequency of the laser. d Intermode beat spectrum at 2400 cm^{-1}	147
5.27	Heterodyne beat experiment. a Setup of the heterodyne beat experiment between a QCL comb and a single-mode DFB-QCL. b Optical spectra of the QCL comb and DFB single-mode QCL. Data published in [229].	149
5.28	Heterodyne beat experiment. a Heterodyne beat signal between the QCL comb and the single-mode DFB QCL. b Heterodyne and intermode beat position measurement while changing the injection current off the broadband quantum cascade laser. Data published in [229].	149
5.29	Heterodyne beat experiment. a Heterodyne beat measurement of a comb-like line and a stable single-mode quantum cascade laser while sweeping the radio-frequency (RF) injection frequency around the cavity round-trip frequency. When sweeping across the resonance of the cavity round-trip, the heterodyne signal can be shifted in frequency by 11 MHz. b Measured intermode beat at three different characteristic injection frequencies at resonance. Data published in [229].	150
5.30	a Intermode beat measurements with increasing RF-power. b Intermode beat spectrum at 10 dBm RF-injection power. Inset: Corresponding intermode beat interferogram taken with a resolution bandwidth of 5 kHz. c Intermode beat spectrum at 26.6 dBm RF-injection power. Inset: Corresponding intermode beat interferogram taken with a resolution bandwidth of 100 kHz. Reprint from [229]	151

Chapter 1

Introduction

1.1 Motivation

We live in an industrial and technological world, where the human footprint on nature is increasing. For example, a busy topic nowadays in science and politics is the effect of humans on the climate [1, 2]. To understand and react to these challenges, better monitoring techniques are essential. It enables the optimization of industrial and chemical products and can help to reduce their impact. It opens new avenues for medical applications and it allows for efficient water quality monitoring, just to name a few. Many of those applications require a precise determination of concentration levels of different substances of interest. Climate science relies on the exact determination of concentration levels of the greenhouse-gases (CO_2 , H_2O , CH_4 , O_3 , ...) in air as well as liquids. Improving the efficiency of engines can be achieved by monitoring the exhaust air composition of engines.

Many different well established methods exist to measure concentrations in the atmosphere and samples [3]. Spectroscopic techniques are specially interesting for sensing of gases and liquids, because it allows for a fast and non-intrusive detection of multi-component trace gases [4]. For example, Fourier transform infrared (FTIR) spectrometers are well established spectroscopic instruments [5, 6]. Nevertheless, these instruments are in general bulky. They feature a limited resolution and the acquisition speed is rather slow and directly linked to the resolution of the scan. The light sources conventionally used in these devices is also relatively weak, prohibiting the sensing of strongly absorbing and thick samples. Even tough MEMS based FTIRs can overcome the problem of size, they suffer from a limited resolution [7].

Laser based spectroscopy allows for a very sensitive, selective and high-resolution

(energy, temporal, spatial) sensing technique [8]. Furthermore it requires none or only small sample preparation. It is versatile, very reliable and robust, making it possible to use in harsh environmental conditions [9].

Especially progress in the telecommunication industry with the development of high-power power, high-efficient and high-volume (therefore low cost) laser-diodes lead to a enormous progress in laser spectroscopy applications. According to Ref. [10], diode laser business makes up for 50 % of the \$7.57B laser industry in 2012. The main driving factor for the industry remains the communications, which makes up for 31% of the laser revenues. In comparison to this, instrumentation and sensors covers only 4%. Therefore, sensor applications which rely on diode-lasers from the communication industry are bound to the wavelength ranges best suited for Telecom applications. This is a less than optimal situation for sensor applications, because the “sweet spot” for sensing light-molecules lies in the mid-infrared spectral range.

This work is dedicated to the development and understanding of broadband quantum cascade lasers (QCLs) emitting radiation in the mid-infrared region [11]. The focus of the work lies on the broadly tunable single-mode and comb-operation of such sources.

1.2 The mid-infrared range

The infrared (IR) spectrum of electromagnetic radiation spans the region between the visible light and microwave region ($710\text{ nm} < \lambda < 1\text{ mm}$). Usually it is divided into three regions, the near-IR region, the mid-IR and the far-IR region (also called the THz-range). The near-IR region approximately spans the wavelength range of $710\text{ nm} < \lambda < 2.5\text{ }\mu\text{m}$, the mid-IR covers a wavelength range of $2.5\text{ }\mu\text{m} < \lambda < 25\text{ }\mu\text{m}$. The remaining IR wavelength range from $25\text{ }\mu\text{m} < \lambda < 1\text{ mm}$ is occupied by the far-IR range [12]

The mid-IR range is specially relevant for science and technology. Since the interaction of matter with light strongly depends on the optical frequency, the absorption strength of each molecule is also a function of wavelength. As an example, fig. 1.1 compares the line strength of nitric oxide in the mid-IR and near-IR region. The mid-IR region absorption at $5.3\text{ }\mu\text{m}$ and $2.6\text{ }\mu\text{m}$ is orders of magnitudes stronger compared to the near-IR bands at $1.8\text{ }\mu\text{m}$ and $1.28\text{ }\mu\text{m}$. This is explained by the fact that most fundamental roto-vibrational bands of light molecules lie within the mid-IR region, whereas it is only possible to access the overtone and combination bands in the near-IR range. The spectrum coverage of the important second and third Telecom windows around $1.3\text{ }\mu\text{m}$ and $1.5\text{ }\mu\text{m}$ wavelength is shown in blue on fig. 1.1. Only the absorption at $1.3\text{ }\mu\text{m}$ is attainable using such sources. In contrast to this, sensors

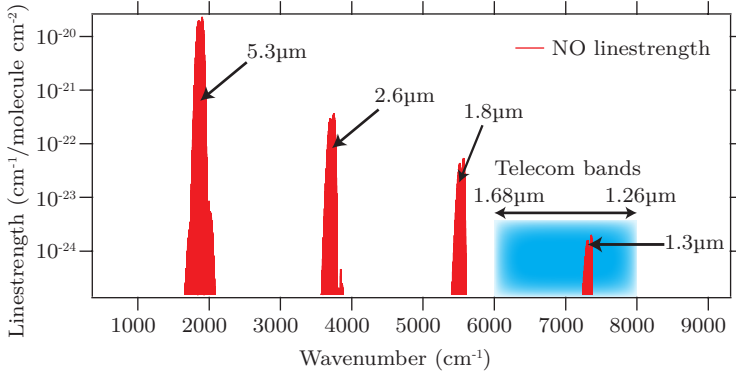


Fig. 1.1: Near-IR to mid-IR line strength comparison of nitric oxide. The absorption bands of nitric oxide are orders of magnitude stronger in the mid-IR (5.3 μm /2.6 μm) region compared to the near-IR (1.8 μm /1.6 μm) region. Source: HITRAN 2008.

in the mid-IR region promise much higher sensitivity due to the increased absorption strength. Indeed, using lasers in this wavelength range concentrations as low as parts per million (ppm 10^{-6}), parts per billion (ppb 10^{-9}) even up to parts per trillion (ppt 10^{-12}) is measurable [9, 13–15].

Mid-infrared applications are manifold. Some possible sectors are environmental monitoring, process monitoring, quality control, leak detection, long-range optical data transmission, medical applications, as well as surveillance- and security applications. As an example, medical applications can profit from the fast and noninvasive technique to determine molecular biomarkers in breath. It carries many information about the health and diseases of the patient [16]. It can be used to detect diabetes, some types of cancer and lung diseases [17–20]. The basis is the exact determination of the concentrations of the complex mix of nitrogen, oxygen, water vapor and carbon dioxide in addition the trace concentrations of several hundred volatile compounds [21]. An example of active research is shown in Ref. [22] that breath contains volatile biomarkers of breast cancer and that these biomarkers can identify women with the disease. Fig. 1.2 illustrates another important feature in the mid-IR range. The two atmospheric transmission windows. They span the wavelength range from 3–5 μm and 8–12 μm . Signals emitted in this wavelength range are less attenuated by water vapor in the atmosphere and can thus travel further distances. Those windows are specially useful for free-space optical communications, remote sensing and thermal imaging. The performance of

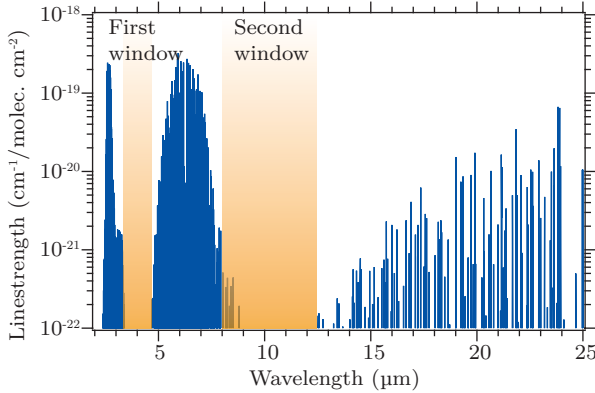


Fig. 1.2: Atmospheric windows in the mid-IR region. The absorption line strength of H_2O shows two transmission windows between 3-5 μm and 8-12 μm . Source: HITRAN 2008.

free-space optical communication links should not be affected by absorbing water vapor present as clouds or fog [23, 24]. Also, atmospheric trace gases are often found in the ppm to ppt concentrations in sensing applications. Therefore even weak interfering water lines can become a problem [4].

1.3 Quantum cascade lasers

Nowadays, the QCL is the dominant semiconductor light source in the mid-IR. It is a unipolar laser based on intersubband transitions in a semiconductor heterostructure [11]. As the emission wavelength of these devices can easily be adjusted by modifying the well and barrier thickness, it becomes possible to cover a very wide mid-IR range using the same material system. Although operation of these devices has been achieved in the Terahertz regime up to wavelengths as long as 250 μm [25, 26] with devices fabricated in the GaAs material system, the best performances have been realized in the mid-IR (from approximately 3 μm to 16 μm) using the InGaAs/InAlAs/InP material system.

Since the first demonstration in 1994 by Faist *et al.* at Bell Labs [11], there has been a tremendous increase in the performance of those devices. The first continuous wave operation of a QCL at room-temperature was demonstrated in 2001 [27]. And nowadays

multi-watt output power in cw at room-temperature with wall-plug efficiency in excess of 10 % are reported. The wavelength that is covered by those high-power devices now spans an important portion of the mid-IR range, namely from 4-9 μm [28–34]. Single ended 4.5 W and 5.1 W output power are reported by Pranalytica, Inc. and the group of Professor M. Razeghi at Northwestern University [33, 34]. The wall-plug efficiency of these devices reaches 20 % in continuous-wave and 27 % in pulsed mode [33]. Another important factor for system integration is the reliability of such devices. High-power QCLs emitting 3 W power have shown operation of over 2'000 hours [34]. Operation temperature of QCLs nowadays exceeds 400 K [35, 36]. Apart from high-power devices, there has been an increased interest in realizing low dissipation devices [37, 38]. These devices are specially interesting for spectroscopic applications. Decreasing the energy-footprint of QCLs allows for easier integration of spectroscopic systems. Single-mode high power devices have also seen a tremendous boost in performance. Applications that rely on high-power single-mode sources, like QEPAS, profits from these sources. High-power single mode DFBs have been demonstrated emitting 2.4 W [39]. Another approach to achieve high-power single-mode emission is the use of a master-oscillator power-amplifier section (MOPA) [40, 41]. Short wavelength Sb-free strain-compensated operation of QCLs down to 3 μm with pulsed power in the watt range and continuous wave operation was recently shown [42–44]. The development of broadband sources and broadly tunable single mode-sources has also seen important advances in the last years. Those will be covered more throughout in section 2.2 and 4.

1.4 Laser spectroscopy

As we have seen in section 1.2, one big advantage is the higher-sensitivity of spectroscopic applications in the mid-IR range compared to the near-IR range. Furthermore, most of the mentioned applications beforehand profit from laser spectroscopy. This section first points out the advantages of laser spectroscopy compared to classical absorption spectroscopy. Afterwards follows a review of a small selection of laser spectroscopic techniques for mid-IR applications. This is not intended to give a full review on possible laser spectroscopic techniques, interested readers are advised to consult Ref [8].

There are many advantages of laser spectroscopy compared to classical absorption spectroscopy. Fig. 1.3 compares both techniques of common setups schematically. The classical absorption spectroscopy shown in figure 1.3a uses a broad, non coherent emission source in combination with a wavelength selecting element in order to obtain the

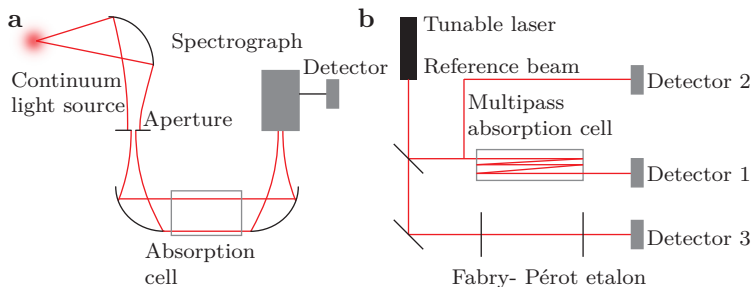


Fig. 1.3: **a** Absorption spectroscopy with a broadband incoherent source and **b** with a tunable single-mode source. Figures adapted from [8].

spectrum as a function of λ . The absorption spectrum is computed as followed [8]

$$P_A(\lambda) = a[P_0(\lambda) - P_T(\lambda)]. \quad (1.1)$$

P_0 is the initial transmitted power without an absorbing species present, whereas P_T is the transmitted power. The factor a accounts for wavelength dependent losses. P_T can be calculated using the Beer-Lambert law

$$P_T(\lambda) = P_0 e^{-\alpha(\lambda)l}, \quad (1.2)$$

where $\alpha(\lambda) = N\sigma(\lambda)$ is the wavelength dependent absorption coefficient, $\sigma(\lambda)$ is the absorption cross section and N number density of absorbing molecules. Among others, important limitations of this techniques are [8],

Resolution

The spectral resolution depends on the spectrometer used and is in general limited. The large dimension of the glowbar becomes a limiting factor for high-resolution spectroscopy. To resolve this problem, an aperture is in general put within the laser beam, which results in a reduction of optical power.

Sensitivity

The sensitivity is limited. The spectral power density of those broadband sources is limited. Intensity fluctuations of the radiation source and the detector also limit the sensitivity. This can partially be overcome with integration techniques, such as signal averaging or lock-in techniques. Of course, this results in longer

acquisition times.

Speed

The measurements of P_0 and P_T are in general performed sequentially. Often long integration times are needed. The dispersive optics can be slow.

Fig.1.3b show a typical setup for laser absorption spectroscopy. The laser beam is split into three different beams. The reference beam P_R does not pass the absorption sample. The measurement beam P_T is transmitted through a multipass cell. A third beam passes through a high-finesse Fabry-Pérot etalon to generate precise frequency markers. Some advantages are [8]

Resolution

Lasers feature extremely narrow linewidths.

Sensitivity

The narrow linewidths results in spectral power densities orders of magnitudes higher than conventional glowbars. Detector noise becomes in general insignificant because of the high power spectral densities. Signal-to-noise ratio can further be improved by stabilizing the power fluctuations of the laser. Because of the high spectral power densities available, long multipass cells are commonly used. This enables the detection trace gases with small absorption coefficients even at very low concentrations.

Ease of use

No monochromator such as a diffraction grating or a Michelson-interferometer is needed. The possibility to easily collimate the beam without any necessary aperture makes it easier to couple the beam into the absorption cell.

Speed

Fast wavelength tuning is possible. The absorption can be measured directly. Time resolved spectroscopy is possible.

1.4.1 Long-path absorption spectroscopy

In trace gas sensing applications, the number density of absorbing molecules N often is very small. Detection limits of ppb to ppt are not uncommon. One way to increase the sensitivity if we consider Beer-Lamberts absorption law (see eq.1.2) is to simply increase the path length l [9]. To achieve this, the use of multipass absorption cells is commonly used, such as the White or Herriott cells [45, 46]. Already a path length

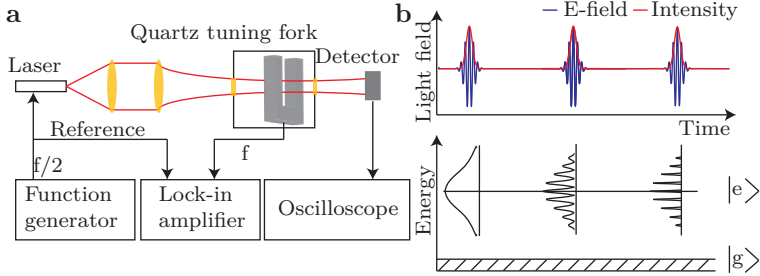


Fig. 1.4: **a** Quartz enhanced photoacoustic spectroscopy. Standard setup as described in Ref. [50].

b Time and frequency interpretation of the interaction of a series of pulses with an atomic system. The bandwidth of the first pulse is much broader than the resonance line. If in resonance, subsequent coherent pulses can then coherently accumulate from the ground state $|g\rangle$ to the excited state $|e\rangle$. Figure inspired by [51].

of 1 m with a typical fundamental absorption cross section of $\sigma(\lambda) = 10^{-18} \text{ cm}^2$, it is possible to detect a concentration of 4 ppb at atmospheric pressure [9]. Astigmatic multipass cells working in the mid-IR wavelength range of 3-11 μm available at *Aerodyne Research* for example allow for a path length of 76 m (100 m) using a base path of only 32 cm (55 cm) [47–49].

1.4.2 Photoacoustic spectroscopy

Another laser spectroscopy application worth mentioning is the photoacoustic spectroscopy. Photoacoustic spectroscopy is another sensitive spectroscopic technique [52] featuring many advantages for real-life applications [3, 53]. The key benefits of this technique are clearly the small size, robustness and its simplicity. Comparable detection limits to multipass absorption spectroscopy with sample sizes as small as $\sim 10 \text{ cm}^2$ are achieved. The first photoacoustic measurements based on laser sources was demonstrated by Kerr and Atwood in 1968 [54]. Pioneering work on trace gas detection using photoacoustic detection with coherent light sources was done by Kreuzer in 1971 [55]. The technique is based on the thermal expansion of the medium heated through absorbing radiation. The incident radiation is modulated at the frequency f , which generates a sound wave at said frequency. This sound wave can be detected using a sensitive

microphone. The detected signal $S(\lambda)$ is proportional to the incident power $P(\lambda)$ [9]:

$$S(\lambda) = C \cdot \alpha(\lambda) \cdot P(\lambda). \quad (1.3)$$

The constant C represents the cell constant. In order to enhance the signal, it is common to surround the gas with a acoustic resonator [53]. The quality factor of the acoustic resonator is Q . As can be seen from eq. 1.3, the detected signal is directly proportional to the absorbed power $P(\lambda)$. An important factor is the modulation speed. It must be smaller than the inverse of the molecular relaxation time, but Q times faster than the inverse molecular diffusion time. The sound wave needs Q laser modulation periods build up the sound wave. The effective integration time is therefore $t = \frac{Q}{f}$. Integration times as high as $t = 0.056$ s are reported this way ($Q = 70$, $f = 1250$ Hz) [56]. However, longer integration times are hard to achieve due to already mentioned molecular diffusion time and other relaxation processes.

One noticeable version of photoacoustic techniques is the quartz-enhanced photoacoustic spectroscopy, which was first reported in 2002 in by Kosterev *et al.* the group of F. Tittel at Rice University [50, 57–59]. A schematic illustration of this technique is shown in figure 1.4a. Instead of storing integrated absorbed energy in the medium, the energy is stored in the sensitive element. Therefore much longer integration times are possible. Typical quality factors of 8000 at atmospheric pressures are available for piezoelectric crystal quartz resonator, resulting in integration times of $t \approx 250$ ms. Quartz-enhanced photoacoustic spectroscopy profits from many factors. Among others, it allows for sample volumes of only ~ 1 mm³ and is immune to environmental acoustic noise. Recently, using a state of the art DFB QCL emitting almost 1 W cw-power, detection limits of N₂O and CO of 4 ppbv respectively 340 pptv were achieved using a QEPAS system [60].

1.4.3 Comb spectroscopy

The ideal spectroscopic technique does not exist. One needs to make a compromise between bandwidth, resolution, spectral power densities, sensitivity, acquisition speed, size and stability. Measurements which need to resolve broadband features might profit from FTIR measurements, but suffer under the low power of the blackbody source. To achieve decent resolution and a high sensitivity long acquisition times are needed. Laser absorption spectroscopy performed with a DFB on the other hand feature in general high power, high resolution but might not be suitable due to the limited tuning width. External-cavity setups allow for very broad but relatively slow single mode tuning. Additional external components are required, which results in a less than

ideal situation for mechanical stability. In combination with the high requirement of the exact alignment of those optical components, it remains a real challenge to build stable field deployable mode-hop free setups. Therefore there is still an urgent need for a spectroscopic technique without any movable parts which combines high bandwidth, low sensitivity, high resolution and rapid data-acquisition.

Recently, frequency combs have seen a lot of interest to serve as a broadband and yet high-brightness sources for spectroscopic applications [51, 61–65]. It is interesting to note that the idea to use a pulsed lasers for high resolution spectroscopy applications dates as far back as the 1970. Its usefulness was already understood before the revolution that was triggered through mode-locked lasers in optical frequency metrology [66–70]. Ramsey spectroscopy can be regarded as the root of direct comb spectroscopy [51]. The early experiments are optical analogs of the Ramsey method [71–73]. As a matter of fact, in these Ramsey experiments applied to two photon transitions linewidths narrower than the pulse bandwidth were measured.

This idea is illustrated in Fig. 1.4b and explained well in the work by Stowe *et al.* [51]. The principle is the use of two or more separated atomic beam interaction zones with a fixed phase using either microwave or optical excitation fields. When passing through the first interaction zone the atomic system sees short pulse excitation. The broadband nature of the pulse excites all electrons from the ground state $|g\rangle$ to an excited state $|e\rangle$. The molecule is found in a coherent superposition of lower and upper state. When the light is on resonance in the next interaction zone, the linewidth subsequently collapses. Only if the light is on resonance, the atomic polarization adds constructively, as shown in Fig. 1.4b. On the other hand, if the light is not on resonance, the following pulses do not arrive in phase with the evolving polarization and the population is again moved to the state $|g\rangle$. Another example of early adaption are the measured Doppler-free absorption spectra using a train of picosecond laser pulses [74, 75]. Furthermore, the idea to use frequency-modulated lasers to achieve the same goal was developed in the same time frame [76–78].

A frequency comb spans a broad bandwidth. However, the spectral resolution and precision are not impaired by this broad spectral coverage. This is due to the long coherence time originating of a fixed phase relationship between the laser modes, which results in a periodic waveform at the round trip frequency. The revolution in direct frequency comb spectroscopy, where the comb frequencies may be absolutely referenced, is the possibility to perform precision spectroscopy over a bandwidth of several tens of nanometers [51, 61].

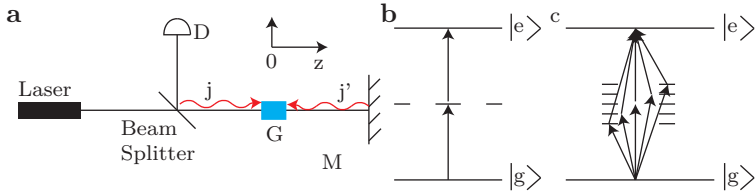


Fig. 1.5: **a** Simple two-photon spectroscopy setup. **b** Two-photon spectroscopy with a cw-laser source. **c** Two-photon spectroscopy with an optical frequency comb. If the modes of a frequency comb are properly phased, a pairwise addition of comb modes in resonance provides an efficient two photon excitation.

Single-photon comb spectroscopy

Single-photon spectroscopy is experimentally the simplest way for direct-comb spectroscopy. The frequency-comb can be regarded as a multi-mode laser with narrow linewidth modes at precisely known optical frequencies. Therefore, methods developed for continuous-wave spectroscopy can be applied with the additional absolute knowledge of f_r and f_0 . One compromise in single-photon direct-comb spectroscopy to be mentioned is the reduced spectral power density compared to a single mode source, since the total power of the laser is distributed between all comb-tooth. Therefore spectroscopy has to be performed with rather low power levels.

Multi-photon comb spectroscopy

Multi-photon absorption techniques [79] are also useful for comb spectroscopy [61, 80]. Among other applications, Doppler-free two-photon spectroscopy is a powerful method for metrological purposes to stabilize a laser line to a narrow absorption linewidth [81–83]. It allows for a very high resolution spectroscopy, since the first-order Doppler effect is canceled. Even though most experiments have been conducted in the near-IR, the existence of strong two-photon absorptions in the mid-IR should not be forgotten. As an example, SF_6 , a widely used gas for trace applications, shows strong two-photon absorption in the mid-IR range [84]. Stabilizing two CO_2 lasers with an output power of 50 mW on a strong two-photon transition, heterodyne-beat linewidths between the two lasers as narrow as 7.9 Hz were measured [85]. Fig. 1.5a shows an illustration of a Doppler free setup, in which co propagating j and counter propagating j' interact with a gas which is found in thermal equilibrium.

The advantage to perform two-photon spectroscopy with a comb is, that it can use

the combined intensity of all pairs of modes which are in resonance. This is illustrated in Fig. 1.5b and c. If the multi-photon detection does not pass through an intermediate state and a pair of modes is in resonance, then all modes of the comb will form a pair of modes. Therefore, the transition rate of a single-mode continuous-wave excitation of a two-photon transition is the same as if you excited the transition with a fundamentally mode-locked laser emitting pulses [86]. This concept of two-photon detection also works with a perfectly FM-laser [78]. This is specially interesting considering the results presented in chapter 5 on frequency-comb operation of QCLs which feature a phase relationship similar to a FM-laser. In the early works of Hänsch *et al.* [78] some very interesting concepts are already found to use such a frequency-modulated laser as an exact ruler in the optical domain if this ruler can be locked to a narrow absorption line. The authors work out the possibility to use this FM-laser to do a Doppler-free two-photon spectroscopy.

The condition on the phase across multiple comb components for a two-photon detection is more strict compared to a single-photon spectroscopy experiment. Therefore, the absorption strength of the signal will depend on the relative atomic resonance frequency ω_{ge} compared to the comb-center frequency ω as well as the position and size of the sample in question. The strongest absorption for a perfectly FM-laser with $\omega_{fg} = 2 * \omega$ is found at a phase delay of π of co propagating and counter propagating at $z=0$. Even though the laser spectrum spans $2 * \Delta\omega$ around the center wavelength ω , it is possible (under ideal conditions) to use the entire power of the laser to contribute to the two photon absorption. This is specially relevant for such an absorption, since the absorption rate is proportional to the square of the laser light intensity $R \propto I^2$.

Mid-IR comb spectroscopy

There is obviously great interest to perform comb measurements in the mid-IR region to profit from the fundamental roto-vibrational absorption bands [87]. Comb spectroscopy in the mid-IR combines broad spectral coverage, high sensitivity with the high spectral resolution of a laser. One important factor is the availability of frequency-comb sources in the mid-IR. This is discussed in detail later in section 5.4. Being the dominant semiconductor laser source in the mid-IR region, comb operation of the QCL is very desiring. The demonstration of optical frequency comb operation of a broadband QCL is shown in chapter 5.

To achieve high-resolution spectroscopy by employing frequency combs, the detection setup must meet several criteria. First, if no prior filtering is desirable, it needs to be broadband. Second, it needs to feature a high resolving power in the frequency domain. In the first direct-frequency comb experiments, the spectral discriminator

was the atomic system under study itself. Early examples are the single-photon spectroscopy of Rubidium [80] or Cesium [62]. The optical excitation is then measured as a fluorescence or ionization of the excited state. Another idea is to use a high-resolution spectrometer to resolve individual comb lines in a parallel way. A relatively simple possibility is the use of a grating-spectrometer [63]. This is often not an adequate solution. The resolving power of the grating (tens of gigahertz) as well as the bandwidth is limited (hundreds of THz). Another method is to use a frequency-comb as a glowbar source in an FTIR. This way, the authors could show that they were able to recover the absorption as well as dispersion spectrum from the inquired sample [96, 97]. One comb spectroscopy technique which absolutely needs to be noted is the coherent dual-comb spectroscopy, which exploits the frequency comb characteristics of equally spaced modes. In essence, the dispersive element is replaced by the equally frequency grid of a second optical frequency comb. This idea leads to this simple and beautiful realization.

Coherent dual-comb spectroscopy

Before the first coherent dual-comb spectrometer in the optical domain was realized, ideas and demonstrations were already realized in the microwave range. The all-electronic terahertz spectrometer presented in Ref [98] was based on picosecond pulses generated by phase-locked monochromatic microwave through nonlinear GaAs transmission line. Their wavelength coverage was a discrete spectrum of lines from 6 to > 450 THz. With this technique they realized hertz-level precision. In 2002, Schiller proposed the realization of a dual-comb setup using optical frequency combs [99]. A few years later, Keilmann F. *et al.* who was already involved in the all-electronic terahertz spectrometer, was able to extend the concept to the optical domain [100]. Nowadays, the coherent dual comb spectrometer is a widely used method in the mid-IR and other wavelength-ranges from which sprout many different applications. [89–91, 101–111]

The working principle is comparable to a FTIR but the interferogram is recorded in the time-domain. Fig. 1.6a illustrates the principle setup for a dual-comb spectrometer. The time domain spectrum is recorded on a detector by superimposing two optical frequency combs with slightly different repetition frequencies. One of the combs acts as a local oscillator, the other comb is sent through the sample. In order to understand the basic principle of dual-comb spectroscopy, consider a coherent frequency comb composed of equally spaced frequencies nf_r , with $n = 1 \dots N$, as illustrated in fig. 1.6b. Superimposing a second coherent frequency comb with a repetition frequency of $f'_r = f_r - \Delta$. Neighboring comb lines will generate a characteristic beating of frequency $n f_r - n(f_r - \Delta) = n\Delta$ on the detector, if the condition $\Delta < \frac{f_r}{2N}$ is fulfilled. This beating provides a phase coherent link between the optical frequency domain and the radio

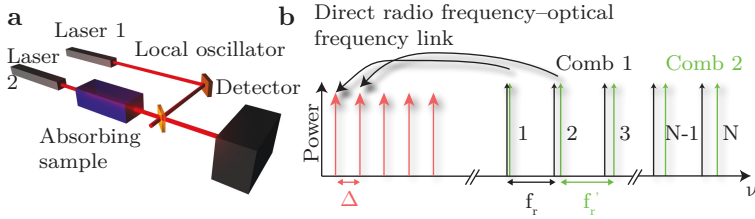


Fig. 1.6: **a** Dual-comb spectroscopy. Two optical combs are superimposed to generate a time-domain scanning interferogram. No moving parts are necessary. **b** Dual-comb spectroscopy explained in the frequency domain. Neighboring modes of the two combs with slightly different repetition frequencies of f_r and $f'_r = f_r - \Delta$ will generate a characteristic beating of frequency $n\Delta$ in the RF-domain.

frequency domain. This beating can be detected using a fast-enough optical detector. Any absorption of light in the comb that passes the sample will be mapped to the RF-domain, enabling a direct measurement of the absorption spectrum. As it becomes visible, this setup does not need any wavelength dispersion element. Furthermore, it measures the whole bandwidth of the frequency comb in one shot. Also, the resolution of this setup is only limited by the stability and linewidth of the optical frequency combs.

Chapter 2

Quantum cascade laser

This chapter is not intended to give a detailed description of the working principle of the quantum cascade laser (QCL). The interested reader is advised to consult a reference book if desired [112]. The objective of this chapter is rather to cover the physical characteristics of the QCL, which are important in the scope of this work, namely broad gain engineering, group velocity dispersion and nonlinear processes. Broad gain engineering is the basis for broadband tuning of QCLs in an external-cavity configuration, see chapter 4. Some of the work presented here on broad gain engineering useful for external-cavity tuning was discussed and published in a review article in *Semiconductor Science and Technology* [113]. This article was published in collaboration with R. Maulini and includes work done during his PhD thesis on broadly tunable mid-infrared quantum cascade lasers [12]. Broad gain engineering is furthermore important for frequency comb operation of QCLs covered in chapter 5. Another important factor for comb operation of QCLs is the group velocity dispersion in these devices. Therefore, the present chapter continues to describe the process of the buried-heterostructure and theory to understand and engineer the group velocity dispersion in these lasers. Nonlinear processes present in QCLs are important to understand the locking principle of QCL frequency-combs. Furthermore, the treatment of the QCL as a nonlinear medium opens new avenues to use the QCL for stabilization and measurement purposes.

2.1 Fundamentals

The quantum cascade laser is a unipolar device, in which the optical transition occurs between quantum confined states in the conduction band of a semiconductor heterostructure. Fig. 2.1a shows a schematic conduction band diagram of such a laser.

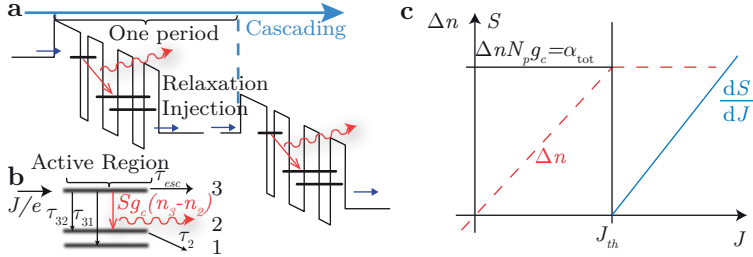


Fig. 2.1: Schematic conduction band diagram of a quantum cascade laser and gain clamping. **a** Cascading of the fundamental period in quantum cascade lasers. One period can be split into two parts, the active region and the relaxation/injection region. **b** Population inversion analysis in a quantum cascade laser transition by a simplified rate equation model. The most important non-radiative lifetimes are indicated. **c** Population inversion as a function of injection current density J assuming zero thermal population. Above threshold when the modal gain overcomes the total losses, the gain is clamped.

In comparison with the first proposal of a semiconductor laser based on a superlattice from Kazarinov and Suris in 1971 [114], the first working device developed at Bell Labs in 1994 by Faist *et al.* [11] was made up from two different regions, the active region and the relaxation/injection region. The separation of one period of the superlattice in these two parts made the laser electrically stable. Cascading of these periods comes naturally. The entire gain medium in quantum cascade lasers is therefore made of N_P repetition of the fundamental period. Each electron undergoes multiple transitions and can in the best case emit N_P photons. Increasing the number of periods is therefore a straight way to increase the slope efficiency $\frac{dP}{dI}$ of QCLs, where P is the optical power and I is the injection current. Furthermore, it also helps reducing the threshold current density J_{th} , since the modal overlap factor Γ of the lasing mode with the gain medium is increased. The additional cost of the increased number of periods is the increased total alignment voltage with the number of periods.

2.1.1 Rate equations

A simple atomic level analysis of QCLs, in which the gain region consists of three states, gives insight into important design parameters of QCLs. Further in chapter 4, we will include an external cavity to the rate equations. The most basic model of a QCL is shown in fig. 2.1b. Due to historic reasons, the system is represented as a

simplified three level system. The rate equations of a single stack QCL are given by

$$\frac{dn_3}{dt} = \frac{J}{e} - \frac{n_3}{\tau_3} - Sg_c(n_3 - n_2) \quad (2.1)$$

$$\frac{dn_2}{dt} = \frac{n_3}{\tau_{32}} - \frac{n_2 - n_2^{\text{therm}}}{\tau_2} + Sg_c(n_3 - n_2) \quad (2.2)$$

$$\frac{dS}{dt} = \frac{c}{n} \left([N_p g_c(n_3 - n_2) - \alpha_{tot}] S + \beta \frac{n_3}{\tau_{sp}} \right) \quad (2.3)$$

where S is the photon flux per unit active region width ($\text{cm}^{-1} \text{s}^{-1}$), n_3 and n_2 are the upper and lower sheet densities per period (cm^{-2}), τ_3 and τ_2 are the total lifetimes of states 3 and 2, τ_{32} is the nonradiative relaxation time from level 3 to level 2, τ_{sp} is the spontaneous emission lifetime, n_2^{therm} is the thermal population of level 2, β is the fraction of spontaneous light emitted into the lasing mode, e is the elementary charge, n is the refractive index of the mode, c is the speed of light in vacuum and J is the injection current density. The total chip losses α_{tot} are the sum of the waveguide losses and the mirror losses. The gain cross section at the peak of the gain curve is given by¹

$$g_c = \frac{\Gamma}{N_p} \frac{4\pi e^2}{\varepsilon_0 n \lambda} \frac{z_{32}^2}{2\gamma_{32} L_p}, \quad (2.4)$$

where Γ is the modal overlap of the lasing mode with the active region, N_p is the number of periods, e is the elementary charge, ε_0 is the vacuum permittivity, n is the refractive index of the active region, z_{32} is the dipole matrix element, γ_{32} is the broadening of the transition, λ the wavelength and L_p the length of one period. The total modal gain of the structure is $G_M = N_p g_c (n_3 - n_2)$.

The gain cross section, multiplied by a lineshape function L_G , is given by

$$g_c(\lambda) = \frac{\Gamma}{N_p} \frac{4\pi q^2}{\varepsilon_0 n \lambda} \frac{z_{32}^2}{2\gamma_{32} L_p} L_G(\lambda_{\text{peak}} - \lambda) \quad (2.5)$$

The total modal gain at wavelength λ of the structure is $G_M(\lambda) = N_p g_c(\lambda) (n_3 - n_2)$.

The threshold condition for a QCL can therefore be calculated. To drive a QCL above threshold, it is necessary that the modal gain G_M overcomes the total losses of

¹Usually, the gain cross section is defined as the one where all periods are put together, that is $g_c = \Gamma \frac{4\pi q^2}{\varepsilon_0 n \lambda} \frac{z_{32}^2}{2\gamma_{32} L_p}$. The rate equations are however written per period, therefore the gain cross section in this work is also defined per period.

the device α_{tot} .

$$J_{th} = e \frac{\frac{G_M}{\alpha_{tot}} + n_2^{therm}}{\tau_{eff}}, \quad (2.6)$$

where we defined the effective lifetime to be $\tau_{eff} = \tau_3 \left(1 - \frac{\tau_2}{\tau_{32}}\right)$. Fig. 2.1c illustrates the evolution of the population inversion as a function of injection current density J assuming zero thermal population. Above threshold when the modal gain overcomes the total losses, the gain is clamped. By setting the time derivative of the rate equations to zero and assuming uniform gain saturation it is possible to extract the slope efficiency of the device yielding

$$\frac{dP}{dI} = \frac{N_P h \nu}{e} \frac{\alpha_{m,1}}{\alpha_{tot}} \frac{\tau_{eff}}{\tau_2}. \quad (2.7)$$

The total losses α_{tot} of a QCL are composed of the waveguide losses α_{wg} and the mirror losses α_m ,

$$\alpha_{tot} = \alpha_{wg} + \alpha_m. \quad (2.8)$$

The mirror losses are a function of the front and back mirror reflectivities (R_1 and R_2) and length of the device L , given by

$$\alpha_m = \frac{1}{2L} \ln \left(\frac{1}{R_1 R_2} \right). \quad (2.9)$$

2.2 Quantum cascade laser broadband design

Broadband gain engineering in QCLs is important for any spectroscopic application that relies on broadly tunable sources. In QCLs, the gain is maximized through the engineering of oscillator strength and the lifetimes. The gain of QCLs can in principle be broadened in two ways. Firstly through the engineering of the well and barrier thicknesses and secondly through the cascading of dissimilar active regions.

Broadband active region designs

With the introduction of two new QCL designs in 2001, namely the bound-to-continuum design [116] and the two-phonon resonance design [117], the performance of QCLs made rapid progress compared with earlier designs [118]. The two-phonon design is very important regarding high-power quantum cascade lasers. It is still a very popular and

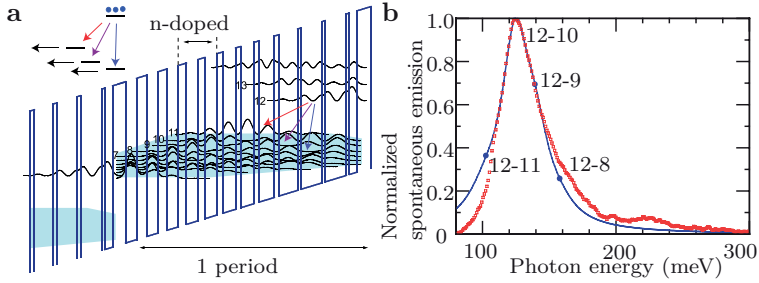


Fig. 2.2: Bound-to-continuum design. **a** QCL active region based on the bound-to-continuum design emitting at $9.75\ \mu\text{m}$. Applied electrical field $35\ \text{kV/cm}$. **b** Simulated and measured electroluminescent spectra. Solid line: Measured luminescence spectrum at $300\ \text{K}$ under a bias of $8\ \text{V}$. Dashed line: Sum of the computed oscillator strengths of the transitions from level 12, taking into account different linewidth broadenings arising from interface roughness scattering. Data published in [113, 115].

widely used design for high power QCLs like the non-resonant extraction (NRE) [29, 119, 120] design used in the $4.3\ \mu\text{m}$ range and the three-phonon extraction design used in the $7\text{--}10\ \mu\text{m}$ range [31, 32] region are in principle derivatives from the two-phonon design. The invention of the bound-to-continuum design was however historically more important with respect to broad gain engineering. Lasers featuring broadband gain while at the same time having high performance experienced a boost with this active region design. Fig. 2.2a shows a typical conduction-band diagram of a bound-to-continuum design. Lasers based on this design were successfully used as a gain medium for broadband tuning by Maulini *et al.* in Ref [115]. The laser transition occurs between a single upper state (12) and a set of delocalized states (11-8) over a chirped superlattice forming a quasiminiband. This results in a large electroluminescent linewidth of typically $\approx 40\text{--}20\ \text{meV}$ ($320\text{--}160\ \text{cm}^{-1}$), depending on the bias voltage. A two-phonon design features over the whole bias voltage a linewidth of $\approx 20\ \text{meV}$ ($160\ \text{cm}^{-1}$) [115, 121]. Due to the fact that all the transitions share the same upper state, laser action at a particular wavelength reduces the gain over the whole range. This reduction is homogeneous if the populations of the lower states are negligible, which is the case due to the fast intraminiband relaxation by emission of optical phonons. Fig. 2.2b shows the electroluminescence spectrum of a $180\ \mu\text{m}$ squared sample at room temperature under an applied bias of $8\ \text{V}$. The FWHM is $36.9\ \text{meV}$ ($297\ \text{cm}^{-1}$). For comparison, a line shape obtained by summing the computed oscillator strengths of the various transitions, assuming Lorentzian broadening, is plotted along the experimental data.

The broadening of the miniband states is so significant, that they are individually indistinguishable and form a continuum. The agreement with the measured spectrum is good except for the energy region near 100 meV. It is attributed to a value of 12 – 11 transition oscillator strength lower than the computed one resulting from dephasing scattering. This shows the limit of the density matrix model used for the calculation and could be resolved by switching to other model approaches, like the nonequilibrium Green's functions.

Considering the gain cross section g_c given in equation 2.4, one can see that the gain decreases linearly with the broadening of the transition γ_{32} . Nevertheless, such QCLs based on the bound-to-continuum design features similarly low threshold currents and output powers [121]. This is mainly due to the larger dipole matrix element in the bound-to-continuum design, which can compensate for the broader transition.

There has been a fair amount of activity lately to come up with new inherently broadband designs by several parties. Some noticeable designs which were successfully tuned over a large bandwidth in an external cavity configuration (see sec. 4) are the dual-upper-state design [123] and its successor, the dual-upper-state to multiple-lower-state design [124, 125]. Another design is the continuum-to-bound [126] and its follower, the continuum-to-continuum design [122] which features multiple upper state transitions from strongly coupled upper states.

The dual-upper-state design was introduced by Fujita *et al.* from Hamamatsu Photonics in 2010. It showed a luminescence linewidth of 40 meV (320 cm^{-1}) at a wavelength of $\lambda=8.4\mu\text{m}$ over the whole applied bias range (5V - 11V). The device reached peak output powers of 400 mW in pulsed operation (100 kHz, 100 ns) up to 400 K. This design was further developed into the dual-upper-state to multiple-lower-state design. The bandstructure of such a design operating at a wavelength of $6.8\mu\text{m}$ is shown in fig. 2.3a [125]. This particular example features a homogeneous linewidth of 74 meV (600 cm^{-1}). Regardless the large linewidth, the output power of this device reaches 700 mW output power in continuous wave operation at 280 K. It should be noted however, that the conduction band diagram of a dual-upper-state to multiple-lower-state design shown in fig. 2.3a is very similar to a traditional bound-to-continuum design shown in fig. 2.2a. The main difference is that the upper laser state 3 and the first excited state 4 are closely spaced by only about 25 meV, whereas the traditional bound-to-continuum designs the transition is considerably larger $\approx 80\text{ meV}$. Furthermore, as it has been pointed out in Ref. [115], the transition from the first excited state to the continuum is already visible in the traditional bound-to-continuum design.

The previously mentioned continuum-to-continuum design by Yao *et al.* achieves a broadening of the linewidth through multiple upper state transitions from strongly

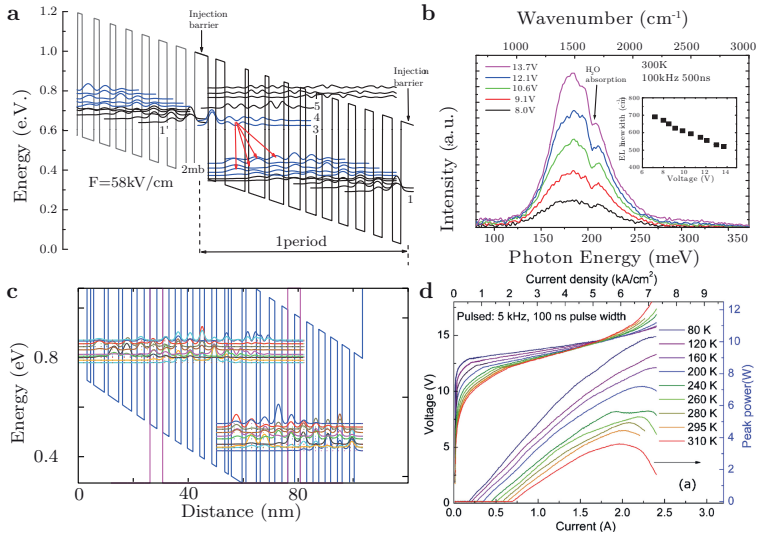


Fig. 2.3: Alternative broadband designs. **a** Bandstructure of a dual-upper-state design. **b** Measured luminescence spectra. Reprinted with permission from Kazuue Fujita *et al.*, APL **98** 231102 (June 2011). © 2011, American Institute of Physics. **c** Simulated bandstructure of a continuum-to-continuum design published in Ref. [122] using the software of our group. **d** Pulsed LIV characteristics of the structure published by Yao *et al.* in [122]. Pulsed operation, 100 ns pulse width, 100 kHz repetition rate. The data is corrected for 74 % collection efficiency and the optical output power is multiplied by two to account for the two facets. Reprinted with permission from Yu Yao *et al.*, APL **97** 081115 (August 2010). © 2010, American Institute of Physics.

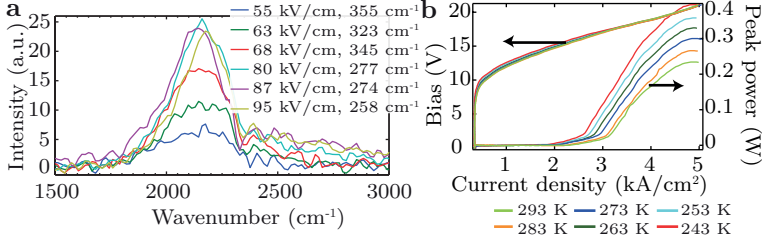


Fig. 2.4: Luminescence and LIV measurements of EV1470D, a redo from the broadband continuum-to-continuum design published in [127]. **a** Luminescence measurements at 20°C (201 ns, 200 kHz) at different applied biases of a 370 μm long ridge. The light is extracted perpendicular to the ridge. The FWHM of the measurement is indicated after the applied field. **b** LIV characteristics of a 3/ mm long device from EV1470D at different temperatures. The data is not corrected for the collection efficiency.

coupled upper states [127]. Fig. 2.2c shows a simulation of the published design. Due to the short injection barrier, the upper laser states couple with the injector states. The measured luminescence linewidth of that design is 53 meV (430 cm^{-1}) at threshold, which corresponds to an alignment voltage of 59 kV/cm. This decreases to about 34 meV (275 cm^{-1}) at an alignment voltage of 95 kV/cm. Regardless the rather large linewidth, the performance of this device is very good. It features peak pulsed output power of ~ 1.75 W per facet at 310 K and 2.5 W at 260 K (3 mm long, 11 μm wide). The LIV of this device down to a temperature of 80 K is shown in fig. 2.3d, the output power is multiplied by a factor of 2 to account for the two facets. A 5.5 μm narrow ridge buried heterostructure design of this design reaches 0.5 W output power in continuous-wave operation at 285 K.

Due to these impressive results, we decided to grow and fabricate an exact redo of the published design in [122]. These results have been published in a master thesis by S. Riedi [128]. Even though we were able to reproduce the electroluminescence linewidth, our results concerning output power and tuning were never as good as the results of the group in Princeton (see section 4 for the EC-tuning discussion). Fig. 2.4a shows the measured luminescence of a 370 μm long ridge at different alignment voltages. The light is collected from the side of the ridge. The measured FWHM varies between 360 cm^{-1} (at 55 kV/cm) to 260 cm^{-1} (at 95 kV/cm). Those measurements are comparable to the measurements presented by Yao *et al.*. Fig. 2.4b shows the measured LIV characteristics at different temperatures. The laser was operated in pulsed mode (100 ns, 100 kHz). The measured peak output power from a single facet, 3 mm long

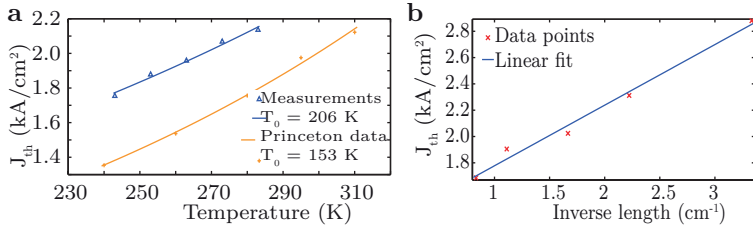


Fig. 2.5: Comparison between the data published in [127] and the redo EV1470D. Characteristic temperature T_0 of EV1470D, a redo from the broadband continuum-to-continuum design published in [127]. **a** Comparison of the threshold current density (J_{th}) and T_0 of the redo and the published data. **b** Calculation of the waveguide losses of EV1470D.

and $10\text{ }\mu\text{m}$ wide ridge, varies between $0.2\text{--}0.4\text{ W}$. This data is however not yet corrected for the collection efficiency of the setup. Taking the usual 65% collection efficiency estimated for our setup (in [122] they estimate 74%), we get 0.51 W peak power at 263 K . Comparing these data to the presented one in the previous section, a similar device (3 mm long, $11\text{ }\mu\text{m}$ wide ridge) produces a peak optical output of 2.5 W at 260 K . Taking the difference in width of the device into account gives a factor 4.5 worse in performance of EV1470D compared to the data published by Yao *et al.*

Fig. 2.5a compares the threshold-currents and the characteristic temperature defined by $J_{th} = J_0 \exp(T/T_0)$ of the published data and the redo EV1470D. Usually a higher characteristic temperature is considered a good thing, since it means the laser-design is less sensitive to a temperature increase. However, too high characteristic temperatures can be an indication of possible current leakage channels in the process or high temperature independent waveguide losses. Furthermore, in our case, we expect the same characteristic temperature as the reference design. We do not believe that the increased T_0 originates from a leakage current. Comparing the rollover-current of EV1470D in fig. 2.4b with the one presented in fig. 2.3d, we realize that our rollover current is lower ($5\text{ kA}/\text{cm}^2$ compared to $\sim 6\text{ kA}/\text{cm}^2$ in the reference design at 295 K) although the doping is nominally the same. The increase in the characteristic temperature can also be explained by increased waveguide losses due to processing (sidewall-roughness, absorption within the cladding, ...). The waveguide losses can be divided into a temperature dependent part and a constant part $\alpha_{wg}(T) = \alpha_{wg,0} + \alpha_{wg,1}(T)$. The characteristic of a good process are low constant waveguide losses. The characteristic temperature in such a case reflects the temperature dependent waveguide losses (carrier leakage into

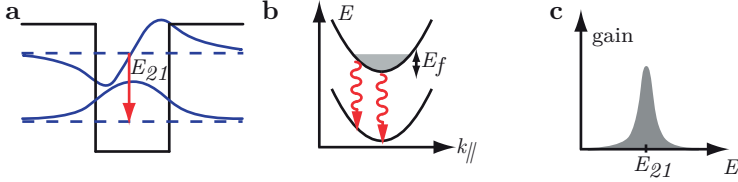


Fig. 2.6: Principal characteristics of an intersubband transition in a quantum well.

the continuum, backfilling and others). We believe we are suffering from considerably higher constant waveguide losses due to processing than the reference design, leading to the higher characteristic temperature. This also explains the lower threshold-current density in the reference design compared to the redo EV1470D. Furthermore, due to stronger photon driven transport in the reference design, the rollover current is pushed to higher values, explaining the discrepancy with our measurement. Higher waveguide-losses also lead to lower tuning ranges in an EC configuration. Together with a rather poor AR coating, this helps to explain the lower tuning ranges we achieved with the redo EV1470D of only 55 % compared with the reference design (see section 4).

We also tried to compare the waveguide losses of our device with the ones from Yao *et al.*. Measuring the $1/L$ characteristics, we get waveguide losses of 3.5 cm^{-1} shown in fig. 2.5b. Comparing the threshold currents before and after depositing an HR coating, we measure waveguide losses of $\alpha_{wg} = 4.3 \text{ cm}^{-1}$. From the published data in [122], we estimate the waveguide losses of the reference design to be $\sim 3.3 \text{ cm}^{-1}$.

Cascading dissimilar active region designs

Since cascading comes naturally in QCLs, the idea to cascade dissimilar active regions was introduced relatively shortly after the first demonstration of the QCL [129, 130]. The principal characteristics of intersubband transitions in quantum wells are illustrated in fig. 2.6. Because they rely on intersubband transitions between confined electronic states in the conduction band heterostructure (see fig. 2.6 a), QCLs feature an atomic-like joint density of states peaked at the transition energy E_{21} (see fig. 2.6 c). As discussed before, they exhibit a relatively narrow gain linewidth of $\approx 20 - 70 \text{ meV}$ full width at half maximum (FWHM) at room-temperature. Furthermore, because the initial and final subbands have the same curvature (neglecting nonparabolicity), this linewidth depends only indirectly on the subband populations through collision processes (see fig. 2.6b). In contrast to this, interband devices feature a broader linewidth, which originates from the opposite curvature of the conduction band and the valence

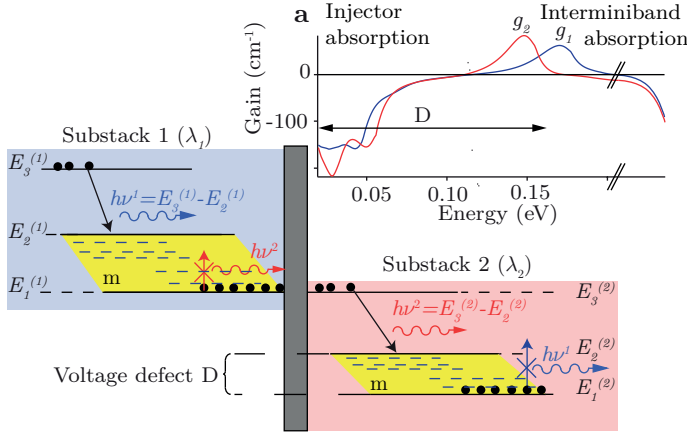


Fig. 2.7: Schematic conduction band diagram of a QCL. It illustrates the cascading principle of QCLs and the possibility to form a broadband emitter by taking advantage of the transparency of the intersubband transition. The broadband emitter is formed by adding different substacks emitting at different frequencies to form the active region. Inset a shows the simulated gain curve of two dissimilar substacks within a QCL as a function of transmission energy.

band in k -space.

Nevertheless QCLs are especially appropriate for broadband applications for the two following reasons. Firstly, intersubband transitions are transparent on either side of their transition energy (see fig. 2.6c). Interband transitions, on the contrary, are only transparent on the low-frequency side of their gain spectrum, and highly absorbing on the high frequency side. Secondly, the cascading principle almost comes naturally because of the unipolar nature of the laser. These two features enable the cascading of dissimilar active-region designs emitting at different wavelengths to create a broadband emitter [129, 130]. In addition, by using designs where a single upper state exhibits allowed transitions to many lower states, active regions with inherently broad gain spectra can be achieved.

Fig. 2.7 shows a schematic conduction band diagram to illustrate these advantages to form a broadband emitter. Quantum wells are transparent to light with frequencies on either side of the intersubband resonant transition, therefore with careful design of two dissimilar substacks, it is possible to prohibit absorption from other pairs of states. Inset a of fig 2.7 shows two gain curves (g_1, g_2) which shows no cross-absorption in the

region of gain. For a better understanding, it is possible to study a simplified three level system. The gain region is assumed to consist of three states, with laser action occurring between levels 3 and 2, whereas the injector is assumed to consist of one level, aligned with the upper level of the next period. The lower energy level of the laser transition is joined with the injector through a miniband (m) consisting of a number of states. Most of the electrons are located in the injector state. By engineering the two substacks carefully, it is possible to prohibit cross-absorption between any pairs of states. This is illustrated on fig. 2.7, photons created by one substack can not scatter any electrons from the injector of the other substack, due to the absence of available states. Fig. 2.7 also illustrates the natural cascading possibility of dissimilar substacks forming a broadband active region.

2.2.1 Rate equations heterogeneous laser

The rate equations developed in section 2.1.1 must be adapted for a heterogeneous laser [12]. We consider a heterogeneous QCL composed of N substacks, where substack i contains $N_{p,i}$ gain stages emitting at wavelength λ_i . The evolution of upper and lower states sheet carrier densities per stage in substack i is $n_{3,i}$ and $n_{2,i}$. The photon flux densities S_{λ_i} at the peak of the gain curves of the individual substacks are described by $3N$ coupled equations:

$$\frac{dn_{3,i}}{dt} = \frac{J}{q} - \frac{n_{3,i}}{\tau_{3,i}} - S_{\lambda_i} g_{c,i}(\lambda_i) (n_{3,i} - n_{2,i}) \quad (2.10)$$

$$\frac{dn_{2,i}}{dt} = \frac{n_{3,i}}{\tau_{32,i}} - \frac{n_{2,i}}{\tau_{2,i}} + S_{\lambda_i} g_{c,i}(\lambda_i) (n_{3,i} - n_{2,i}) \quad (2.11)$$

$$\frac{dS_{\lambda_i}}{dt} = \frac{c}{n} \left[G_M(\lambda_i) - \alpha_{\text{tot},i} \left(J, S_{\lambda_1, \dots, N} \right) \right] S_{\lambda_i} \quad (2.12)$$

where $i = 1, \dots, N$, $g_{c,i}(\lambda)$ is the gain cross section per stage introduced in eq. 2.5, S_{λ_i} is the photon flux at wavelength λ_i per unit width, and

$$G_M(\lambda) = \sum_{i=1}^N N_{p,i} g_{c,i}(\lambda) (n_{3,i} - n_{2,i}) \quad (2.13)$$

is the total modal gain summed over all the substacks. One should be aware of the simplistic model of these rate equations, since they only take into consideration the photon flux densities at the peak of the gain curves and neglect any possible photon flux at different wavelengths. Furthermore, for simplicity, we neglected the spontaneous emission. For the gain cross section, we take the wavelength dependent gain

cross section introduced in eq.2.5. This introduces the effect of overlapping gain of one substack to the other. However, each substack can also introduce non-resonant losses, as a function of injection current density and optical flux density in this substack, possibly at the emission wavelength of another substack². This was added phenomenologically in the loss term of each substack i , $\alpha_{\text{tot},i}(J, S_{\lambda_1, \dots, \lambda_N})$, by introducing a loss parameter which also depends on the injection current density J and all the individual optical flux densities $S_{\lambda_1}, \dots, S_{\lambda_N}$. The first thing that we need to be aware of in the introduced equations is, assuming straight sidewalls, the conservation of current density J in each substack. The origin of the inhomogeneous behavior in a heterogeneous cascade can now be found by combining the conservation of current density J in combination with the photon driven transport in each substack, given by $\tau_{\text{photon},i}^{-1} = S_{\lambda_i} g_{c,i}(\lambda_i) (n_{3,i} - n_{2,i})$. Let us consider the case in which one substack is lasing at wavelength λ_i . The total modal gain $G_M(\lambda_i)$ at this wavelength will be clamped. The other substacks j see however less or no photon driven transport due to the gain location of $g_{c,j}(\lambda_j)$. Therefore, by increasing the current density in the substack, the population inversion in stack j will further increase until the total modal gain at this stack $G_M(\lambda_j)$ will also overcome the total losses $\alpha_{\text{tot},j}$.

2.3 Quantum cascade laser fabrication

This section covers the principle growth and processing steps to realize buried-heterostructure QCLs and covers the applied mounting techniques useful for high-performance QCL operation. Apart from the design of the active region, the processing plays a crucial role in the device performance. The growth of the QCLs is realized by a combination of molecular beam epitaxy (MBE) and metal organic vapor phase epitaxy (MOVPE). Growth and nearly all processing is carried out in FIRST, a shared cleanroom facility for advanced micro- and nanotechnology located at ETH Zürich on the campus of Höggerberg.

Special notice has to be given to A.Y. Cho and J.R. Arthur when it comes to MBE growth and the realization of QCLs. It was only possible to grow QCL active regions with the required precision and quality after the development of the MBE growth in a ultrahigh vacuum chamber by them at Bell Laboratories[131]. The growth of the active region is carried out here at ETH by Dr. Mattias Beck on a solid-source MBE (V80H, VG Semicon). The MOVPE growth is carried out by Dr. Emilio Gini.

²Resonant cross-absorption is already fully included in the rate-equation model without the additional loss terms.

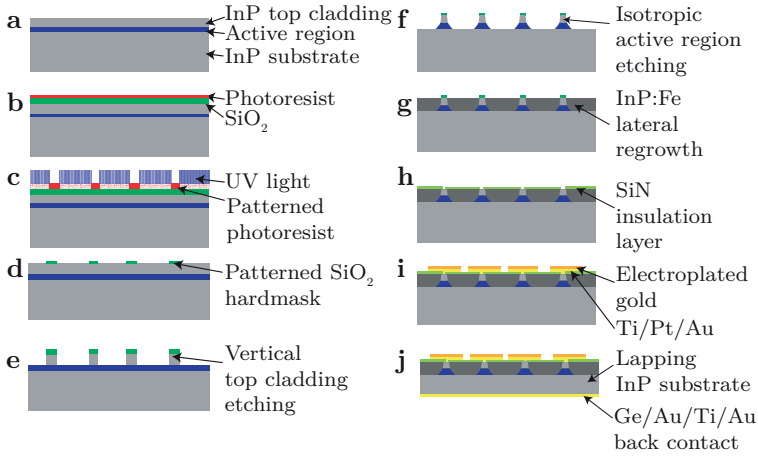


Fig. 2.8: Buried-heterostructure processing steps.

2.3.1 Buried-heterostructure

The employed and processed QCLs which are presented in this thesis are all processed using a buried-heterostructure process. The first mid-IR QCLs were realized using a traditional ridge process. The realization of a laterally regrown buried heterostructure and the subsequent first demonstration by Beck *et al.* in the year 2002 of a room-temperature continuous-wave QCL however clearly empathized the importance of good thermal properties and low optical losses [27, 132]. Furthermore, the invention of the buried-heterostructure QCL helped for the deposition of anti-reflection coatings, which is tremendously important for external-cavity configurations for efficient feedback. The lower residual reflectivity of the AR-coated facets of the buried-heterostructure geometry compared to ridge waveguides is attributed to reduced edge effects during vacuum deposition. A lot of work has been done by Bismuto *et al* on the improvement of the buried-heterostructure process, leading to the inverted buried-heterostructure design [133]. This greatly simplified process featuring many advantages is not covered in this thesis, since the most important results were achieved with QCLs processed in the “traditional” buried-heterostructure geometry.

The processing steps to realize a buried-heterostructure QCL are shown in fig. 2.8 a-j.

- a The active region sequence is grown by MBE on a low doped ($2 \times 10^{17} \text{ cm}^{-3}$) InP 2 in substrate. A nominally very low doped ($2 \times 10^{16} \text{ cm}^{-3}$) top cladding of 2-3 μm thickness is grown subsequently by MOVPE.
- b A $\approx 400 \text{ nm}$ thick SiO_2 layer is deposited by plasma enhanced chemical vapor deposition (PECVD). A thin layer of photoresist is spun on the SiO_2 .
- c Using UV photolithography, the waveguide pattern is transferred to the photoresist.
- d The waveguide pattern is subsequently transferred to the SiO_2 hard mask by reactive ion etching (RIE) using Ar/CHF_3 . The residual photoresist is removed by a oxygen plasma followed by an acetone bath.
- e Vertical sidewalls of the InP top cladding are achieved by using an anisotropic $\text{HCL}:\text{CH}_3\text{COOH}$ (1:3) etching solution.
- f The active region is etched using an isotropic etching solution $\text{HBr}:\text{HNO}_3:\text{H}_2\text{O}$ (1:1:10).
- g The SiO_2 hard mask is also used for the selective planarization regrowth of insulating iron doped InP ($\text{InP}:\text{Fe}$) in the MOVPE.
- h The SiO_2 is removed by HF and an insulating SiN layer is grown by PECVD and opened on the conducting InP involving a photolithography step and RIE.
- i The top $\text{Ti}/\text{Pt}/\text{Au}$ (30 nm/40 nm/150 nm) contact is evaporated using e-beam evaporation. To pattern the contact pads, a lift-off process on negative photoresist is carried out. Electroplated gold is subsequently deposited on the pads.
- j In the final processing steps, the substrate is lapped down to $\approx 180 \mu\text{m}$. This step is important for better heat transport in case of epi-side up mounting. Furthermore it facilitates greatly the cleaving of the thin ridges. The last step consists of the deposition of an ohmic back contact of $\text{Ge}/\text{Au}/\text{Ni}/\text{Au}$ (18 nm/60 nm/10 nm/180 nm).

The mounting of QCLs is usually done epi-side up on copper submounts. However, to increase the performance of QCLs in continuous-wave operation, epi-side down mounting on diamond submounts was also realized. This is possible due to the planarization step in the buried-heterostructure process.

2.4 Group velocity dispersion in quantum cascade lasers

The group velocity v_g as well as the group velocity dispersion (GVD) is an important concept to understand when considering the transport of energy in a dispersive medium. As an example, it plays a crucial role in the ability to generate a frequency comb output in a QCL. The section starts with the formal introduction of the group velocity and its dispersion. To better understand the importance of the GVD, the section will continue with an explanation of the dispersion of the Fabry-Pérot modes in a laser cavity. Then it will give a detailed analysis of the calculation of the GVD in a buried-heterostructure QCL.

In general, the group velocity is associated with the propagation speed of a pulse of energy in a dispersive medium. The pulse $\Psi(z, t)$ is represented as a sum of plane-waves propagating in the z direction,

$$\Psi(z, t) = \int_{-\infty}^{\infty} U(k) e^{i(\omega t - kz)} dk. \quad (2.14)$$

$U(k)$ is the complex amplitude of plane waves with wave number k . It should be noted that the solution $\Psi(z, t)$ is not limited to pulses, it is entirely dependent on the amplitude and phase distribution of $U(k)$. The Fourier spectrum of the field $\Psi(z, t)$ is given by $|U(k)|^2$. Due to the dispersion relation $|k| = \omega \sqrt{\epsilon \mu} = n(\omega) \frac{\omega}{c}$, not all plane waves travel with the same speed. By expanding $\omega(k)$ around k_0 we get

$$\omega(k) = \omega_0 + \left(\frac{d\omega}{dk} \right)_0 (k - k_0) + \dots, \quad (2.15)$$

where ω_0 and k_0 are the center frequency and wave number of the Fourier spectrum. Equation 2.14 becomes

$$\Psi(z, t) = e^{i(\omega_0 t - k_0 z)} \mathcal{A} \left[z - \left(\frac{d\omega}{dk} \right)_0 t \right]. \quad (2.16)$$

\mathcal{A} is the envelope function traveling undistorted apart from a phase factor at the *group velocity*

$$v_g = \left(\frac{d\omega}{dk} \right) = \frac{c}{n + \omega \left(\frac{dn}{d\omega} \right)} = \frac{c}{n_g}, \quad (2.17)$$

where n_g is the group refractive index. The *phase velocity* is given by $v_p = \frac{c}{n(\omega)}$.

In the context of wave propagation in guided media, the refractive index n needs to be replaced by the *effective index of refraction for the mode* $n_{eff} = \frac{\beta}{\omega/c}$, where β

is the z component of the wave vector, the so called propagation constant. A different definition of group velocity useful when dealing with guided modes is therefore

$$\frac{1}{v_g} = \frac{d\beta}{d\omega}. \quad (2.18)$$

To the first order, the envelope travels undistorted in the medium, regardless of dispersion. The effect is a mere difference in speed between the group velocity and the phase velocity. The distortion is governed by higher order terms of the expansion of $\omega(k)$ in eq. 2.15, leading to the definition of the GVD

$$\text{GVD} = \frac{d^2\beta}{d\omega^2} = \frac{d}{d\omega} \left(\frac{1}{v_g} \right). \quad (2.19)$$

The units for the GVD are s^2/m , but it is usually expressed in fs^2/mm . It is useful to note, that the group-velocity dispersion is often defined with respect to wavelength rather than the angular frequency, called D_λ . The units are usually expressed in $\text{ps}/(\text{nm km})$. It is possible to convert between GVD and D_λ using the equation [134]

$$D_\lambda = -\frac{2\pi c}{\lambda^2} \text{GVD}. \quad (2.20)$$

To avoid confusion, it is important to notice that the GVD and D_λ have opposite signs.

2.4.1 Fabry-Pérot emission spectrum

As illustrated in fig. 2.1c, the gain is clamped above threshold. A QCL should therefore lase on just a single mode. However, nonlinear effects in QCLs are responsible that those lasers operate in a multi-mode regime shortly after threshold (see section 2.5). Without any or only weakly nonlinear locking mechanism present, modes above threshold will lase on the dispersed Fabry-Pérot modes.

Fig. 2.9 shows a simulated transmission of a Fabry-Pérot etalon with an intensity reflectivity of $R=0.3$ as a function of phase $\Phi = \frac{2\pi n}{\lambda}l$ and optical frequency ν , where l is the spacing of the two etalon mirrors. The free-spectral range (FSR), which corresponds to the energy spanning between two neighboring modes, of a Fabry-Pérot etalon without any dispersion at normal incidence is given by

$$\Delta\nu = \nu_{m+1} - \nu_m = \frac{(m+1)c}{2nl} - \frac{mc}{2nl} = \frac{c}{2nl}. \quad (2.21)$$

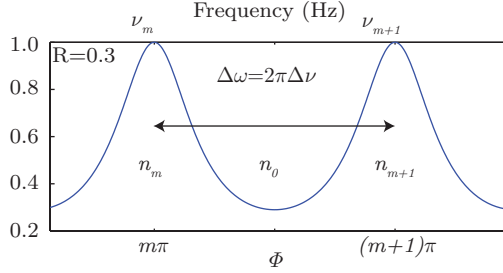


Fig. 2.9: Fabry-Pérot mode spacing in a dispersive medium. The mode spacing is given by the group velocity and the cavity length $\Delta\nu = \frac{v_g}{2l}$.

The refractive index of a dispersed medium is however a function of frequency $n(\omega)$. To calculate the FSR of a Fabry-Pérot etalon forming a laser cavity in a QCL we need to take this dispersion into account. As illustrated in fig. 2.9 we set the refractive index of the medium to be n_0 in the middle of the two resonances m and $m+1$. Neglecting second order terms, the refractive indices at the resonances are therefore $n_m = n_0 - \frac{dn}{d\omega} \frac{\Delta\omega}{2}$ and $n_{m+1} = n_0 + \frac{dn}{d\omega} \frac{\Delta\omega}{2}$. Calculating the FSR results in

$$\begin{aligned}
 \Delta\nu &= \frac{(m+1)c}{2n_{m+1}l} - \frac{(m)c}{2n_m l} \\
 &= \frac{(m+1)c}{2\left(n_0 + \frac{dn}{d\omega} \frac{\Delta\omega}{2}\right)l} - \frac{(m)c}{2\left(n_0 - \frac{dn}{d\omega} \frac{\Delta\omega}{2}\right)l} \\
 &= \frac{(m+1)c\left(n_0 - \frac{dn}{d\omega} \frac{\Delta\omega}{2}\right) - (m)c\left(n_0 + \frac{dn}{d\omega} \frac{\Delta\omega}{2}\right)}{2\left(n_0^2 - \left(\frac{dn}{d\omega} \frac{\Delta\omega}{2}\right)^2\right)l} \\
 &= \frac{cn_0 - c\frac{dn}{d\omega} \frac{\Delta\omega}{2} - (m)c\frac{dn}{d\omega} \frac{\Delta\omega}{2}}{2n_0^2 l} \\
 &= \frac{c\left(n_0 - \frac{dn}{d\omega} \omega\right)}{2n_0^2 l} \\
 &= \frac{cn_0^2}{2n_0^2 l\left(n_0 + \frac{dn}{d\omega} \omega\right)} \\
 \Delta\nu &= \frac{c}{2l\left(n_0 + \frac{dn}{d\omega} \omega\right)} = \frac{v_g}{2l}. \tag{2.22}
 \end{aligned}$$

In this derivation, we neglected all quadratic terms of $\frac{dn}{d\omega} \Delta\omega$. Furthermore we used $m\Delta\omega = \omega \gg \frac{\Delta\omega}{2}$.

As it is clear from the above derivation, the inclusion of the dispersion up to the first order does not lead to a dispersed Fabry-Pérot spectrum. The dispersion of the resonator modes are governed by the GVD of the modes. Therefore a low GVD is a key element to generate an optical frequency-comb characterized by equally distant comb lines.

2.4.2 Calculation of the group velocity dispersion in a QCL

In order to calculate the total GVD of a QCL, we first identify the contributions to the GVD in a buried-heterostructure QCL. We include three contributions to the GVD in our calculations. First, we account for the GVD due to material dispersion (GVD_{InP}). In the calculations, the iron-doped InP (InP:Fe) is assumed to have the same dispersion as InP. Second, the vertical and lateral modal GVDs of the guided mode ($\text{GVD}_{\text{vert,lat}}$). Third, the GVD due to the gain and loss in the active region (GVD_{gain}). Due to the mode profile, the total GVD is calculated as a sum of the individual terms weighted by the vertical or lateral modal overlap $\Gamma_{\text{vert,lat}}$, resulting in

$$\text{GVD}_{\text{tot}} = \Gamma_{\text{lat}} \text{GVD}_{\text{vert}} + (1 - \Gamma_{\text{lat}}) \text{GVD}_{\text{InP}} + \Gamma_{\text{vert}} \text{GVD}_{\text{lat}} + \Gamma_{\text{vert}} \Gamma_{\text{lat}} \text{GVD}_{\text{ar}}. \quad (2.23)$$

To illustrate that better, fig. 2.10 shows a schematic of the vertical and lateral modal overlap of the active region. Let us have a look at the first term of eq. 2.23, $\Gamma_{\text{lat}} \text{GVD}_{\text{vert}}$. The GVD_{vert} arises from the wavelength dependent overlap between the active region and the cladding in the vertical direction, the vertical modal dispersion. This is indicated by the black bar labeled with a 1 in the figure. Looking at the lateral modal profile, it becomes clear, that not all the mode is affected by this dispersion. The tails of the lateral modal profile see only InP in the vertical direction, indicated by the dashed black bar labeled with a 2. The calculated modal-dispersion has therefore to be multiplied by the modal overlap Γ_{lat} . The GVD_{vert} also includes the InP material dispersion and the dispersion due to the doping profile in the top-cladding. By multiplying the GVD_{vert} with Γ_{lat} , we have however neglected the modal overlap of the tails with InP in the lateral direction. This needs to be added to the total GVD, resulting in the second term $(1 - \Gamma_{\text{lat}}) \text{GVD}_{\text{InP}}$. The third term, GVD_{lat} , arises from the modal dispersion in the lateral direction. For the same reasoning as before, the modal overlap needs to be multiplied by Γ_{vert} . For the calculation of the lateral modal dispersion it is important to take zero material dispersion, since the total material dispersion is

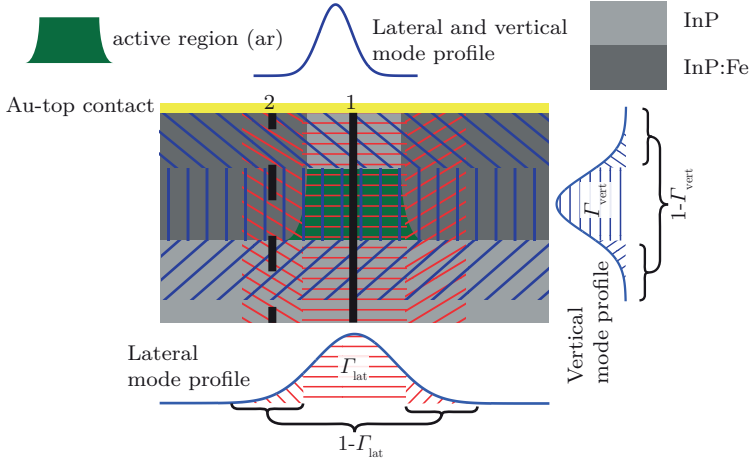


Fig. 2.10: GVD calculation in a QCL. The individual GVD contributions need to be multiplied by the respective modal overlap.

already taken into account with the first two terms. The last term of eq. 2.10, the GVD due to the gain and loss, GVD_{ar} , needs to be multiplied by the modal overlap in both directions $\Gamma_{\text{vert}}\Gamma_{\text{lat}}$.

This is due to the fact that the computation of the GVD_{vert} already includes the . The following sections describe the procedure taken to calculate the individual GVDs.

2.4.3 Material dispersion

The refractive index dispersion of the III-V material system is of paramount importance for a low GVD in QCL. The established material system for mid-IR QCLs is the GaInAs/InAlAs system grown on InP. Fig. 2.11a shows the refractive index of the binary III-V semiconductor compounds of InP/InAs/GaAs/AlAs from Ref. [135, 136]. Data on the ternary compounds is sparse, therefore only the ternary compound of $\text{Al}_{0.3}\text{Ga}_{0.7}\text{As}$ is shown. Looking at the refractive index n , it becomes clear that the material system features a low GVD in the region of $\lambda = 6 - 10 \mu\text{m}$. To calculate the GVD of InP, the data is further fitted using a lattice-vibration oscillator model by

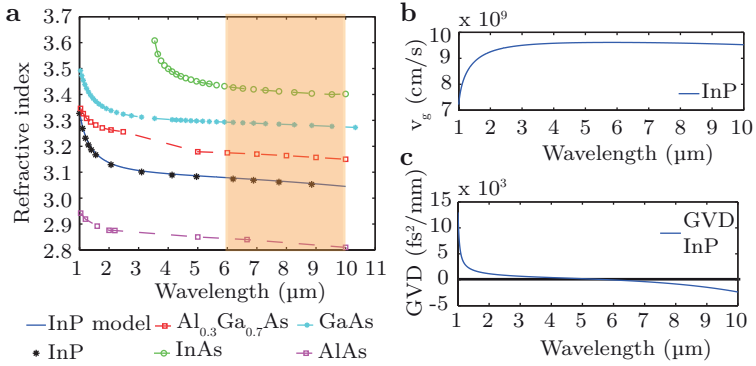


Fig. 2.11: Refractive index and GVD of material systems used for mid-IR QCLs. **a** Refractive index of different binary III-V semiconductor compounds and of Al_{0.3}Ga_{0.7}As. **b** Group velocity of InP as a function of wavelength. **c** GVD of InP as a function of wavelength.

Pikhtin and Yas'kov [135]. The refractive index is given by

$$n^2 = 1 + \frac{A}{\pi} \ln \frac{E_1^2 - (\hbar\omega)^2}{E_0^2 - (\hbar\omega)^2} + \frac{G_1}{E_1^2 - (\hbar\omega)^2} + \frac{G_2}{E_2^2 - (\hbar\omega)^2} + \frac{G_3}{E_3^2 - (\hbar\omega)^2}, \quad (2.24)$$

with $A = 0.7\sqrt{E_0}$, $E_0 = 1.345$ eV, $E_1 = 3.2$ eV, $E_2 = 5.1$ eV, $E_3 = 37.64 \times 10^{-3}$ eV, $G_1 = 57.889$ eV², $G_2 = 65.937$ eV² and $G_3 = 0.392 \times 10^{-2}$ eV².

The fitted refractive index of InP is further used to calculate the group velocity v_g of InP shown in fig. 2.11b. Fig. 2.11c shows the computed GVD of InP as a function of wavelength. It shows that InP features a low GVD in the region of 6-7 μm.

2.4.4 Modal dispersion

The waveguide of the QCL is naturally also a source of the GVD. The waveguide cladding in a buried-heterostructure QCL is composed vertically mainly of low doped InP and laterally of iron-doped InP. Fig. 2.12a shows two vertical mode profiles at a wavelength of 6 μm and 7 μm. As it can be seen, the penetration of the mode in the cladding depends on the wavelength. Therefore the effective index of refraction of the mode n_{eff} has a strong wavelength dependence.

Using the Maxwell equations, it is possible to calculate the effective index of re-

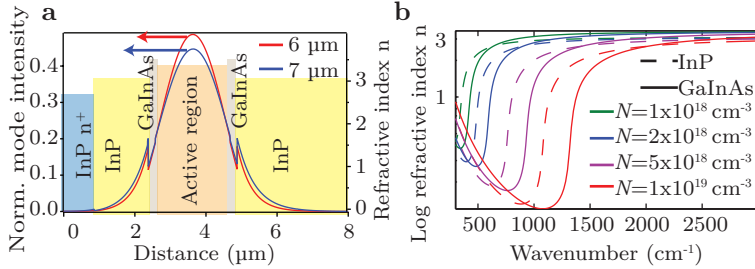


Fig. 2.12: Waveguide design of QCLs. **a** Illustration of the TM-mode penetration in the cladding as a function of wavelength. **b** Refractive index as a function of wavelength of heavily doped InP and GaInAs forming a guiding plasmon layer in the QCL.

fraction of the mode n_{eff} . To calculate the vertical GVD_{vert} of the mode, we use the program *guide* which has been developed in our group, which is based on a transfer matrix formalism. This program is used to calculate the TM-eigenmodes in the vertical direction of a waveguide. To calculate the dispersion due to the lateral confinement, we resort to an analytical solution of the problem, described in [137].

The GVD_{vert} includes the dispersion of the doped layers due to free-carrier absorption and material dispersion. The highly doped InP n^+ region close to the top-contact layer as well as the GaInAs layers have an important effect on the GVD, due to the altered optical properties of the material. To account for these free-carrier concentration, a Drude like approximation is considered, using for the free-electron mass the effective mass m^* . The resulting dielectric function is given by

$$\varepsilon(\omega) = \varepsilon_{sc} \left(1 - \frac{\omega_p^2}{\omega^2 + i\omega\gamma} \right). \quad (2.25)$$

The plasma frequency is defined as

$$\omega_p = \sqrt{\frac{Ne^2}{\varepsilon_0 \varepsilon_{sc} m^*}}. \quad (2.26)$$

The simulation of the refractive index of InP and lattice matched GaInAs as a function of doping N is shown in fig. 2.12b, taking a typical damping coefficient $\gamma = \frac{1}{150 \text{ fs}}$. This corresponds roughly to the scattering time of electrons in a semiconductor. The used electron effective mass m^* of InP is 0.08 and of GaInAs is 0.043 [138]. In a plasmon

enhanced waveguide, the low refractive index of the highly-doped top layer is used to push away the mode from the top contact [139]. Apart from the guiding effect, we are interested on the resulting GVD due to the free-carriers.

To sum up the theoretical description of the GVD of the III-V materials and the modal dispersion, fig.2.13a shows the simulated n_{eff} and n_{group} of the lateral and vertical confinement of a typical mid-IR buried heterostructure waveguide. The width of the waveguide is $4.5\mu\text{m}$. The InP top-cladding is in total $3\mu\text{m}$ thick, including a highly doped $N = 5 \times 10^{18} \text{ cm}^{-3}$ $0.4\mu\text{m}$ thick plasmon layer. The simulated n_{eff} vertical is lower compared to the lateral for the following reason. The dispersion of the InP is taken into account already at the step when computing n_{eff} by *guide*, whereas the dispersion of InP due to the lateral overlap with InP is taken into account when summing the individual GVD terms. The plasmon resonance is clearly visible on the group refractive index of the vertical mode.

The effect on the GVD of the plasmon layer for different plasmon doping concentrations is shown in fig.2.13b. As it can be seen, with increasing doping, the resonance is moving to lower wavelength. However, the increased effect on the refractive index helps to push away the mode from the resonance, effectively reducing the absorption of the mode at that resonance. This is the reason that the GVD decreases with increasing doping. Fig.2.13c shows the spectral region featuring a low GVD for the case of the $N = 5 \times 10^{18} \text{ cm}^{-3}$ doped plasmon layer. To illustrate the strong effect of the width (and also height) of the active region on the GVD, it also shows the final GVD of a $2.8\mu\text{m}$ wide ridge QCL. As it can be seen, a flat and almost zero GVD can be engineered.

2.4.5 Dispersion due to the gain

The gain and losses of the active region in a QCL will lead to a non-negligible contribution to the dispersion of the refractive index. The refractive index $n(\omega)$ describes the response of a material system to electromagnetic radiation. To account for the absorption or gain present in the media, the refractive index is a complex number $n(\omega) = n - ik$, where k is the extinction coefficient. The absorption coefficient $\alpha \equiv \frac{1}{I} \frac{dI}{dz}$ is linked to the extinction coefficient through $\alpha = \frac{4\pi}{\lambda} k$. There is a direct connection between the dispersion of a medium and the complex refractive index, which we will illustrate below.

To calculate the linear response of a system to an applied electrical field using the quantum mechanical theory, one way is to use the density matrix formulation [140]. The nonlinear response is treated later in the following section 2.5 discussing nonlinearities present in the QCL medium. The diagonal entries of the density matrix ρ_{nm} give the

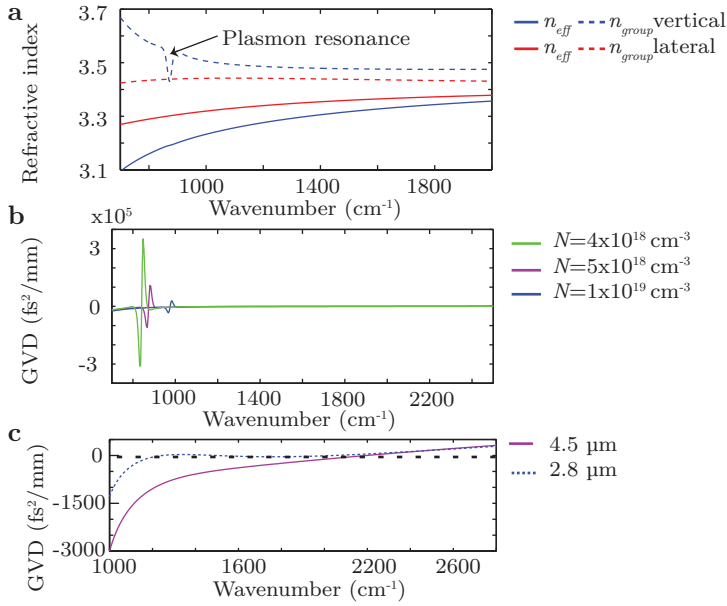


Fig. 2.13: GVD due to the waveguide. **a** Lateral and vertical effective refractive index and group refractive index of a 4.5 μm wide buried-heterostructure QCL. **b** GVD due to the plasmon doping concentrations. **c** Effect of the waveguide width on the GVD.

probabilities that the system is in state n . The off-diagonal entries are only non-zero if the system is in a coherent superposition of eigenstates n and m . The evolution of the density matrix is given by

$$\dot{\rho} = \frac{-i}{\hbar} [H, \rho]_{nm} - \gamma_{nm} (\rho_{nm} - \rho_{nm}^{(\text{eq})}). \quad (2.27)$$

The second term accounts for the decay rate at which the system in state ρ_{nm} relaxes into the equilibrium value $\rho_{nm}^{(\text{eq})}$. The Hamiltonian operator is given by $H = H_0 + V(t)$, where H_0 is the Hamiltonian of the unperturbed system and $V(t)$ is the interaction Hamiltonian. The Hamiltonian used to calculate the interaction is given by

$$V(t) = -e\mathbf{r}\mathbf{E}(t), \quad (2.28)$$

where \mathbf{r} is the position operator and $\mathbf{E}(t) = \sum_p \mathbf{E}(\omega_p) e^{-i\omega_p t}$ is the applied field. Evaluating the solution of the perturbation expansion up to the first order, it is possible to calculate the linear susceptibility. By calculating the expectation value of the induced dipole moment and compare it to the polarization we get the susceptibility tensor in Cartesian components i, j

$$\chi_{ij}^{(1)}(\omega_p) = \frac{N}{\varepsilon_0 \hbar} \sum_{nm} (\rho_{nm}^{(0)} - \rho_{nn}^{(0)}) \frac{\mu_{mn}^i \mu_{nm}^j}{(\omega_{nm} - \omega_p) - i\gamma_{nm}}. \quad (2.29)$$

N denotes the atom number density, $\mu_{nm} = -e\langle n|\mathbf{r}|m\rangle$ are the matrix elements of the dipole moment operator, $\omega_{nm} = \frac{E_n - E_m}{\hbar}$ and ω_p is the angular frequency of the electromagnetic radiation. The tensor reduces to a scalar product in an isotropic material. In the case of a QCL, only the z component of the electric field will couple to the intersubband transition. Therefore the tensor can also be reduced to a scalar product only containing χ_{zz} .

The susceptibility is a complex number $\chi = \chi' + i\chi''$. The link between the real and imaginary part is established through the Kramer-Kroenig relations. The Kramer-Kroenig relations read as followed [141]

$$\begin{aligned} \chi'(\nu) &= \frac{2}{\pi} \int_0^\infty \frac{s\chi''(s)}{s^2 - \nu^2} ds \\ \chi''(\nu) &= \frac{2}{\pi} \int_0^\infty \frac{\nu\chi'(s)}{\nu^2 - s^2} ds. \end{aligned} \quad (2.30)$$

The relationship between χ' and χ'' as a function of the damping coefficient γ_{mn} is shown in fig. 2.14a. The imaginary part of χ is an even function around ω_0 , whereas

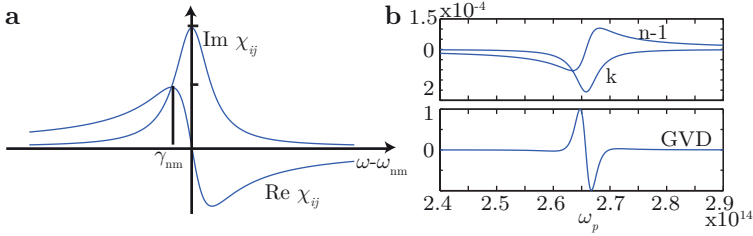


Fig. 2.14: Kramer-Kroenig relations. **a** Illustration of the relationship between real and imaginary part of the first order susceptibility χ . **b** Normalized GVD to illustrate the effect of the gain.

the real part is an odd function.

It is however not straight forward to get a direct connection between the gain and the refractive index of a medium, since $n = (1 + \chi)^{\frac{1}{2}}$. Therefore the refractive index needs to be approximated to $n \approx 1 + \frac{1}{2}(\chi) = 1 + \frac{1}{2}(\chi' + i\chi'')$, resulting in

$$n \approx 1 + \frac{1}{2}\chi' \quad (2.31)$$

$$\alpha \approx -\frac{2\pi}{\lambda}\chi'' \quad (2.32)$$

Those equations in combination with the Kramer-Kroenig relations allows us to compute the refractive index n , the group refractive index n_g and the GVD if we have knowledge of the gain curve in a QCL.

Before analyzing the GVD due to QCL gain it is interesting to have a first look at the implication of those findings on the linewidth of a QCL. To predict the linewidth of semiconductor lasers the Shawlow-Townes formula has to be corrected by the linewidth enhancement factor (also called alpha factor, $\alpha_{Henry} = \frac{\Delta n}{\Delta k}$) found by C. Henry [142, 143]. Spontaneous emission resulting in a net gain change leads to relaxation oscillation to restore the steady state condition. This has an effect on the refractive index, increasing the linewidth by a factor of $1 + \alpha_{Henry}^2$. It was already pointed out by Faist *et al.* in the first paper demonstrating the QCL in 1994 that the QCL features a small alpha factor compared to interband semiconductor laser due to its gain profile [11]. This arises from the atomic like joint-density of states, the gain peaks at the emission frequency as shown in fig. 2.6c. At gain maximum, any variations in the carrier number should have essentially zero effect on the refractive index variations. Recently a setup was realized measuring intrinsic linewidths of mid-QCL corresponding to hundreds of Hz [144],

followed by real measurements of free-running QCLs featuring linewidths of 1 MHz at room-temperature and recently sub-kilohertz linewidth and absolute frequency was shown by locking a QCL to a molecular sub-Doppler reference [145, 146].

The effect of a gain medium on the GVD is shown in fig. 2.14b. The gain is assumed to be a simple Lorentzian for illustrative purposes. The top part of the figure shows the gain and the corresponding refractive index change. Since it is a gain medium, the extinction coefficient is negative, corresponding to a gain of $\approx 3.6 \text{ cm}^{-1}$. The normalized GVD is shown in the bottom part of the figure, illustrating the dispersive effect of the gain on the GVD in case of a Lorentzian gain shape.

To compute the GVD due to the gain and loss present in a QCL cavity, it is necessary to go beyond a simple Lorentzian lineshape of the gain curve and simulate the gain and loss in a QCL more accurately. To accomplish this, we use a simulation software developed by Terazzi *et al.* based on a density matrix model extended to the whole structure, which includes gain and loss mechanism between all subband pairs [147, 148]. It is called *sewlab* and it computes the total scattering rate of each state as a sum of longitudinal optical phonon, alloyed disorder, ion, interface roughness, and photon scattering rates. The losses at which the gain clamps are computed as a combination of the mirror losses and waveguide losses $\alpha_{\text{tot}}(\lambda) = \alpha_{\text{m}} + \alpha_{\text{wg}}(\lambda)$. The waveguide losses are simulated for each wavelength in *guide*.

Since the gain curve has an important effect on the GVD in a QCL, we also have to consider the case of inhomogeneously broadened gain curves arising when cascading dissimilar substacks to broaden the gain. However, our simulation software can not treat an inhomogeneous system, therefore an iterative approach must be taken. The software takes as an input parameter the bias voltage. Among others, one can extract the optical power, gain and current density. The parameter which is conserved in a QCL is however the current and not the applied field. It is therefore not possible to cascade different structures in one input file and align all of them at the same field. Therefore, to compute the total gain curve that clamps at $\alpha_{\text{tot}}^{(k=1)}(\lambda_i)$ for each individual substack i due to the photon flux, an iterative approach on the individual gain curves is taken. The index (k) was introduced to indicate the step number of the iterative process, with $\alpha_{\text{tot}}^{(1)}(\lambda_i)$ representing the initial total losses.

To better understand this approach, it is useful to take a look at the rate equations presented for a heterogeneous QCL in eq. 2.10-2.13 in section 2.2.1. These rate equations take the inhomogeneous behavior of the substacks into account. The rate of change of the photon flux at wavelength λ_i in eq. 2.12 is proportional to $G_{\text{M}}(\lambda_i) -$

$\alpha_{\text{tot},i}^{(1)}(J, S_{\lambda_{1,\dots,N}})$. The modal gain is given by

$$G_M(\lambda) = \sum_{i=1}^N N_{p,i} g_{c,i}(\lambda) (n_{3,i} - n_{2,i}). \quad (2.33)$$

Let us assume we simulate the j^{th} stack. We can rewrite the previous equation to

$$G_M(\lambda) = N_{p,j} g_{c,j}(\lambda) (n_{3,j} - n_{2,j}) + \sum_{i \neq j}^N g_i^{(1)}(J, S_{\lambda_i}). \quad (2.34)$$

We fix the current density to J_{set} at which we want to evaluate the total modal net gain of the QCL composed of dissimilar substacks. This current density induces a photon flux density in the substack S_{λ_i} . We can substitute the cross gain and absorption arising from the other substacks into the constant $\delta_j^{(1)} = \sum_{i \neq j}^N g_i^{(1)}(J_{\text{set}}, S_{\lambda_i})$. The constant $\delta_i^{(k)}$ also depends on J_{set} and $S_{\lambda_{1,\dots,N}}$. As a new total loss for the simulation we simply take the old total losses and subtract $\delta_j^{(1)}$. The new estimated total losses are $\alpha_{\text{tot},j}^{(2)}(J_{\text{set}}, S_{\lambda_{1,\dots,N}}) = \alpha_{\text{tot},j}^{(1)}(J_{\text{set}}, S_{\lambda_{1,\dots,N}}) - \delta_j^{(1)}$. These new losses therefore include resonant and non-resonant cross-absorption from all the other substacks for a set value of the current density J_{set} .

Using the simulation tool *sewlab*, we can compute the individual gain curves and current densities, including the photon flux density $g_i^{(k)}(J, S_{\lambda_i}^{(k)})$ for all substacks. The photon flux density will depend on the iteration round (k), since the waveguide losses are altered at each round. All resonant and non-resonant absorption will be included in $g_i^{(k)}(J, S_{\lambda_i}^{(k)})$. In contrast to the pure rate equation model, it is therefore not necessary anymore to include the non-resonant absorption in the initial losses, resulting in losses that do not depend on the current density J , and which are given by $\alpha_{\text{tot},i}^{(1)}$. The iteratively approached total modal gain at each step at the set current density J_{set} is given by $G_M^{(k)} = \sum_i^N g_i^{(k)}(J_{\text{set}}, S_{\lambda_i}^{(k)})$. First, the total modal gain of the first iteration is calculated, leading to $G_M^{(1)}$ from which each $\delta_i^{(1)}$ can be deduced. Afterwards, a new simulation run with the new total losses $\alpha_{\text{tot},i}^{(2)}(J_{\text{set}}, S_{\lambda_{1,\dots,N}}^{(1)})$ is carried out. This process is continued until the iteratively approached total modal gain $G_M^{(k)}(\lambda_i)$ simulated using the total losses $\alpha_{\text{tot},i}^{(k)}(J_{\text{set}}, S_{\lambda_{1,\dots,N}}^{(k-1)})$ clamps approximately at the original waveguide losses.

Let us apply this model to calculate the gain clamping and GVD of a QCL composed of three different substacks. First, each individual gain curve is simulated setting the losses to $\alpha_{\text{tot}}^{(1)}(\lambda_i) = \alpha_m + \alpha_{\text{wg}}(\lambda)$. The overlap factor is set to Γ_i in the simulation program (~ 0.3 for a design composed of 3 substacks). This ensures that the

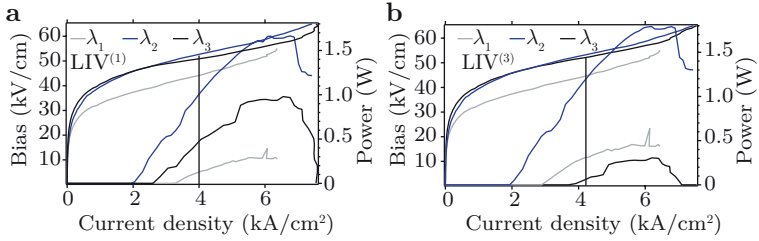


Fig. 2.15: Iterative LIV simulation of all three substacks. The active region width was set to $8\mu\text{m}$, the number of periods to 17 and the facet reflectivity to 0.25. **a** LIV after the first iterative process. **b** LIV after the third iterative process.

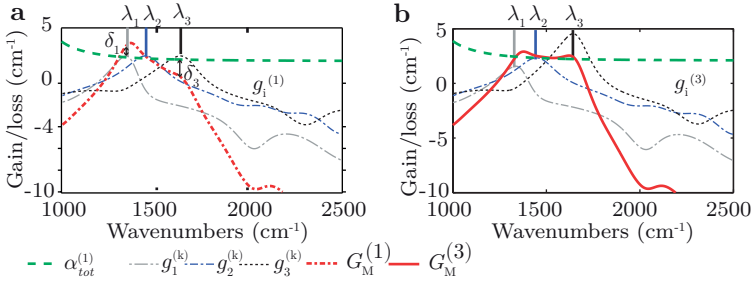


Fig. 2.16: Iterative GVD calculation for heterogeneous cascade. **a** GVD due to the gain after the first iterative process. **b** GVD due to the gain after the third iterative process.

gain clamps at the advertised losses. However, the losses in the active region per substack are reduced due to the decreased modal overlap. Fig. 2.15a shows the simulated LIVs⁽¹⁾ of the individual substacks for the first round. We chose a current density to calculate the total modal gain $G_M^{(1)}$ where all substacks are lasing, indicated with a black line at $J_{\text{set}} = 4 \text{ kA/cm}^2$ in fig. 2.15a. Fig. 2.16a shows the individual gain curves $g_i^{(1)}(J_{\text{set}}, S_{\lambda_i}^{(1)})$ of the three substacks. In a second step, the individual gain curves $g_i^{(1)}(J_{\text{set}}, S_{\lambda_i}^{(1)})$ are summed together giving $G_M^{(1)} = \sum_i g_i^{(1)}(J_{\text{set}}, S_{\lambda_i}^{(1)})$. The resulting total gain $G_M^{(1)}(\lambda_i)$ is then compared to the aimed at losses $\alpha_{\text{tot}}^{(1)}(\lambda_i)$ at the peak of the gain curve of the individual substacks. This is illustrated in fig. 2.16a. The individual substacks all peak at the fixed losses $\alpha \approx 2.5 \text{ cm}^{-1}$. The summed $G_M^{(1)}(\lambda_i)$ is far of from the desired value of $\alpha_{\text{tot}}^{(1)}(\lambda_i)$ due to gain and absorption between the substacks. The difference between the simulated and desired value is $\delta_i^{(1)}$, where $\delta_i^{(1)}$ is the difference $\delta_i^{(1)} = G_M^{(1)}(\lambda_i) - \alpha_{\text{tot}}^{(1)}(\lambda_i)$. In the case illustrated in fig. 2.16a, $\delta_2^{(1)} = 0.03 \text{ cm}^{-1}$ is almost 0, whereas $\delta_1^{(1)} = 0.91 \text{ cm}^{-1}$ and $\delta_3^{(1)} = -1.93 \text{ cm}^{-1}$ need strong adjustments. For the next simulation run, the total losses of the individual substacks i are set to $\alpha_{\text{tot},i}^{(2)}(J_{\text{set}}, S_{\lambda_{1,\dots,N}}^{(1)}) = \alpha_{\text{tot}}^{(1)}(\lambda_i) - \delta_i^{(1)}$. The total gain can then be evaluated at J_{set} giving $G_M^{(2)}$. The value of the total gain is only justified at this specific current density, since the cross gain and absorption was assumed to be constant and was evaluated at this current density. This process is done iteratively about three times to give a gain curve $G_M^{(3)}$ in which each individual gain curve matches approximately the simulated waveguide losses $\alpha_{\text{tot}}(\lambda)$.

The results of this iterative process to calculate the LIVs⁽³⁾ and gain of an active region composed of three substacks is shown in fig. 2.15b and 2.16b. The LIVs⁽³⁾ of the substacks emitting at $\lambda_{1,2}$ changed quite drastically due to the changed waveguide losses. The gain shows the three individual substack gains peaking at $\lambda_{1,2,3}$. As it can be seen, the total losses used in the simulation are considerably different varying from 1.6 cm^{-1} for $g_1^{(3)}(J_{\text{set}}, S_{\lambda_1}^{(3)})$ to 4.5 cm^{-1} for $g_3^{(3)}(J_{\text{set}}, S_{\lambda_3}^{(3)})$. However, if you sum the different gains after three iterations resulting in $G_M^{(3)}$, the total gains at the peak wavelength equal the total losses $G_M^{(3)}(\lambda_i) = \alpha_{\text{tot}}^{(1)}(\lambda_i)$.

The results of the simulated gain and computed GVD of a single bound-to-continuum active region is illustrated in fig. 2.17 in dotted lines. The strength of the GVD around the center frequency of the gain strongly depends on the width of the gain curve and the clamping of the gain curve. The computed GVD due to the total gain for a heterogeneous cascade QCL $G_M^{(3)}$ is shown in fig. 2.17. As it can be seen, due to the "flat top" of the gain curve in QCLs composed of several substacks, the GVD arising from the gain features a region with essentially zero dispersion. This region is indicated by the

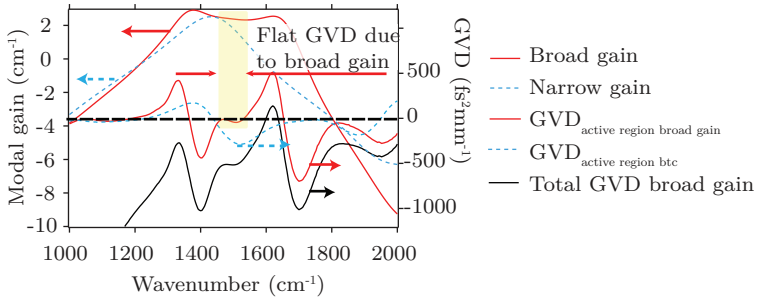


Fig. 2.17: GVD calculation in QCLs. GVD of due to a narrow-band active region (bound-to-continuum) and heterogeneous broadband active region. The total GVD including all different GVD terms for the broadband active region is shown as the solid black line.

red arrows. Compared with the GVD in a homogeneously broadened QCL there are several important differences. First, the width of the gain curve will increase or decrease the spectral width of the flat part, it will however not influence its value. Furthermore, the total losses strongly affect the GVD when slightly detuned from the peak gain in a homogeneously broadened laser. The flat top part of the GVD of a broadband QCL composed of several substacks however stays at zero. Loosely speaking, the two “wings” before and after the flat region will absorb all GVD due to the gain.

Finally, the solid black line in fig. 2.17 shows the resulting GVD of the broadband QCL composed of 3 substacks including all different terms of the GVD discussed beforehand. It includes the GVD due to the gain, InP, waveguide dispersion and the free-carrier absorption in the doped layers.

2.5 Nonlinearities in QCLs

Intersubband transitions are especially interesting to exploit nonlinear interactions. The possibility to design the energy eigenstates in such systems allows for the engineering and optimization of the optical nonlinearities [149, 150]. The second- and third order nonlinear susceptibilities depend to the third respectively fourth power on the optical dipole matrix element z_{ij} . The dipole extension is in the order of nanometers compared to Ångström in atomic dipoles. The flexibility in design of the resonances has led to interesting applications in QCLs, such as the generation of terahertz radiation due to second-order nonlinear interactions in a dual-color mid-IR room-temperature

QCL [151]. By integrating a dual-period distributed feedback grating, single mode THz operation was recently achieved [152]. Sum frequency generation in dual-color QCLs and second harmonic generation is also possible [153, 154].

Naturally, the third order nonlinearities can also be tailored in quantum-well systems. The investigation of third order nonlinearity in quantum-wells systems revealed very large values of $\chi^{(3)}$ of the order of $1 \times 10^{-4} \frac{\text{m}^2}{\text{V}^2}$ [155]. This large value of $\chi^{(3)}$ has been used in several experiments to demonstrate different third-order nonlinear effects in quantum-well systems. Walrod *et al.* showed nondegenerate four-wave mixing in a two level quantum-well system [156]. Optical phase conjugation has been realized in a quantum-well system [157]. Other studies confirmed the large value of the third order susceptibility and elaborated further on the versatility and design freedom of the quantum well system [158–160].

If the interaction of matter with radiation depends on higher order terms than only the first-order, the induced polarization can be expressed as a power series in \mathbf{E} , giving³

$$\mathbf{P}(\mathbf{x}, t) = \varepsilon_0 \left(\chi^{(1)} \mathbf{E}(\mathbf{x}, t) + \chi^{(2)} \mathbf{E}(\mathbf{x}, t)^2 + \chi^{(3)} \mathbf{E}(\mathbf{x}, t)^3 + \dots \right), \quad (2.35)$$

where $\chi^{(2)}$ and $\chi^{(3)}$ are the second-order and third-order nonlinear optical susceptibilities. To describe the interaction at higher order, a tensor notation is necessary. Using a tensor notation, the dielectric polarization is written as

$$P_i = \varepsilon_0 (\chi_{ij} E_j + \chi_{ijk}^{(2)} E_j E_k + \chi_{ijkl}^{(3)} E_j E_k E_l + \dots). \quad (2.36)$$

Again, since only the z component of the electric field will couple to the intersubband transition, we can reduce the tensor to a scalar product $\chi_{zzz}^{(2)}$ and $\chi_{zzz}^{(3)}$. The higher order susceptibility can be calculated by the same perturbation expansion as was used to evaluate the linear susceptibility.

The general equation resulting of the perturbation expansion of $\chi^{(2)}$ and $\chi^{(3)}$ are large sums. The expression for $\chi^{(3)}$ for example, has 48 different terms [140]. However, looking at a special case, the calculation of the nonlinear susceptibility often simplifies. For this reason, we only consider a two level atom when treating the nonlinear susceptibility of a QCL as it is done in chapter 6 of *Nonlinear Optics by R. Boyd* [162]. Apart from resulting in a vastly simpler treatment of the nonlinear interaction, there are other advantages to this technique. It allows for example to account for power broadening, saturation effects, Rabi oscillations and optical Stark shifts. Since we are

³ An alternative notation used in many textbooks [141, 161] for the dielectric polarization is, $P_i = \varepsilon_0 \chi_{ij} E_j + 2d_{ijk} E_j E_k + 4\chi_{ijkl} E_j E_k E_l + \dots$.

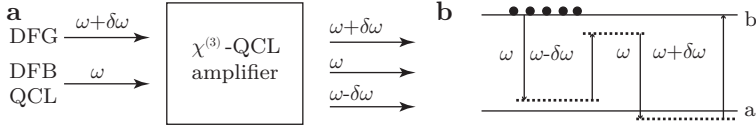


Fig. 2.18: $\chi^{(3)}$ and four-wave mixing in a two level system. **a** Four-wave mixing. **b** Energy level description of the four-wave mixing process under population inversion.

mainly interested in a possible coherent power transfer between adjacent modes in multi-mode operation due to four-wave mixing processes (see sec. 2.6.2) in a two level system, we concentrate on this case here. Furthermore, this situation describes accurately the experiments performed by Friedli *et al.* to measure the nonlinear response of a QCL amplifier [163]. To measure the $\chi^{(3)}$ in a QCL amplifier, a four-wave mixing experiment in a QCL amplifier was set up. The pump and probe beams are a single mode quantum cascade laser and a broadly tunable source (Ekspla PG711/DFG). This is illustrated in fig. 2.18a.

In fig. 2.18b the considered three level system is shown. The power of the pump wave at ω is much stronger than the probe field at detuned frequency $\omega + \delta$. The results developed for the optical wave mixing phenomena in a two-level system finds the effective third order nonlinearity to be

$$\chi_{\text{eff}}^{(3)}(\delta\omega, \Delta) = \frac{2\delta N |\mu_{ab}|^4 (\delta\omega - \Delta - i\frac{1}{T_2}) (-\delta\omega + i\frac{2}{T_2}) (\Delta + \frac{i}{T_2})^{-1}}{3\epsilon_0 \hbar^3 (\Delta - \delta\omega + i\frac{1}{T_2}) D^*(\delta\omega)}. \quad (2.37)$$

The parameters δN represent the volume population inversion per QCL period, μ_{ij} is the matrix element of the dipole moment operator, $\Delta = \omega - \omega_{ba}$ is the detuning from the pump wave from the intersubband transition. T_1 and T_2 are the relaxation and dephasing time. The value $D(\delta\omega)$ is given by

$$D(\delta\omega) = \left(\delta\omega + \frac{i}{T_1} \right) \left(\delta\omega - \Delta + \frac{i}{T_2} \right) \left(\Delta + \delta\omega + \frac{i}{T_2} \right) - \Omega^2 \left(\delta + \frac{i}{T_2} \right), \quad (2.38)$$

where Ω is the Raby frequency, defined by $\Omega = 2|\mu_{ab}||E|/\hbar$. Considering eq. 2.38, it becomes clear that the third order nonlinear susceptibility also depends on the laser intensity through the Rabi frequency. For this reason it is called an effective susceptibility. By setting $\Omega = 0$ we recover $\chi^{(3)}$ from the perturbation theory. In Ref. [163], we calculate a $\chi^{(3)} = 2.5 \times 10^{-15} \text{ m}^2 \text{ V}^{-2}$ in the low field limit. This corresponds well with the measured $\chi^{(3)} = (0.9 \pm 0.2) \times 10^{-15} \text{ m}^2 \text{ V}^{-2}$.

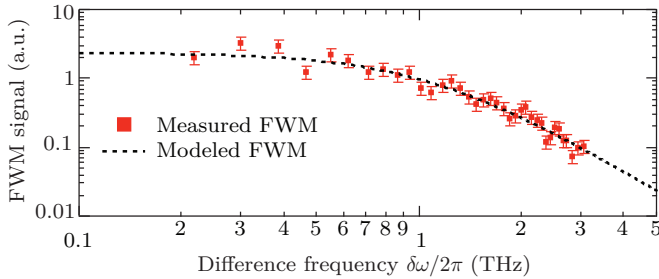


Fig. 2.19: Four-wave mixing signal as a function of difference frequency. Reprint from [163].

The width of the resonance depends on the relaxation and dephasing time in the QCL. Since the timescale for both processes is in the order of ps in a QCL, which is much faster than the carrier diffusion time, the bandwidth attainable through four-wave mixing processes is large compared to interband lasers. Fig. 2.19 shows the generated four-wave mixing signal as a function of the detuning. The measured roll-off frequency is ≈ 1 THz. This is orders of magnitudes more compared with early four-wave mixing experiments due to spatial hole burning performed in interband lasers, where the bandwidth was limited to a few GHz [164]. However, even in interband lasers there are processes attributed to spectral hole burning and carrier heating which are fast enough and allow a coupling of up to hundreds of GHz [165, 166]. Those high bandwidths are of paramount importance in the discussion of the multi-mode and comb operation of QCLs, since it allows to establish coupling between neighboring modes. Usual mode-spacings in QCLs are about 15 GHz for a 3 mm and 7.5 GHz for a 6 mm long device.

2.6 Parametric coupling

This section gives a review of the concept of coupled waves and its utilization to find approximate solutions of Maxwell's equations of light propagating in a nonlinear medium. Approximate solutions to many physical problems can be found relatively easily using this coupled-wave theory. Among others it is possible to find the relationship between the absorption and the refractive index of a material, find solutions for phase gratings, explain coupled waves in integrated optics and explain nonlinear optics (parametric coupling). This section is not intended to give a full review of the concept of coupled

waves neither of nonlinear optics, since a complete summary would be out of the scope of this work. For further studies please refer to references [141, 161, 162, 167].

2.6.1 Theory

The concept of coupled waves describes the propagation of optical waves in a dielectric medium characterized by some kind of spatial or temporal perturbation of the dielectric polarization. Wave propagation in transparent and nonlinear medium is governed by the basic wave equation

$$\nabla^2 \mathbf{E}(\mathbf{x}, t) - \frac{1}{\varepsilon_0 c^2} \frac{\partial^2 \mathbf{D}}{\partial t^2} = 0, \quad (2.39)$$

where \mathbf{D} is the displacement field including linear and nonlinear contributions, given by the material equation $\mathbf{D} = \varepsilon_0 \mathbf{E} + \mathbf{P}$. It can therefore be rewritten to

$$\nabla^2 \mathbf{E}(\mathbf{x}, t) = \mu_0 \varepsilon_0 \frac{\partial^2 \mathbf{E}(\mathbf{x}, t)}{\partial t^2} + \mu_0 \frac{\partial^2 \mathbf{P}(\mathbf{x}, t)}{\partial t^2}, \quad (2.40)$$

where $c = \frac{1}{\sqrt{\mu_0 \varepsilon_0}}$ is the speed of light, $\mathbf{P}(\mathbf{x}, t)$ is the dielectric polarization of the medium, ε_0 and μ_0 are the electric and magnetic permeabilities of vacuum.

The dielectric polarization $\mathbf{P}(\mathbf{x}, t)$ is now decomposed into two parts, $\mathbf{P}_0(\mathbf{x}, t)$ for which a solution of the wave equation exists, and $\mathbf{p}(\mathbf{x}, t)$, which represents the perturbation caused by the nonlinear interaction. If the unperturbed system is originally a linear and isotropic medium, $\mathbf{P}(\mathbf{x}, t)$ can be written as

$$\mathbf{P}(\mathbf{x}, t) = \mathbf{P}_0(\mathbf{x}, t) + \mathbf{p}(\mathbf{x}, t) = \varepsilon_0 \chi(\mathbf{x}) \mathbf{E}(\mathbf{x}, t) + \mathbf{p}(\mathbf{x}, t). \quad (2.41)$$

By using the relations of the speed of light in vacuum $c_0^2 = \frac{1}{\mu_0 \varepsilon_0}$ and $n(\mathbf{x}) = (1 + \chi(\mathbf{x}))^{1/2}$, the wave-equation including the perturbation can be rewritten as

$$\nabla^2 \mathbf{E}(\mathbf{x}, t) - \left(\frac{n(\mathbf{x})}{c_0} \right)^2 \frac{\partial^2 \mathbf{E}(\mathbf{x}, t)}{\partial t^2} = \mu_0 \frac{\partial^2 \mathbf{p}(\mathbf{x}, t)}{\partial t^2}. \quad (2.42)$$

By setting the perturbation term $\mathbf{p}(\mathbf{x}, t) = 0$, we find the familiar second-order wave equation of a linear medium

$$\nabla^2 \mathbf{E}(\mathbf{x}, t) - \left(\frac{n(\mathbf{x})}{c_0} \right)^2 \frac{\partial^2 \mathbf{E}(\mathbf{x}, t)}{\partial t^2} = 0. \quad (2.43)$$

Solutions of Eq. (2.43) are of the form

$$\mathbf{E}(\mathbf{x}, t) = \mathbf{U}(x, y) e^{i(\omega_n t - \beta_n z)}, \quad (2.44)$$

where β_n is the propagation constant, ω_n are the angular frequencies and $\mathbf{U}(x, y)$ is the complex electric field distribution. The angular frequencies are linked to the propagation constant β_n through the effective index of refraction of the mode n (n_{eff_n}), giving $\omega_n = \frac{c}{n_{eff_n}} \beta_n$.

In the coupled wave approach, an appropriate set of N unperturbed modes forms a complete basis to the problem. Therefore any solution of the perturbed medium can be found by a linear superposition of these modes. Since we will apply the discussion of the coupled modes to the case of non-linear effects, its wise to define the E-field as a real quantity, leading to

$$\mathbf{E}(\mathbf{x}, t) = \frac{1}{2} \sum_{n=\pm 1, \dots, \pm N} A_n(z) \mathbf{E}_n(\mathbf{x}, t) = \sum_{n=\pm 1, \dots, \pm N}^N A_n(z) \mathbf{U}_n(x, y) e^{i(\omega_n t - \beta_n z)}. \quad (2.45)$$

where $A_n(z)$ describes the amplitude and phase of the coupled modes, and $A_{-n} = A_n^*$, $U_{-n} = U_n^*$ and $\omega_{-n} = -\omega_n$, $\beta_{-n} = -\beta_n$.

Inserting Eq.(2.45) into Eq.(2.42) and utilizing Eq.(2.43), one finds the equation

$$\sum_{n=\pm 1, \dots, \pm N} \left(-i\beta_n \frac{dA_n}{dz} \mathbf{E}_n(\mathbf{x}, t) + \frac{1}{2} \frac{d^2 A_n}{dz^2} \mathbf{E}_n(\mathbf{x}, t) \right) = \mu_0 \frac{\partial^2 \mathbf{p}(\mathbf{x}, t)}{\partial t^2}. \quad (2.46)$$

Eq.(2.46) can be split into a set of $2N$ differential equations by applying the orthogonality of the modes. Furthermore assuming the slowly varying amplitude approximation, with $\frac{d^2}{dz^2} A_n \ll \beta_n \frac{d}{dz} A_n$, the N coupled wave equations finally read

$$\frac{dA_n}{dz} = \frac{i\mu_0}{TW_n\beta_n} e^{i\beta_n z} \int_{-\infty}^{+\infty} dx dy \int_0^T dt e^{-i\omega_n t} \mathbf{U}_n^*(x, y) \frac{\partial^2 \mathbf{p}(\mathbf{x}, t)}{\partial t^2}, \quad (2.47)$$

where W_m represents the normalized energy of each mode and T is the integration time.

The physics of the medium is expressed by the relationship of the electric field $\mathbf{E}(\mathbf{x}, t)$ and the perturbation of the dielectric polarization

$$\mathbf{p}(\mathbf{x}, t) = F\{\mathbf{E}(\mathbf{x}, t)\}. \quad (2.48)$$

2.6.2 Wave mixing

Both, three-wave mixing and four-wave mixing are present in a QCL due to the large $\chi^{(2)}$ and $\chi^{(3)}$ in intersubband transitions, as it was discussed in section 2.5. Furthermore, the bandwidth is large enough to allow coupling between neighboring longitudinal modes. The formalism of the coupled-wave equations just introduced in the previous section is ideal to study the phenomena of nonlinear optics. For simplicity, we start with the study of three wave-mixing phenomena and consider four-wave mixing in the next step.

Three-wave mixing

The perturbation of the dielectric polarization in the case of a three-wave mixing process in a QCL is given by the scalar form

$$p(\mathbf{x}, t) = \varepsilon_0 \chi^{(2)} E^2(\mathbf{x}, t). \quad (2.49)$$

When dealing with nonlinear optics, we have to consider the electric field as a real valued and physical quantity. The total field $E(\mathbf{x}, t)$ is a superposition of three-waves with angular frequency ω_1, ω_2 and ω_3 ,

$$E(\mathbf{x}, t) = \frac{1}{2} \sum_{q=\pm 1, \pm 2, \pm 3} A_q(z) U_q(x, y) e^{i(\omega_q t - \beta_q z)}, \quad (2.50)$$

Again, A_m describes the amplitude and phase of the coupled modes.

Considering eq. 2.35, the second order perturbation of the dielectric polarization can therefore be written as

$$p(\mathbf{x}, t) = \frac{1}{4} \varepsilon_0 \sum_{r, q=\pm 1, \pm 2, \pm 3} \chi^{(2)} [A_q(z) A_r(z) U_q(x, y) U_r(x, y) e^{i[(\omega_q + \omega_r)t - (\beta_q + \beta_r)z]}]. \quad (2.51)$$

Inserting eq. 2.51 in eq. 2.47 and after spatial integration, considering the amplitude A_3 of $E_3 = (A_3 U_3(x, y) e^{i\omega_3 t} + c.c.)$, we get

$$\begin{aligned}
\frac{dA_3}{dz} &= \frac{i\mu_0\varepsilon_0}{4T\beta_3} e^{i\beta_3 z} \int_T dt \chi^{(2)} e^{-i\omega_3 t} \frac{\partial^2}{\partial t^2} \sum_{\substack{r, q= \\ \pm 1, \pm 2, \pm 3}} [A_q(z) A_r(z) e^{i[(\omega_q + \omega_r)t - (\beta_q + \beta_r)z]}] \\
&= \frac{-i\mu_0\varepsilon_0}{4T\beta_3} e^{i\beta_3 z} \int_T dt \chi^{(2)} e^{-i\omega_3 t} \sum_{\substack{r, q= \\ \pm 1, \pm 2, \\ \pm 3}} (\omega_q + \omega_r)^2 [A_q(z) A_r(z) e^{i[(\omega_q + \omega_r)t - (\beta_q + \beta_r)z]}] \\
&= \frac{-i\mu_0\varepsilon_0\chi^{(2)}}{4T\beta_3} \int_T dt \sum_{\substack{r, q= \\ \pm 1, \pm 2, \pm 3}} (\omega_q + \omega_r)^2 [A_q(z) A_r(z) e^{i[(\omega_q + \omega_r - \omega_3)t - (\beta_q + \beta_r - \beta_3)z]}],
\end{aligned} \tag{2.52}$$

We get all possible combination of frequencies, the sum and differences of the original frequencies ω_1 , ω_2 and ω_3 . It is important to notice that the integral over the period T is only non-zero if the frequencies ω_1 , ω_2 and ω_3 are commensurate. This is one frequency is the sum or difference of the two others, or one frequency is the double of another. We assume, for example, $\omega_3 = \omega_1 + \omega_2$. One solution is $q = 1$ and $p = 2$ as well as the possible permutations $q = 2$ and $p = 1$. This gives us the following coupled wave equations:

$$\begin{aligned}
\frac{dA_1}{dz} &= \frac{-i\mu_0\varepsilon_0\chi^{(2)}}{2\beta_1} \omega_1^2 A_2^* A_3 e^{-i(\Delta\beta)z} \\
\frac{dA_2}{dz} &= \frac{-i\mu_0\varepsilon_0\chi^{(2)}}{2\beta_2} \omega_2^2 A_1^* A_3 e^{-i(\Delta\beta)z} \\
\frac{dA_3}{dz} &= \frac{-i\mu_0\varepsilon_0\chi^{(2)}}{2\beta_3} \omega_3^2 A_1 A_2 e^{i(\Delta\beta)z}.
\end{aligned} \tag{2.53}$$

Where we have defined $\Delta\beta = \beta_3 - \beta_1 - \beta_2$ as the phase-matching condition.

It is common to define the coherence length $l_c = \frac{2\pi}{\Delta\beta}$. The coherence length is a measure of the maximum crystal length that is useful in producing the second-harmonic power. The coupled-wave equations describe the exchange of energy between the different modes of frequency ω_1 , ω_2 and ω_3 . One important fact to notice, though not zero, the relative phases of the different modes are fixed.

Other possible solutions are second harmonic generation $\omega_3 = 2\omega_1$ and difference frequency generation $\omega_3 = \omega_1 - \omega_2$. This was successfully applied to Mid-IR QCLs to generate Terahertz radiation [151].

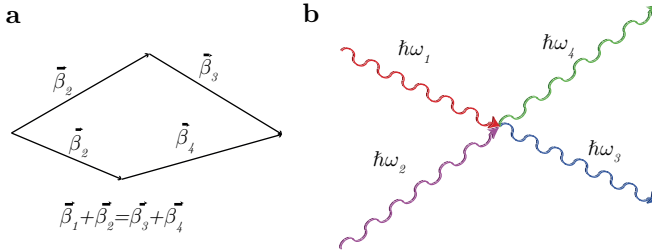


Fig. 2.20: Four wave mixing: **a** Phase matching condition and **b** interaction of four photons fulfilling the energy conservation $\hbar\omega_1 + \hbar\omega_2 = \hbar\omega_3 + \hbar\omega_4$.

Four-Wave Mixing

The third-order nonlinear polarization is the source of different phenomena. Among others there is the third-harmonic generation, stimulated Raman scattering, stimulated Brillouin scattering, four-wave mixing and optical Kerr effect. Using the same formalism of coupled-waves derived in section 2.6.1, we can derive the coupled equations describing the four-wave mixing in a third-order nonlinear medium and the Kerr-effect. Fig. 2.20 illustrates schematically the four-wave mixing process. Fig. 2.20 a) shows the phase-matching condition whereas b) shows the interaction of 4 photons which must satisfy the energy conservation $\hbar\omega_1 + \hbar\omega_2 = \hbar\omega_3 + \hbar\omega_4$.

The perturbation of the dielectric polarization in a third-order nonlinear medium in the scalar form is given by

$$p(\mathbf{x}, t) = \varepsilon_0 \chi^{(3)} E^3. \quad (2.54)$$

In the case of four-wave mixing, the total field can be written as a sum of four modes

$$E(\mathbf{x}, t) = \sum_{q=\pm 1, \pm 2, \pm 3, \pm 4} \frac{1}{2} A_q(z) U_q(x, y) e^{i(\omega_q t - \beta_q z)}, \quad (2.55)$$

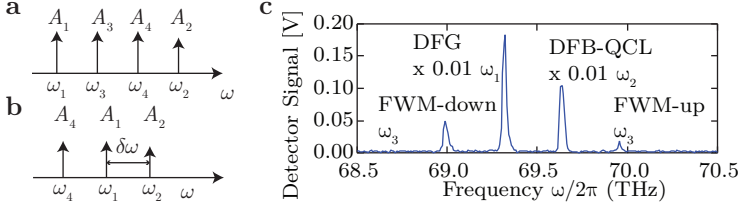


Fig. 2.21: Coupled wave equations for non-degenerate and degenerate four wave mixing: **a** Non-degenerate four-wave mixing with $\omega_1 + \omega_2 = \omega_3 + \omega_4$. **b** Degenerate four-wave mixing with $\omega_4 = 2\omega_1 + \omega_2$. **c** FWM up- and down signal generated in a QCL amplifier. Reprint from [163].

this is a sum of 512 terms. The perturbation of the dielectric polarization is therefore

$$\begin{aligned}
 p(\mathbf{x}, t) = & \frac{1}{8} \varepsilon_0 \sum_{\substack{r, q, p = \\ \pm 1, \pm 2, \\ \pm 3, \pm 4}} \chi^{(3)} \\
 & \times [A_q(z) A_r(z) A_p(z) U_q(x, y) U_r(x, y) U_p(x, y) e^{i[(\omega_q + \omega_r + \omega_p)t - (\beta_q + \beta_r + \beta_p)z]}]
 \end{aligned} \quad (2.56)$$

Inserting eq. (2.56) into eq. (2.47), after spatial integration, considering the amplitude A_4 , we get

$$\begin{aligned}
 \frac{dA_4}{dz} = & \frac{-i\mu_0 \varepsilon_0 \chi^{(3)}}{8T\beta_4} \int_T dt \sum_{\substack{r, q, p = \\ \pm 1, \pm 2, \pm 3}} (\omega_q + \omega_r + \omega_p)^2 \\
 & \times [A_q(z) A_r(z) A_p(z) e^{i[(\omega_q + \omega_r + \omega_p - \omega_4)t - (\beta_q + \beta_r + \beta_p - \beta_4)z]}].
 \end{aligned} \quad (2.57)$$

Again, for the four waves to be coupled, the frequencies must be commensurate. Consider the non-degenerate case $\omega_1 + \omega_2 = \omega_3 + \omega_4$ illustrated in fig. 2.21a. Terms for $\omega_4 = \omega_1 + \omega_2 - \omega_3$ which do not vanish when integrating over a period T are $q, p, r = 1, 2, -3$ and all possible permutations, which are in total 6. Another possibility is the degenerate form $2\omega_1 = 2\omega_1$. Another possibility is $\omega_3 = -\omega_4$, with $q = -4$ and $p = \pm 1, r = \mp 1, p = \pm 2, r = \mp 2$ and $p = \pm 3, p = \mp 3$. And $\omega_2 = -\omega_4$ and $\omega_1 = -\omega_4$ including all possible permutations. The final coupled wave equations in the case of

four-wave mixing are

$$\begin{aligned}
 \frac{dA_1}{dz} &= \frac{-i\mu_0\varepsilon_0\omega_1^2\chi^{(3)}}{8\beta_1} \left(\underbrace{6A_3A_4A_2^*e^{-i(\Delta\beta)z}}_Q + \underbrace{3A_1[|A_1|^2 + 2|A_2|^2 + 2|A_3|^2 + 2|A_4|^2]}_R \right) \\
 \frac{dA_2}{dz} &= \frac{-i\mu_0\varepsilon_0\omega_2^2\chi^{(3)}}{8\beta_2} \left(6A_3A_4A_1^*e^{-i(\Delta\beta)z} + 3A_2[|A_2|^2 + 2|A_1|^2 + 2|A_3|^2 + 2|A_4|^2] \right) \\
 \frac{dA_3}{dz} &= \frac{-i\mu_0\varepsilon_0\omega_3^2\chi^{(3)}}{8\beta_3} \left(6A_1A_2A_4^*e^{i(\Delta\beta)z} + 3A_3[|A_3|^2 + 2|A_1|^2 + 2|A_2|^2 + 2|A_4|^2] \right) \\
 \frac{dA_4}{dz} &= \frac{-i\mu_0\varepsilon_0\omega_4^2\chi^{(3)}}{8\beta_4} \left(6A_1A_2A_3^*e^{i(\Delta\beta)z} + 3A_4[|A_4|^2 + 2|A_1|^2 + 2|A_2|^2 + 2|A_3|^2] \right),
 \end{aligned} \tag{2.58}$$

with $\Delta\beta = \beta_3 + \beta_4 - \beta_1 - \beta_2$ being the phase matching condition. The result can be separated into two parts, Q and R . The first result, Q , represents the result of the mixing of the three other waves and is proportional to $A_3A_4A_2^*$. The second result, R , only modifies the propagation constant of the same wave and it is proportional to $2I - I_q$ with $I = I_1 + I_2 + I_3 + I_4$. This is the optical Kerr effect. Often this term is itself separated into two parts, the cross-phase modulation (XPM) and the self-phase modulation (SPM). The XPM represents the change of the optical phase of a light beam when interacting with another light beam of intensity I_{XPM} . It is represented by a nonlinear change in the refractive index as a function of intensity and is proportional to the nonlinear refractive index n_2 and is given by $\Delta n = 2n_2(I_2 + I_3 + I_4) = 2n_2I_{\text{XPM}}$. The SPM modulation term arises from the phase-change the wave induces from its own intensity and can as well be represented by a change of refractive index, $\Delta n = n_2I_1$.

Considering the results presented in [163] discussed beforehand where we measured $\chi^{(3)}$ by mixing a single mode DFB-QCL and a tunable DFG source in a QCL amplifier, we have to adapt the coupled wave equations due to the degenerate nature of the mixing. The mixing process is illustrated in fig. 2.21b, where $\omega_4 = 2\omega_1 - \omega_2$. Here the generated wave through the four-wave mixing process is the wave labeled FWM-down shown in fig. 2.21c. Due to the degeneracy, the number of permutations reduces from 6 to 3 ($q, p, r = 1, 1, -2$) and the coupled wave equation, omitting the optical Kerr effect, for FWM-down is

$$\frac{dA_4}{dz} = \frac{-i\mu_0\varepsilon_0\omega_4^2\chi^{(3)}}{8\beta_4} 3A_1^2A_2^*e^{i\Delta\beta z}. \tag{2.59}$$

2.6.3 Four-wave mixing in a QCL amplifier

To account for the gain medium, the coupled wave eq. 2.59 need to be adjusted. The gain can be treated exactly as a perturbation of the first order, with the definition of $g = k\chi''$ (see 2.32). The perturbation is

$$p = i\chi'' E(\omega_4) = \frac{ig \sum_{q=\pm 4} A_q e^{i(\omega_q t - k_q z)}}{2\beta} \quad (2.60)$$

This gives the following coupled wave equation due to the gain

$$\frac{dA_4}{dz} = \frac{\mu_0 \varepsilon_0 \nu_4^2 (2\pi)^2 g}{2 \left(\frac{2\pi}{\lambda_4}\right)^2} A_4 = \frac{\frac{1}{c^2} \widehat{\mu_0 \varepsilon_0} \frac{c^2}{\nu_4^2 \lambda_4^2} g}{2} A_4 = \frac{g}{2} A_4. \quad (2.61)$$

The final equation including four-wave mixing and gain therefore reads

$$\frac{dA_4}{dz} = \frac{-i\mu_0 \varepsilon_0 \omega_4^2 \chi^{(3)}}{8\beta_4} 3A_1^2 A_2^* e^{i(\Delta\beta)z} + \frac{g}{2} A_4. \quad (2.62)$$

Chapter 3

Dielectric mid-infrared anti- and high-reflection coatings

This chapter gives an overview of anti-(AR) and high reflection (HR) dielectric coatings deposited on the facet of a QCL. It starts with a short introduction and continues with a description of used coating-materials during the course of this work. Afterwards follows the theoretical treatment including a brief discussion on single- and multi layer coatings. Based on the theoretical background, the chapter continues to explain the coating optimization and calculation algorithm developed during the course of this PhD. The end of the section describes two different measurement methods for AR coatings followed by coating characterization of examples of coatings deposited using the available electron-beam evaporation systems in the clean room of FIRST at the ETH Zürich.

3.1 Introduction

Dielectric AR- and HR coatings play a crucial role in most of today's optical systems, including applications involving lasers. By altering the mirror losses $\alpha_m = \frac{1}{2L} \ln \left(\frac{1}{R_{\text{front}} R_{\text{back}}} \right)$ of the laser, where L is the device length and $R_{\text{front,back}}$ are the front and back intensity reflectivities, one affects strongly the laser performance. The effect on the laser performance of the mirror losses can be understood by looking at eq. 2.6-2.8. Altering the mirror losses changes the threshold current as well as the slope-efficiency of the QCL, therefore the power of the device strongly depends upon them.

Using appropriate front and back coatings, it is possible to considerably increase

the device output power and wall-plug efficiency [30]. A HR coating on the back facet decreases the mirror losses α_m of the device, therefore reducing the threshold current of the device. Eq. 2.7 however also reveals that the slope efficiency of the front facet of a HR back coated device increases when decreasing the total losses α_{tot} . Apart from increasing the output power of the device, a good HR back coating also increases the tuning range of an external-cavity QCL (see sec. 4.2.5). Usually a combination of an insulation layer and a gold coating ($\sim 300 \text{ nm Al}_2\text{O}_3 / 100 \text{ nm Au}$) is used as a HR coating. This ensures a high reflectivity ($\approx 98 \%$) while still limiting the thickness of the coating. However, sometimes a dielectric HR coating is more desirable. In case the facet to which the coating is applied is used to out couple the beam, a dielectric coating is preferable [27]. Nowadays, they are used in low-dissipation devices featuring small cavity length $\sim 1 \text{ mm} - 500 \mu\text{m}$ for power scaling [37, 38]. Also high-power continuous-wave lasers risk to dissipate too much heat in the absorbing metallic HR coatings possibly damaging the coating. To increase the laser induced damage threshold a carefully designed low absorbing dielectric HR coatings is favorable. The deposition of an AR coating on the front-facet is also desirable for many applications, especially the ones involving an external resonator. A very low reflectivity ($< 1 \%$) of the front facet effectively reduces the effect of the chip-laser cavity. This permits the external-cavity laser to lase on all external-cavity modes and not only the ones in proximity to chip modes.

The deposition of high-quality AR coatings in the mid-IR region faces important challenges. First of all, the available material systems which are transparent in the mid-IR range are sparse. Even materials with small absorption coefficients pose problems when employed as a coating for a laser due to the high field intensities, especially in continuous-wave operation. As an example, an $\text{Al}_2\text{O}_3/\text{a-Si}$ front AR coatings used on a laser featuring an output of 160 mW emitting at $7 \mu\text{m}$ did not withstand the high field intensities produced on the $4 \mu\text{m}$ wide facet, albeit the low absorption coefficient of $k_{\text{Al}_2\text{O}_3} \approx 5 \times 10^{-3}$ and $k_{\text{aSi}} \approx 3 \times 10^{-3}$ [136, 168]. Second, due to the large wavelength in the μm range, the deposited coatings are usually thick. Internal stress during deposition in combination with those thick layers often results in a flaking of the coating. The design of broadband coatings often requires multiple coating layers, resulting in film thicknesses which are usually larger than $1 \mu\text{m}$. The adhesion and environmental resistance of large total thin films can be increased by pre treating the substrate surface (e.g. Argon sputtering) or employing adhesion layers (SiO , MgO , Y_2O_3) before, after and in between different material layers.

3.2 Thin film materials in the mid-IR

Physical vapor deposition (PVD) is a common way to deposit thin film coatings for optics and laser applications in the mid-IR. Our clean room facilities allow the use of e-beam evaporation and boat evaporation. Furthermore, we have the possibility to use argon sputtering on the substrate. However, the ion gun was not used to realize ION-assisted deposition in the course of this work, due to the missing possibility to simultaneously deposit and bombard the substrate.

To fabricate HR coatings and zero reflectivity and broadband AR coatings, the availability of low index (~ 1 -2.5) and high index (~ 2.5 -4) materials is crucial. Widespread used low-index materials in the mid-IR range for laser applications are metal-oxides and fluorides. Metal-oxides are often preferable in laser applications. They can be easily combined with ion assistance to give compact and durable thin films. One advantage over fluorides is the missing water absorption lines characteristic for fluoride layers. Suitable metal-oxide coatings which are transparent deep into the mid-IR range are however hard to find and rare earth fluorides ($\text{YF}_3/\text{YbF}_3/\text{BaF}_2$) are clearly the better choice if the wavelength is $\geq 6\text{ }\mu\text{m}$. Fluorides feature very large transparency windows covering the wavelength range from $\sim 300\text{ nm}$ - $15\text{ }\mu\text{m}$. The deposition of those fluoride films to produce low absorbing layers is very delicate [169]. The material of choice used to be thorium fluoride until the 1980, which featured high damage thresholds and is more robust against peeling and cracking [170, 171]. The radioactive nature however lead to increased research for alternative materials. BaF_2 and YbF_3 in combination with ion-assisted deposition showed damage thresholds comparable to conventional ThF_3 coatings [172]. Our material of choice for QCLs coatings is YF_3 , which showed comparable, though slightly stronger absorption and lower damage thresholds results as BaF_2 and YbF_3 . BaF_2 shows very low absorption values of $\sim 10^{-5}$ up to wavelengths of $10\text{ }\mu\text{m}$ [168].

E-beam evaporation and ION-assisted deposition system risk to crack the fluoride bonds leading to deficiencies in fluorides. This is especially problematic for YF_3 , which decomposes into $3\text{YF}_2 \rightarrow \text{Y} + \text{YF}_3$. Increased absorption is therefore due to the metallic Y present within the coating layers [169]. Comparing the color before and after evaporation using boat evaporation and e-beam evaporation unveils a change in the color of the target in the case of the e-beam evaporation from white to something slightly gray, whereas during the boat evaporation the material keeps its color. Therefore our evaporation method of choice for YF_3 is by boat. ION-assisted deposition however works well with YbF_3 . The valence band of Yb allows the formation of divalent fluorides, YbF_2 .

The main problem of fluorides films, the low packing density when evaporated conventionally, can be overcome by ION-assisted deposition. The low packing density leads to a very strong uptake of water from air in such films. Fig. 3.3b shows a measured water absorption line of an YbF_3 coating deposited by e-beam. ION-assisted deposition helps to produce much denser films. This has two positive effects. The films are mechanically more stable allowing thicker depositions and are essentially free of water [169]. The risk of ION-deposited thin-films is however the strong oxidation of YbF_2 bonds forming oxide layers of up to 20 nm thickness. Therefore special care to prevent this must be taken for such films. Nevertheless, the lower absorption, missing water lines and higher packing density of ION-assisted YbF_3 are definitely very important points and it should be revisited as a low index material of choice for our QCLs.

Among others, commonly used high index materials in the mid-IR range are ZnS, ZnSe, Ge and Si. Our high-index material of choice at the beginning of this work was ZnS and at a later stage ZnSe. The deposition of ZnS and ZnSe was done using a small physical vapor deposition system featuring two boat evaporators. The main problem of the deposition of ZnS and ZnSe are the generated toxic compounds during the evaporation, hydrogen sulfide (H_2S) and the far more dangerous hydrogen selenide (H_2Se). Both substances have a bad smell and are easily detectable by the nose in very low concentrations (ppb). The threshold limit value is as low as 0.05 ppm for H_2Se . The relatively small evaporation chamber and the use of protective gas masks when opening the chamber allowed the use of these material in the University of Neuchâtel. However the bigger evaporation chambers and the shared clean room facilities of FIRST at ETH made it impossible to use those materials further. In the course of this work we therefore had to find alternatives for high index materials. Suitable materials were found in Ge and Si. Both work well in combination with YF_3 and layers as thick as $2\text{ }\mu\text{m}$ can be grown this way. However, the study by Rahe *et al.* [172] again revealed that Ge in Ge/ZnSe coatings induces non-negligible absorption, leading to lower damage-threshold values. The best results were achieved by a combination of YbF_3/ZnS and BaF_2/ZnS . Since ZnS is much less toxic than ZnSe, this combination of AR coating should be kept in mind for further potentially more powerful continuous-wave QCLs.

3.3 Theory

This section gives an overview of the matrix formulation of isotropic layered media for TM-polarized and TE-polarized light. This is a condensed treatment, for the throughout derivation interested readers are advised to consult *Optical Waves in Layered*

Media by Pochi Yeh [173]. The matrix formulation is used as the basis for calculating thicknesses of dielectric AR- and HR-coatings of our lasers. To calculate the transmittance, reflectance and absorption of electromagnetic radiation we resort to Maxwell's equations:

$$\nabla \times \mathbf{E} + \frac{\partial \mathbf{B}}{\partial t} = 0 \quad (3.1)$$

$$\nabla \times \mathbf{H} - \frac{\partial \mathbf{D}}{\partial t} = \mathbf{J}, \quad (3.2)$$

$$\nabla \cdot \mathbf{D} = \varrho, \quad (3.3)$$

$$\nabla \cdot \mathbf{B} = 0. \quad (3.4)$$

The variables \mathbf{H} and \mathbf{E} are the magnetic field vector and the electric field vector, \mathbf{B} and \mathbf{D} are the magnetic induction and the electric displacement. Maxwell's equation are complemented by the material equations,

$$\mathbf{D} = \varepsilon \mathbf{E} = \varepsilon_0 \mathbf{E} + \mathbf{P}, \quad (3.5)$$

$$\mathbf{B} = \mu \mathbf{H} = \mu_0 \mathbf{H} + \mathbf{M}. \quad (3.6)$$

where \mathbf{P} and \mathbf{M} are the electric and magnetic polarizations. In this chapter dealing with dielectric coatings, the response of the medium is considered to be linear, that is $\mathbf{P} = \varepsilon_0 \chi \mathbf{E}$, where χ is the electric susceptibility.

In a homogeneous and isotropic media, the wave-equations for a linear medium can be derived leading to

$$\nabla^2 \mathbf{E} - \mu \varepsilon \frac{\partial^2 \mathbf{E}}{\partial t^2} = 0, \quad (3.7)$$

with $\varepsilon = \varepsilon_0(1 + \chi)$. In case of a nonmagnetic medium ($\mu = \mu_0$), this is the same equation as Eq.2.40 already encountered when treating the non-linear response of electromagnetic radiation, simply neglecting all nonlinear terms. Using Stokes and Gauss divergence theorem, it can be shown, that the normal components of \mathbf{D} and \mathbf{B} and the tangential components of \mathbf{E} and \mathbf{H} are continuous across the interface of two medias, if the surface charge density and surface current density are both zero.

This continuity leads directly to the kinematic properties of reflection and refraction of an incident plane wave $\mathbf{E}_i e^{i(\omega t - \mathbf{k}_i \cdot \mathbf{r})}$ satisfying the wave equation 3.7, the well known Snell's law: $n_1 \sin(\alpha_1) = n_2 \sin(\alpha_2)$. In case of normal incidence, the more interesting problem however is the dynamic part, that is the amplitudes of transmitted and reflected waves.

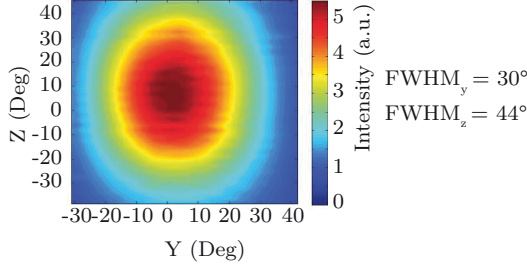


Fig. 3.1: Typical far-field measurement of a buried-heterostructure QCL. The ridge width is approximately $10\mu\text{m}$, the laser wavelength is $\lambda = 9\mu\text{m}$.

The laser output is strongly diffracted at the laser facet, leading to a far field featuring a FWHM of $\sim 30 - 50^\circ$. Fig. 3.1 shows a typical far-field measurement of a buried-heterostructure QCL emitting radiation at $\lambda = 9\mu\text{m}$. The ridge width is approximately $10\mu\text{m}$. The measured FWHM_y in the y-direction is 30° . In the growth direction, the measured FWHM_z is 44° . Therefore, the propagation constant β of the diffracted output beam propagating in the coating does not have to be perpendicular to the facet of the laser. Considering this strong diffracted beam, it is interesting to develop a formalism to calculate the coating reflectance and transmittance of plane waves as a function of angle. Compared with earlier AR coating treatment for QCLs [12], the matrix formulation which will be developed will not be restricted to zero angle incidence light, making it more versatile. Therefore, it can take into account the diffracted beam at the output of the facet and the possible facet reflection of a coated laser in case light is back-coupled through a high-NA lens.

Fig. 3.2a illustrates two different possible propagation constants $\beta_{1/2}$. The QCL laser output is always TM-polarized (p-polarized) with respect to the waveguide. With respect to dielectric coatings applied to the surface, the output is seen as either TM-polarized, illustrated in Fig. 3.2b and TE-polarized, illustrated in Fig. 3.2c. The general solution of the wave equation 3.7 giving the superposition of reflected and refracted wave on a boundary surface is given by

$$\mathbf{E} = \begin{cases} (\mathbf{E}_1 e^{-i\mathbf{k}_1 \cdot \mathbf{r}} + \mathbf{E}'_1 e^{-i\mathbf{k}'_1 \cdot \mathbf{r}}) e^{i\omega t} & \text{if } x < 0, \\ (\mathbf{E}_2 e^{-i\mathbf{k}_2 \cdot \mathbf{r}} + \mathbf{E}'_2 e^{-i\mathbf{k}'_2 \cdot \mathbf{r}}) e^{i\omega t} & \text{if } x > 0. \end{cases} \quad (3.8)$$

For a TM-polarized wave shown in Fig. 3.2b, the continuity of \mathbf{E}_z and \mathbf{H}_y gives

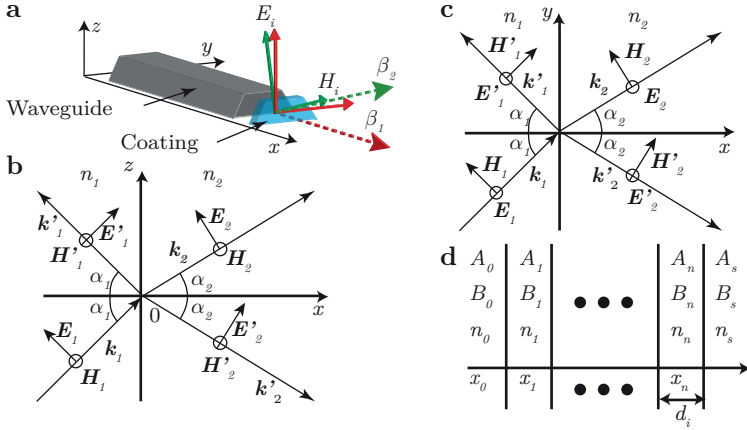


Fig. 3.2: Propagation of electromagnetic radiation at dielectric boundaries. **a** TM-polarized output of the QCL. Two different possible propagation constants $\beta_{1/2}$. **b** Reflection and refraction of a TM-polarized wave with respect to the applied dielectric coating. The magnetic field vectors are chosen to give a positive power flow. **c** Reflection and refraction of a TE-polarized wave with respect to the applied dielectric coating. **d** Multilayer propagation of electromagnetic radiation.

the following relations

$$(E_1 + E'_1) \cos(\alpha_1) = (E_2 + E'_2) \cos(\alpha_2), \quad (3.9)$$

$$\sqrt{\frac{\epsilon_1}{\mu_l}} (E_1 + E'_1) = \sqrt{\frac{\epsilon_2}{\mu_l}} (E_2 + E'_2). \quad (3.10)$$

This can be written in matrix form,

$$D(1) \begin{pmatrix} E_1 \\ E'_1 \end{pmatrix} = D(2) \begin{pmatrix} E_2 \\ E'_2 \end{pmatrix}, \quad (3.11)$$

$$\rightarrow \begin{pmatrix} E_1 \\ E'_1 \end{pmatrix} = D(1)^{-1} D(2) \begin{pmatrix} E_2 \\ E'_2 \end{pmatrix}, \quad (3.12)$$

with

$$D_{\text{TM}}(i) = \begin{pmatrix} \cos(\alpha_i) & \cos(\alpha_i) \\ \sqrt{\frac{\varepsilon_i}{\mu_i}} & -\sqrt{\frac{\varepsilon_i}{\mu_i}} \end{pmatrix}. \quad (3.13)$$

$D(i)$ is the dynamic matrix for a TM-polarized wave. The derivation of the dynamic matrix for a TE-polarized wave is the same and leads to the result

$$D_{\text{TE}}(i) = \begin{pmatrix} 1 & 1 \\ \sqrt{\frac{\varepsilon_i}{\mu_i}} \cos(\alpha_i) & -\sqrt{\frac{\varepsilon_i}{\mu_i}} \cos(\alpha_i) \end{pmatrix}. \quad (3.14)$$

In case for a nonmagnetic medium ($\mu_i = \mu_0$), the two dynamic matrices can be simplified to

$$D_l = \begin{cases} \begin{pmatrix} \cos(\alpha_l) & \cos(\alpha_l) \\ n_l & -n_l \end{pmatrix} & \text{for TM-polarized wave,} \\ \begin{pmatrix} 1 & 1 \\ n_l \cos(\alpha_l) & -n_l \cos(\alpha_l) \end{pmatrix} & \text{for a TE-polarized wave.} \end{cases} \quad (3.15)$$

As expected, at zero angle incidence, the dynamic matrices of the TM- and TE-polarized light are the same.

Considering Fig.3.2b, we are interested in the propagation across multiple thin-films of thickness d_i and refractive index n_i . The indices A_i and B_i represent the amplitudes of the right and left traveling waves. The dynamic matrix of the TM-polarized wave describes the transition at the interface of two materials of refractive index n_1 and n_2 . To fully describe the propagation in a thin-film, we need to introduce the propagation matrix P_i , with

$$P_i = \begin{pmatrix} e^{i\varphi_i} & 0 \\ 0 & e^{-i\varphi_i} \end{pmatrix}, \quad (3.16)$$

where φ_i is the phase change acquired by the light propagating through the medium of thickness d_i and is given by

$$\varphi_i = \frac{2\pi n_i d_i}{\lambda} \cos(\alpha_i). \quad (3.17)$$

It is afterward straight forward to write the whole propagation illustrated in Fig. 3.2d

in matrix form

$$\begin{pmatrix} A_0 \\ B_0 \end{pmatrix} = \begin{pmatrix} M_{11} & M_{12} \\ M_{21} & M_{22} \end{pmatrix} \begin{pmatrix} A_s \\ B_s \end{pmatrix}, \quad (3.18)$$

with the matrix M given by

$$M = D_1^{-1} \left[\prod_{l=1}^N D_l P_l D_l^{-1} \right] D_S. \quad (3.19)$$

The amplitude reflection and transmittance functions are simply calculated by

$$r = \frac{B_0}{A_0} = \frac{M_{21}}{M_{11}} \quad (3.20)$$

$$t = \frac{A_s}{A_0} = \frac{1}{M_{11}}. \quad (3.21)$$

If both surrounding media n_0 and n_s of the multilayer coating are non-absorbing, the reflectance R and transmittance T is consequently given by

$$R = |r|^2 = \left| \frac{M_{21}}{M_{11}} \right|^2 \quad (3.22)$$

$$T = \frac{n_s \cos(\alpha_s)}{n_0 \cos(\alpha_0)} |t|^2 = \frac{n_s \cos(\alpha_s)}{n_0 \cos(\alpha_0)} \left| \frac{1}{M_{11}} \right|^2. \quad (3.23)$$

The absorption of the thin-film materials is taken into account by the complex refractive index $n = n_R + in_I$. The imaginary part of the refractive index is linked to the absorption coefficient $\alpha = \frac{4\pi n_I}{\lambda}$. In the case the absorption coefficient for the materials is known, the total absorbance can easily be calculated by the formula $A = 1 - R - T$, reflecting the conservation of energy.

3.3.1 Single- and multi layer coatings

The first coatings which were developed for external-cavity QCL operations were based on a single layer coating run of ZnS. Solving the previous problem analytically, the minimum reflectance of a quarter wave is achieved if the thickness is

$$d = \frac{\lambda}{4n}. \quad (3.24)$$

To achieve zero reflectance however, the dielectric material must have exactly a refractive index of $n_2 = \sqrt{n_{eff} n_3}$, where $n_3 = 1$ is the refractive index of air and n_{eff} is

the effective refractive index of the mode. Therefore, to achieve zero-reflectance (at zero angle), it is necessary to combine two materials with different refractive index. Those coatings are commonly called v-coatings, which stands for the resulting v-shape of the AR coating as a function of wavelength. There is another important advantage of v-coatings to single layer quarter wave stacks apart from zero reflectance. The ideal quarter wave plate for a QCL has a refractive index $n \approx \sqrt{3.4} = 1.85$. This results in effective layer thickness of the quarter wave of $1.35 \mu\text{m}$ at $\lambda = 10 \mu\text{m}$. The combination of a low refractive index material with a high-refractive index material in v-coatings allows for generally thinner effective layers. A YF_3/ZnSe coating with zero reflectance is in total $1.05 \mu\text{m}$ thick. The first v-coatings which were achieved in the group were based on a combination of YF_3 and ZnSe [12]. The advance of broadband QCLs spanning an ever bigger bandwidth however requires the development of broadband anti-reflection coatings for those laser. To prohibit the lasing of parasitic chip modes in an external-cavity configuration, a laser featuring a flat broadband inhomogeneous gain needs a decreased reflectance over the whole bandwidth for single-mode operation (see sec. 4.2.3). A combination of two v-coatings, resulting in four layers ($\text{YF}_3/\text{Ge}/\text{YF}_3/\text{Ge}$) gives low reflectance over a broad bandwidth. With adequate pre-cleaning procedures of the substrate (Ozone, AR-sputtering), the total film thicknesses of $\sim 2 \mu\text{m}$ was found to be still thin enough to prevent the coating from peeling off.

3.3.2 Design and optimization of coatings

Using the matrix formulation, we are able to quickly calculate the transmittance (T), reflectance (R) and absorbance (A) of a coating containing n -layers. We developed a computer program which is based on a genetic algorithm available in MATLAB to solve for a minimum of a fitness function. We chose a genetic algorithm since it allows for very complex problem solving, containing possibly hundreds of layers (chirped-period layers, graded-multilayer coatings). Each individual is a n -dimensional vector, representing the thickness of each layers. The program calculates T , R , A as a function of wavelength. To calculate the ideal thicknesses of a broadband multilayer coating, the fitness-function is usually a least-square sum of R over the desired wavelength range.

It is simple to adjust the program to different fitness functions. For example the optimization of coatings for high-reflectance is a simple minimization of the fitness function $(1-R)$. The coating can be optimized for any arbitrary reflection x with a fitness function of $(x-R)$. For high power lasers this program can easily be used to develop coatings which also minimize the absorbance in the coating by adjusting the fitness function.

Since the program can also treat T , R , and A as a function of incidence angle,

the diffraction of a QCL output can be taken into account in the fitness function. For normal incidence, we usually put $\alpha = 0$ and calculate a least square sum over the desired wavelength range. If we take the angular dependence into account, we need to generate two matrices (diffraction in y and z -direction) calculating R , T and A as both a function of wavelength and angle. The calculated matrices R contain the individual matrix elements $R_{i,j} = R(\alpha_i, \lambda_j)$. To account for the power distribution (see fig. 3.1) we multiply each column of $R_{i,j}$ by a vector of length i with a Gaussian-distribution of FWHM representing the diffracted power output of a QCL (FWHM_z TM/ FWHM_y TE). As in the case for the normal incidence, the fitness-function is usually a least-square sum of all the elements of the matrix $R_{i,j}$. One of the example coatings shown in fig. 3.3b is simulated taking into account the diffraction at the laser interface.

3.4 Characterization of coatings

Threshold current density

It is possible to estimate the waveguide losses and the performance of the AR coating by measuring the threshold currents of the as cleaved laser, the HR coated laser and the AR/HR coated laser. Since the threshold current density is proportional to the total losses, the ratio of the threshold currents before and after coating is given by

$$\rho = \frac{J_{\text{th,HR}}}{J_{\text{th,Cleaved}}} = \frac{\alpha_{\text{wg}} - \frac{1}{2L} \ln(R_{\text{facet}} R_{\text{HR}})}{\alpha_{\text{wg}} - \frac{1}{2L} \ln(R_{\text{facet}}^2)}. \quad (3.25)$$

Reformulating this we get the reflectivity of the deposited HR coating as followed

$$R_{\text{HR}} = R_{\text{facet}}^{(2\rho-1)} e^{-2L\alpha_{\text{wg}}(\rho-1)}. \quad (3.26)$$

Given the fact that we know the cleaved facet reflectivity $R_{\text{facet}} = 0.29$ and the reflectivity of the deposited HR coating of about $R_{\text{HR}} = 0.98 \approx 1$, we can deduce the waveguide losses.

$$\alpha_{\text{wg}} = \frac{1}{2L(1-\rho)} \ln \left(\frac{R_{\text{HR}}}{R_{\text{facet}}^{(2\rho-1)}} \right). \quad (3.27)$$

We can in addition measure the ratio of the threshold currents before and after AR coating the device, we can measure the reflectivity of the deposited AR coating at the

peak of the gain curve of our device

$$\rho_{\text{AR}} = \frac{J_{\text{th,AR}}}{J_{\text{th,HR}}} = \frac{\alpha_{\text{wg}} - \frac{1}{2L} \ln(R_{\text{HR}} R_{\text{AR}})}{\alpha_{\text{wg}} - \frac{1}{2L} \ln(R_{\text{HR}} R_{\text{facet}})}. \quad (3.28)$$

Analogous as before we can therefore deduce the reflectivity

$$R_{\text{AR}} = R_{\text{HR}}^{(\rho_{\text{AR}}^{-1})} R_{\text{facet}}^{\rho_{\text{AR}}} e^{-2L\alpha_{\text{wg}}(\rho_{\text{AR}}^{-1})} \approx R_{\text{facet}}^{\rho_{\text{AR}}} e^{-2L\alpha_{\text{wg}}(\rho_{\text{AR}}^{-1})}. \quad (3.29)$$

Broadband AR coating measurements using a Fourier-transform interferometer

The characterization technique of AR-coatings using the threshold-current density presented in the previous section does not give any information on the wavelength dependence of such coatings. Using this technique on broadband QCLs can result in wrong measurements, since it only gives an information at what current density the modal gain at an arbitrary wavelength within the gain spectrum overcomes the losses at said wavelength $G_M(\lambda) = \alpha_{\text{tot}}(\lambda)$.

To characterize the transmittance and reflectance as a function of wavelength of deposited coatings, we resorted to a method employing a Fourier-transform interferometer. If the coherence length of the source is lower than the thickness of the sample, the transmittance of a layer must be calculated by spectral averaging [173]. If the spread of the phase shift of an incoherent source is bigger than π ($|\Delta\varphi| > \pi$, where $\varphi = \frac{2\pi}{\lambda} n d \cos(\alpha)$) then the transmittance is no longer a periodic function of layer thickness. The transmittance of a thick and completely transparent plate of a non-coherent broadband light source (glowbar in the FTIR) is given by

$$\langle T \rangle = \frac{1}{\lambda_2 - \lambda_1} \int_{\lambda_1}^{\lambda_2} T(\lambda) d\lambda = \frac{T_{12} T_{23}}{1 - R_{12} R_{23}}, \quad (3.30)$$

where $T_{i,j}/R_{i,j}$ is the transmittance and reflectance of the interfaces. In order to apply this formula to calculate the transmittance of a InP substrate, the resolution of the scan must be lower than the spacing of the Fabry-Pérot etalon of the InP substrate.

A reference sample of double side polished very-low doped InP ($1 \times 10^{15} \text{ cm}^{-3}$) must be put into the evaporator together with the actual samples. Regardless of the low doping, the reference sample might have a non-negligible absorption coefficient. This has been taken into consideration by adapting Eq. 3.30. The absorption coefficient only varies slowly over the spectral averaged signal, therefore the absorption term in Airy's formula can be treated as a constant. The final transmittance of an absorbing tick

layer is given by

$$\langle T \rangle = \frac{T_{12}T_{23}e^{-\alpha d}}{1 - R_{12}R_{23}e^{-2\alpha d}}, \quad (3.31)$$

Three measurements must be taken, the background-scan I_0 , the mean transmittance through an uncoated reference sample I_{InP} and the mean transmission trough a one side coated reference sample $I_{\text{AR/HR}}$. $\langle T_{\text{InP}} \rangle = \frac{I_{\text{InP}}}{I_0}$ allows to extract the constant $e^{-d\alpha}$, and the transmittance measurement $\langle T_{\text{AR/HR}} \rangle = \frac{I_{\text{AR/HR}}}{I_0}$ allows to extract R_{12} and T_{12} in case of a non-absorbing coating $R_{12} + T_{12} = 1$. If the coating is absorbing, the results of the measurement are not accurate and show a higher reflectivity than it is actually the case.

3.5 Coating examples

In the course of this work, the deposited AR-coatings for EC-QCL applications were all v-coatings, whose results can be found in chapter 4. This section presents the possibility to use the material system YF_3/Ge as HR and broadband AR coatings. It also illustrates the shortcomings in e-beam evaporated YF_3 for broadband AR coatings.

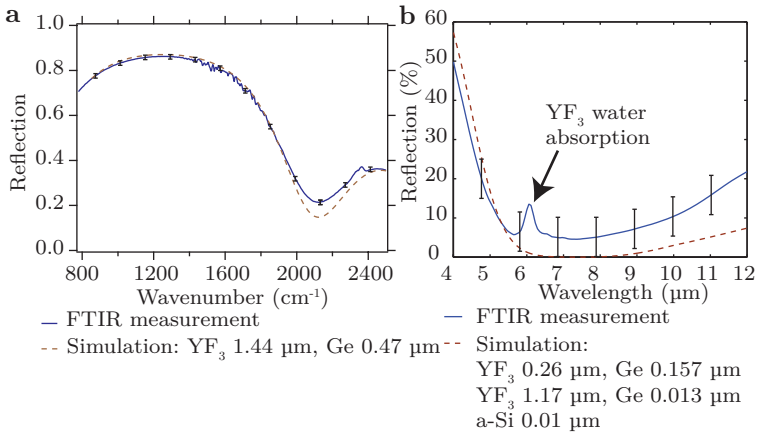


Fig. 3.3: HR and broadband AR coating measurements using the FTIR. **a** Simulation and measurement of dielectric HR-coating. **b** Simulation and measurement of broadband AR-coating taking the diffracted output beam of the laser into account.

Fig. 3.3a shows the simulated and measured dielectric HR coating. The HR-coating was optimized to have a maximum reflection at $8\text{ }\mu\text{m}$ (1250 cm^{-1}). The deposited coating consists of $1.44\text{ }\mu\text{m}$ of YF_3 and 470 nm of Ge, resulting in a total thickness of $1.9\text{ }\mu\text{m}$. Reflection coefficients of $>80\%$ are achieved. Such coatings are interesting to use as HR-coating on the front facet. They should also be considered to be used on epi-side down mounted devices, minimizing the risk of a short circuit after a metallic HR coating.

Fig. 3.3b shows the simulated and measured dielectric broadband AR coating. The coating is optimized for minimal reflection between in the $6\text{--}8.1\text{ }\mu\text{m}$ range (1666 cm^{-1} - 1235 cm^{-1}). Furthermore, the diffraction of the laser beam was taken into account, see sec. 3.3.2. The material sequence is $\text{YF}_3/\text{Ge}/\text{YF}_3/\text{Ge}$ finished by a 10 nm thick Al_2O_3 passivation layer. The optimized thicknesses for the layers are $259\text{ nm}/157\text{ nm}/1.17\text{ }\mu\text{m}/14\text{ nm}$. The 10 nm thick passivation layer is also taken into account during the optimization process. For normal incidence, the layer thickness l is obvious from the measurement, that the coating is not performing as nice as the simulation would suggest. The bump at $6\text{ }\mu\text{m}$ is attributed to the strong water absorption of the YF_3 layer. The overall reflectance is $4.5\text{--}5.5\%$ in the region of interest (apart from the water lines). The discrepancy between the simulation and the measurement is explained by the bad YF_3 deposition technique, using e-beam. As discussed in the previous section, this results in the formation of the metallic Yttrium, increasing considerably the absorption. 4 layer AR-coatings deposited nowadays using boat-evaporation for YF_3 show performances as expected by the simulation resulting in low reflectivity coatings ($<1\%$) over a broad bandwidth [174].

The layer thicknesses of the coating shown in fig. 3.3b were optimized taking the diffraction of the laser beam into account. It is therefore interesting to compare the optimal layer thicknesses of this simulation with the one optimized for normal incidence. The optimized layer thicknesses for a diffracted laser beam are ($259\text{ nm}/157\text{ nm}/1.17\text{ }\mu\text{m}/14\text{ nm}$). The optimized layer thicknesses for a plane wave at normal incidence are ($259\text{ nm}/157\text{ nm}/1.224\text{ }\mu\text{m}/9.6\text{ nm}$). The first two layers are exactly the same, whereas the last two layers show a noticeable difference. Neglecting the last passivation layer of Al_2O_3 , the optimized coating for a diffracted beam is slightly shorter, by about 3% .

Looking at the measurements, the FTIR measurement is not very accurate. It depends strongly on the placing of the sample in the FTIR sample compartment. If the measurement is performed well and the coating is not absorbing, we estimate a measurement accuracy of about $\pm 1\%$. The measurement of the HR-coating in fig. 3.3a shows error-bars of $\pm 1\%$. The measurement agrees well over most the wavelength

range with the simulation. However, if the coating is absorbing, we have errors in the measurement of 8-15 %. The error bars in fig.3.3b are $\pm 5\%$ and the measurement still does not fit within the error. Regardless of these strong errors, the measurement is still valuable, as it gives an idea of the efficiency of the applied coating as a function of wavelength.

Chapter 4

Broadband external-cavity quantum cascade laser

In this chapter we will discuss the goals, theory and achievements of using a QCL as a gain medium for external-cavity tuning. It summarizes the results and knowledge gained in working with external-cavity QCLs (EC-QCLs) using QCLs with different active region designs. It starts with an introduction of broadband EC-QCL tuning. Then it will give a summary of the EC setups used in our experiments, accompanied by a rate equation model for EC-QCLs to complete the set of rate equations shown in section 2.1.1. This will lead to the discussion of the importance of broad gain engineering (see section 2.2) and broad and low reflectivity AR-coating (see section 3). This is followed by a presentation and discussion of measurements we achieved using a single stack, heterogeneous and multi-stack QCLs based on the bound-to-continuum design. Figure 4.1 summarizes the achieved tuning in the scope of this work of EC-QCLs and compares it to previous work, covering the technologically interesting wavelength range $\lambda = 7.5\text{ }\mu\text{m}-11.5\text{ }\mu\text{m}$. To round off the chapter and to underline the continuous interest in EC-QCLs, I will give a short resume of published work employing an EC-QCLs. These results are also published in a topical review paper in Semiconductor Science and Technology [113].

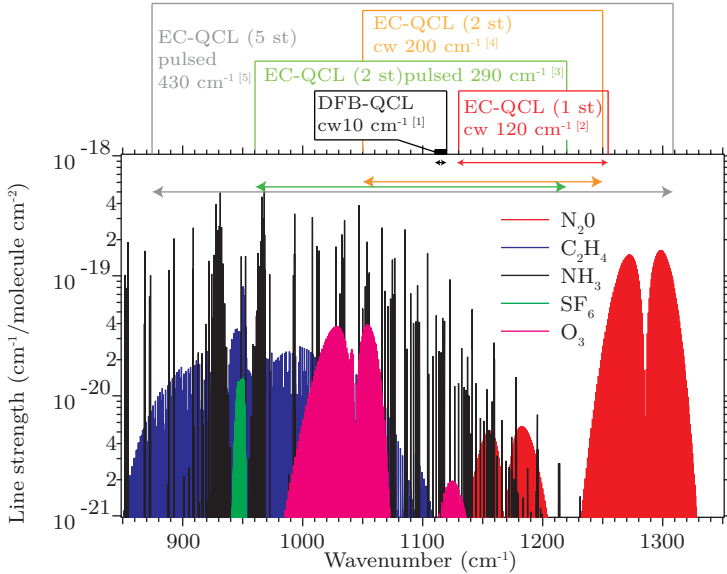


Fig. 4.1: Summary of EC-QCL tuning achieved using different active region designs. The results are compared to a standard distributed feedback (DFB)-QCL process to illustrate the increased tuning range of EC-QCLs. Different tuning curves are achieved either in pulsed or continuous-wave operation employing different active region designs. To date, the emission of a QCL is generally broadened by combining dissimilar sub-stacks (ST) in one active region. The different tuning results are superimposed on HITRAN simulation of abortion spectra to illustrate the possibility to tune over entire absorption bands with one EC-QCL. Sources: (1) [36], (2) [175], (3), [176], (4) [177], (5) [178]. Reprint from [113].

4.1 Introduction

Thanks to its properties, the QCL attracted a lot of attention for spectroscopic applications right from the beginning. The characteristics the QCL had to feature to become a useful light source for first sensing applications were single-frequency emission and the frequency had to be tunable. It was only two years after the first demonstration of the QCL that J.Faist *et al.* and C. Gmachl *et al.* demonstrated the first DFB-QCLs [179, 180]. Shortly after in 1998, first results using a room temperature DFB-QCL demonstrating spectroscopic measurements were reported [181] and high-resolution spectroscopy was shown [182]. The field evolved quickly, reflecting the large interest in using DFB-QCLs for various applications. Only a few years later several groups worldwide have demonstrated a number of spectroscopic techniques employing DFB-QCLs [183].

DFB-QCLs are very useful spectroscopic sources but their main disadvantage is their limited tuning capability. They owe their success to their small size, the ruggedized single-mode emission and the mode-hop free tuning capability. A thermal tuning of $\sim 10\text{ cm}^{-1}$ - 20 cm^{-1} can be achieved using one single device when slow temperature tuning is applied [36]. However, fast temperature tuning by the injection current through Joule heating is lower and is limited to $\sim 2 - 3\text{ cm}^{-1}$. To achieve broader tuning ranges using DFB-QCLs, another proposed solution is the fabrication of a DFB-QCL Array [184]. In Ref. [185], the authors report a monolithic array of 32 DFB lasers whose wavelengths span a range of 220 cm^{-1} . Combining the DFB-array in a MOPA configuration helps to boost the output power of these devices. Peak output powers of 2.7 to 10 W were demonstrated recently on an array of MOPA-QCLs covering the wavelength range $9.2\text{--}9.8\text{ }\mu\text{m}$ [186]. Nevertheless, the drawbacks of this approach are the difficulties arising from the various performances of the lasers in the array (single-mode selection, variability in threshold, slope-efficiency, output-power), resulting in a lower yield, and the spatial separation of the emitted beams not originating from a single QCL emitter, requiring beam combining to be useful in potential applications. Another way to increase the limited tuning range of DFBs is the use of sampled gratings. At a wavelength of $4.8\text{ }\mu\text{m}$, a two-section, sampled grating, DFB-QCLs can be electrically tuned over 120 cm^{-1} [187].

Using a grating-coupled external-cavity (EC)-QCL overcomes the limited tuneability of DFB-QCLs. It comes at an additional price of supplementary components and a more complex handling. The first EC-QCL was demonstrated in 2001 [188] at cryogenic temperature by Luo *et al.*. Shortly after, in 2002, Totschnig *et al.* from the University of Technology of Vienna, Austria, reported an EC-QCL operating in pulsed

mode at room temperature at a wavelength of $10.4\mu\text{m}$ [189]. In the same year, Luo *et al.* achieved single-mode operation over a broader tuning range, obtaining a grating tuning of 120 nm (54 cm^{-1}) at 84 K at a wavelength of $5.1\mu\text{m}$ [190]. Combining temperature and grating tuning, they could extend the tuning range to 91 cm^{-1} . The suitability of this system for spectroscopic applications was also demonstrated in the same paper as measurements of a water absorption line at $5.083\mu\text{m}$ were presented. Further studies were done by the same group to improve the performance and understanding of EC-QCLs, and measurements of temperature fine-phase tuned EC-QCL were presented [191]. The invention of the bound-to-continuum design (see sec.2) combined a large gain with a broad spectrum, making the QCL an ideal gain medium. EC-QCLs using this active region could be tuned over 150 cm^{-1} in pulsed mode at room temperature [115].

4.2 Theory

4.2.1 External-cavity setups

Adding a grating-coupled EC-system is a widely used technique to alter a free running semiconductor laser into a tunable single mode source. An EC-system is made of three main elements, the gain element, in our case the QCL chip, the collimating lens and the grating which acts as a wavelength filter element within the system [192]. The two most common grating coupled EC-systems for semiconductor lasers are the Littman-Metcalf [193] and the Littrow configuration. Both setups have been used and studied in conjunction with a QCL as a gain medium [194].

Fig. 4.2 shows different realizations of the Littrow configuration. The main advantages of this configuration compared with the Littman-Metcalf configuration are the

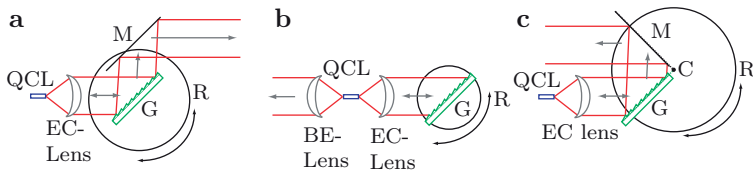


Fig. 4.2: EC-QCL configurations. **a** Littrow configuration. The first order diffracted beam is back coupled into the laser, the zeroth order beam is outcoupled through a mirror. **b** Littrow back-extraction setup. **c** Modified Littrow front extraction setup to prevent the walk-off of the outcoupled beam [195]

increased feedback of the setup and the easier alignment of the optical components. The first-order diffracted beam is back coupled into the laser, whereas the zeroth order beam is collected through an additional mirror. Coarse tuning is achieved through rotation of the grating G. The back-extraction setup shown in Fig. 4.2 b) shows a popular modification of the standard Littrow configuration [175, 196–198]. Instead of collecting the zeroth order beam of the grating, an additional lens is added to the setup at the back facet of the gain medium. This allows for a complete separation of the mechanically moving parts and the outcoupled beam. Furthermore, employing this configuration, we could show that the output power in this configuration is increased by a factor > 10 [175]. The increased output power from 1.5 mW to 20 mW in continuous-wave was attributed to the low zeroth-order output coupling efficiency (5 %) of our grating. Even though this configuration suffers under slightly lower tuning ranges, see section 4.2.5 for theory and 4.4 for measurements, the benefit of the stable beam in conjunction with an increased output power often outweighs this deficit, especially for highly alignment sensitive spectroscopic setups. Broadband tuning records during this work were all achieved using the standard configuration shown in Fig. 4.2 a), whereas the broadband spectroscopy results in section 4.6 are achieved using the back-extraction configuration. Other modified geometries, such as the one shown in 4.2 c), prevent the walk-off of the outcoupled beam [195].

4.2.2 Lens and grating

Of paramount importance for good EC-QCL tuning is the employed lens and a good grating. The results of the single stack and heterogeneous-stack EC-QCL were all preformed using a germanium f/0.6 lens with a diameter of 24 mm [175, 177]. The lens is coated with a broadband AR coating covering 3 to 12 μm . Fig. 4.3a shows the back-extraction setup using the large germanium lens. To increase the feedback and the versatility of the system, another more compact EC-setup was developed, which was used for the multi-stack EC-QCL measurements [178]. To shrink the dimensions of the EC, the main factor to change is the lens focal length. We therefore switched to aspheric molded lenses from LightPath Technologies with a clear aperture of only 4.0 mm. The IR glass used is BD-2, a $\text{Ge}_{28}\text{Sb}_{12}\text{Se}_{60}$ compound. Further advantage of the chalcogenide glass compared to germanium are lower coefficient of linear thermal expansion and the decreased change of refractive index as a function of temperature ($\frac{dn}{dT}$). Furthermore the BD-2 glass can be operated up to 130 °C, whereas germanium suffers from increased absorption loss with increasing temperature, especially relevant above 40 °C. The lens features a numerical aperture of $\text{NA}=0.85$ with an effective focal length of 1.87 mm. The lens has a 7-11 μm broadband anti-reflection coating. The

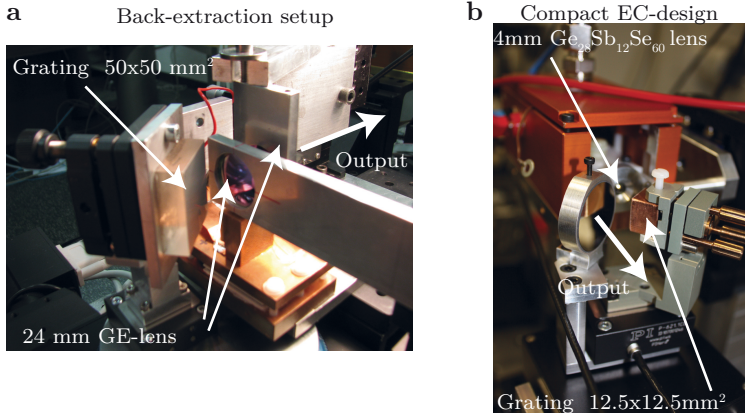


Fig. 4.3: **a** Back-extraction setup used in the broadband spectroscopic measurements. The front- and back-extraction lens are both Ge f/0.8 lenses of 24mm diameter. **b** Redesign of the external cavity setup for the very broadband tuning of the five color active region. The miniaturization of the setup was necessary to limit constraints of tuning capability due to simple geometric reasons. The redesign features a very small yet high NA lens and a very small grating.

gratings used in the original the single-stack and heterogeneous-stack EC-QCLs are all $50 \times 50 \text{ mm}^2$. To shrink the EC-QCL and taking advantage of the small Lightpath lens, we used specially fabricated gratings of $12.5 \times 12.5 \text{ mm}^2$ ordered from Lightpath. Fig.4.3b shows the redesigned EC-QCL setup with featuring the new lens and smaller grating.

The grating in the EC-setup acts as an wavelength filter. The bandwidth of the grating is can be estimated by [199]

$$\Delta\lambda = \frac{\lambda}{|m|N} = \frac{\lambda d \cos\theta}{a}, \quad (4.1)$$

where N is the number of illuminated grating lines, λ is the wavelength and m is the diffraction order. Since a shorter focal-length results in much lesser grating lines illuminated, the filter efficiency of the smaller EC-setup is strongly decreased. In the case of the short focal length lens, the collimated beam diameter is only $\approx 1.6 \text{ mm}$.

4.2.3 External-cavity quantum cascade laser rate-equations

Homogeneous gain region

Compared with the rate-equations shown in section 2.1.1 for a quantum cascade laser, the rate equation for an EC-QCL have to take into account the external resonator and several factors must be considered. Firstly, we have to introduce two distinctive optical flux densities, representing the total photon flux per unit active region width ($\text{cm}^{-1}\text{s}^{-1}$) in the chip Fabry-Pérot (FP) modes (S_{FP}) and EC modes (S_{EC}). Secondly, we must account for the longer round trip time of the EC-photons. We therefore multiply their speed by ρ_{cav}^{-1} , where $\rho_{\text{cav}} = 1 + L/nl$ is the ratio of the optical path lengths of the chip and the EC, l is the length of the chip, n its refractive index and L is the length from the front facet to the grating. Thirdly, one must include different total loss terms for the chip modes $\alpha_{\text{tot}}^{\text{FP}}$ and the EC modes $\alpha_{\text{tot}}^{\text{EC}}$. Fourthly, the gain cross section per period (cm^{-1}) of the EC modes depends on the gain profile. g_{FP} is the gain cross section per period of the FP-chip modes at the peak of the gain curve $g_c(\lambda_{\text{peak}})$, whereas g_{EC} reflects the gain cross section per period $g_c(\lambda)$ at the wavelength λ within the gain curve of the QCL.

The rate equations for an EC-QCL are [12]:

$$\frac{dn_3}{dt} = \frac{J}{e} - \frac{n_3}{\tau_3} - [S_{\text{FP}}g_{\text{FP}} + S_{\text{EC}}g_{\text{EC}}](n_3 - n_2) \quad (4.2)$$

$$\frac{dn_2}{dt} = \frac{n_3}{\tau_{32}} - \frac{n_2 - n_2^{\text{therm}}}{\tau_2} + [S_{\text{FP}}g_{\text{FP}} + S_{\text{EC}}g_{\text{EC}}](n_3 - n_2) \quad (4.3)$$

$$\frac{dS_{\text{FP}}}{dt} = \frac{c}{n} \left((N_p g_{\text{FP}}(n_3 - n_2) - \alpha_{\text{tot}}^{\text{FP}})S_{\text{FP}} + \beta_{\text{FP}} \frac{n_3}{\tau_{\text{sp}}} \right) \quad (4.4)$$

$$\frac{dS_{\text{EC}}}{dt} = \frac{1}{\rho_{\text{cav}}} \frac{c}{n} \left((N_p g_{\text{EC}}(n_3 - n_2) - \alpha_{\text{tot}}^{\text{EC}})S_{\text{EC}} + \beta_{\text{EC}} \frac{n_3}{\tau_{\text{sp}}} \right). \quad (4.5)$$

where n_3 and n_2 are the upper and lower sheet densities per period (cm^{-2}), τ_3 and τ_2 are the total lifetimes of states 3 and 2, τ_{32} is the non radiative relaxation time from level 3 to level 2, n_2^{therm} is the thermal population of level 2 and β is the fraction of spontaneous light emitted into the lasing mode. The total chip losses $\alpha_{\text{tot}}^{\text{FP}}$ are the sum of the waveguide losses and the mirror losses of the anti-reflection coated chip. The losses of the EC are given by $\alpha_{\text{tot}}^{\text{EC}} = \alpha_{\text{wg}} + \frac{1}{2L} \ln \frac{1}{R_{\text{EC}}R_2}$, where α_{wg} are the waveguide losses and $R_{2,\text{EC}}$ are the back facet mirror reflectance and the EC reflectance. R_{EC} is defined as $R_{\text{EC}} = (r_1 + \eta T_1 T_2 \sqrt{R_G})^2$, with r_1 being the amplitude reflectance of the front facet, $T_{1,2}$ is the front facet and lens transmittance, η is the coupling of the reflected wave into the waveguide mode, and R_G is the grating reflectance. As the gain

cross section, which is a function of wavelength for those equations, we use the gain cross section multiplied by the lineshape function, which was introduced in eq. 2.5.

The free running QCL will lase on the center modes at the peak of the gain curve $g_c(\lambda_{\text{peak}})$. The relative tuning of the free running wavelength is defined by $\Delta\lambda/\lambda_c$, where $\lambda_c = (\lambda_{\text{max}} + \lambda_{\text{min}})/2$ and $\lambda_{\text{min/max}}$ is the shortest respectively the largest achievable wavelength using one chip in the EC-setup.

The coarse tuning range of the external cavity laser can be obtained by studying the steady state solutions of 4.4 and 4.5. Since the FP and EC-modes share the same active gain media, they share the same electronic populations n_3 and n_2 . Neglecting the spontaneous emission into the lasing mode, the only possible steady state solution with $S_{\text{EC}} \neq 0$ is $(N_p g_{\text{EC}}(n_3 - n_2) - \alpha_{\text{tot}}^{\text{EC}}) = 0$. This is only possible as long as the condition

$$\frac{g_{\text{EC}}}{g_{\text{FP}}} \geq \frac{\alpha_{\text{tot}}^{\text{EC}}}{\alpha_{\text{tot}}^{\text{FP}}} \quad (4.6)$$

is fulfilled.

To increase the tuning range, it is therefore necessary to increase the gain g_{EC} with respect to g_{FP} . This can be achieved by broadening the gain curve. Another aspect influencing the tuning range can be controlled through the deposition of coatings on the laser facet. By depositing a high-reflectance coating on the back facet and an anti-reflectance coating on the front facet of the chip, it is possible to increase the relative losses of the FP-chip modes compared to the losses of the EC-modes.

Therefore another key element of an EC-setup is the quality of the anti-reflection (AR) coating deposited on the front facet of the QCL to suppress chip modes while increasing the feedback to the QCL. A major problem of the first EC-QCLs was the missing anti-reflection coating on the front facet. The mid-IR range requires the deposition of a relatively thick substrates to form a quarter wave layer. Thermal cycling of these devices resulted often in flaking off of the AR coating due to different thermal expansions of the AR coating and the substrate. Room-temperature operation of QCLs made it possible to develop very efficient AR coatings, increasing tremendously the performance of EC-QCLs. Additionally, the development of the buried-heterostructure [132] helped to improve the efficiency of the AR coatings. The lower residual reflectivity of the AR-coated facets of the buried-heterostructure geometry compared to ridge waveguides is attributed to reduced edge effects during vacuum deposition.

Heterogeneous gain region

Since the gain spectrum of a heterogeneous quantum cascade structure is inhomogeneously broadened, it behaves differently from usual structures such as the bound-to-continuum design. In particular, laser action at the grating selected wavelength, only clamps the gain at this particular wavelength at its threshold value and not the entire gain curve as in the case of homogeneous broadening. The condition $g_{\text{EC}}/g_{\text{FP}} \geq \alpha_{\text{tot}}^{\text{EC}}/\alpha_{\text{tot}}^{\text{FP}}$ seen in Eq. 4.6 still holds, but it only gives the wavelength range over which single-mode tuning is possible at threshold. In order to investigate theoretically the behavior above threshold we resorted to a rate equation model [12].

Let us consider a heterogeneous QCL composed of N substacks, where substack i contains $N_{p,i}$ gain stages emitting at wavelength λ_i . The rate equations are similar to eq. 2.10-2.13 which were introduced for a heterogeneous-cascade QCL without an EC. The main difference is the inclusion of the EC optical field. Furthermore, since we are only interested in steady-state solutions in single mode-operation, we did not include chip FP modes in the equations. To describe transient behavior, these modes can be included as described earlier in the text. Lasing of parasitic chip FP modes occurs when the condition $G_{\text{M}}(\lambda) = \alpha_{\text{FP}}(\lambda)$ is fulfilled. For simplicity, we neglected the spontaneous emission. The evolution of upper and lower states sheet carrier densities per stage in substack i , $n_{3,i}$ and $n_{2,i}$, and the photon flux density S_{EC} at the grating selected wavelength λ_{EC} are described by $2N + 1$ coupled equations:

$$\frac{dn_{3,i}}{dt} = \frac{J}{q} - \frac{n_{3,i}}{\tau_{3,i}} - S_{\text{EC}}g_{c,i}(\lambda_{\text{EC}})(n_{3,i} - n_{2,i}) \quad (4.7)$$

$$\frac{dn_{2,i}}{dt} = \frac{n_{3,i}}{\tau_{32,i}} - \frac{n_{2,i}}{\tau_{2,i}} + S_{\text{EC}}g_{c,i}(\lambda_{\text{EC}})(n_{3,i} - n_{2,i}) \quad (4.8)$$

$$\frac{dS_{\text{EC}}}{dt} = \frac{c}{n} \left[G_{\text{M}}(\lambda_{\text{EC}}) - \alpha_{\text{EC}} \right] S_{\text{EC}} \quad (4.9)$$

where $i = 1, \dots, N$, $g_{c,i}(\lambda)$ is the gain cross section per stage, S_{EC} is the total photon flux per unit width, and

$$G_{\text{M}}(\lambda) = \sum_{i=1}^N N_{p,i} g_{c,i}(\lambda) (n_{3,i} - n_{2,i}) \quad (4.10)$$

is the total modal gain summed over all the substacks.

4.2.4 External cavity quantum cascade laser pulsed and continuous-wave operation

Even though high performance continuous-wave operation of QCLs at room temperature with multi-watt output power and wall-plug efficiency in excess of 10% has become available, operating an EC-QCL in pulsed mode still offers several advantages and is suitable for many applications, as it effectively lowers the requirements on the gain medium and allows more flexibility in setting the total system thermal dissipation.

To understand the dynamic behavior of the spectral features of an EC-QCL at the beginning of each pulse, it is possible to study the set of rate equations presented in section 4.2.3. The dynamic behavior has been studied at the beginning of EC-tuning employing a bound-to-continuum quantum cascade laser operating in pulsed mode by Maulini *et. al* in [115]. Those findings were at a later date verified by Hinkov *et al* in [200]. Mode competition arises at the beginning of each pulse if an EC-QCL is operated in pulsed mode. This is due to the different round trip times of the FP-chip modes (30 ps for a 1.5 mm long device) and the EC-modes (570 ps for a 8 cm long free-space segment). At the beginning of the pulse, the shorter round trip time of the FP cavity enables a faster growth of the chip modes. The EC-mode takes over later because of the increased round trip time. First the chip FP-modes start to lase and the photon flux increases. The population inversion $\Delta n = n_3 - n_2$ decreases because of stimulated emission until the net modal gain $G = g_c \Delta n - \alpha_{FP}$ is zero. At this moment S_{FP} saturates and is stable. S_{EC} continuous to grow because its net gain is still positive if the condition 4.6 is fulfilled. The additional photon flux S_{EC} further reduces the population inversion until the gain cannot compensate the losses of the FP-chip modes any longer. Thus they eventually vanish, and only the EC modes are present. The measurements and the simulations both show single mode operation after ~ 10 ns for a 8 cm long external cavity configuration.

Pulse chirp arising from Joule heating is a negative side effect of driving an EC-QCL in pulsed mode. Pulse chirp limits the spectral resolution of spectroscopic measurements, therefore a good understanding of this phenomenon can help to estimate and limit this effect. Fig. 4.4 shows spectral measurements of an EC-QCL operated in pulsed mode with a repetition rate of 198 kHz and a pulse width of 200 ns. The QCL is mounted epi-down on a diamond submount to decrease the thermal resistance of the chip to reduce pulse chirp to a minimum. The thermal resistance of this device is 4.3 K/W [177]. The linewidth of the EC-QCL pulse increases with increasing current. Close to threshold (320 mA) it is 0.5 cm^{-1} and peaks at 1.1 cm^{-1} at 600 mA and stays about constant up to 990 mA. The linewidth of the EC-QCL stabilizes itself when it

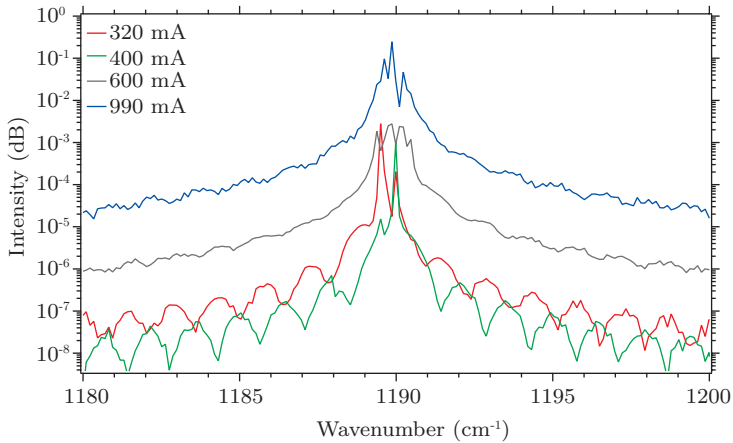


Fig. 4.4: Measurement of the linewidth variations arising from Joule heating of an EC-QCL in pulsed mode operation. All the measurements were taken at a repetition rate of 198 kHz and measured using an FTIR Nicolet 800. Reprint from [113].

reaches the linewidth given by filter function of the grating.

From the previous discussions of the mode-evolution in EC-QCLs and of pulse chirp, it becomes obvious that an EC-QCL that operates in continuous-wave will neither suffer from the limited SMSR ratio observed in pulsed mode EC-QCLs nor from pulse chirp. This has been confirmed experimentally by measuring instrument-limited SMSRs of 30 dB and an upper limit to the instantaneous laser linewidth to 5 MHz ($2 \times 10^{-4} \text{ cm}^{-1}$) by heterodyne beating of an EC-QCL and a single-mode FP QCL [201]. Those two features promise very high-resolution and very low detection limits for spectroscopic applications using continuous-wave EC-QCLs.

Using an EC-QCL pulsed at 33 kHz with a 50% duty cycle by coarse wavelength scans, Wysocki *et al.* demonstrated a spectroscopic measurements of broadband absorbing species [195]. Quartz enhanced photoacoustic spectrum of a gas mixture containing 7.2% ethanol and 0.24% H_2O in N_2 was measured. They estimated their actual resolution of the system to be $\sim 1.2 \text{ cm}^{-1}$. This is in good agreement with our own measurements.

4.2.5 External-cavity quantum cascade laser tuning analysis

The rate equation analysis gives us important insight into the limiting tuning achievable in an EC-configuration. Eq. 4.6 suggests that to increase the tuning range there are several important factors to consider. First of all, one needs to increase the gain at the lasing wavelength of the external cavity g_{EC} with respect to the gain at the peak wavelength g_{FP} . Methods to achieve this in QCLs has been discussed extensively in sec 2.2. Second of all, one needs to minimize the ratio between the total FP chip losses and the total EC-losses ($\frac{\alpha_{tot}^{FP}}{\alpha_{tot}^{EC}}$). The total losses of the FP chip or the EC-setup are given by

$$\alpha_{tot}^{EC,FP} = \alpha_W + \frac{1}{2L} \ln \left[\frac{1}{R_{1/EC} R_2} \right], \quad (4.11)$$

$$\alpha_{tot}^{EC} = \alpha_{wg} + \alpha_M^{EC} \quad (4.12)$$

$$\alpha_{tot}^{FP} = \alpha_{wg} + \alpha_M^{FP}, \quad (4.13)$$

where α_W are the waveguide losses, L is the length of the chip, $R_{1,2}$ is the front and back-reflection of the FP chip. R_{EC} is the total external-cavity reflection given by $R_{EC} = \left[r_1 + T_1 T_L \sqrt{R_G(\lambda)} \sqrt{\eta(\lambda)} \right]^2$, where r_1 is the amplitude reflection coefficient of the front facet, T_1, T_L are the intensity transmittance coefficients of the front facet and the lens. R_G is the wavelength dependent grating reflection coefficient and η is the coupling efficiency at wavelength λ .

Taking the total derivative of the ratio $\frac{\alpha_{tot}^{FP}}{\alpha_{tot}^{EC}}$,

$$d \left(\frac{\alpha_{tot}^{EC}}{\alpha_{tot}^{FP}} \right) = \frac{\alpha_M^{FP} - \alpha_M^{EC}}{(\alpha_{wg} + \alpha_M^{FP})^2} d\alpha_{wg} + \frac{1}{\alpha_{wg} + \alpha_M^{FP}} d\alpha_M^{EC} - \frac{\alpha_{wg} + \alpha_M^{EC}}{(\alpha_{wg} + \alpha_M^{FP})^2} d\alpha_M^{FP} \quad (4.14)$$

another important factor is starting to show up for good external-cavity tuning, namely low waveguide losses. It is not only that the waveguide losses have a direct influence on the tuning through the first term in Eq. 4.14, it is also that a lower waveguide loss increases the effect of lowering the EC losses and increasing the FP losses. The waveguide losses also have a direct influence on the possible useful length of the FP chips. Increasing the chip length directly decreases the tuning range, however a low waveguide losses ($\approx 2 \text{ cm}^{-1}$) decreases this influence dramatically.

Another interesting question to ask is, whether a high-reflection (HR) on the back facet of the FP chip helps to increase the tuning range. You could argue that the effect

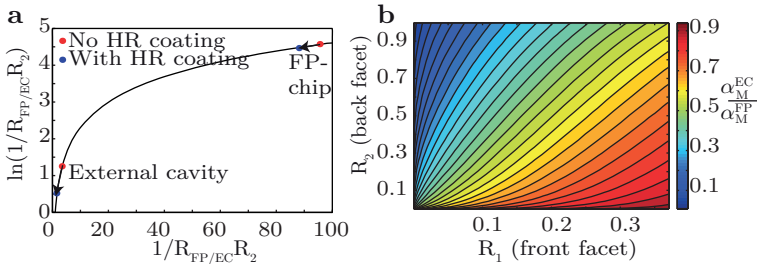


Fig. 4.5: Comparison of EC-QCL with and without HR coating on the back facet. **a** Schematic illustration of the effect of an HR coating on the total mirror losses in the case of a FP chip and in the case of the external-cavity. **b** Simulation of the ratio of the chip mirror losses versus the EC mirror losses as a function of front and back reflection of the FP chip.

of the coating on the FP chip losses and the EC losses are equal. Interestingly this is not the case and it helps indeed. The effect on the mirror losses are more pronounced on the total mirror losses of the EC-setup α_M^{EC} in comparison with the total mirror losses of the FP chip α_M^{FP} . As shown on Fig. 4.5a R_{EC} is bigger compared with the reflectance of the FP chip before applying the HR coating. Therefore, changing the reflectance of the back-facet with an HR coating has a positive effect on the tuning range due to the logarithmic dependence on the mirror losses. Fig. 4.5b shows a simulation of the expected ratio of $\frac{\alpha_M^{EC}}{\alpha_M^{FP}}$, with $T_L=0.98$ and $R_G = 0.95$. Studying this plot it is clear that a EC-setup which allows for an HR-coating at the back facet will yield better tuning performance. Indeed, in all our studies comparing the tuning ranges of an EC back-extraction setup with a conventional front extraction setup employing an HR-coated chip resulted in larger tuning ranges of at least 4 % of for the later.

4.3 Room-temperature continuous-wave operation of an external-cavity quantum cascade laser

In 2007 we realized a continuous-wave EC-QCL at room-temperature (20 °C) [175]. Compared to earlier continuous-wave-results [201], one main advantage was the possibility to run the EC at room-temperature. Running EC-QCL above the condensation point of water has many advantages. If the laser needs to be cooled below this point, the realization of an EC-QCL setup becomes more challenging. Peltier cooled QCLs running at low temperatures without an additional resonator are in general put into a

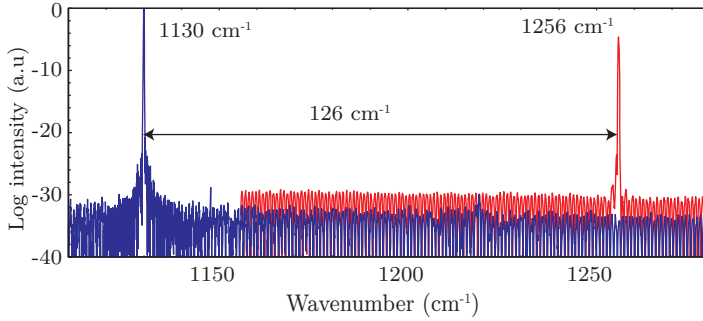


Fig. 4.6: Room-temperature continuous-wave operation of an EC-QCL, showing the shortest and longest-wavelength single-mode spectra. Data published in [175]

air tight laser box to avoid condensation. However, in case of an EC-QCL, the whole setup needs to be purged [199].

The active region of the gain element used in the setup is based on the bound-to-continuum design. The design in Å grown lattice matched on InP is as followed: **44**/**17**/**9**/**53**/**11**/**52**/**12**/**47**/**13**/**42**/**15**/**39**/**16**/**34**/**18**/**31**/**21**/**28**/**25**/**27**/**32**/**27**/**36**/**25** ($n_s = 1.2 \times 10^{11} \text{ cm}^{-2}$) where the InAlAs barriers are in bold print and InGaAs wells in roman numerals. The active region was processed in a buried-heterostructure for better heat-extraction and therefore enabling the continuous-wave-operation. Using a 1.5 mm long, 8 μm wide laser a tuning range of 0.88 μm (126 cm^{-1}) in continuous-wave operation was realized. The wavelength could be adjusted from 7.96 μm (1256 cm^{-1}) to 8.84 μm (1130 cm^{-1}). This corresponds to a tuning of over 10.4 % around the center wavelength. Fig. 4.6 shows the shortest- and longest-wavelength single-mode spectra of the laser measured with a FTIR spectrometer.

The front facet reflectivity was decreased using a bilayer ZnSe/YF₃ AR coating. Using the threshold current measurements (see sec. 3.4), we get a residual reflectivity of only $R_{\text{AR}} = 0.23 \%$ of the front facet. As discussed in the chapter 3, the combination of using a high and low index material for the coating allows for zero-reflectivity at one wavelength. This low reflectivity is however also attributed to the burier-heterostructure geometry which allows for a more homogeneous deposition of the coating on the front-facet. The low residual reflectivity of the AR-coated facet ensured the suppression of the chip modes. AR-coatings of this high quality enables us to achieve gap-free tuning by grating rotation alone. The mode hops occur only on the extended-cavity modes that are separated by 0.1 cm^{-1} .

By this, we have demonstrated that a EC-QCL setup mode hop free tuning should theoretically be possible by modulating just two parameters, namely the length of the EC, and the rotation angle of the grating. This is of importance as the mode-hop-free tuning can be achieved at a constant current and would mean only small involuntary change in the output power.

Furthermore, we developed the EC back-extraction setup discussed in section 4.2.1. Even though the tuning range of this setup was only 76 cm^{-1} (compared to 126 cm^{-1} in the front extraction setup), we were able to increase output power from 1.5 mW to 20 mW. The reduced tuning range in continuous-wave operation was mainly attributed to the less than optimal designed back-extraction setup for heat-extraction, limiting the tuning range limit mainly due to gain starving. The tuning differences between the two setup were less pronounced in pulsed operation.

4.4 Heterogeneous room-temperature continuous-wave operation of an external-cavity quantum cascade laser

A first heterogeneous active region operating in pulsed mode was tuned successfully by Maulini *et al.* over 265 cm^{-1} from $2.25 \mu\text{m}$ to $8.16 \mu\text{m}$ in 2006 [176]. This is a substantial increase compared to the single stack active regions based on the bound-to-continuum design which can be tuned over $\approx 150 \text{ cm}^{-1}$ in pulsed mode. However, the presented device was limited to low duty cycle pulsed operation because its high active region doping and because of the simple ridge-processing and mounting used. In order to demonstrate continuous-wave operation, we grew another epiwafer of the same active region design, but with lower active region and waveguide doping. The two designs in Å grown lattice matched on InP are the following: Design A $8.2 \mu\text{m}$: **43**/18/**7**/55/**9**/53/**11**/48/**14**/37/**15**/35/**16**/33/**18**/31/**20**/29/**24**/29/**26**/27/**30**/27 ($n_s = 1.0 \times 10^{11} \text{ cm}^{-2}$); Design B $9.3 \mu\text{m}$: **39**/22/**8**/60/**9**/59/**10**/52/**13**/43/**14**/38/**15**/36/**16**/34/**19**/33/**23**/32/**25**/32/**29**/31 ($n_s = 1.0 \times 10^{11} \text{ cm}^{-2}$) where the InAlAs barriers are in bold print and InGaAs wells in roman numerals. The wafer was processed in buried-heterostructure and devices were mounted epi-side down on diamond submounts to minimize thermal resistance [177].

A combination of HR and AR coatings was deposited on the facets of a $11.8 \mu\text{m}$ -wide, 3 mm-long chip. From measured threshold current densities of the as-cleaved and the AR coated front facet of the laser, a residual reflectivity of 0.245 % was calculated. Again, we attribute this lower residual reflectivity compared to ridge waveguides to the buried-heterostructure geometry which reduces edges effects during vacuum deposition.

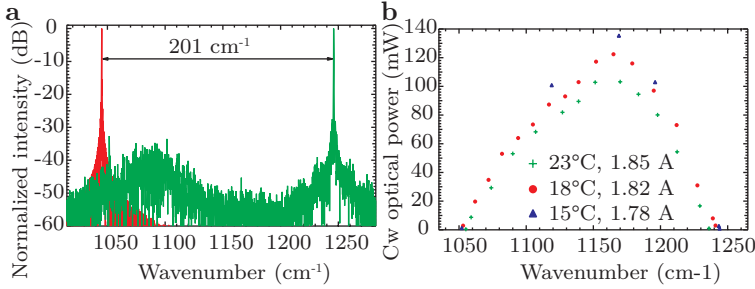


Fig. 4.7: Top: High resolution spectra at the extremes of tuning range of a continuous-wave heterogeneous EC-QCL with two different active region types. The chip could be tuned over 201 cm^{-1} (18% of center frequency) with a SMSR $>35\text{ dB}$. Bottom: continuous-wave output power of the same laser as a function of frequency for three different sets of operation conditions. A tuning of 172 cm^{-1} with $>20\text{ mW}$ of continuous-wave output power at 18°C was demonstrated. Reprint from [177].

First, we explored the tuning properties of our device in pulsed operation (400 ns, 99 kHz) at 30°C and 1.6 A. We were able to tune the device from $9.87\text{ }\mu\text{m}$ (1013 cm^{-1}) to $7.66\text{ }\mu\text{m}$ (1305 cm^{-1}). The operation spanning over $2.2\text{ }\mu\text{m}$ (292 cm^{-1}) equals 25% of center wavelength, which is slightly greater than that for ridge waveguide of the same active region. We attribute this to the lower waveguide losses and lower residual reflectivity of the more uniform AR coating on the coupling facet and the superior interface quality along the ridge, resulting in a smooth spectral gain shape as well. From earlier experiments, we know that the FP modes, centered at 1080 cm^{-1} , are only present within the first 12-15 ns of the pulse [176] until mode competition has built up. At the gain maximum ($\sim 1200\text{ cm}^{-1}$), we observed a peak power of 800 mW and a threshold current density of 2.97 kA/cm^2 , which is very close to the threshold current value of the as-cleaved front facet without EC feedback. We conclude that the optical feedback of the EC results in an effective reflectivity of 27%.

We then tested our device in continuous-wave mode. We were able to tune from $9.6\text{ }\mu\text{m}$ (1045 cm^{-1}) to $8.0\text{ }\mu\text{m}$ (1246 cm^{-1}) while operating the device between 13°C and 18°C (Fig. 4.7b). This covers a tuning range of $1.6\text{ }\mu\text{m}$ (201 cm^{-1}), which is equal to 18% of the center wavelength. The SMSR was more than 35 dB over the entire tuning range. Bottom part of Fig. 4.7b shows the continuous-wave output power of the EC as a function of lasing frequency. The output power was in excess of 20 mW over 162 cm^{-1} at 23°C and over 172 cm^{-1} at 18°C . At the gain maximum, at a heat sink temperature

of 15 °C, we measured a continuous-wave output power of 135 mW.

4.5 External-cavity quantum cascade laser based on multiple substack active region

To cover an ever bigger wavelength range, we decided to incorporate more than 2 dissimilar substacks into the gain region. These results are presented in the paper by Hugi *et al.*[178] and are part of the review paper [113]. Increasing the number of dissimilar active region designs to more than two is becoming increasingly difficult, due to cross-absorption. Therefore a powerful simulation tool is necessary that can predict the loss of each active region to minimize cross-absorption. To design the active region consisting of 5 different dissimilar substacks in Ref[178], we used a simulation software developed in our group based on a density matrix model extended to the whole structure, which also includes second order gain and loss mechanism between all subband pairs [147, 148]. It computes the total scattering rate of each state as a sum of longitudinal optical phonon, alloyed disorder, ion, interface roughness and photon scattering rates. This allows us to simulate each cascade individually, and extract the Bloch gain at each simulated point in the I-V curve.

Fig. 4.8a shows a inherently broadband bound-to-continuum design featuring a small period length L_P emitting at a wavelength of $\lambda=11.5\mu\text{m}$. The laser transition

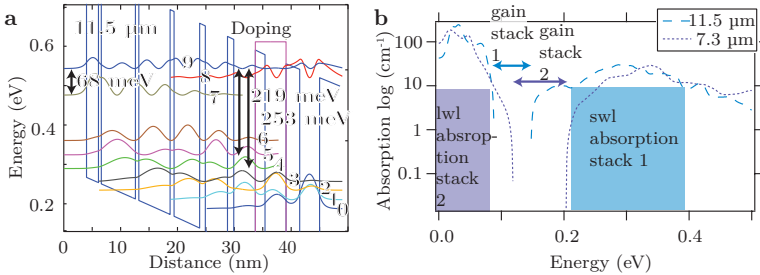


Fig. 4.8: Broadband design to avoid cross absorption. **a** Conduction band diagram of a short bound-to-continuum under an applied bias of 60 kV/cm. The wavelength is $11.5\mu\text{m}$ designed to avoid cross-absorption at higher energies. **b** Simulation of the absorption of the longest respectively shortest wavelength stack in a five stack active region. The long wavelength (lwl) stack is optimized to have low absorption up to high energies, whereas the short wavelength (swl) stack is optimized to avoid cross-absorption at low energies.

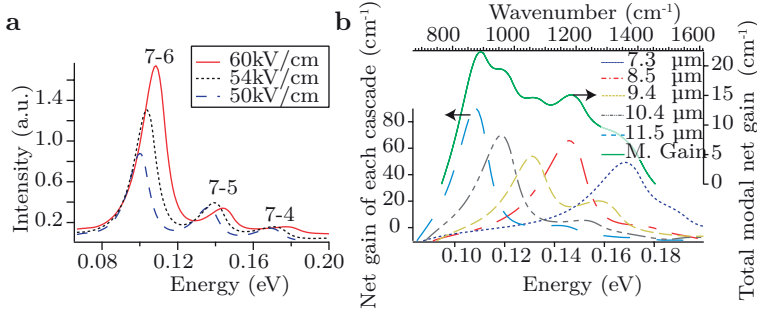


Fig. 4.9: Short bound-to-continuum design. **a** Simulated electroluminescent spectra under different applied bias. Due to the relatively large applied fields on these structures, the 8-7 and 8-6 transition are clearly distinguishable in the simulations. **b** Simulated net gain including resonant absorption losses of individual cascades. All cascades are simulated at approximately the same current density of 6.5 kAcm^{-2} . The total modal net gain, is the sum of all gains of the cascades times the modal overlap. Reprint [178].

occurs between a single upper state (7) and a set of delocalized states (6-4). This is the substack emitting at the longest wavelength in the five stack configuration. Therefore it is necessary to avoid cross-absorption with the short-wavelength stack which features gain to energies as high as 200 meV. The energy difference $E_{86}=160 \text{ meV}$ to $E_{85}=196$ is smaller than the short wavelength energy. The population of state 6, 5 and 4 are already significant with respect to state 8 to contribute to the absorption. To realize a mostly transparent stack up to 200 meV emitting at a wavelength of $11.5 \mu\text{m}$, the first excited state 8 is pushed away from the active region into the injector. The goal is to minimize the optical dipole matrix elements z_{86} , z_{85} and z_{84} . Possible cross-absorption between state 9 and lower laser states 5 and 4 are already in the high energy region $> 220 \text{ meV}$. To decrease the possible contribution of state 6 to 9, the energy difference $E_{79}=68 \text{ meV}$ should be further increased. Furthermore, all our designs have a $\Delta_{\text{inj}} \approx 162 \text{ meV}$ to avoid thermal backfilling.

Fig. 4.8b shows the simulated absorption on a log scale of the two most extreme wavelength stacks at an injection current density of 6.5 kA/cm^2 of the five stack gain region. The low energy absorption of the short wavelength stack is pushed away from the gain of the long wavelength stack, whereas the long wavelength stack avoids cross-absorption with the short wavelength stack at higher energies.

Fig. 4.9a shows the simulated luminescence spectra at different bias of the design

shown in Fig. 4.8a. The different transitions extending up to an energy to 180 meV are distinguishable individually. This broad gain is also consequence of the rather large alignment bias on these structures due to the short period length L_P .

In the grown total gain region, we use 5 distinctive cascade designs to form the active region. Their gains peak at the wavelengths of 7.3 μm , 8.5 μm , 9.4 μm , 10.4 μm and 11.5 μm . The different designs in \AA grown lattice matched on an low doped InP substrate are as followed: 7.3 μm : **40/15/10/48/12/47/13/42/15/32/17/30/18/28/23/26/34/24** ($n_s=1.52 \times 10^{11} \text{ cm}^{-2}$), 8.5 μm : **40/18/8/53/10/48/11/43/14/36/17/33/24/31/34/29** ($n_s=1.65 \times 10^{11} \text{ cm}^{-2}$), 9.4 μm : **40/19/8/56/10/51/11/42/13/32/15/32/20/31/29/30** ($n_s=1.28 \times 10^{11} \text{ cm}^{-2}$), 10.4 μm : **38/21/7/59/8/53/9/42/12/38/13/37/17/34/24/32** ($n_s=1.28 \times 10^{11} \text{ cm}^{-2}$), 11.5 μm : **38/21/5/60/6/55/7/45/10/39/11/38/17/37/24/35** ($n_s=1.35 \times 10^{11} \text{ cm}^{-2}$), where InAlAs barriers are in bold print and InGaAs wells in roman numerals. The substack emitting at 8.5 μm wavelength was later grown as a single active region in [202]. The high-power and broadband nature of the single substack was confirmed with these measurements. Tuning of the spontaneous emission of almost 100 cm^{-1} was shown while still exhibiting extraordinary continuous wave output power of 450 mW and wall-plug efficiencies in pulsed of 11.5% at 300 K.

Fig. 4.9b shows the simulated net gain of each cascade and the total modal net gain of the active region. The total modal net gain, which includes resonant absorption losses, is calculated by multiplying all gains of the cascades emitting at λ_i with their appropriate modal overlap Γ_i . All cascades were simulated at approximately the same current density of 6.5 kAcm^{-2} without any optical field. Additionally each individual cascade should peak its gain at the same current density. We ensured this by adjusting the doping of each active region individually.

We use a symmetric active region design for the arrangement of the cascades. Fig. 4.10a shows the waveguide modes of wavelength λ_i and illustrates the symmetric arrangement of the cascades. The short wavelength cascades are in the center, whereas the longer wavelength cascades are placed symmetrically around the center with increasing wavelength. The confinement in the waveguide of the shorter wavelength photons is higher compared to the lower energy photons. This leads to an increase in net modal gain of our structure. Due to the symmetric arrangement we achieve a bigger total modal overlap $\sum \Gamma_i^{\text{Symmetric}} > \sum \Gamma_i^{\text{Non-symmetric}}$. This structure therefore exhibits a larger total modal gain $G_M = \sum \Gamma_i g_i$. Additionally this placement of the cascades helps to reduce the cross-absorption present within the active region regardless the careful design, since the high-energy photons are centered and the overlap with the low energy cascades is reduced.

Fig. 4.10b shows the measured luminescence spectra at 300K of a 300 μm long and

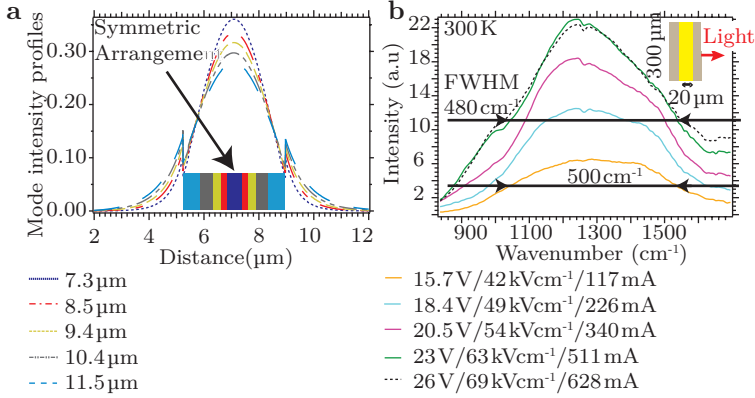


Fig. 4.10: **a** Modal intensity profile and symmetric cascade arrangement. Reprint [178]. **b** Luminescence measurement of a 300 μm × 20 μm wide ridge. The traces are corrected for the spectral response of the detector. The FWHM is 480 cm⁻¹ at the rollover current of 511 mA and 500 cm⁻¹ at 117 mA.

20 μm wide buried-heterostructure ridge at a temperature of 300 K. The light is collected from the side of the sample through the InP substrate as illustrated in the inset. We measure a FWHM of 60 meV (480 cm⁻¹) at the rollover current of 8 kA/cm².

The growth and processing of the sample is optimized for pulsed operation. The active region is grown in a molecular beam epitaxy reactor lattice matched on a low doped ($1 - 2 \times 10^{17} \text{ cm}^{-3}$) InP substrate. The active region consists of 1×10 (7.3 μm), 2×5 (8.5 μm), 2×6 (9.4 μm), 2×9 (10.4 μm), 2×12 (11.5 μm) cascades. With a total of 74 stages, the thermal run-away effect will prevent this chip from continuous wave operation at room-temperature. Subsequently an InP top cladding, composed of a highly doped 850 nm ($7 \times 10^{18} \text{ cm}^{-3}$) thick and lowly doped 4 μm ($2 \times 10^{16} \text{ cm}^{-3}$) thick layer, is grown in a MOVPE reactor. The epilayer is then further processed in a buried heterostructure fashion [177]. The chips are then cleaved, mounted and soldered epi-up on copper submounts.

Fig. 4.11a shows the light-current-voltage characteristics of a typical 3 mm long device as cleaved for different temperatures. Peak output powers (doubled per facet) of 1.2 W at 273 K are measured. Fig. 4.11b shows the emission spectra of a high-reflection (HR) coated 21.5 μm wide and 3 mm long laser at room-temperature. The chip emits radiation covering the wavelength range from 893 cm⁻¹ ($\lambda = 11.2 \mu\text{m}$) to 1250 cm⁻¹ ($\lambda = 8 \mu\text{m}$) with a small gap highlighted in yellow from 1081 cm⁻¹ to 1117 cm⁻¹.

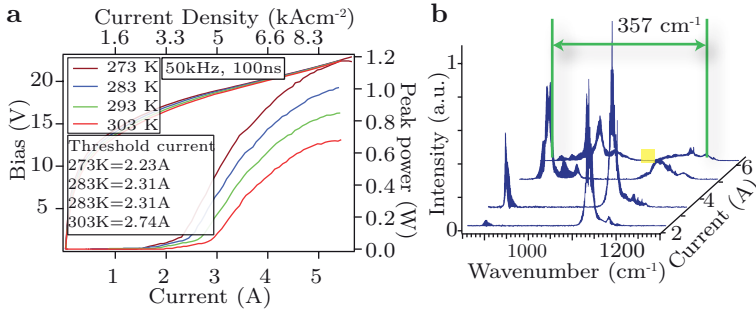


Fig. 4.11: Broadband laser characteristic. **a** As cleaved light-current-voltage characteristic of a typical 3 mm long and 20 μm wide ridge at different temperatures. The power collected on one facet is doubled to account for the power of the back facet. **b** Laser spectra taken at currents of 2.3 A, 3.4 A, 5.1 A and 6.15 A at 273 K (50 kHz, 100 ns). Reprint [178].

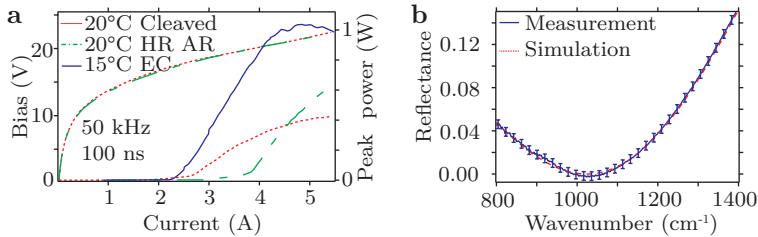


Fig. 4.12: Anti-reflection coating for broadband tuning in an external-cavity configuration. **a** Light-current-voltage characteristics of an as cleaved (red) and HR and AR coated (green) broadband 5-stack QCL. The light-current-voltage characteristic of the HR and AR coated chip in an external-cavity configuration at 15 $^{\circ}\text{C}$ is shown in solid blue. A peak output power of more than 1 W is measured. **b** Anti-reflection coating measurement on a reference sample using the FTIR. The deposited v-coating shows a reflection of < 10 % over the whole tuning range. Reprints from [178].

A very low reflection AR coating is important to guarantee a large tuning range. Therefore the QCL which was later used in EC-tuning experiments, the light, current and voltage characteristics were measured carefully before coating, after HR coating and after the deposition of the AR-coating. Fig.4.12a shows the light and voltage versus current characteristics of the as cleaved QCL as well as HR coated on the back and AR coated on the front facet QCL. The peak optical output power of the as cleaved laser is 420 mW, with a threshold current density of 3.94 kAcm^{-2} . The AR coating is a bi-layer dielectric coating composed of YF_3 and ZnSe . We designed the AR coating to have its minimal reflectance at 1023 cm^{-1} . The threshold current density of the HR/AR coated chip increases to 5.78 kAcm^{-2} . The peak optical output power nevertheless increases to 600 mW due to the increase in the slope efficiency.

The performance of the AR coating can be estimated in the two ways presented in the chapter 3 covering the coatings. Either through the use of the different current densities or using the FTIR (see sec. 3.4). The waveguide losses measured by the change of the threshold current density $\rho = 0.796$ using Eq.3.27 results in $\alpha_{wg} = 5.82 \text{ cm}^{-2}$. The threshold current density changed by a factor of $\rho_{AR} = 1.68$ before and after AR coating, therefore we deduce by using Eq. 3.29 a reflectivity of the deposited AR coating to be $R_{AR} = 2.7\%$. This measurement however does not give us any information about the efficiency of the deposited AR coating as function of wavelength. To further characterize the deposited coating, we measured the reflectance of the coating using transmittance measurements of the FTIR on a reference sample. Fig. 4.12b shows a reflectance measurements of an AR coated reference sample deposited at a later date under the same conditions. Even though the deposited AR coating is only composed of 2 layers and is optimized for zero reflectivity at a certain wavelength, the deposited coating features $< 10\%$ reflectance over the whole bandwidth of interest.

For the EC-tuning experiments, we used the redesigned setup described in the previous sec. 4.2.1. The chip was operated in pulsed mode with 15 ns pulse width and 1 MHz repetition rate. The heat sink temperature was maintained at 15°C . Fig. 4.13 shows the tuning of the EC-QCL with its corresponding peak optical power at 1.5 % duty cycle at 15°C . Furthermore, the drive current of the QCL is indicated for each measurement step in Fig. 4.13. The EC-QCL could be tuned over $\Delta\lambda = 3.8 \mu\text{m}$ (432 cm^{-1}) from $11.4 \mu\text{m}$ (877 cm^{-1}) to $7.6 \mu\text{m}$ (1316 cm^{-1}). This corresponds to a relative tuning of $\Delta\lambda/\lambda_C = 40\%$ around the center wavelength. This corresponds to an improvement of 188 % and 63 % compared to the tuning of 150 cm^{-1} of a single stack and 265 cm^{-1} of a heterogeneous cascade presented in [115] and [176].

At 1.5 % duty cycle (15 ns, 1 MHz), the peak optical power measured at $8.47 \mu\text{m}$ (1180 cm^{-1}) is 1 W, with an average output power of 15.1 mW. The peak optical output

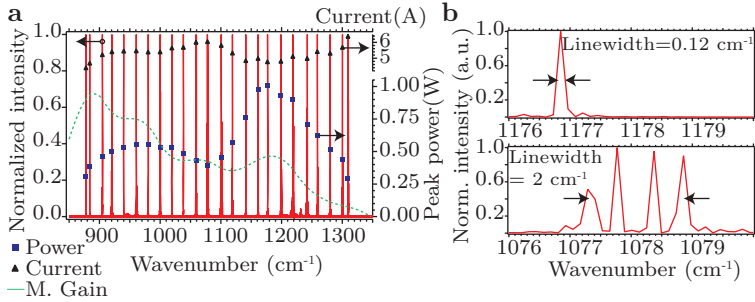


Fig. 4.13: **a** Tuning behavior with corresponding peak optical output power of the EC-QCL at various wavelengths. Measurements were taken at 15 °C at a duty cycle of 1.5 % (15 ns, 1 MHz) at different currents. **b** Magnification of the spectra for linewidth comparison of the EC-QCL at 1080 cm⁻¹ and 1180 cm⁻¹. Reprints from [178].

power never drops below 290 mW over the whole spectral tuning range. Similar tuning (438 cm⁻¹) and peak optical power (1 W) were measured at 1 % duty cycle (100 ns, 100 kHz).

Fig. 4.13b shows two magnification of the spectra measured at 1180 cm⁻¹ as well as 1080 cm⁻¹. The linewidth of the EC-QCL varies between 2 cm⁻¹ and <0.12 cm⁻¹, limited by the resolution of the instrument. Pulse chirp can be excluded as the reason for the linewidth variations due to the short pulse time (15 ns), furthermore this would manifest itself in similar broadening at both wavelengths. We attribute this increase in linewidth to the limited resolving power of our grating given by Eq. 4.1. The limited filter efficiency of our grating and the presence of stationary points in the gain curve of the QCL are responsible for the variations of linewidth observed over the tuning curve. Measurements with a different collimating lens, which results in a larger beam waist, exhibit lower linewidth variations. The lower illustration of Fig. 4.13 shows 4 distinctive modes, all spaced by FP mode spacing of ≈ 0.5 cm⁻¹.

4.6 Broadband external-cavity quantum cascade laser absorption spectroscopy

In the course of this work, we performed some simple proof-of-principle absorption spectroscopy measurements using the heterogeneous-active region discussed in section 4.4. The measurement was done with the help of Joachim Mohn, Bela Tuzson,

Lukas Emmenegger from the EMPA, whom I am very grateful for their help. This work was done in collaboration with BLOCK engineering.

The detection of chemical warfare agents in the 8-12 μm range using laser spectroscopy is of great interest for many security applications. Using laser photoacoustic spectroscopy with a CO_2 laser tuned over 32 laser modes in the wavelength range of 9.6 μm to 10.2 μm , Pushkarkdy *et al.* showed detection thresholds of 1.2 ppb [203]. Extending the covered frequency range further and allowing a gap free tuning through an EC-QCL would greatly enhance possible application scenarios. Since a lot of those gases feature rather large absorption spectra, increasing the frequency coverage drastically helps reduce false positive alarms. The following gases are measured as accepted stimulants for explosives detection:

1. Diisopropyl methanephosphonate (DIMP) - $\text{C}_7\text{H}_{17}\text{O}_3\text{P}$ - Nerve gas precursor for Sarin.
2. Dimethyl methyl phosphonate (DMMP) - $\text{C}_3\text{H}_9\text{O}_3\text{P}$ - An accepted never gas simulant.
3. Tri-ethyl phosphate (TEP) - $\text{C}_6\text{H}_{15}\text{O}_4\text{P}$ - An accepted nerve gas simulant.

In Fig. 4.14 the setup which was used for the spectroscopy measurements is illustrated. The laser is run in pulsed mode (200 kHz repetition rate, 100 ns pulse width) at 20 °C with an average output power of 10.84 mW. For the spectroscopic measurements, the laser beam was over modulated with a burst period of 1 ms and a duty cycle of 50 %. This was done to be frequency compatible with the pyroelectric detector LME 316. The output beam of the EC-QCL passes first a beam splitter. Beam 1 is either directed into an FTIR Nicolet 800 or into a pyroelectric detector for power measurement. To switch between the FTIR and the pyroelectric detector, a removable mirror, mounted on a magnetic stage was used. The pyroelectric detector is calibrated using the movable Ophir power meter at the beginning of the experiment. Beam 2 passes through a parabolic mirror before passing through the gas cell with an effective path length of 2.5 m. The laser intensity that passes through the gas cell is measured using a MCT detector and a Signal Recovery 7280 DSP Lock-In Amplifier.

The measurement procedure was the following:

1. The gas cell is purged with N_2 .
2. A reference scan of N_2 is taken.
3. The gases to measure (DIMP, TEP, DMMP) are filled in the gas cell.

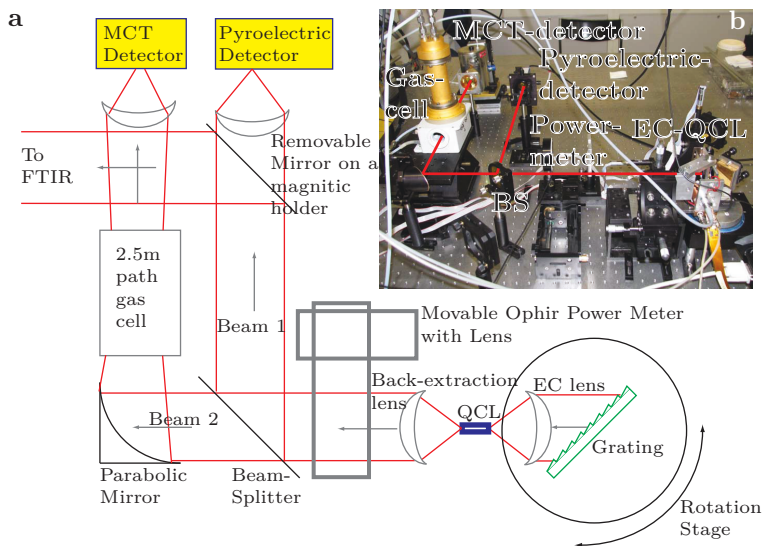


Fig. 4.14: EC-QCL Setup Back-Extraction setup. **a** Schematic setup illustration. We employed a back-extraction EC-configuration to avoid walking of the beam. **b** Picture of the actual setup implementation.

4. An absorbance scan is taken.

The ratio of the scan with the measurement gas to the N_2 scan gives the transmittance measurements. The EC-QCL gas absorption measurements are compared to measurements of the same gas using an FTIR, an Ansco with 9.8 m optical path length and a resolution of 16 cm^{-1} . The gas is generated by simply injecting a certain amount of liquid in a bag. The measurement of the concentration of the gases is done using an flame ionization detector measurement. The flame ionization detector is calibrated with propane (C_3H_8) and for all gases a response factor of 1 is assumed. Those measurements are not precise, due to the unknown response factor of the gases. Furthermore, the gases are transported from EMPA to the ETH Zürich in bags. DIMP is transported in a 22.5 l volume Teflon bag, whereas TEP and DMMP both are transported in specially ordered aluminum bags of 8 l volume. TEP and DMMP were found to be unstable in Teflon bags. Concentration controls with a time slot of 24 h showed that especially the TEP concentration clearly decreased (80%). We suspected that

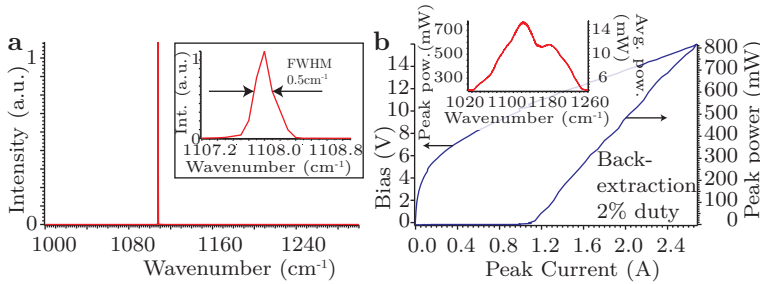


Fig. 4.15: Back-extraction EC-QCL characterization. **a** EC-QCL laser spectrum at the center of the gain curve featuring a FWHM of 0.5 cm^{-1} . Inset: closeup of the single mode laser spectrum. **b** LIV at the center of the gain curve at 2% duty cycle (200 ns, 100 kHz) at 20°C . Inset: Output power over the whole tuning range.

hydrolysis is the reason for the decreased concentration and spend more time to purge the bags with N_2 prior to filling it with the gas. Also, we observed a strong temperature dependence of the concentration of the gases, especially DMMP. Nevertheless, the measurements give a rough estimate of the concentration. The measured concentration of the gases are: DIMP ($100\text{ }\mu\text{l}/22.5\text{ l}$) $\sim 270\text{ ppm}$, TEP ($50\text{ }\mu\text{l}/8.5\text{ l}$) $\sim 45\text{ ppm}$, DMMP ($50\text{ }\mu\text{l}/8.5\text{ l}$) $\sim 300\text{ ppm}$ (when heating the bag with heat gun, $\approx 500\text{ ppm}$),

Fig. 4.15a shows the EC-QCL laser spectrum at the center of the gain curve. The inset in Fig. 4.15a shows a zoom of the same spectrum in the region of interest. The laser line-width is $\approx 0.5\text{ cm}^{-1}$ arising from Joule-heating. This ultimately limits the resolution of this setup in pulsed mode. Tuning over 22.5% using the back-extraction setup was demonstrated, which is slightly less compared to the 25% for the front-extraction setup.

On Fig. 4.15b the light-current-voltage measurement at a constant heat sink temperature of 20°C of the EC-QCL setup in the center of the gain curve is shown. We observe a peak output power of over 810 mW , which corresponds to an average power of 16.2 mW . The inset of Fig. 4.15b shows the peak and average output power of the EC-QCL at 20°C over the whole tuning range without realigning the lens or the grating. The output power never drops below 200 mW peak power over the whole tuning range.

Fig. 4.16a,b and c show the measured scans of DIMP, TEP and DMMP. The scans are compared with the measured FTIR spectra with a resolution of 16 cm^{-1} . Due to the better resolution of our setup of 0.5 cm^{-1} , the spectra measured with the EC-QCL are

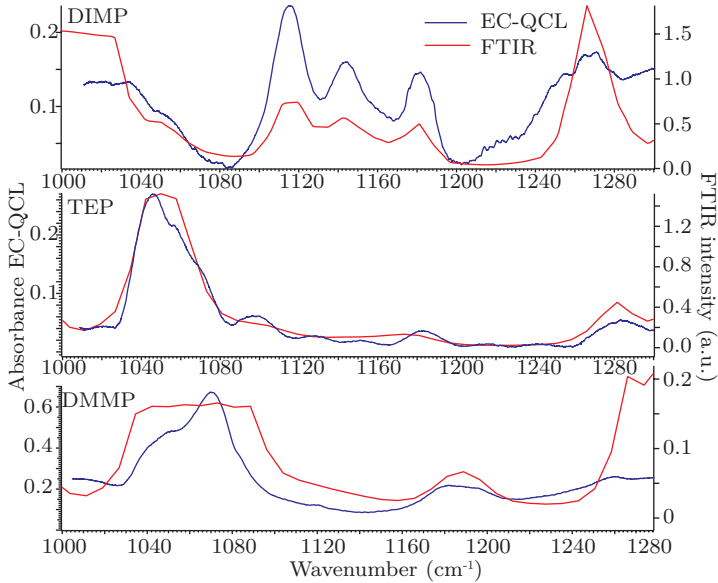


Fig. 4.16: Spectroscopy measurements comparing EC-QCL measurements with FTIR measurements. **a** 270 ppm DIMP. **b** 45 ppm TEP. **c** 500 ppm DMMP.

better resolved. There are some striking discrepancies of the spectra measured with the EC-QCL and the FTIR at the outer scanning ranges for DIMP and DMMP. One reason could be the increased contribution of the parasitic modes in a pulsed EC configuration at the beginning of each pulse when the EC-mode builds up. Measurements showed that those parasitic modes are found between 1080 cm^{-1} and 1140 cm^{-1} . However, the spectra of TEP seems to be very well reproduced over the whole tuning range. Comparing the absorption spectra of the three substances, the spectra of TEP is much less affected by those parasitic modes, since the absorption in this wavelength range is about 4 times smaller compared with the peak absorption of DIMP and DMMP. We have not performed any time-resolved absorption spectra measurements, which should have avoided the problem of the pulse build-up of the EC.

4.7 External-cavity quantum cascade laser activities

The interest of spectroscopic groups to use EC-QCLs for gas probing grew with the progress of the EC-QCL in terms of tuneability, output-power, reliability and operating temperature. Trace gas sensing applications, like environmental monitoring, emission measurements, remote sensing, applications in medicine and life sciences [204], industrial process control, security and fundamental science, all profit from those technological advances in EC-QCL. Different techniques for absorption spectroscopy were demonstrated using EC-QCLs [195, 205]. Pioneer work and development has been done by the group of F.Tittel at Rice University [199].

EC-QCLs show excellent performances in applications using pure intensity modulation, either through current modulation or through an external AM-modulator. Quartz-enhanced photoacoustic spectroscopy [58, 59, 206–209] shows very high sensitivity (ppm to ppb). Compared to multi pass absorption spectroscopy, this technique requires only a very small sample volume ($< 1 \text{ mm}^3$), and the sensitivity is limited to the thermal quartz tuning fork noise and is immune to environmental noise. Furthermore, it is specially appropriate for applications using a broadly tunable EC-QCL, since it is intrinsically wavelength independent. To increase the sensitivity and resolution of the detection, it is possible to use a EC-QCL operated in continuous-wave and use an external modulator. Using a quartz tuning fork as a mechanical chopper, and a mode hop free EC-QCL setup, it is possible to achieve high resolution spectroscopy. Scans of up to 2.5 cm^{-1} with a resolution of $< 0.001 \text{ cm}^{-1}$ (30 MHz) were demonstrated within the tuning range of the EC-QCL [195].

EC-QCLs are especially adapt for spectroscopic applications requiring a broad tuneability. An example among many is the use of the EC-QCL as a local oscillator for heterodyne detection [210]. With a tuning of 100 cm^{-1} , high-resolution broadband thermal infrared heterodyne spectro-radiometry was shown recently [211]. There are also applications which profit from wavelength restrictions. Using external cavity quantum cascade laser-based Faraday rotation spectroscopy, detection limits of as low as 0.38 parts per billion by volume are reached [212]. The advantage to use a high-resolution EC-QCL is, that it allows targeting the optimum $Q_{3/2}(3/2)$ molecular transition at 1875.81 cm^{-1} of the NO fundamental band.

Applications relying on direct wavelength modulation, greatly profit from fast tuning EC-QCLs. It enables for example the monitoring of turbulent gas systems and helps to reduce $1/f$ noise. Therefore, industries and research groups keep decreasing the size of the EC-QCL to increase the tuning speed [213].

Further characterization techniques of EC-QCLs employing near-infrared frequency

combs underline the continued interest of these devices [214]. This technique is especially interesting as it allows for a real-time (20 ns) monitoring of the EC-QCL. Frequency noise and linewidth characterization of EC-QCLs reveal different FWHM of EC-QCL linewidths of 15 MHz (50 ms), 4 MHz (1.3 ms) and 1 MHz (10 μ s) depending on the integration time. The frequency-noise power spectral density was found to be similar though slightly higher than in DFB-QCLs. This increase is attributed to the additional acoustic noise of the external-resonator.

The alternative broadband designs discussed in section 2.2, namely the continuum-to-bound, the continuum-to-continuum and the dual-upper-state to multiple-lower-state design, were also successfully employed in EC-QCL configurations. The continuum-to-bound design could be tuned over 190 cm^{-1} at a wavelength of $\lambda=8\text{ }\mu\text{m}$ in pulsed mode at 0°C . The continuum-to-continuum design was successfully tuned over 350 cm^{-1} in pulsed mode at a center wavelength of $\lambda=4.8\text{ }\mu\text{m}$ [215, 216]. A 1.5 mm long laser of our redo EV1470D discussed in section 2.2 of this structure could only be tuned over 191 cm^{-1} . We explain this discrepancy by the increased waveguide losses and a rather bad (5%) residual reflectivity of our AR-coating. The dual-upper-state to multiple-lower-state design was successfully tuned over 321 cm^{-1} in pulsed and 248 cm^{-1} in continuous-wave operation at a center wavelength of $\lambda=4.8\text{ }\mu\text{m}$ [217].

Furthermore, an Sb-free quantum cascade laser processed emitting in the $3\text{--}4\text{ }\mu\text{m}$ range based on a classical bound-to-continuum design was also successfully tuned over a wavelength range of 275 cm^{-1} reaching a wavelength as short as $3.15\text{ }\mu\text{m}$ [42].

The development and advancement of the EC-QCL attracted many research groups attention [218–225]. Thanks to the large industrial and commercial potential of such sources, the industry shows continuous interest in such sources for commercial purposes [196, 197, 203, 213, 226, 227].

4.8 Broadband QCL as white light source

This section is strictly speaking not concerned with external-cavity operation of broadband QCLs. It is however related to this chapter in the sense that it illustrates the possibility to use the prior mentioned broadband QCL sources as a white light source. The spectral separation of the light is done using an FTIR. Each spectroscopic application in the mid-IR requires a specific source. Conventional FTIRs, for example, use a glowbar emitting broadband radiation in the mid-IR. Sorokin *et al.* used a mid-IR mode-locked solid-state laser emitting at $2.4\text{ }\mu\text{m}$ based on $\text{Cr}^{2+}:\text{ZnSe}$ as a high-brightness source for the FTIR [228]. They achieved a detection limit of 0.2 ppbv of HF with only 1 second averaging, whereas the traditional tungsten glowbar would

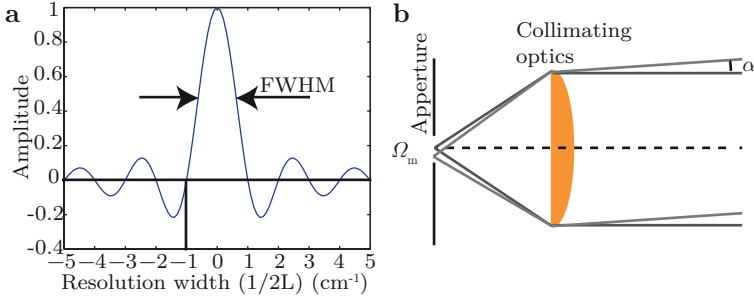


Fig. 4.17: Resolution limits of an FTIR. **a** The finite path difference is responsible for a sinc profile in the acquired spectrum. **b** Resolution limit governed by the finite aperture with of the FTIR light-source. Figures inspired by [5]

have taken hours to reach this limit. Furthermore, by using laser frequency combs as the light source of Fourier transform spectroscopy, it is possible to record well-resolved broadband absorption as well as dispersion spectra in a single experiment [96]. In this section we present a heterogeneous broadband active region to be used as high brightness and high-resolution source in an FTIR and examine their potential to replace the glowbar. To illustrate this possibility, we benchmarked a broadband QCL operated in pulsed mode with a FTIR under comparable conditions.

Those measurements were only possible with the help of several people which we would like to acknowledge. The broadband QCL laser was delivered by Alpes Lasers, special thanks goes to Dr. Stéphane Blaser. There was also a close collaboration with the EMPA who provided us with a lot of knowledge about temperature and output power stabilization of QCLs. Special thanks goes to Dr. Bela Tuzson and Dr. Lukas Emmenegger.

4.8.1 FTIR resolution limits

The resolution limit in an FTIR is limited mainly by two factors. The first and most obvious one is the finite path length of the moving mirrors. The acquired interferogram of a classical Michelson interferometer of a single-mode laser, assuming 100 % optical and beamsplitter efficiency, is given by [5]

$$I(x) = \frac{1 + \cos(2\pi\sigma_0 x)}{2}, \quad (4.15)$$

where x is the delay and σ_0 is the carrier wavenumber. Due to the finite path difference, this interferogram has to be multiplied by a boxcar function of length $2L$. The factor 2 originates from the symmetry of the acquired interferogram. In the spectral domain, the multiplication of a boxcar corresponds to the convolution of a sinc, illustrated in fig.4.17a, with its zero crossing at $\frac{1}{2L}$. This leads to the resolution limit of an FTIR and a true linewidth profile with a FWM given by [5]

$$\text{FWHM} = 1.207 \frac{1}{2L}. \quad (4.16)$$

The second effect is a geometric problem and concerns the finite entrance aperture size. The interference pattern in an FTIR is generated by the interference of two plane waves. To generate a plane wave, an indefinitely small light source, a point source, must be placed in the focal point of the collimating optics. The finite aperture has the effect that the collimated beam from the aperture diverges at a finite angle α . This error will accumulate over the path in the interferogram by a factor of $x \cos(\alpha)$. Therefore the aperture must fulfill the condition

$$1 > \frac{\Omega_m R}{4\pi}, \quad (4.17)$$

where Ω_m is the solid angle of the aperture and $R = 2L\sigma$ is the resolving power. To achieve high resolution spectra with an FTIR it is therefore important to aperture the glowbar accordingly. As a consequence, the available intensity to perform the scan decreases with increasing resolution.

By using a QCL as a white light source, some of those restrictions can be overcome. The QCL has an intrinsic small aperture size for measurements with very high resolution (10 μm). The output power of a QCL is bigger than what can be achieved with a glowbar, therefore a better signal-to-noise ratio should be possible. Another important advantage is the possibility to modulate fast for advanced detection techniques. Furthermore, the small size of the QCL makes small integration possible (MEMS-FTIRs).

4.8.2 Characterization

The goal of the measurement is to compare the performance of an FTIR using a glowbar as a light source against a broadband QCL as a light source. As it was explained beforehand, the aperture of the glowbar limits the resolution of the FTIR. The aperture of the glowbar was set to 1 mm during the whole experiment. This aperture was chosen, since it is a good aperture for the highest resolution scan performed during this experiment for this specific wavelength. Therefore the chosen aperture for this

measurement is orders of magnitude worse than the one of a QCL. The differences in the measurement would become even more pronounced if the resolution of the scan would be considerably increased.

The measured quantity is the signal-to-noise ratio (SNR) which compares the spectrum of a single scan S_i with the spectrum of an averaged background scan S_{avg} .

$$S_{\text{avg}} = \frac{\sum_N S_i}{N} \quad (4.18)$$

$$\text{SNR}_i \text{ (db)} = 10 \times \log \left(\left| \frac{S_{\text{avg}} - S_i}{S_{\text{avg}}} \right| \right). \quad (4.19)$$

All measurements are done under the same conditions. The scan speed of the FTIR is set to 10 kHz. The gain is set to 0, and a Mertz apodization function is chosen.

The laser is driven in an laser box developed by Aerodyne Research Inc. for highly sensitive gas measurements employing QCLs. The laser temperature is set to 10 °C, the cooling water is regulated to 15 °C. The cooling water is not only used to extract the heat generated by the Peltier, it is also used to control the temperature of the box. This is achieved by cooling the lid of the box and stabilizing therefore the whole box to 15 °C. The temperature of the laser is controlled by a Peltier, whose temperature is controlled by a thermistor featuring a resistance of 10 kΩ. The thermistor allows for a better temperature accuracy compared with the usually used PT100 sensors. Furthermore, the small difference in water temperature and Peltier temperature assures that the Peltier does not have to work too hard, which could potentially lead to variations in the stabilization temperature. We estimate the final temperature to be accurate to ± 1 mK.

The operation of the QCL in pulsed mode ensures that the whole spectrum is covered by pulse chirp. Fig.4.18a shows the average output power measured using the Aerodyne box. The repetition rate is set the 2 MHz, the pulse width to 22 ns (measured to be 16 ns). There is an additional burst setting with 90 μs burst width and a repetition rate of 10 kHz. Therefore the peak output power of the device is about 240 mW. To further characterize the output of the laser using this box, we measured the temporal profile of the pulse using a fast room-temperature MCT detector. The output of the laser is focused on the detector. The signal is amplified by 38 dB using a SONOMA Instruments 317 10 kHz-2.5 GHz amplifier. The time trace is taken with a Tektronik Oscilloscope DPO4034 featuring a bandwidth of 350 MHz (2.9 ns). The measured time trace is shown in fig.4.18b. We measure a true pulse width of about 16 ns. The pulse shape is looking good with no strong overshoot.

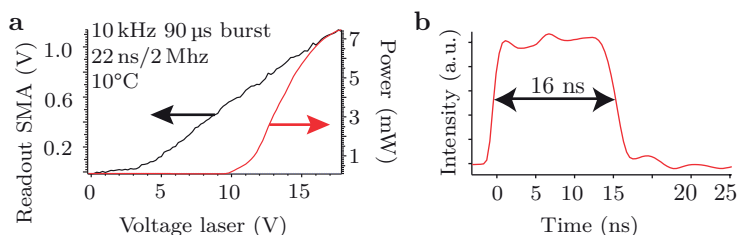


Fig. 4.18: Characterization of the Aerodyne laser box. The laser is fabricated and mounted at Alpes Lasers, the characterization is done at ETH. **a** Output power. **b** Pulse shape.

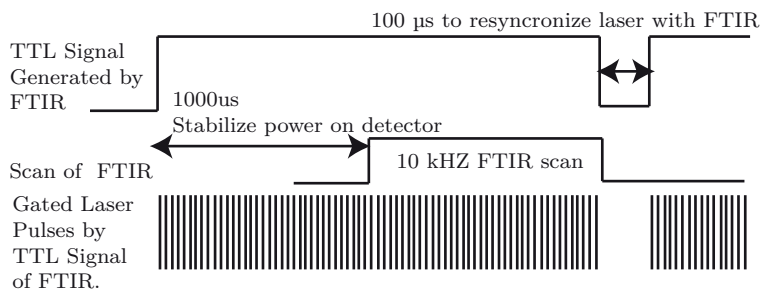


Fig. 4.19: FTIR and laser synchronization during the acquisition of spectra.

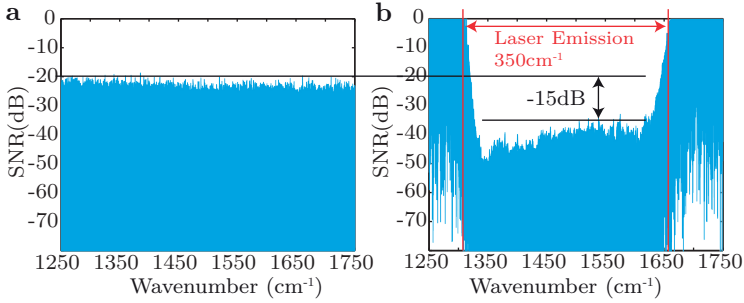


Fig. 4.20: SNR comparison between a glowbar and a broadband QCL in a FTIR. **a** SNR of the glowbar. **b** SNR of the broadband QCL.

The best results in the SNR ratio for the QCL are found when the FTIR acquisition and the QCL are synchronized. The pulser voltage is set to 17 V with 22 ns pulses at a rep rate of 2 MHz. This synchronization is illustrated in fig.4.19. The QCL output is switched off through the TTL signal of the FTIR. When the TTL signal is set to one before a scan, we program the FTIR to wait for 1 sec for the laser output power to stabilize. After the scan, the FTIR TTL is set to 0 for 100 μ s before the next scan is started.

The measurements with the laser show a better SNR for all tested resolutions. At a resolution of 5 cm^{-1} , the gain is about 5-10 dB. The best results were however achieved at the highest measured resolution, at 0.5 cm^{-1} . The results of 90 scans are shown in fig.4.20a and b. The left side shows the measured SNR with a glowbar. The right side shows the measured SNR of the QCL. The SNR is about 15 dB lower compared with the glowbar over the emission wavelength of the QCL (350 cm^{-1}).

Those measurements illustrate the possible SNR gain when using a QCL as a white-light source. The spectral coverage of the glowbar is naturally much broader than what is attainable with a QCL. The lower spectral coverage however can have some advantage in linear spectroscopy applications. In a spectroscopic application, not only the total power is of essence, but often the detector must be operated in a linear regime. By concentrating on the spectral region of interest with a QCL, the saturation power on the detector with unwanted optical frequencies is reduced. A very broadband glowbar has a narrow peak in at the centerburst of the FTIR. A narrower source has the power distributed over a bigger portion of the interferogram therefore the integrated power at the wavelength of interest is going to be bigger.

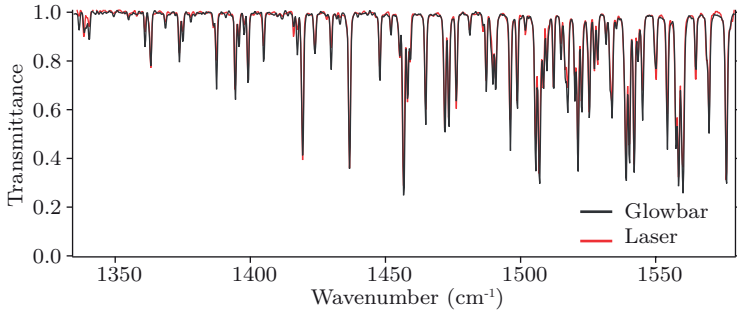


Fig. 4.21: Water absorption spectra measured using an FTIR using as a light source a conventional glowbar and a broadband QCL driven in continuous-wave operation.

The center wavelength of these devices is about $7\mu\text{m}$. Therefore the radiation is absorbed by atmospheric water lines. We used this to compare a atmospheric water spectrum recorded with a conventional glowbar to a laser run in continuous-wave. For this prove of principle measurement, the temperature stabilization and current-driver (Lightwave LDX-3232) were not optimized for low noise. The background scans and sample scans were each time averaged a 100 times. The resolution was set to 0.6cm^{-1} , in order to omit to resolve the individual lines of the laser modes. The glowbar was set to an aperture of 1 mm. For both scans the DTGS detector was used. Fig.4.21 shows the measured spectra. As it can be seen, the two spectra look alike, proving that a QCL can indeed be used as a glowbar replacement.

Chapter 5

Frequency-comb operation of QCLs

This chapter is dedicated to the findings of frequency-comb operation of QCLs. The chapter is structured as followed. First, it will give an introduction to the subject of optical frequency combs and QCL comb operation. Afterwards, the chapter continues by describing fundamental mode-locking followed by a introduction to the concept of a frequency-comb featuring a frequency-modulated like output. The next section treats state-of the art mid-IR mode-locked sources. It continues with a short description of semiconductor mode-locked sources. These two sections on mid-IR combs and semiconductor comb sources help to put the developed broadband QCL comb in context. The next section treats Kerr-combs, a novel technique to generate optical frequency combs. Nowadays, these Kerr-combs also penetrate into the mid-IR region. It goes on by describing possible characterization methods of frequency-comb outputs, introducing the intermode beat spectroscopy. Finally, the chapter finishes with the data and findings of the frequency-comb operation of broadband QCLs. It presents a broadband and compact semiconductor frequency comb generator in the mid-IR, where the modes of a continuous wave free-running broadband QCL are phase-locked featuring a frequency-modulated like output. The main results presented in this section are published in [229].

Due to the nature of the intermode beat spectroscopy setup, there is possible confusion between RF-frequencies measured by the spectrum analyzer and optical frequencies. To clearly distinguish these two frequencies throughout the text the following convention is used: ν indicates frequencies measured in the electrical domain, meaning readout frequencies of the spectrum analyzer, whereas ω and f stands for frequencies in the optical domain including wavenumber. The variables ν_{rt} and $f_{rep} = \frac{\omega_{rep}}{2\pi}$ are strictly speaking the same. Depending on the context in the text, either one is chosen.

5.1 Introduction

5.1.1 Optical frequency combs

The maturing technique in the last two decades of optical frequency combs resulted in an enormous unfolding of an application space. This has ultimately led to the Nobel Prize in Physics in 2005 to Theodor W. Hänsch and John L. Hall for "for their contributions to the development of laser-based precision spectroscopy, including the optical frequency comb technique" [230].

The optical frequency-combs opened new avenues for many fields such as fundamental time metrology, spectroscopy and frequency synthesis. Due to the popularity of the research, several review articles on optical-frequency combs producing femto-second laser pulses exist, for example by Diddams *et al.* and Sibbett *et al.* to name two [231, 232]. In particular, spectroscopy by means of optical frequency combs surpassed the precision and speed of Fourier spectrometers. Such a new spectroscopy technique is specially relevant for the mid-IR range where lie the fundamental roto-vibrational bands of most light molecules. Most mid-IR comb sources are based on down conversion of near-IR mode-locked ultrafast lasers using non-linear crystals (see sec. 5.4). Another comb generation mechanism is used in micro cavity based combs. The equidistant modes are formed from a continuous wave pumping an ultra-high Q micro resonator (see sec. 5.6). Nevertheless, these combs depend on a chain of optical components. Therefore to widen the spectroscopy applications of such mid-IR combs, a more direct and compact generation scheme, using electrical injection, is preferable. There is still a lack of a compact mode-locked semiconductor laser source in the mid-IR region. Being the dominant semiconductor laser source in the mid-IR region, the QCL is the ideal light source to fulfill those requirements.

Optical frequency combs [70] act as rulers in the frequency domain. Their optical output frequency is composed of equally distant comb lines, therefore each frequency can be described as $f(m) = f_{ceo} + m f_{rep}$, where the f_{rep} is the repetition frequency and f_{ceo} is the carrier-envelope offset frequency. As it was discussed in section 2.4, the GVD in a laser cavity is responsible to form a spectrum of unequally spaced comb lines. Therefore to form those equally distant comb lines, it is necessary to overcome the natural dispersion arising in a laser cavity by an appropriate phase-locking mechanism.

The common intuitive picture to illustrate how such frequency combs are generated is done by studying the emission of short mode-locked pulses in a laser-cavity. Fig. 5.1a shows the E-field and the intensity of a fundamentally mode-locked laser. The round-trip time T of the optical pulse in the cavity is given by the cavity length L and the mean group velocity v_g . It reads as $T = \frac{2L}{v_g}$. Since the group velocity and the

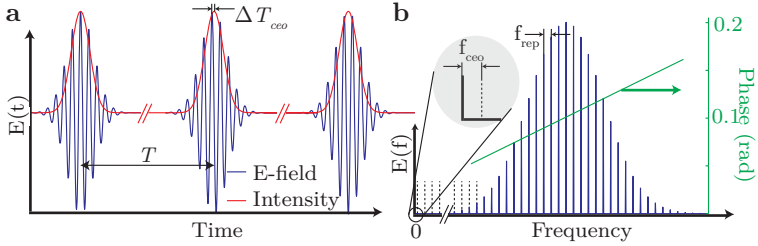


Fig. 5.1: Mode-locked laser output. **a** E-field and intensity of a mode-locked laser. **b** Optical spectrum and phase of a mode-locked laser.

phase velocity are not equal, there is a phase angle difference of $\varphi_{ceo} = \Delta T_{ceo} 2\pi f_0$ from pulse to pulse, called the carrier-envelope offset phase, with f_0 being the carrier frequency. The carrier-envelope offset frequency and the carrier-envelope offset phase are linked by $\varphi_{ceo} = 2\pi \frac{f_{ceo}}{f_{rep}}$.

Regardless of a nonzero carrier-envelope offset, the envelope-function of the E-field is periodic in time in a mode-locked laser. The envelope function of the E-field therefore fulfills the condition $A(t - T) = A(t)$. In case the envelope-function of the E-field is periodic in time, the E-field of the laser output can be analyzed as a supermode with carrier angular frequency ω_c and envelope function $A(t)$. This means the E-field can be expressed as a sum of Fourier-components

$$E(t) = \text{Re} \left\{ A(t) e^{i\omega_c t} \right\} = \frac{1}{2} \left(\sum_n A_n e^{-i2\pi(f_{ceo} + n f_{rep})t + \varphi_n + c.c.} \right), \quad (5.1)$$

where A_n are the complex Fourier components of $A(t)$. Therefore, the spectrum of a periodic pulsed output is formed through a spectrum of equally spaced comb lines.

Their equally distant comb-lines allow for an extremely accurate frequency comparisons with a direct link between the microwave and optical spectral ranges. This link is seen by investigating eq. 5.1. The optical frequency in the THz range is linked to the RF-domain by $f_{opt} = f_{ceo} + n f_{rep}$. The integer n is large and both f_{ceo} and f_{rep} are in the MHz-GHz domain.

5.1.2 Prior work on QCL comb operation

Nowadays the QCL covers the entire mid-IR spectral range and features output powers of several watt in continuous-wave at room temperature. Broad gain (see sec. 2 and 4)

can be engineered through quantum design and by cascading dissimilar substacks. But due to the fast laser dynamics in a QCL, comb-operation of QCLs is different to traditional mode-locking of diode lasers.

When operated in continuous wave, quantum cascade lasers with a Fabry-Pérot cavity usually switch from single-mode to multi-mode operation when driven above a critical current. The multi-mode operation is accompanied by the observation of an intermode beat, which is the radio-frequency spectrum of the intensity near the round-trip frequency, ν_{rt} . The mechanism driving this behavior have been attributed to spatial hole burning and Risken-Nummedal-Graham-Haken [233] instability and are specific to the QCL due to the fast gain recovery process. The gain recovery in QCLs ($\tau \approx 0.3$ ps) is orders of magnitudes faster than the round trip time in the cavity ($\tau_{rt} = 66$ ps for a 3 mm long device). This prohibits the formation of stable pulses, since the wings of the pulse see higher gain than the peak of the pulse, resulting in a lengthening of the pulse, making stable fundamental mode-locking hard to reach. Work has been done trying to generate pulsed emission from a QCL. Wang *et al.* engineered a QCL featuring a diagonal design to increase the upper state lifetime [234]. Pulsed emission was achieved when modulating a short-section at the cavity round trip time [235]. Nevertheless, the results were sobering. The device could be mode-locked close to threshold over a short dynamic range. Additionally, the bandwidth of the locking was limited (15 cm^{-1} at 77 K). Also, the pulse shape in the limited locking range already showed extended wings, originating from the fast laser dynamics. Furthermore, the device did not operate CW at room-temperature. The conclusion is, that fundamental mode-locking is incompatible with todays high-power, high-temperature continuous wave QCLs and a more appropriate locking mechanism must be found.

5.2 Fundamental mode-locking

As it was explained beforehand, the intuitive picture to form a frequency-comb is by producing a laser output featuring short coherent pulses, usually ps to fs long. The goal of this section is to give a short overview of common and well-established frequency-comb sources producing high-energy pulsed output.

The formation of the short pulses is a resonant process. While the pulse circulates in the cavity it becomes shorter with each round-trip to the limit of pulse broadening processes (gain, dispersion, ...) inherent in the laser cavity. The longitudinal modes in the cavity are thus frequency-locked and interfere coherently to form those ultra short pulses. Active mode-locked laser results were achieved by active loss modulation in the cavity already in the year 1964 [236]. Passive frequency locking however does

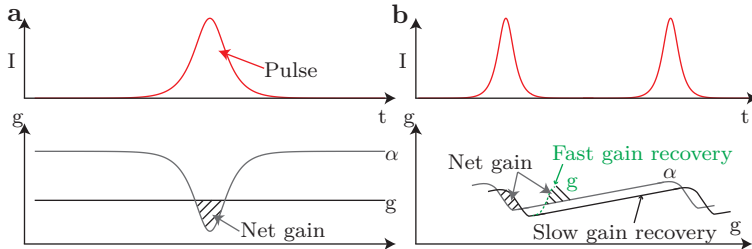


Fig. 5.2: Fast **a** and slow **b** saturable absorber. There is a short net-gain window smaller than the pulse width available to successively shorten the pulse.

not require an active stabilization. Passive frequency locking is usually realized by the incorporation of a saturable absorber. The loss of a saturable absorber depends on the intensity I of the light [162]

$$\alpha = \frac{\alpha_0}{1 + \frac{I}{I_0}}. \quad (5.2)$$

The parameter α_0 is the low-intensity absorption coefficient and I_0 is the saturation intensity at which the absorption is at -3 dB from its original value. The locking mechanism employing a saturable absorber is a well understood and analyzed process [237–239]. The first continuous-wave mode-locked (as opposed to Q-switched) dye-laser used a slow saturable absorber [240]. It was however not understood in the beginning, how a slow saturable absorber can produce such short pulses. Therefore, the first theory treated the effect of a fast saturable absorber. In this case, illustrated in fig. 5.2a, the losses are lowered below the gain when the pulse hits the saturable absorber, which leads to a net gain for a short period of time. To understand the working principle of a slow saturable absorber, the dynamics of the gain medium needs to be taken into account, as shown in fig. 5.2b. One can show that it is possible to generate pulses much shorter than the recovery time of the saturable absorber. The edge of the laser pulse decreases the loss of the saturable absorber. Due to gain depletion, the net-gain window remains short, leading to the formation of the pulses. This intuitive picture furthermore illustrates the problem if the gain-recovery is faster than the round-trip time, as is the case in the QCL. The recovery time of the gain g illustrated in the dotted green line in fig. 5.2b is fast compared to the round-trip time, leading to a positive net gain after the pulse has passed. The solution will not be stable, since the wing of the pulse will already see this net gain. It should be noted, that a slow saturable absorber

can also be used without any gain saturation effects, as it occurs in soliton-mode locked lasers [241].

A milestone in mode-locking of lasers was the realization of the first mode-locked Ti:sapphire ($\text{Ti:Al}_2\text{O}_3$) laser using Kerr-mode locking (KML) [242]. Further advances in mode-locking were achieved by the introduction of the semiconductor saturable absorber mirrors (SESAM) and the saturable Bragg reflectors (SBR) [243, 244]. Ti:sapphire lasers featuring a wide gain-bandwidth and ultra short pulses lead to high-peak powers. Today's solid state lasers achieve high average power of 141 W (gain medium $\text{Yb:Lu}_2\text{O}_3$) [245]. The peak power of today's mode-locked solid state laser is in the order of 10^5 - 10^6 W. Those high peak powers are a key ingredient for frequency comb generation in the mid-IR region through non-linear mixing processes. Another important breakthrough for pulse compression and octave spanning comb generation was the use of highly nonlinear optical fibers for pulse compression [246]. Self-referenced octave spanning combs employing the f-2f method become therefore possible [247–249].

5.3 Frequency-modulation mode-locking

One has to be however careful with the direct link between a frequency-comb and a mode-locked laser emitting pulses. As it was pointed out beforehand, the emission of coherent pulsed laser light is a sufficient condition for a laser to be considered as a frequency-comb. The inverse is however not generally true. Not every frequency-comb has to emit a train of pulses. An example are microcavity frequency combs. Even though microcavity-based frequency combs have shown "true" comb operation with millihertz stability, their output is sometimes nearly unmodulated in time [250, 251].

Strictly speaking, the only requirement for an optical frequency-comb is the equidistant comb lines, and not the emission of high energy pulses. Therefore, in the time domain, the requirement is the periodicity of the waveform at the round-trip frequency, not the generation of high intensity pulses. Looking at the definition of a perfectly frequency-modulated (FM) signal, we get

$$E(t) = E_0 \cos(2\pi f_c t + m \cos(2\pi f_{rep} t)), \quad (5.3)$$

where $m = \frac{f_\Delta}{f_{rep}}$ is the modulation index and f_Δ is the peak frequency deviation. The bandwidth of the signal is approximately $2f_\Delta$.

The simulation of such a perfectly FM-signal is shown in fig. 5.3a. Since a FM-modulated signal is periodic in the time domain, it can be expressed as a sum of equidistant comb lines in the frequency domain. Expressing the time-domain signal as

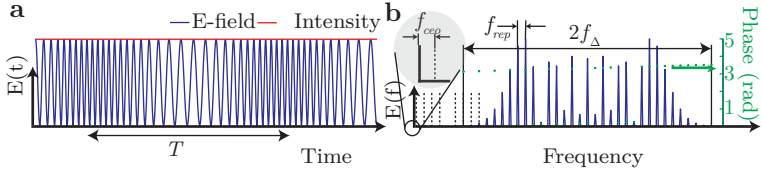


Fig. 5.3: Frequency comb laser output with perfect FM-phase and amplitude relations.

a sum of equally distant comb lines, one obtains [252]

$$E(t) = E_0 \sum_{n=-\infty}^{\infty} J_n(m) \cos \left(2\pi (f_c + n f_{rep}) t - |n| \frac{\pi}{2} \right), \quad (5.4)$$

where $J_n(m)$ is the n -th Bessel-function. The amplitude and phase configuration of a perfectly FM-signal is shown in fig. 5.3b. Even though a FM-signal contains an infinite amount of sidebands, most of the signal is found in the bandwidth of $2f_{\Delta}$.

Again, the carrier frequency can be expressed as $f_c = f_{ceo} + n f_{rep}$. Therefore, all requirements to be an optical frequency comb is also fulfilled by an optical signal with a FM output. All the definitions of the carrier-envelope offset frequency and its associated carrier-envelope frequency shift are still valid. The slip of the phase compared with the envelope is however hidden, since the envelope is constant.

The laser is "FM locked" if the output of a laser is composed of a frequency-modulated optical wave [76, 253]. If there is an appropriate coupling between longitudinal modes in the laser cavity, it is possible that an FM-supermode [76] with a certain phase and amplitude distribution quenches the other modes. The resulting spectrum has equally spaced comb lines with a fixed phase relationship. It should be noted however, that the output of such a FM-supermode is not a perfect FM-signal, since it would require the exact amplitude and phase configuration given by Bessel functions shown in eq. 5.4. Therefore, even for an FM-like signal output of a laser, there is still some residual variation on the intensity at the round-trip frequency of the laser arising from the coherent superposition of all the modes. We call this residual beating intermode beat. This helps to clearly distinguish the difference with the strong beatnote which is observed for a mode-locked laser when all phasors add up to form high-energy pulses.

A locking mechanism which results in different phase and amplitude configuration that can lead to FM-like outputs is the locking of the beat frequencies between adjacent modes rather than the locking of the frequency of the modes themselves [253]. Suppose

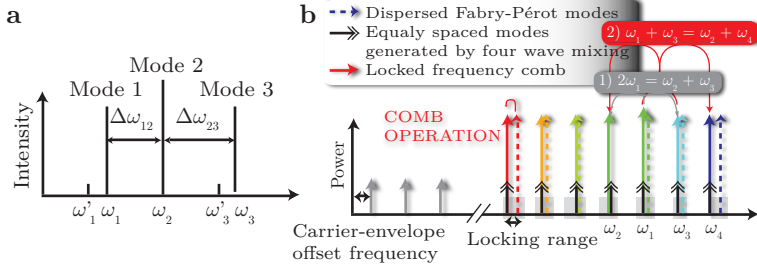


Fig. 5.4: Locking of the beat frequencies. **a** Dispersed three mode operation at $\omega_{1,2,3}$ and generated beat frequencies at $\omega'_{1,2,3}$. Graph adapted from [253]. **b** Generation of optical frequency comb spectrum. The dispersed Fabry-Pérot resonator modes lock to the equally spaced modes generated by four-wave mixing processes. Reprint from [229].

the laser oscillates at three frequencies $\omega_{1,2,3}$ with intensity I_i as illustrated in fig. 5.4a. Due to four-wave mixing resulting from third-order nonlinear effects (see sec. 2.6), the two frequencies ω_1 and ω_2 spaced by the beat frequency $\Delta\omega_{12}$ generate a third frequency ω'_3 . This oscillation at frequency ω'_3 pulls the mode 3 to oscillate at the same frequency, resulting in $\omega_3 \equiv \omega'_3$. This locking occurs if the difference of the mode generated by four-wave mixing and the original mode is small and the four-wave mixing signal generated is strong enough. In other words, the GVD of the modes must be small enough and the $\chi^{(3)}$ in the medium large. This leads to an equally spaced comb of modes with one common beat frequency $\Delta\omega_{23} \equiv \Delta\omega_{12}$. Depending on the relative phase of the different phases, the locking can be of type AM or FM. As shown in fig. 5.4b in the case of a laser featuring N -modes, the result will be a proliferation of modes due to degenerate and non-degenerate four-wave mixing processes.

There have been several papers discussing and proving the possibility to actively force such a locking by introducing an intracavity phase modulator in a He-Ne and Nd:YAG laser system [77, 254]. Furthermore, Tiemeijer *et al.* demonstrated passive FM-mode locking in a InGaAsP semiconductor laser [252]. The cause of the locking are nonlinear interactions arising from spectral hole burning in the laser cavity. This process occurs at the picoseconds time-scale, therefore the bandwidth of the FWM-signal is large enough to couple the modes. In their conclusion the authors note that "FM supermode operation will be obtained for any sufficiently well-behaved semiconductor laser" [252]. The locking mechanism between beat frequencies is also similar to what occurs in microcavity resonators [255].

The prospect to achieve a frequency-comb output with a frequency-modulated like output in a QCL is very tempting. In fact, since the intensity of a perfectly frequency-modulated laser is constant, the power envelope of such a beam would not be perturbed by the fast gain-recovery of the quantum cascade laser while the spectrum of such a laser would also be composed of equally spaced and discrete spectral lines. Furthermore, as in radio, a frequency-modulated signal may have better immunity against noise compared to an amplitude-modulated signal. In addition, a constant output power can be more preferable for linear spectroscopy applications in order to avoid additional complexities caused by nonlinear interactions.

5.4 Mid-infrared comb sources

Due to the large possible application space, the generation of optical frequency combs in the mid-IR region has seen a lot of improvement up to today. Schliesser *et al.* recently published a review article covering mid-IR frequency combs [95].

There is a lot of ongoing work trying to widen the penetration of solid-state combs in the mid-IR region [256]. One material system showing good performance at larger wavelength is based on Cr^{2+} dopant in combination with a II-VI compound, specifically ZnS and ZnSe [257]. Cr^{2+} shows the broadest bandwidth of all solid state laser materials. Therefore, these laser systems feature broad bandwidth (2-3 μm). They operate in continuous-wave at room-temperature. In single frequency operation, they reach multi-watt output powers [258] and tuning-ranges from 1.8 μm to 3.1 μm have been shown [259]. Mode-locking was achieved using different saturable absorber techniques [260–262]. Due to the large gain bandwidth of Cr^{2+} , these laser systems achieve pulse widths as short as 95 fs [261]. The output power these mode-locked lasers is in the order of tens of mW up to 200 mW [263]. Also noteworthy are lasers based on Ho:YLF, which reach 1.6 W of output power at 2.06 μm [264]. Although nowadays operated in Q-switched configuration at room-temperature, Fe^{2+} doped ZnS, ZnSe and ZnTe could bring solid-state mode-locked lasers up to wavelength ranges of 3.5-5.5 μm [265, 266]. Other possible generation schemes are through supercontinuum generation in nonlinear fibers [267, 268] and fiber-laser comb sources emit wavelength at around 2 μm using Er and Tm-doped fibers [269, 270].

Up to today, the direct generation of mode-locked optical-frequency combs is limited to about 3 μm . Therefore, mid-IR comb sources penetrating longer wavelength are usually based on the down conversion of near-infrared comb sources by using non-linear optical crystals. The two main generation mechanisms are either through difference-frequency generation (DFG) or optical parametric oscillations (OPO). DFG is illus-

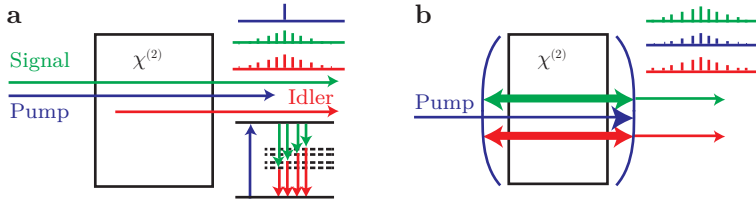


Fig. 5.5: **a** Mid-IR comb generation through difference-frequency generation (DFG) on a nonlinear crystal. **b** Mid-IR comb generation using the divide-and-conquer approach in a optical-parametric oscillator (OPO). Figure adapted from [95].

trated in fig. 5.5a. The signal source consists of a frequency-comb of equally distant comb lines $f_{\text{signal}} = f_{\text{ceo}} + n f_{\text{rep}}$ is superimposed with a continuous-wave pump laser emitting radiation at f_{pump} on a second-order nonlinear crystal [91, 271]. The pump source does not have to be a single-mode source and can also be a frequency comb source [272]. Due to nonlinear interaction (see sec. 2.6.2), a difference frequency is generated given by $f_{\text{idler}} = f_{\text{pump}} - f_{\text{signal}}$. Instead of using two different sources as the pump and signal in the setup, another possibility is to use the broadband nature of the comb and effectively generate mid-IR radiation by mixing different teeth of of one comb, resulting in $f_{\text{idler}} = (n - m) f_{\text{rep}}$ [273, 274]. The periodically-poled lithium niobate (PPLN) is a good candidate as nonlinear crystal for frequencies up to $\sim 5 \mu\text{m}$. Usual power per mode is tens of nW with a spectral spanning about 500 cm^{-1} [95]. At higher wavelength, other nonlinear materials must be used. For example GaSe, with which frequency combs up to $17 \mu\text{m}$ have been produced. The reached bandwidth is about 300 cm^{-1} with 50 nW per mode [95]. The first time-domain mid-IR frequency comb spectrometer developed by Keilmann *et al.* employed GaSe emitting at $10 \mu\text{m}$ [100]. Both mid-IR combs were generated through the mixing of individual comb lines of a Ti:Sapphire mode-locked laser. Recently, Keilmann *et al.* demonstrated a mid-IR comb based on DFG with 700 cm^{-1} available bandwidth [275]. The mid-IR output was generated by focusing the output of a Er fiber laser and a supercontinuum pulse generated in a nonlinear optical fiber using the same fiber laser on a GaSe crystal. This comb could be tuned from $600\text{-}2500 \text{ cm}^{-1}$, that is from $4\text{-}17 \mu\text{m}$, with about 1 nW per mode.

In an OPO, the non-linear crystal is placed within a cavity. The generated signal is resonant with this cavity and can overcome the threshold for parametric oscillation. Fig. 5.5b shows the case in which also the idler is resonant with the cavity. This OPO configuration helps to increase the efficiency of the generated idler and signal.

Frequency combs having a maximum bandwidth of $0.3\mu\text{m}$ which are tunable from $2.8\text{--}4.8\mu\text{m}$ featuring an output power of 1.5 W were realized in this way by Adler *et al.* using a PPLN crystal [276]. Also noteworthy is the recent development of the so called "divide-and-conquer" method [263, 277–279]. The method is to merge the idler and signal comb in the OPO into one comb, therefore the signal and idler are at half the pump center frequency. In [277] the researchers used a PPLN crystal pumped by a Ti:Sapphire laser. The generated comb emits at $1.55\mu\text{m}$. The spectral coverage was further pushed into the mid-IR by using an Er-doped fiber as a pump source emitting at $1.56\mu\text{m}$ [278]. This produced a comb spanning $2.5\text{--}3.8\mu\text{m}$ with an output power of 60 mW . To penetrate larger wavelengths, the PPLN was exchanged with an GaAs crystal [263]. The pump laser was a $\text{Cr}^{2+}:\text{ZnSe}$ laser emitting at $2.45\mu\text{m}$. The resulting spectra coverage is $1\mu\text{m}$ at $4.9\mu\text{m}$. Recently, an octave-spanning comb using this method using a TM-fiber laser as a pump source on a GaAs nonlinear element was demonstrated [279]. The comb emits radiation from $2.6\text{--}6.1\mu\text{m}$ featuring an average power of 37 mW . It becomes clear, that these techniques naturally profit from the advance of fiber and solid-state combs featuring emission at $2\text{--}3\mu\text{m}$.

5.5 Mode-locked semiconductor lasers

Mode-locking semiconductor laser is very interesting for several applications which requires dense and low-power integration [280, 281]. The generated equal frequency grid of a mode-locked laser can for example be used as an effective source for a wavelength-division multiplexed system.[282] With ever increasing demands on bandwidth in data-communication applications and system designs, research how to efficiently generate integrated mode-lock semiconductor lasers continuous [283]. Apart from quantum-well lasers, lasers based on quantum-dot gain are also successfully mode-locked [284]. These sources are very promising, due to their potential large attainable bandwidth. Mode-locked operation in [285] reached a bandwidth of about $\Delta\lambda = 14\text{ nm}$, which corresponds to a spectral coverage at a center wavelength of $1.26\mu\text{m}$ of $\frac{\Delta\lambda}{\lambda} = 1.1\%$. The maximum reached average power is 45 mW . Looking at possible attainable bandwidths from state-of-the-art quantum-dot external-cavity diode lasers, which reach tunings of $\sim 200\text{ nm}$ at $1.2\mu\text{m}$, spectral coverages of 15% seems plausible [286]. Broad wavelength tuning of 136 nm of a mode-locked quantum-dot laser in an external-cavity configuration was also recently shown [287].

Alternatively of incorporating the saturable absorber monolithically into the semiconductor laser-cavity, external cavity configurations employing an external saturable absorber in a vertical-external-cavity surface-emitting-laser (VECSEL) configuration

show up to today the broadest results. Optically pumped systems reach bandwidths of $\Delta\lambda = 20$ nm at a center wavelength of $\lambda = 1.037$ μm , giving a spectral coverage of $\frac{\Delta\lambda}{\lambda} = 2\%$ [288]. Average powers of up to 1 W for such configurations are reported [289].

5.6 Kerr-combs

Kerr-combs feature a novel way of generating an optical frequency comb output. The optical comb spectrum is generated by pumping an ultra-high quality-factor whispering-gallery mode microresonator with a single-mode continuous-wave source [255, 290]. The small size of the microresonator allows for the development of a compact frequency comb generator, with a possible frequency coverage of the entire mid-IR frequency range. Through third-order nonlinear interactions in the microresonator, a comb of equally spaced frequencies is generated. Two pump photons at frequency f_{pump} are absorbed and generate two equally spaced photons (idler and signal) fulfilling the energy conservation $hf_{\text{signal}} + hf_{\text{idler}} = 2hf_{\text{pump}}$, where h is the Planck-constant. This effect is cascaded resulting in a wide frequency-comb spectrum. The process is similar as the locking of the beat frequencies in frequency-modulated mode-locking discussed in section 5.3. The full dynamics of the Kerr-comb generation are however complicated. The understanding of those dynamics is essential to generate low-noise combs and to evaluate other suitable material systems to extend the wavelength coverage [291, 292].

A milestones in microresonator combs is the realization of octave spanning combs generated in fused-silica and silicon-nitride microresonators [293, 294]. In [293] the generated comb spans from 0.99 to 2.17 μm . Furthermore the comb could be continuously tuned by more than the FSR, a key ingredient for high-resolution spectroscopic applications. Another milestone is the full stabilization of such combs by controlling the frequency and power of the pump laser [250].

Apart from silica, Kerr-combs were demonstrated in several different material systems, including CaF_2 [295, 296], and Si_3N_4 resonators [297, 298]. Other work demonstrated that the coupling waveguide and the microresonator can be realized monolithically [299]. The work of Braje *et al.* furthermore illustrated the possibility to use a highly-nonlinear fiber cavity as the nonlinear medium [300]. All this work on different material systems clearly illustrates the universality of the presented frequency-comb generator. To expand Kerr combs in the mid-IR region it comes down to finding the right material system in the mid-IR range to fabricate a high-Q cavity. To fabricate a compact mid-IR Kerr-comb a suitable pump source can be found in single-mode continuous-wave high-power QCLs [39].

A suitable material to generate an optical frequency comb in the mid-IR in a crys-

talline microresonator was found in MgF_2 [301]. The material system shows the desired anomalous GVD in the mid-IR range. It features a wide transparency window up to about $7\mu\text{m}$. Furthermore, the sign of the temperature coefficient of the refractive index ($\frac{dn}{dT}$) and the thermal expansion coefficient are positive, allowing thermal self-locking. As a pump source, a tunable OPO ($2.4\text{--}2.5\mu\text{m}$) was used. Using different microresonator sizes, repetition rates of $10\text{--}110\text{GHz}$ were produced. The emission wavelength was $2.45\mu\text{m}$, featuring a bandwidth of 200nm . This corresponds to a spectral coverage of $\frac{\Delta\lambda}{\lambda} = 8\%$. High power per mode are measured and ranges from $\mu\text{W}/\text{mode}$ to mW/mode . In order to extend the comb center wavelength deeper into the mid-IR region, the coupling fiber (high losses) must be replaced and the pump-source must be adapted.

5.7 Characterization

5.7.1 FTIR and second-order autocorrelation

The only requirement for an optical-frequency comb is the equidistant spacing of all modes. This should be possible by simply measuring a high resolution spectrum of the laser. The spectrum of a QCL is usually measured through a Fourier-transform interferometer. The interferogram obtained through a Michelson interferometer

$$I(\tau) = \int_{-\infty}^{+\infty} E(t)E^*(t - \tau)dt, \quad (5.5)$$

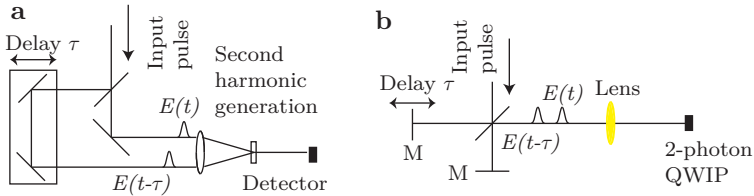


Fig. 5.6: **a** Background-free intensity autocorrelation setup. The input pulse is split into two separate pulses, one of which is delayed by τ . The two pulses are then spatially overlapped on a nonlinear-medium, in this example a second-harmonic-generation crystal. **b** Fringe-resolved autocorrelation setup. Figures adapted from [302].

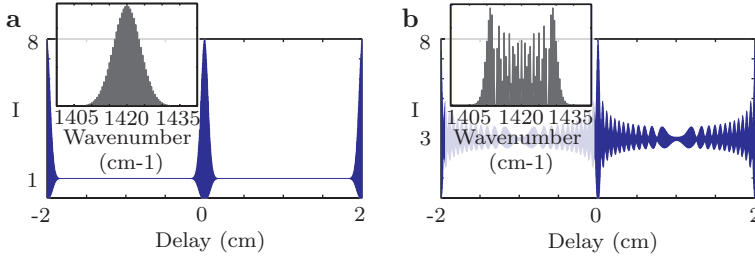


Fig. 5.7: Simulated fringe-resolved interferometric autocorrelation trace of **a** a mode-locked laser emitting a train of pulses and (inset: spectra) **b** a laser featuring a perfectly FM-output (inset: spectra).

does not reveal any phase information of the sampled field $E(t)$. The Fourier transform of said function only gives information about the spectrum

$$|E(\omega)|^2 = \mathcal{F}(I(\tau)). \quad (5.6)$$

The requirements of the resolution to characterize an optical frequency comb however makes this method inapt. Already the measurement of an unlocked multi-mode QCL would require a resolution of several tens of MHz. This corresponds to a delay length of several meters for the FTIR.

Therefore, the assessment of the coherence properties of a mode locked laser is usually performed by an autocorrelation measurement on a non-linear crystal to reveal the time structure of the optical pulse [303–305]. The setup is shown in Fig. 5.6 **a**. The normalized measured intensity autocorrelation is

$$A^{(2)}(\tau) = \frac{\int_{-\infty}^{\infty} I(t)I(t-\tau)dt}{\int_{-\infty}^{\infty} I^2(t)dt}, \quad (5.7)$$

where I is the intensity of the pulse. This technique is however not applicable to characterize QCLs in the mid-IR due absence of high-energy pulses. It is possible to use a two-photon quantum-well infrared photodetector (QWIP) Michelson-interferometer configuration, as it was done in [233]. The setup is illustrated in fig. 5.6b. If we write the E-field as $E(t)e^{i\omega t}$ the measured quantity of a two-photon QWIP in a Michelson-

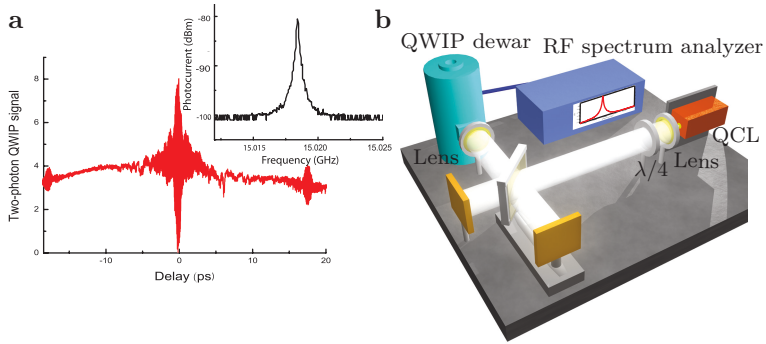


Fig. 5.8: **a** 2-photon QWIP measurements from a buried heterostructure QCL ($\lambda = 8\mu\text{m}$). The inset shows the measure intermode beat at the round-trip frequency. Reprinted figure 16 with permission from Gordon *et al.*, Phys. Rev. A, 77, 053804 2008. © 2008 by the American Physical Society. **b** Intermode beat spectroscopy setup. Reprint from [229]

interferometer configuration is the interferometric autocorrelation

$$I(\tau) = \int_{-\infty}^{\infty} |E(t + \tau) e^{i\omega_c \tau} + E(t)|^4 dt \quad (5.8)$$

For a mode-locked laser emitting a train of pulses, the ratio between the background at $\tau > T$, where τ is the delay and T is the width of the pulse is given by

$$\frac{I(0)}{I(\tau > T)} = \frac{8}{1}. \quad (5.9)$$

A simulation of a mode-locked laser featuring a mode-spacing of 0.5cm^{-1} is shown in fig. 5.7a. The 8:1 ratio is clearly visible. The inset shows the spectrum of the simulated laser.

This ratio however changes for a laser running in continuous-wave with randomly varying phases to

$$\frac{I(0)}{I(\tau > T)} = \frac{8}{2}. \quad (5.10)$$

This is the same ratio one would expect from an incoherent source.

The strong intermode beat featuring linewidths in the kHz were first thought to be a clear signature of mode-locking and pulsed emission of QCLs [306]. When it became possible to characterize those QCLs further by measuring an autocorrelation trace due to the advancement of the 2-photon QWIP, the results showed that the device was not emitting single pulses, since the measured ratio was never the required 8:1, proving that the devices never emitted single pulses. However, looking at the interferometric autocorrelation traces published by Gordon *et al.* in [233], it is striking that the traces seem feature very particular patterns. One such trace of a buried-heterostructure QCL emitting radiation at $\lambda = 8\ \mu\text{m}$ is shown in fig. 5.8a. The ratio is neither 8:1 nor 8:2, but closer to 8:3. Furthermore, there are some clear signatures at half the round-trip time.

Since we are expecting a phase-relationship similar to an FM-output in a QCL, it is also interesting to simulate the interferometric autocorrelation trace of a perfect FM-signal. This is shown in fig. 5.7b. As it can be seen, the ground-line of a perfect FM-signal has a ratio of 8:3, similar to a single-mode laser with associated phase-jumps. Furthermore, there are important structures during the whole interferogram, especially at half-round trip time featuring peak values of 8:3.5.

5.7.2 Intermode beat spectroscopy

This section gives detailed description of the intermode beat spectroscopy. The intermode beat spectroscopy setup is shown in fig. 5.8b. The laser light is collimated through an anti-reflection coated ZnSe lens. The light passes through an anti-reflection coated quarter-wave plate to reduce effect of feedback originating from reflections from optical components. The light passes through an Fourier transform infrared spectrometer from Bruker (IFS 66/S) and is focused through an anti-reflection coated ZnSe lens on a quantum well infrared photodetector cooled to liquid nitrogen temperature. The Fourier transform infrared spectrometer is run in step scan. At each sampling step we record the RF spectrum at the round-trip frequency of the laser. At the same time, we record the intensity component of the interferogram through the bias current of the quantum well infrared photodetector.

The QWIP characteristics are as followed. The dewar features a broadband-AR coated ZnSe window. The device size is $80 \times 113\ \mu\text{m}$ and mounted at 45° resulting in an effective optical area of $80 \times 80\ \mu\text{m}$. The device accepts horizontally polarized light. Fig. 5.9a shows the transmission and fit at room-temperature of a single-pass. Fig. 5.9b shows the I-V in the dark at liquid nitrogen temperature. Our device response is up to about 12 GHz nearly flat. Nowadays, employing sophisticated processing and mounting, QWIPs reach impressive maximum response frequencies of up to 100 GHz [307].

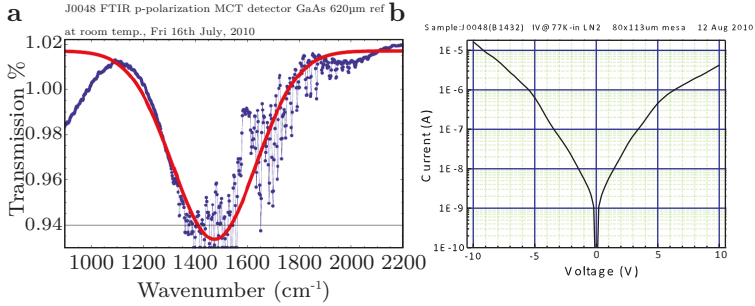


Fig. 5.9: QWIP characteristics. **a** Transmission measurements and fit at room-temperature of a single-pass. **b** I-V in the dark at liquid nitrogen temperature. Data is provided by H.C. Liu.

Intermode beat interferogram analysis

To gain an insight on the respective phases and coherence properties of the modes, we present an interferometric technique where the autocorrelation of the intermode beat is measured using a Michelson interferometer. The quantity measured

$$I(\nu, \tau) = \left| \mathcal{F} \left\{ \underbrace{|E(t) + E(t + \tau)|^2}_{Int(t, \tau)} \right\} \right| \quad (5.11)$$

is the absolute value of the Fourier component of the intensity on the detector at frequency ν over a chosen resolution-bandwidth of the spectrum analyzer. \mathcal{F} stands for the Fourier transform which is applied to the time dependent intensity. $I(0, \tau)$ is the normal intensity interferogram measured in a Fourier transform infrared spectrometer. In contrast to the intensity interferogram, the intermode beat interferogram, $I(\nu_{rt}, \tau)$, is a function of both amplitude *and phase* of the modes, as it is going to be shown later by the mathematical treatment. The normal intensity interferogram measured in a Fourier transform infrared spectrometer is $I(0, t)$. Furthermore, in analogy with Fourier spectroscopy, the Fourier transform

$$\mathcal{J}(\nu_{rt}, \omega) = \mathcal{F}(I(\nu_{rt}, \tau)) \quad (5.12)$$

will yield the intermode beat spectrum, which roughly indicates the spectral regions contributing to the intermode beat.

Intermode beat spectroscopy model

This section will give a mathematical treatment of the acquired intermode beat interferogram. The goal is to write the acquired intermode beat interferogram in matrix form.

An optical frequency comb can be written as a sum of equidistant modes with amplitude a_k and phase Φ_k . The optical frequency spacing in mode-locked lasers is $\Delta\omega = 2\pi f_{rep}$. The carrier wave is given by ω_0 . The resulting field is therefore

$$E(t) = \sum_k a_k e^{i(\omega_0 + k\Delta\omega)t + \Phi_k}. \quad (5.13)$$

The delayed field is given by

$$E(t - \tau) = \sum_l a_l e^{i(\omega_0 + l\Delta\omega)(t - \tau) + \Phi_l}. \quad (5.14)$$

Assuming a 50:50 beamsplitter, the total intensity after the beam has traveled through the interferometer is

$$\begin{aligned} Int(t, \tau) &= \left| \left[\frac{1}{2} E(t) + \frac{1}{2} E(t - \tau) \right] \right|^2 = \frac{1}{4} \{ [E(t) + E(t - \tau)] [E(t) + E(t - \tau)]^* \} \\ &= \frac{1}{4} \left\{ \underbrace{E(t)E^*(t) + E(t - \tau)E^*(t - \tau)}_{A=} + \underbrace{E(t)E^*(t - \tau) + E^*(t)E(t - \tau)}_{B=} \right\}. \end{aligned} \quad (5.15)$$

Now we will combine Eq. (5.13), (5.14) and (5.15). For clarity, we will analyze term A and B separately.

$$\begin{aligned} A &= E(t)E^*(t) + E(t - \tau)E^*(t - \tau) \\ &= \sum_k \sum_l a_k a_l e^{i[(l-k)\Delta\omega t + (\Phi_l - \Phi_k)]} + \sum_k \sum_l a_k a_l e^{i[(l-k)\Delta\omega(t - \tau) + (\Phi_l - \Phi_k)]} \\ &= \sum_k \sum_l a_k a_l e^{i[(l-k)\Delta\omega t + (\Phi_l - \Phi_k)]} + \sum_k \sum_l a_k a_l e^{i[(l-k)\Delta\omega t + (\Phi_l - \Phi_k)]} e^{-i[(l-k)\Delta\omega \tau]} \\ &= \sum_k \sum_l a_k a_l e^{i[(l-k)\Delta\omega t + (\Phi_l - \Phi_k)]} \{ 1 + e^{-i[(l-k)\Delta\omega \tau]} \}. \end{aligned} \quad (5.16)$$

This can be rewritten by grouping the terms with $m = |l - k|$ as a sum over mode pairs

$m=l-k$ [112].

$$\begin{aligned} A &= \sum_k \sum_m a_k a_{k+m} e^{i[m\Delta\omega t + (\Phi_{k+m} - \Phi_k)]} \{1 + e^{-i[m\Delta\omega\tau]}\}. \\ &= \sum_k \sum_m a_k a_{k+m} e^{i[m\Delta\omega t]} \{1 + e^{-i[m\Delta\omega\tau]}\} (e^{i(\Phi_{k+m} - \Phi_k)}). \end{aligned} \quad (5.17)$$

Now we restrict the sum to positive values of m and group the terms k, m and $k + |m|, -|m|$.

$$A = \sum_k \sum_{m \geq 0} a_k a_{k+m} e^{i[m\Delta\omega t]} \{1 + e^{-i[m\Delta\omega\tau]}\} (e^{i(\Phi_{k+m} - \Phi_k)}) + c.c. \quad (5.18)$$

Now we will look at term B of Eq. 5.15.

$$\begin{aligned} B &= E(t)E^*(t - \tau) + c.c. \\ &= \sum_k \sum_l a_l e^{i[(\omega_0 + l\Delta\omega)t + \Phi_l]} * a_k e^{-i[(\omega_0 + k\Delta\omega)(t - \tau) + \Phi_k]} + c.c. \\ &= \sum_k \sum_l a_k a_l e^{i[(l-k)\Delta\omega t + \overbrace{(\omega_0 + k\Delta\omega)\tau}^{=\Omega(\omega_0, k, \tau)} + (\Phi_l - \Phi_k)]} + c.c., \end{aligned} \quad (5.19)$$

where we have introduced the term $\Omega(\omega_0, k, \tau) = (\omega_0 + k\Delta\omega)\tau$. Again we can sum over mode pairs of $m = l - k$

$$B = \sum_k \sum_m a_k a_{k+m} e^{i[m\Delta\omega t + \Omega(\omega_0, k, \tau) + (\Phi_{k+m} - \Phi_k)]} + c.c. \quad (5.20)$$

And again we will sum over positive values of m and group k, m and $k + |m|, -|m|$

$$\begin{aligned} B &= \sum_k \sum_{m \geq 0} a_k a_{k+m} e^{i[m\Delta\omega t + \Omega(\omega_0, k, \tau) + (\Phi_{k+m} - \Phi_k)]} \\ &\quad + a_k a_{k+m} e^{i[-m\Delta\omega t + \Omega(\omega_0, k+m, \tau) - (\Phi_{k+m} - \Phi_k)]} \\ &\quad + c.c. \end{aligned} \quad (5.21)$$

Now we need to write out the complex conjugate term and regroup the expression

$$\begin{aligned}
 B &= \sum_k \sum_{m \geq 0} a_k a_{k+m} e^{i[m\Delta\omega t + \Omega(\omega_0, k, \tau) + (\Phi_{k+m} - \Phi_k)]} \\
 &\quad + a_k a_{k+m} e^{i[m\Delta\omega t - \Omega(\omega_0, k+m, \tau) + (\Phi_{k+m} - \Phi_k)]} \\
 &\quad + a_k a_{k+m} e^{-i[m\Delta\omega t + \Omega(\omega_0, k, \tau) + (\Phi_{k+m} - \Phi_k)]} \\
 &\quad + a_k a_{k+m} e^{-i[m\Delta\omega t - \Omega(\omega_0, k+m, \tau) + (\Phi_{k+m} - \Phi_k)]} \\
 &= \sum_k \sum_{m \geq 0} a_k a_{k+m} e^{im\Delta\omega t} \left(e^{i\Omega(\omega_0, k, \tau)} + e^{-i\Omega(\omega_0, k+m, \tau)} \right) e^{i(\Phi_{k+m} - \Phi_k)} \\
 &\quad + c.c.
 \end{aligned} \tag{5.22}$$

We can now insert A of Eq. (5.18) and B of (5.22) in (5.15).

$$\begin{aligned}
 Int(t, \tau) &= \frac{1}{4} (A + B) \\
 &= \frac{1}{4} \sum_k \sum_{m \geq 0} a_k a_{k+m} e^{im\Delta\omega t} e^{i(\Phi_{k+m} - \Phi_k)} \\
 &\quad \times \left(1 + e^{-im\Delta\omega\tau} + e^{i\Omega(\omega_0, k, \tau)} + e^{-i\Omega(\omega_0, k+m, \tau)} \right) + c.c.
 \end{aligned} \tag{5.23}$$

In eq. 5.11, a Fourier transform is performed by the spectrum analyzer on the measured intensity $Int(t, \tau)$. For the intermode beat spectroscopy we are mainly interested in the frequency components ν where we observe the characteristic beating between different pairs of modes. The intermode beat spectroscopy can in principle be performed between any pairs of modes. The most obvious choice is of course at the round-trip frequency ν_{rt} , with $m = 1$. The final result for $I(\nu_{rt}, \tau)$ is therefore:

$$\begin{aligned}
 |\mathcal{F}_{\nu_{rt}} \{Int(t, \tau)\}| &= |Int(t, \tau, m = 1)| \\
 &= \left| \frac{1}{4} \sum_k a_k a_{k+1} e^{i\Delta\omega t} e^{i(\Phi_{k+1} - \Phi_k)} \right. \\
 &\quad \times \left(1 + e^{-i\Delta\omega\tau} + e^{i\Omega(\omega_0, k, \tau)} + e^{-i\Omega(\omega_0, k+1, \tau)} \right) + c.c. \left. \right| \\
 &= \left| \frac{1}{4} e^{i\Delta\omega t} \sum_k a_k a_{k+1} e^{i(\Phi_{k+1} - \Phi_k)} \right. \\
 &\quad \times \left(\underbrace{1}_{\Psi_1} + \underbrace{e^{-i\Delta\omega\tau}}_{\Psi_2} + \underbrace{e^{i\Omega(\omega_0, k, \tau)}}_{\Psi_3} + \underbrace{e^{-i\Omega(\omega_0, k+1, \tau)}}_{\Psi_4} \right) + c.c. \left. \right|
 \end{aligned} \tag{5.24}$$

Taking a closer look at eq. 5.24 we get for each pair of modes a sum of 4 complex

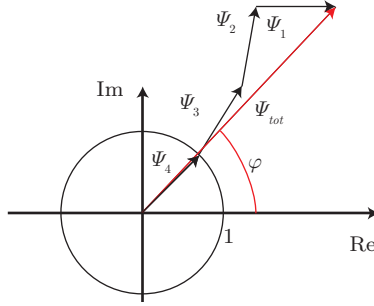


Fig. 5.10: Intermode beat spectroscopy measurement complex plane analysis.

vectors Ψ_i with amplitude 1 whose phase depend on the delay τ and the relative phase difference $\Phi_{k+1} - \Phi_k$. This is illustrated in fig.5.10. We can therefore rewrite the equation to

$$\begin{aligned}
 & \left| \mathcal{F}_{\nu_{rt}} \{Int(t, \tau)\} \right| \\
 &= \left| \frac{1}{4} e^{i\Delta\omega t} \sum_k a_k a_{k+1} |\Psi_{tot}(k, \omega_0, \Delta\omega, \tau)| e^{-i\varphi(k, \omega_0, \Delta\omega, \tau)} e^{i(\Phi_{k+1} - \Phi_k)} + c.c. \right|.
 \end{aligned} \tag{5.25}$$

Those results allow us to draw some conclusions on the intermode beat interferogram. First of all, the intermode beat interferogram is insensitive to a translation of the input signal, since

$$\begin{aligned}
 & \left| \mathcal{F}_{\nu_{rt}} \{Int(t, \tau)\} \right| = \left| \mathcal{F}_{\nu_{rt}} \{Int(t + \Delta t, \tau)\} \right| \\
 &= \left| \frac{1}{4} e^{i\Delta\omega t} e^{i\Delta\omega \Delta t} \sum_k a_k a_{k+1} |\Psi_{tot}(k, \omega_0, \Delta\omega, \tau)| e^{-i\varphi(k, \omega_0, \Delta\omega, \tau)} e^{i(\Phi_{k+1} - \Phi_k)} + c.c. \right| \\
 &= \left| \frac{1}{4} e^{i\Delta\omega t} \sum_k a_k a_{k+1} |\Psi_{tot}(k, \omega_0, \Delta\omega, \tau)| e^{-i\varphi(k, \omega_0, \Delta\omega, \tau)} e^{i((\Phi_{k+1} - \Phi_k) + \Delta\omega \Delta t)} + c.c. \right|
 \end{aligned} \tag{5.26}$$

The intermode beat interferogram is only sensitive to relative phase differences between the modes $(\Phi_{k+1} - \Phi_k)$. Therefore, adding a constant term originating from a translation in time to this relative phase difference will not alter the intermode beat interferogram. Second, the intermode beat interferogram is insensitive to mirroring

of the input signal, $|\mathcal{F}_{\nu_{rt}} \{Int(t, \tau)\}| = |\mathcal{F}_{\nu_{rt}} \{Int(-t, \tau)\}|$ Furthermore, since the intermode beat interferogram is only sensitive to the difference in phases between adjacent modes, the difference in phases must be in the interval of $-\pi < (\Phi_{k+1} - \Phi_k) < \pi$. It would however be premature to state that every amplitude and phase configuration will lead to a different characteristic intermode beat interferogram. Further studies are necessary to investigate on this point.

To further simplify the notation, eq.5.26 can be expressed in matrix notation. Since we are only interested in the absolute value of the Fourier-component at the round-trip frequency ν_{rt} , we are only interested in the amplitude of eq. 5.25. The rows of matrix (\mathcal{P}) are the different discrete delays τ_u separated by $\Delta\tau$, which is nothing else than the sampling spacing of the FTIR. The matrix of course also depends on the starting point of the first sample τ_s .

$$|\mathcal{F}_{\nu_{rt}} \{Int(\tau)\}| = \frac{1}{4} (\mathcal{P}_{\tau_s} \Phi + \overline{\mathcal{P}_{\tau_s} \Phi})$$

$$\text{with } \mathcal{P}_{\tau_s} = \begin{pmatrix} \mathcal{P}_{11}^{\tau_s} & \mathcal{P}_{12}^{\tau_s} & \dots & \mathcal{P}_{1n}^{\tau_s} \\ \mathcal{P}_{21}^{\tau_s} & \mathcal{P}_{22}^{\tau_s} & \dots & \mathcal{P}_{2n}^{\tau_s} \\ \vdots & \vdots & \ddots & \vdots \\ \mathcal{P}_{n1}^{\tau_s} & \mathcal{P}_{n2}^{\tau_s} & \dots & \mathcal{P}_{nn}^{\tau_s} \end{pmatrix} \text{ and } \Phi = \begin{pmatrix} e^{i(\Phi_2 - \Phi_1)} \\ e^{i(\Phi_3 - \Phi_2)} \\ \vdots \\ e^{i(\Phi_{n+1} - \Phi_n)} \end{pmatrix}$$

$$\mathcal{P}_{ij}^{\tau_s} = a_j a_{j+1} \left(1 + e^{-i\Delta\omega(\tau_s + u\Delta\tau)} + e^{i\Omega(\omega_0, j, \tau_s + u\Delta\tau)} + e^{-i\Omega(\omega_0, j+1, \tau_s + u\Delta\tau)} \right) \quad (5.27)$$

We have developed several MATLAB programs to simulate the intermode beat interferogram. Simulating the intermode beat interferogram using the set of equations 5.27 is until now by far the fastest solution. It allows to simulate entire real world intermode beat interferograms on medium sized computers in a short time.

Discussion on intermode beat interferograms and spectroscopy

This section covers two simulation of optical frequency combs with different phase configurations (fundamentally mode-locked and FM-mode locked) and one simulation of a laser with random-varying phases. This will help to illustrate the insight you can get in the phase and the coherence properties of the laser by doing an intermode beat interferogram. To have comparable results between simulation and measurements of intermode beat interferograms, we need to clarify a point considering the acquisition of the intermode beat interferogram. We use a photoconductive QWIP for our measurement and the photocurrent is proportional to the intensity of the light $I_{\text{photo}} \propto |E|^2 \propto Int$. The signal is then fed onto a spectrum analyzer measuring a power dissipated over a 50Ω

resistor $P = RI_{\text{photo}}^2$. The same conventions as for the development of the intermode beat spectroscopy model in the previous section 5.7.2 are taken, I_{photo} stands for a photo-current, E for the electrical field, Int is the optical intensity and P stands for the measured electrical power dissipated over the 50Ω resistor. When acquiring the intermode beat interferogram, the spectrum analyzer measures the electrical power in dBm. This measured power does not corresponds to the optical intensity, but has a square dependence on it $P \propto Int^2$. In a conventional FTIR, the measured intensity interferogram is directly proportional to the measured DC-photocurrent I_{DC} of the detector. Therefore, the Fourier-transform of of said interferogram gives the spectral distribution of the optical intensity. The intensity interferogram does not have this ambiguity one needs to be aware of when taking the intermode beat interferogram. When acquiring the intermode beat interferogram using the QWIP, we usually acquire the intensity interferogram by measuring the DC-current of the photodetector.

Depending on the case, the intermode beat measurements are either presented as they were measured in the spectrum analyzer or are corrected for this quadratic behavior. If the measurement are left uncorrected, the simulations are adapted to take this quadratic dependence of the measured power P into account. To clearly distinguish the two scenarios, we label axes of the graphs strictly in the following manner:

- If we plot the power dissipated on the resistor of the spectrum analyzer, meaning we do not correct the data we label the axis with: **Power**.
- If the intermode beat interferogram and spectrum and interferogram are corrected to be proportional to the light intensity label the axis with: **Intensity**.

The intensity interferogram is not affected by this labeling, as it does not need to be treated specially.

Pulsed mode-locked laser Fig.5.11a shows the simulation of a fundamentally mode-locked laser with 0.25 cm^{-1} mode spacing. The intermode beat interferogram of such a laser features a maximum at zero delay. In order to confirm the simulated intermode beat interferogram of a fundamentally mode-locked laser, we performed the intermode beat spectroscopy on a fundamentally mode-locked fiber laser from TOP-TICA. Fig.5.11b shows the measured intermode beat interferogram. The intermode beat interferogram shows a maximum at zero path difference, as expected from a fundamentally mode-locked laser. Furthermore, the overall shape agrees well with the simulated one.

As it was already noted beforehand, in analogy with Fourier spectroscopy, the Fourier transform will yield the intermode beat spectrum, which roughly indicates the

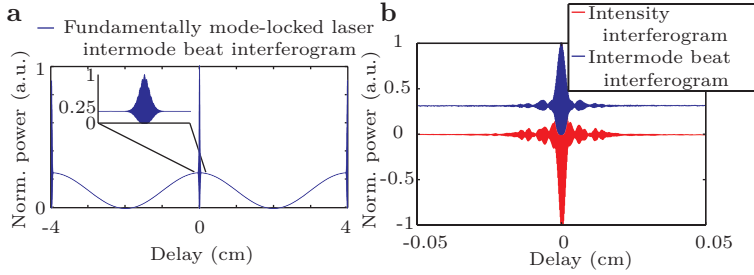


Fig. 5.11: Intermode beat interferogram of a fundamentally mode-locked laser. **a** Simulation of a laser with 0.25 cm^{-1} mode spacing. Inset: Zoom at zero delay. **b** Measurement of fundamentally mode-locked fiber laser of TOPTICA. Data published in [229].

spectral regions contributing to the intermode beat. To further elaborate this, let us try to connect the intermode beat interferogram to the DC-interferogram in the case of a fundamentally mode-locked laser. For this, we set the relative phases to a constant of all modes in eq. 5.24. The term which is modulating the interferogram, is the sum of $\Psi_1 + \Psi_2 + \Psi_3 + \Psi_4$. We will rewrite the terms and separate the slowly moving parts from the fast moving parts. We get

$$\Psi_{tot} = 1 + e^{-i\Delta\omega\tau} + e^{i(\omega_0+k\Delta\omega)\tau} + e^{-i(\omega_0+(k+1)\Delta\omega)\tau} \quad (5.28)$$

$$= (1 + e^{-i\Delta\omega\tau}) + (e^{i(\omega_0+k\Delta\omega)\tau} + e^{-i(\omega_0+k\Delta\omega)\tau} e^{-i\Delta\omega\tau}). \quad (5.29)$$

The intermode beat interferogram is modulated with $e^{-i\Delta\omega\tau}$. When $\tau = \frac{T}{2} = \frac{\pi}{\Delta\omega}$, then $e^{-i\Delta\omega\tau} = e^{-i\pi} = -1$ and eq. 5.29 is 0. This is observed in the simulation of fig. 5.11a when the intermode beat interferogram is 0 at 2 cm delay.

Lets consider the case where τ is small compared to the round-trip time $T = \frac{2\pi}{\Delta\omega}$. When τ is small, eq. 5.29 simplifies to

$$\Psi_{tot}(\tau \ll T/2) = 2 + 2 \cos([\omega_0 + k\Delta\omega]\tau). \quad (5.30)$$

The resulting normalized intermode beat interferogram is therefore

$$I(\nu_{rt}, \tau) = \frac{1}{2} + \frac{\sum_k a_k a_{k+1} \cos([\omega_0 + k\Delta\omega]\tau)}{2 \sum_k a_k a_{k+1}}. \quad (5.31)$$

To compare the intermode beat interferogram with the intensity interferogram, let us

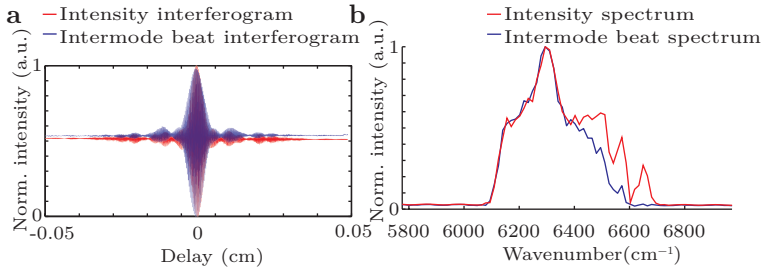


Fig. 5.12: Intermode beat interferogram and spectrum of a fundamentally mode-locked laser TOPTICA femto-second laser source corrected for the quadratic response. **a** Intermode beat interferogram. **b** Intermode beat spectrum. Data published in [229].

rewrite the normalized intensity interferogram. We set $m = 0$ in eq. 5.23 for the same multi mode laser composed of equidistant modes with individual amplitudes a_k . The normalized intensity interferogram is therefore

$$I(0, \tau) = \frac{1}{2} + \frac{\sum_k a_k^2 \cos([\omega_0 + k\Delta\omega] \tau)}{2 \sum_k a_k^2}. \quad (5.32)$$

Comparing eq. 5.32 with eq. 5.31 illustrates the close resemblance between the intermode beat interferogram and the intensity interferogram for small τ . The main difference is that the superposition of cosine waves is weighted by the product of neighboring modes field amplitudes $a_k a_{k+1}$ instead of the intensity of the single-mode.

To illustrate this close correspondence, we corrected the intermode beat interferogram shown in fig. 5.11b for the quadratic response of the spectrum analyzer response and plotted it alongside with the intensity interferogram in fig. 5.12a. Fig. 5.12b shows the corresponding intermode beat and intensity spectra.

Eq. 5.31 also illustrates that the intermode beat spectrum can be used to identify the modes which contribute to the beating at the round trip frequency. A very sharp intermode beat could arise from a beating of a small fraction of modes, whereas the rest of the spectrum is not coherently coupled. Comparing the intermode beat spectrum to the intensity spectrum gives an answer to this question.

This argument of the intermode beat spectroscopy is valid even if the laser output is only lightly modulated, as it is the case for a laser featuring a FM-like output. In the case of a laser featuring a FM-like output, the output only modulates at low values compared to the total intensity. One could therefore argue, that only a small portion

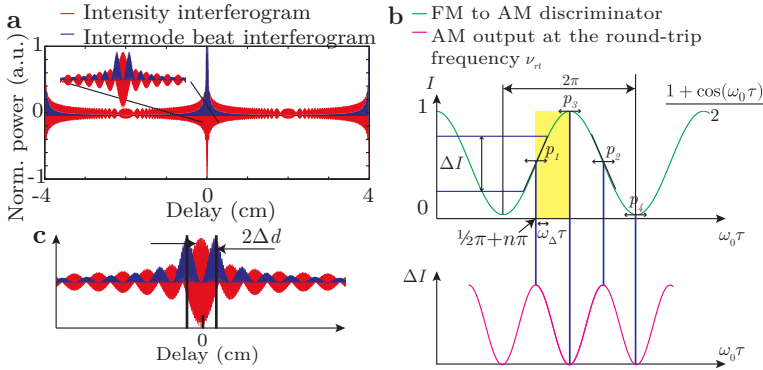


Fig. 5.13: Intermode beat interferogram FM-output. **a** Simulation of a laser with 0.25 cm^{-1} mode spacing featuring a perfect FM-amplitude and phase configuration. **b** Generated photocurrent in a optical beam-splitter discriminator. **c** Characteristic discriminator efficiency as function of delay. Graph inspired by [308].

of the modes contribute to the intermode beat. Therefore, taking an intermode beat spectrum and comparing it to the laser spectrum gives a clear answer if the observed intermode beat is really originating from a coherent sum of modes originating from the whole laser spectrum.

One limitation one has to be aware of when using the intermode beat interferogram is the resolution bandwidth of the spectrum analyzer. The results on the coherence properties of the analyzed laser are limited by the chosen resolution bandwidth.

FM mode-locked laser Fig. 5.13a shows the simulation of an intermode beat interferogram of a laser with a perfect FM-amplitude and phase configuration. As it can be seen, the observed intermode beat interferogram is qualitatively totally different from the one of a fundamentally mode-locked laser. First of all, at zero-delay difference, the intermode beat interferogram is zero. This is due to the fact that for a FM-signal the output power is constant.

Not at zero delay, the Michelson-interferometer can be thought as an optical-discriminator for a FM signal. The use of a optical discriminator using a beam-splitter discriminator is well explained by Kaminow [308]. One way to look at it is by considering the phase relations of a FM-signal. If the arm is not at zero-delay difference, the difference in path length between the two arms will alter the perfect FM-phase relation of the recombined signal, resulting in a beating at the round-trip frequency.

We will analyze the use of an FTIR as an optical discriminator by studying the output of an FTIR when the input is an optical FM-signal. We do this by looking at a signal which is frequency modulated at a fixed mirror displacement τ from zero delay. First, consider a single-mode laser with an optical carrier frequency ω_0 . The FTIR output of a monochromatic wave is a cosine wave. Adapting eq. 4.15, the normalized output of an FTIR signal for a monochromatic wave at carrier angular frequency ω_0 is given by

$$I(\tau) = \frac{1}{2} + \frac{1}{2} \cos(\omega_0 \tau), \quad (5.33)$$

where τ is the time delay. This is illustrated in units of $\omega_0 \tau$ in the top part of fig. 5.13b. The period of oscillation is therefore 2π . The E-field of a FM-signal is given by

$$E(t) = E_0 \cos(\omega_0 t + m \cos(2\pi\nu_{rep} t)), \quad (5.34)$$

where $m = \frac{\omega_\Delta}{2\pi f_{rep}}$. This frequency modulated optical signal will alter the instantaneous optical angular carrier frequency ω_0 with a maximum angular frequency excursion of ω_Δ . At a constant delay τ , this has the effect of moving on the horizontal axis in the top part of fig. 5.13b by a maximum amount of $\omega_\Delta \tau$. This in turn alters the output intensity of the FTIR at the round-trip frequency ν_{rep} . This amplitude modulation at the frequency ν_{rep} at the delay τ can be measured with a spectrum analyzer.

As illustrated in fig. 5.13b, to get a maximum amplitude of the AM-output, the signal of the delay τ should be chosen to be

$$\omega_0 \tau = \frac{\pi}{2} + n\pi. \quad (5.35)$$

Furthermore, the excursion of the FM-signal in the discriminator is proportional to $\tau\omega_\Delta$. Therefore, to prohibit wash out this excursion should not be bigger than

$$\omega_\Delta \tau < \frac{\pi}{2}. \quad (5.36)$$

. The region without wash out is indicated in yellow in the top part of fig. 5.13b.

It is possible to extract the modulation depth of the perfect FM-source using the intermode beat spectroscopy. Looking at the characteristic pattern around zero delay of a FM-source in fig. 5.13c, we define the separation of the two peaks where the discriminator is the strongest as $2\Delta d$. Looking at eq. 5.36, the maximum discriminator efficiency is at the limit where $\omega_\Delta \tau = \frac{\pi}{2}$. The maximum angular frequency excursion

is therefore given by

$$\omega_{\Delta} = \frac{\pi}{2} \frac{c}{\Delta d}, \quad (5.37)$$

and the signal bandwidth in wavenumber is therefore

$$\text{Bandwidth} = 2\omega_{\Delta} [\text{cm}^{-1}] = \frac{1}{2\Delta d}. \quad (5.38)$$

In order to increase the optical discriminator efficiency by a factor of two, it is possible to realize a balanced optical discriminator setup as suggested in [308].

The response of the discriminator is shown in the lower part of fig. 5.13b. As it can be seen, due to the periodic reappearance of maxima in eq. 5.35 at a frequency of $n\pi$, the measured intermode beat interferogram at ν_{rt} has a strong frequency component at twice the carrier frequency ω_0 . The generated intermode beat interferogram of a FM-signal has a carrier wave of $2\omega_0$. This is illustrated in fig. 5.13b. Since the phase change is only π , the generated signal at point p_1 and p_2 are almost equal. The same goes for p_3 and p_4 . This results in a frequency doubling of the carrier wave. This is however only the case for a perfectly non distorted discriminator. Since the discriminator is a cosine wave, there are harmonics which are generated, and the spectrum of the intermode beat interferogram features all possible combinations of the carrier wave frequencies. To illustrate this behavior further, we conducted some simulations on a FM-signal and compared it to the intermode beat spectra of the TOPTICA femto-second laser source. The top of fig. 5.14a shows the intermode beat spectrum and intensity spectrum of a perfect FM-signal over the whole sampling bandwidth of the simulation. The strongest signal is found around twice the optical carrier wave $2\omega_c$. The intermode beat spectrum signal is the weakest around the optical carrier wave ω_c (though not zero). To illustrate this, the bottom of fig. 5.14a shows the normalized intermode beat spectrum and the intensity spectrum around the fundamental optical carrier frequency ω_c . Comparing these results to the intermode beat spectrum of the TOPTICA femto-second laser source shown in fig. 5.14b, the difference is well visible. There are no harmonic components generated for a fundamentally mode-locked laser.

Intermode beat interferogram of an unlocked laser with varying phases

Fig. 5.15a and b show the simulation of an intermode beat interferogram of an unlocked laser with random varying phases. This corresponds to the case in which the resolution bandwidth of the spectrum analyzer is too low to measure the dispersion of the modes. Even when choosing modes that have amplitudes given by a frequency-modulated laser, assuming phases that would experience random diffusion on a short time compared to

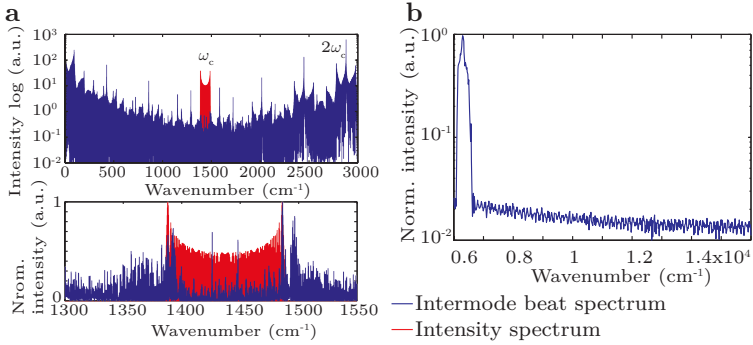


Fig. 5.14: Intermode beat spectrum harmonic frequencies. **a** Intermode beat spectrum simulation of a FM-source. The quadratic dependence on the acquisition has been omitted in the simulation not to generate higher order terms. **b** Measured intermode beat spectrum of the TOPTICA femto-second laser over the whole range. The data has been corrected for the nonlinear response of the spectrum analyzer. Reprint from [229].

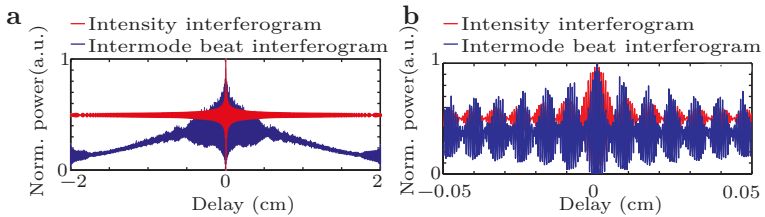


Fig. 5.15: Intermode beat interferogram random varying phases. **b** and **c** Simulation of an intermode beat interferogram and intensity interferogram for a laser with varying phase configuration with time. The mode spacing is 0.25 cm^{-1} .

the integration time. The interferogram is also qualitatively completely different from the one observed for a fundamentally mode-locked laser and a FM mode-locked laser.

5.8 Frequency-comb operation of broadband quantum cascade lasers

The strong third order nonlinearity $\chi^{(3)}$ (see sec. 2.5) in a QCL in combination with the low GVD in a broadband QCL (see sec. 2.4) leads to an efficient locking of the beat frequencies. This combination of four-wave mixing based mode proliferations with quantum cascade laser based gain leads to a phase relation similar to the one of a FM-laser. The section presents the findings of a QCL comb based on a heterogeneous active region composed of 3 substacks. The laser chips are delivered by Alpes Lasers. The comb center carrier wavelength is at $7 \mu\text{m}$. We identify a narrow drive current range where intermode beat linewidths as narrow as $f < 10 \text{ Hz}$ are measured. We find comb bandwidths of $\frac{\Delta\lambda}{\lambda} = 4.4\%$ with $\leq 200 \text{ Hz}$ intermode stability. Furthermore, the intermode beat can be pulled by RF-injection over a frequency range of 65 kHz .

The total output power of the device as a function of current at -20°C is shown in fig. 5.16a. To illustrate the potential of this laser chip when mounted for efficient heat extraction, fig. 5.16b shows the LIV characteristics in continuous-wave operation of a HR-back coated 4.5 mm long device which is mounted epi-side down on a diamond-submount. The temperature is controlled by a thermistor close the chip. Output

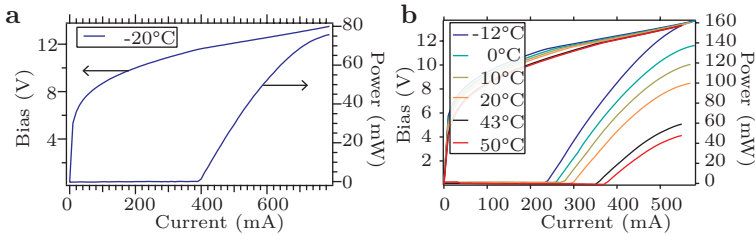


Fig. 5.16: LIVs and intermode beat. **a** Light intensity - current - voltage characteristic at -20°C . The laser is delivered by Alpes Lasers. The measurements are carried out at ETH. Data published in [229]. **b** Light intensity - current - voltage at different temperatures of an epi-down mounted QCL on a diamond-submount. The laser chip is delivered by Alpes Lasers. The epi-down mounting and characterization is done at ETH. **c** Narrow intermode beat, with a full-width at half-maximum of $< 10 \text{ Hz}$ at the onset of the multi-mode emission. The resolution bandwidth of the spectrum analyzer is set to 10 Hz .

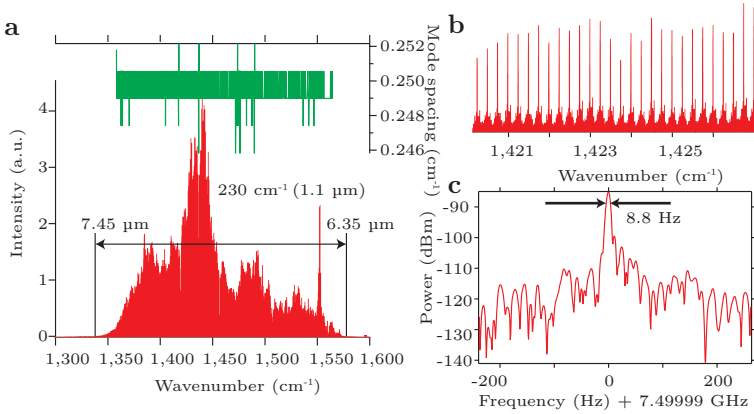


Fig. 5.17: High resolution (0.0026 cm^{-1}) Fourier transform infrared spectrometer spectra and measured mode spacing at a current of 740 mA at -20°C . Reprint from [229]

powers of 40 mW in continuous-wave operation at 50°C are reached. The characteristic temperature ($J_{\text{th}} = J_0 \exp(T/T_0)$) of the laser is $T_0 = 168 \text{ K}$ for pulsed operation. For continuous-wave operation, $T_0 = 110 \text{ K}$ for the epi-side up mounted laser, whereas $T_0 = 135 \text{ K}$ for the epi-side down mounted device.

The laser spectra displayed in fig. 5.17a were measured using a high-resolution Fourier transform infrared spectrometer and show a single set of longitudinal modes extending over $1.1 \mu\text{m}$, with no measurable dispersion within the resolution (0.0026 cm^{-1} , 78 MHz) of the spectrometer over the whole dynamic range. All instabilities related to multiple transverse modes can be completely neglected. Fig. 5.17b shows a section of the measured high-resolution spectra. It illustrates the regular peaks of the modes.

The device switches to multi-mode operation at $I = 460 \text{ mA}$, shortly above threshold ($I_{\text{th}} = 400 \text{ mA}$). The spectrum, which is initially spread over $\Delta\omega = 40 \text{ cm}^{-1}$, broadens progressively to $\Delta\omega = 230 \text{ cm}^{-1}$ at the maximum current. To investigate to what extent the modes are coupled, we first measure the intermode beat using the fast quantum-well infrared photodetector, see fig. 5.9. Uncoupled modes (such as those originating from two free-running lasers driven in a similar way to our device) would generate a spectrum with a 5–10 MHz linewidth [309]. In contrast, as shown in fig. 5.17c, such a measurement performed just above the onset of multi-mode operation shows a linewidth with a full-width at half-maximum of only $\Delta\nu = 8.8 \text{ Hz}$. For this current, the spectrum is already $\Delta\omega \approx 15 \text{ cm}^{-1}$ wide and contains 60 modes. This very narrow

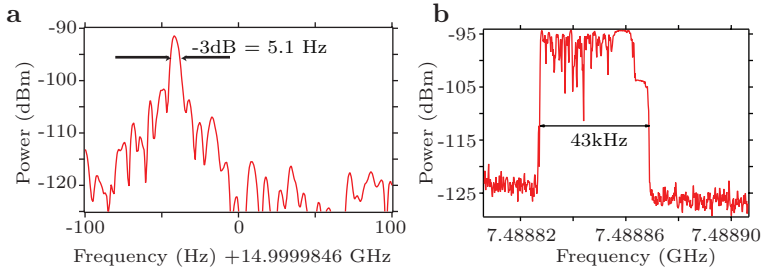


Fig. 5.18: Narrow intermode beat measurements. **a** At twice the round-trip frequency. **b** At the round-trip frequency. The data was acquired over 1 hour with max hold on to illustrate the drift.

intermode beat is observed over the current range $I \approx 460\text{--}480\text{ mA}$. At higher temperatures (13°C), this regime is more dominant and the comb spans up to 60 cm^{-1} (240 modes) with an intermode beat linewidth of 200 Hz .

Even though our detector has a cut-off frequency of about 12 GHz , we were able to measure the intermode beat at the first harmonic of the intermode beat. Fig. 5.18a shows the measurement. The filter-type for this measurement was set to FFT, which allowed us to measure down to a RBW of 5 Hz . The sweep-time is 0.8 s . The high quality of the intermode beat spectrum is also observed at twice the round-trip frequency. We measure a FWHM of only 5 Hz , which is again limited by the RBW of our instrument. We can however not make any safe statement comparing the average power with the measured power at 15 GHz , due to the cut-off of the detector.

Those narrow intermode beat measurements reflect also the stability of our setup. The width of the measured intermode beat strongly depends on the integration time and setup alignment. The QCL-comb is very sensitive to any optical feedback, current noise and slow temperature drifts. Fig. 5.18b shows a measurement taken to illustrate this point. The spectrum analyzer detector was set to max-hold. The acquisition time was set to $\approx 1\text{ h}$. The narrow intermode beat actually drifts by about 43 kHz due to feedback and temperature drifts in this specific measurement.

At a current of $\geq 480\text{ mA}$, the intermode beat abruptly becomes wider to $\Delta\nu \approx 48\text{ kHz}$. When the current is increased to 500 mA , the spectrum spans $\sim 100\text{ cm}^{-1}$ and the intermode beat widens to $\Delta\nu < 250\text{ kHz}$. Above 510 mA , the single narrow intermode beat splits into two distinct broadened peaks spaced by 14 MHz . A selected set of spectra indicating the power per mode (between 1 mW and $3\text{ }\mu\text{W}$) is displayed

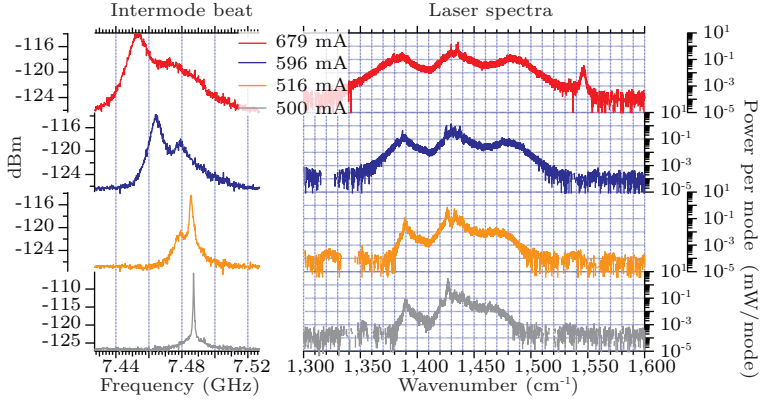


Fig. 5.19: Intermode beat measurements and corresponding laser spectra at different currents at $-20\text{ }^{\circ}\text{C}$. Data published in [229].

on the right side of fig. 5.19. The figure illustrates the progressive broadening of the laser bandwidth with the accompanied increase of the intermode beat linewidth from the kHz to the MHz regime. The abrupt change in intermode beat linewidth from the Hz to the kHz regime is also reflected in the amplitude noise spectra shown in 5.20. The noise is measured by focusing the QCL output directly on the QWIP. The noise floor is measured while operating the quantum cascade laser below threshold. In the narrow intermode beat regime of a few hundred Hz, we do not observe any additional amplitude noise compared to the measured noise floor. This is illustrated in fig. 5.20a. However, as shown in fig. 5.20b, the abrupt change of the intermode beat linewidth to tens of kHz is accompanied by a sudden increase in the amplitude noise. The additional phase noise translates into amplitude noise. The gradual shift from the kHz intermode beat regime to the MHz regime at higher injection currents is also reflected in the amplitude noise spectra. At higher currents, the amplitude noise in the kHz region is lower whereas the MHz region clearly has stronger noise components.

To get further insight into the respective phases and coherence properties of the modes, we performed the intermode beat spectroscopy as it was discussed in sec. 5.7.2. Fig. 5.21a shows two successive scans of the intermode beat interferogram $I(\nu_{rt}, \tau)$ acquired with a resolution-bandwidth of 100 kHz at the round-trip frequency, measured at 90 min interval at an injection current of 490 mA. They are compared to the zero frequency component $I(0, \tau)$. Random varying phases would generate an intermode

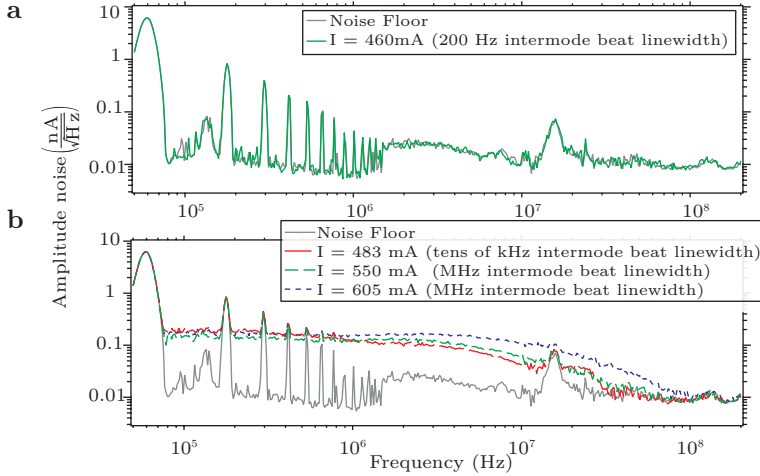


Fig. 5.20: Amplitude noise of the broadband quantum cascade laser at different bias currents at -20°C . **a** Amplitude noise for injection currents with intermode beat linewidths in the Hz range. **b** Amplitude noise for injection currents with increased intermode beat linewidths (kHz-MHz). Data published in [229]

beat interferogram $I(\nu_{rt}, \tau)$ roughly proportional to the zero frequency component around zero time delay (see fig. 5.15). In contrast, the measured signal $I(\nu_{rt}, \tau)$ shows long-term stability with a minimum at zero time delay, proving a well-defined phase relation between the modes. In addition to this, the device is not fundamentally mode-locked producing single pulses, since the measurement and the simulation for a conventional mode-locked laser shown in fig. 5.11 also show a maximum at zero-delay difference.

The phase relation cannot be easily inferred from the measurement of $I(\nu_{rt}, \tau)$ however. To help its interpretation, we compare it to the one predicted for a purely frequency-modulated signal in fig. 5.21b. The phases are such that the amplitude modulation of the signal is strongly damped at the zero path difference, for $\tau = 0$, as it would be for a frequency-modulated laser. In general, the comparison clearly emphasizes the frequency modulation characteristics of the output of the laser, as expected by the short lifetime of the excited state. A minimum of the intermode beat is always observed for $\tau = 0$ over all injected currents, proving that the device never produces single pulses. The intensity of the modulation of the laser output is never greater than

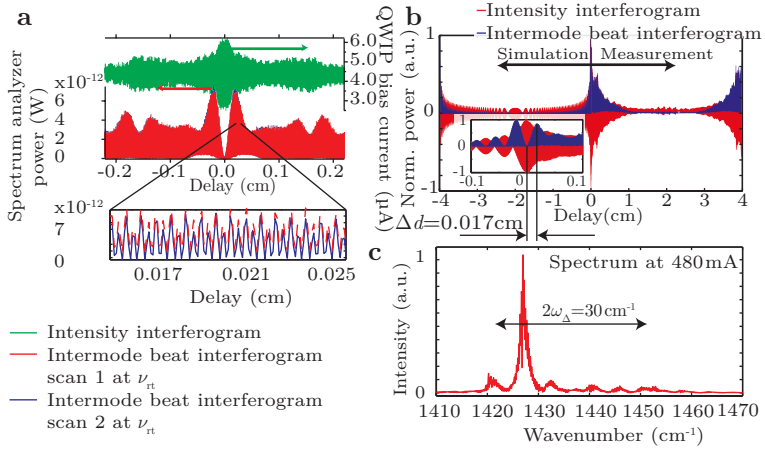


Fig. 5.21: Intermode beat spectroscopy. **a** Intensity interferogram and intermode beat interferograms measured in two successive scans separated by 90 min, at 490 mA. The resolution bandwidth is 100 kHz. **b** Comparison of the measured intermode beat interferogram at 480 mA with the intermode beat interferogram simulations of a perfectly frequency-modulated (FM) signal. Inset, magnified view of region at zero delay. Data published in [229].

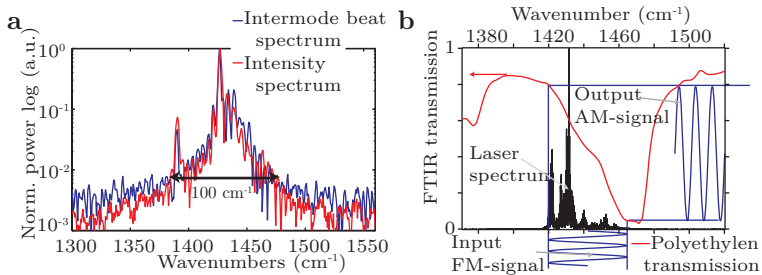


Fig. 5.22: Intermode beat spectroscopy. **a** Comparison of the intermode beat spectrum, $\mathcal{J}(\nu_{rt}, \omega)$, and the intensity spectrum, $\mathcal{J}(0, \omega)$, at an injection current of 500 mA. Data published in [229]. **b** Optical discriminator by a sheet of polyethylene that features a wavelength dependent absorption.

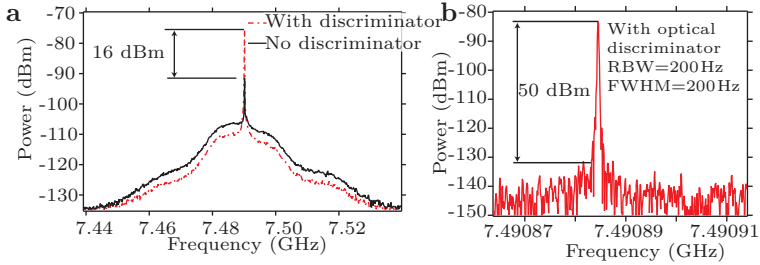


Fig. 5.23: Polyethylene discriminator. **a** Intermode beat in the kHz range with and without optical discriminator. **b** Intermode beat in the Hz range after putting an optical discriminator.

2%, indicating a mostly constant amplitude.

The inset of fig. 5.21b furthermore shows the position of the measured maximum of the intermode beat interferogram. The maximum is found at a delay of $\Delta d = 0.017$ cm. Using eq. 5.38, we can estimate the signal excursion assuming a perfectly FM-output. We get a maximum frequency excursion in wavenumber of $\omega_{\Delta} = 15 \text{ cm}^{-1}$ which corresponds to a total signal bandwidth of approximately 30 cm^{-1} . The spectral coverage at this current of 480 mA is about 40 cm^{-1} . The spectrum at 480 mA injection current and the calculated signal bandwidth is compared in fig. 5.21c. We do not expect those two bandwidths to be exactly equal, as the output does not have a perfect FM amplitude and phase configuration. When increasing the current of the QCL, the FWHM of the intermode beat becomes wider. But also the amplitude of the intermode beat increases, indicating stronger modulation. Even though the spectrum of the laser broadens, the measured frequency-excursion assuming a perfect FM-output decreases. At 490 mA, the measured bandwidth is 25 cm^{-1} . At 500 mA, the measured FM-signal excursion decreases to 18.6 cm^{-1} . We attribute this to the increased phase noise, the increased intermode beat and the altered amplitude configuration that comes along when increasing the current.

The intermode beat spectrum $\mathcal{I}(\nu_{rt}, \omega)$ and the intensity spectrum $\mathcal{I}(0, \omega)$ are compared in fig. 5.22a, showing that the entire laser spectrum is contributing to the intermode beat. Regardless of the kHz intermode beat linewidth we have a comb-like spectrum, since the mode spacing does not fluctuate more than the chosen resolution bandwidth of the spectrum analyzer over the whole laser spectrum.

To further confirm the frequency-modulated nature of the laser, we put a sheet of polyethylene that features a wavelength dependent absorption between the laser

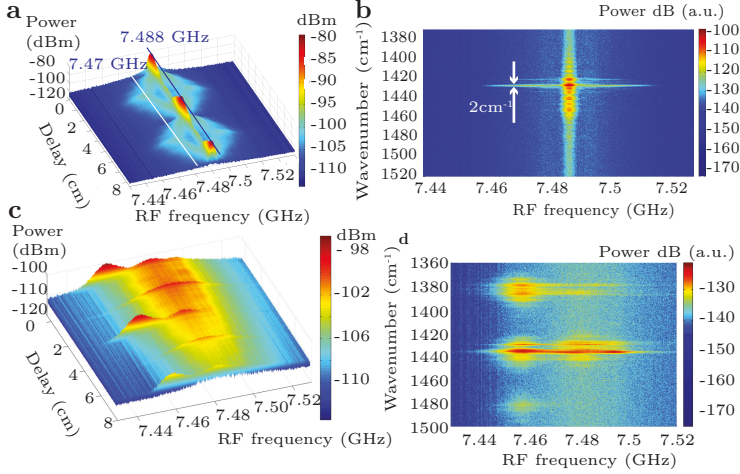


Fig. 5.24: Intermode beat spectroscopy. **a** Intermode beat interferogram at a injection current of ($I = 480$ mA). The radio-frequency (RF) span is 100 MHz with a resolution bandwidth of 2 MHz. **b** Corresponding intermode beat spectrum. **c** Intermode beat interferogram at a high injection current ($I = 679$ mA). The radio-frequency (RF) span is 100 MHz with a resolution bandwidth of 2 MHz. **d** Corresponding intermode beat spectrum. Data published in [229].

and the detector. This sheet acts as an optical discriminator that can convert the frequency modulation of the laser output to an amplitude modulation signal. This is illustrated in fig. 5.22b. As expected from a frequency-modulated signal, we find that the amplitude of the intermode beat at the detector increases. This amplification factor was measured to be 10–18. Fig. 5.23a shows the 16 dBm increase we measure on the spectrum analyzer when the device operates in the kHz intermode beat regime. Only the part of the modes which contribute to the narrow kHz regime intermode beat are amplified. This confirms that locking has a strong FM-component. The modes which generate the noise-floor at -105 dBm featuring a width of about 60 MHz at -130 dBm are not amplified but attenuated. This infers either that the modes are unlocked or there is a weak coupling between the modes which is of the AM-type. Fig. 5.23b shows the measured intermode beat in the Hz regime when employing the discriminator. We measure a SNR of 50 dB.

The measurement of the whole RF spectrum around ν_{rt} as a function of delay τ

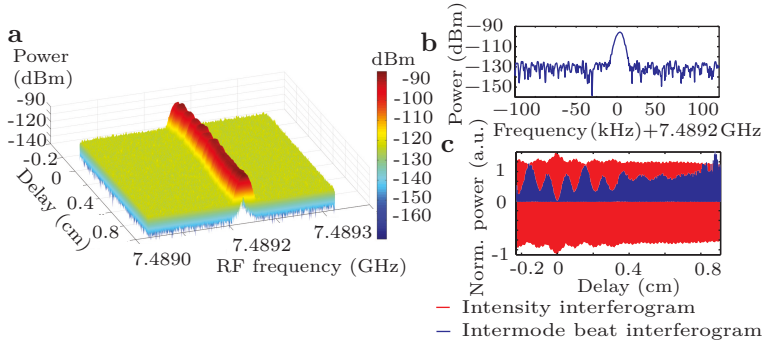


Fig. 5.25: Intermode beat interferogram of a QCL comb featuring Hz intermode beat linewidths. **a** Full intermode beat interferogram. **b** Sample of the intermode beat at sampling position 12 of the intermode beat interferogram. **c** Comparison of the intermode beat and intensity interferogram.

yields important information on the mechanisms that destabilize the comb. Fig. 5.24a shows an example of an acquired intermode beat interferogram over the whole span of the spectrum analyzer at a current of 480 mA with a resolution-bandwidth of 100 kHz. The noise floor already visible in fig. 5.23a features a qualitatively different intermode beat interferogram than the intermode beat at ν_{rt} . It has a maximum at $T/2$, which is a feature of counter-propagating pulses, as in a harmonically mode-locked laser. The intermode beat spectrum $\mathcal{J}(\nu, \omega)$ of fig. 5.24a is shown in fig. 5.24b. The intermode beat spectrum reveals that only a small portion ($\sim 2 \text{ cm}^{-1}$) of the modes actually contribute to the noise-floor. The modes are located at the center of the laser spectrum.

Another example of an intermode beat spectroscopy of the whole RF spectrum is shown in fig. 5.24c at a high current ($I = 679 \text{ mA}$) where the intermode beat has now two peaks and a wide RF spectrum. The different behaviour of the peak at $\nu = 7.4587 \text{ GHz}$ and at $\nu = 7.4840 \text{ GHz}$ are evident from the interferogram shown in fig. 5.24c; the Fourier transform shown in fig. 5.24d of this characteristics shows that the oscillation at $\nu = 7.4840 \text{ GHz}$ involves mostly peaks at the centre of the spectrum (around $\omega = 1,430 \text{ cm}^{-1}$) while the oscillation at $\nu = 7.4587 \text{ GHz}$ locks modes over a wide frequency range from $\omega = 1,500 \text{ cm}^{-1}$ to $\omega = 1,360 \text{ cm}^{-1}$.

The intermode beat spectroscopy in the case where the intermode has a FWHM of a few hundred hertz is a bit more challenging, due to the fact that the comb is very sensitive to any optical feedback. This is especially problematic in the case of

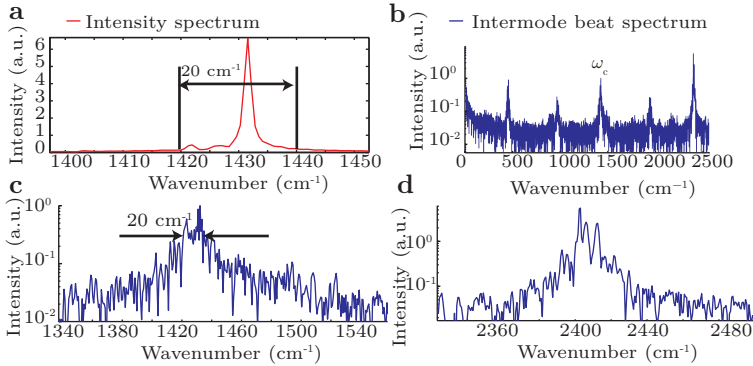


Fig. 5.26: Intensity and intermode beat spectrum in the Hz regime. **a** Intensity spectrum. **b** Intermode beat spectrum showing the whole acquired spectrum. **c** Intermode beat spectrum at the fundamental frequency of the laser. **d** Intermode beat spectrum at 2400 cm⁻¹.

the intermode beat spectroscopy setup, due to the perfectly collimated beam and the moving mirror altering the feedback mechanism drastically during a scan. Regardless of that, we were able to measure an intermode beat interferogram with a delay of 1 cm. The full intermode beat interferogram is shown in fig. 5.25a. The span of the spectrum analyzer could be reduced from 100 MHz from previous intermode beat interferograms to 200 kHz in the Hz case. It was not possible to decrease the span further, due to the temperature drifts. Furthermore, the RBW is decreased to 5 kHz, giving a better SNR ratio in the span. Fig. 5.25b shows a single spectrum analyzer scan at the sampling position 12 of the intermode beat interferogram. Fig. 5.25c shows the intensity interferogram together with the intermode beat interferogram. As it can be seen, the FM-nature with the minimum at zero delay is also present, proving that the device is not fundamentally mode-locked.

The spectrum of the laser emitting in the Hz range for this case is shown in fig. 5.26a. As it can be seen, the spectrum covers roughly 20 cm⁻¹. In this case, there is a strong single peak present in the spectrum. The intermode beat spectrum over the whole bandwidth ω is shown in fig. 5.26b. The strong nonlinear response of the optical discriminator is visible and the spectrum resembles strongly the one of a perfectly FM-signal shown in fig. 5.14a. To calculate these intermode beat spectra, all intermode beat interferogram were corrected for the quadratic response. Fig. 5.26c shows the intermode beat spectrum at the fundamental carrier frequency. As it can be

seen, the width of the intermode beat spectrum also covers the 20 cm^{-1} , the shape is however different compared to the spectrum. As it was discussed beforehand, the intermode beat spectrum is given by the Fourier-transform of eq. 5.31. The intermode beat interferogram is proportional to the product of the neighbouring field intensities $a_k a_{k+1} (\cos(\omega_0 + \Delta\omega))\tau$. As we already noted, the spectrum has a single very strong peak. Due to the multiplication with weak neighbouring peaks, the spectrum is strongly altered and shows this flatter spectrum. Fig. 5.26d shows a zoom of the intermode beat spectrum at 2413 cm^{-1} . Simulations show that the intermode beat interferogram at twice the carrier frequency would probably gain another factor of roughly 5 compared to the signal at 2413 cm^{-1} , see fig. 5.14a. However, we can not see this frequency in our intermode beat spectrum due to sampling decisions which were taken at the point of the measurement.

To further characterize the comb, a heterodyne beat experiment between a comb-line and a single-mode distributed feedback quantum cascade laser was realized. The setup is illustrated in fig. 5.27a. Fig. 5.27b shows the spectra of the single-mode quantum cascade laser alongside the comb spectra covering 60 cm^{-1} featuring an inter-mode beat linewidth of $\leq 200\text{ Hz}$.

Fig. 5.28a shows the corresponding heterodyne beat signal between the QCL comb and the single-mode DFB QCL. A narrow linewidth of 1.3 MHz is measured, which simply reflects the temperature and current stability of our setup. The increased phase-noise reflected by the kHz intermode beat directly translates into a broader linewidth of about 20 MHz in comb-like spectra.

The measurements show that the low GVD, as well as the existence of non-linearities, tend to lock the modes together. This locking can also be enhanced through RF-injection. Such injection locking has been already successfully applied to terahertz quantum cascade laser, enabling the demonstration of pulsed mode-locking operation. In our experiment, 11 dBm of RF power is injected via a bias-tee close to the round-trip frequency of 7.5 GHz with an estimated injection loss of -34.5 dB . The direct current is set to 494 mA . While sweeping the RF frequency we measure the heterodyne beat of one comb-like line and the single-mode quantum cascade laser, as illustrated in fig. 5.29a. Fig. 5.29a shows the change in the heterodyne beat position and proves that we are able to actively change the mode-spacing. The inter-mode beat with RF-injection around resonance is shown in fig. 5.29b. Unlike previous attempts [310], it shows the expected collapse of the inter-mode beat at the round-trip frequency to the resolution of the spectrum analyzer. The round-trip frequency can be pulled over more than 65 kHz . There are approximately 167 modes between the peak of the laser and the mode beating with the single-mode quantum cascade laser. Changing the round-trip frequency by 65 kHz

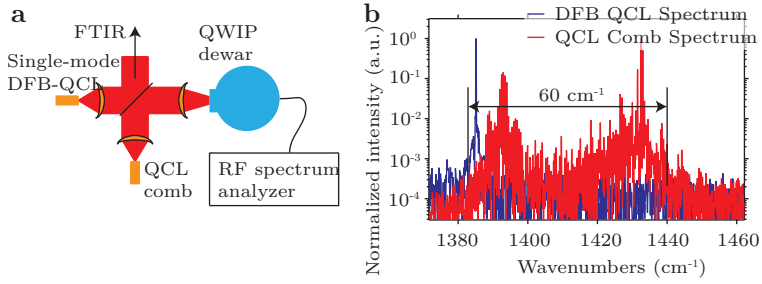


Fig. 5.27: Heterodyne beat experiment. **a** Setup of the heterodyne beat experiment between a QCL comb and a single-mode DFB-QCL. **b** Optical spectra of the QCL comb and DFB single-mode QCL. Data published in [229].

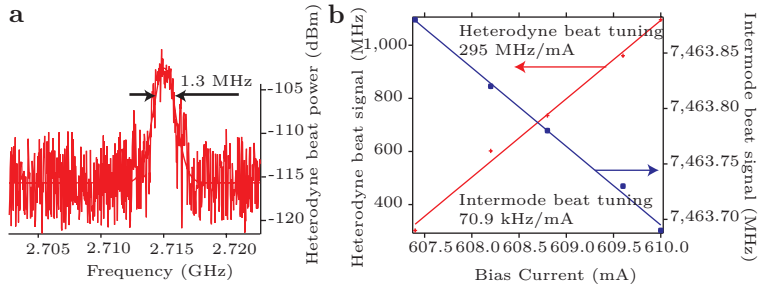


Fig. 5.28: Heterodyne beat experiment. **a** Heterodyne beat signal between the QCL comb and the single-mode DFB QCL. **b** Heterodyne and intermode beat position measurement while changing the injection current off the broadband quantum cascade laser. Data published in [229].

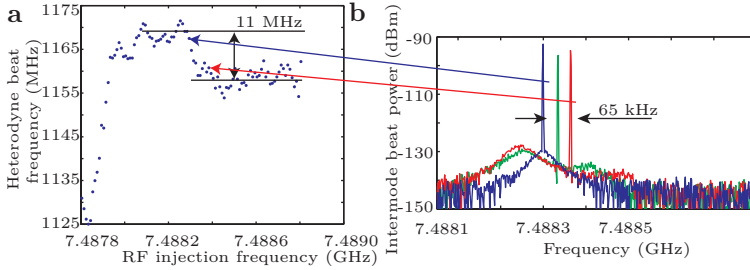


Fig. 5.29: Heterodyne beat experiment. **a** Heterodyne beat measurement of a comb-like line and a stable single-mode quantum cascade laser while sweeping the radio-frequency (RF) injection frequency around the cavity round-trip frequency. When sweeping across the resonance of the cavity round-trip, the heterodyne signal can be shifted in frequency by 11 MHz. **b** Measured intermode beat at three different characteristic injection frequencies at resonance. Data published in [229].

should therefore result in a change of $167 \times 65 \text{ kHz} = 10.9 \text{ MHz}$ in the heterodyne beat signal, which agrees with the measured 11 MHz. It should be noted, that the carrier frequency offset can be adjusted by the injected direct current, as illustrated in fig. 5.28b. Since the distributed-feedback quantum-cascade-laser emission wavelength is kept constant, the tuning coefficient of $\Delta\nu_{\text{het}} (\text{mA}) = 295 \text{ MHz/mA}$ in the heterodyne beat is a direct measurement of the possibility of setting the carrier envelope offset frequency. However, changing the injection current also slightly alters the repetition frequency. Therefore we also record the intermode beat during this current change. We measure an intermode beat tuning of 70.9 kHz/mA . This leads to a maximum frequency shift of the heterodyne signal of $\Delta\nu_{\text{het}} (\text{mA}) \leq 70.9 \text{ kHz/mA} \times 400 = 28.4 \text{ MHz/mA}$, where 400 is the number of comb lines in the case the comb-like spectra covers 100 cm^{-1} . This shows that the shift of the heterodyne beat signal is due to the change in the carrier frequency offset. Furthermore, the mode-spacing can be set through the RF-injection. Therefore it is possible to fully stabilize quantum cascade laser frequency combs [247]. However, as the RF injected power is increased to 26.6 dBm, the inter-mode beat interferogram resembles that of a fundamentally mode-locked laser, and, unlike at 11 dBm injection, the inter-mode beat spectrum clearly shows that only a small fraction of 18% of the modes contribute to the injection locked inter-mode beat. Fig. 5.30a shows the intermode beat under RF-injection with increasing RF-power. The locking of the comb can be enhanced when injecting a 10 dBm RF-signal. Further increasing the power shows a clear transient region. To further elaborate this transient region

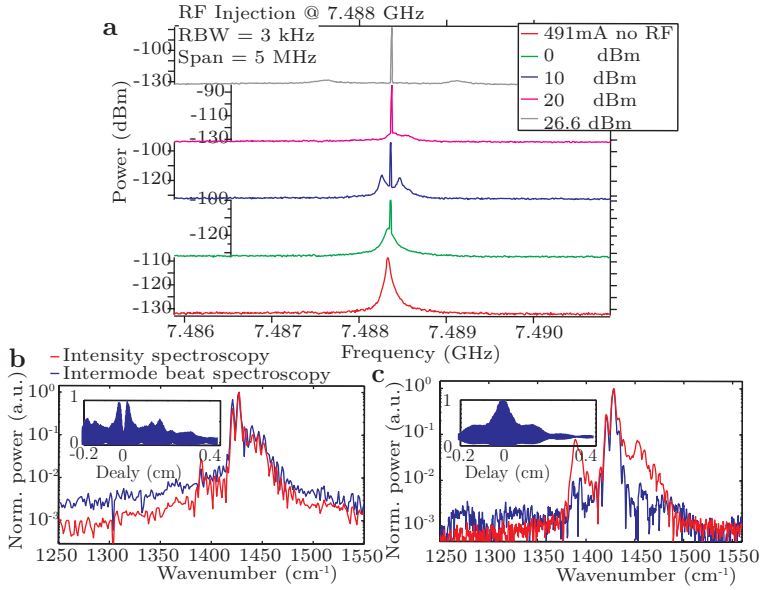


Fig. 5.30: **a** Intermode beat measurements with increasing RF-power. **b** Intermode beat spectrum at 10 dBm RF-injection power. Inset: Corresponding intermode beat interferogram taken with a resolution bandwidth of 5 kHz. **c** Intermode beat spectrum at 26.6 dBm RF-injection power. Inset: Corresponding intermode beat interferogram taken with a resolution bandwidth of 100 kHz. Reprint from [229]

we performed an intermode beat spectroscopy at the two points of interest, at 10 dBm shown in fig. 5.30b and at 26.6 dBm shown in fig. 5.30c. The insets of both figures show the measured intermode beat interferograms. At 10 dBm RF-injection power the frequency-modulated nature of the laser output is preserved, since the intermode beat interferogram shows a minimum at zero path difference. On the other hand, at 26.6 dBm RF-injection power, the intermode beat interferogram starts to resemble the one of a fundamentally mode-locked laser. But when comparing the intermode beat spectra to the intensity spectra for the two cases in fig. 5.30b and c, it becomes obvious that not all laser modes are locked at high RF-injection power.

Chapter 6

Conclusions and perspectives

The presented work concentrates on the study and development of broadband QCLs. This includes design, simulation, fabrication and coating of such devices for different applications. One of those applications is the use of broadband QCLs in an external-cavity configuration. The design of a single-stack bound-to-continuum design operated in continuous-wave at room-temperature is first presented. Tuning of 126 cm^{-1} is achieved, corresponding to a tuning of $\frac{\Delta\lambda}{\lambda} = 10.4\%$ around the center wavelength of $8.4\text{ }\mu\text{m}$. In a modified back-extraction external-cavity setup we measured an optical power of 20 mW . This result was further improved by tuning a dual-stack continuous-wave QCL over 200 cm^{-1} , featuring an optical output power of up to 140 mW at the gain center. The achieved tuning around the center-wavelength could be improved to $\frac{\Delta\lambda}{\lambda} = 18\%$ at a center wavelength of $8.7\text{ }\mu\text{m}$. This active region was also used to perform absorption spectroscopy of three different gases relevant for security applications. We demonstrated broadband spectroscopy over 280 cm^{-1} in pulsed operation using one single gain element. Next, a five-stack active region is presented emitting radiation between $7.6\text{--}11.4\text{ }\mu\text{m}$. We achieved a record tuning of 438 cm^{-1} . This corresponds to a tuning of $\frac{\Delta\lambda}{\lambda} = 40\%$. The measured peak output power was up to 1 W . Furthermore we demonstrated the usefulness of broadband QCLs as white-light sources. We replace the conventional glowbar in an FTIR with a broadband QCL run in pulsed-mode. Under similar conditions, we measure superior SNR of 15 dB compared to the glowbar.

The last chapter demonstrates a mid-IR optical frequency comb generator based on a QCL. We present a mid-IR QCL free-running optical frequency comb covering 60 cm^{-1} corresponding to 308 nm in wavelength. The center wavenumber is 1430 cm^{-1} , corresponding to $7\text{ }\mu\text{m}$ in wavelength. The total wavelength coverage is therefore $\frac{\Delta\lambda}{\lambda} = 4.4\%$. To characterize the laser further, we introduce the novel concept of

the intermode beat spectroscopy. We identify that the phase signature of the comb strongly resembles that of a frequency-modulated signal and is stable over time. The locking mechanism responsible for the formation of the frequency comb is found to be four-wave mixing. Key physical properties of materials used in quantum cascade lasers in frequency combs are therefore strong third-order optical nonlinearities and a low GVD. The effect of these optical nonlinearities and the GVD is discussed in chapter 2. Altogether, this system offers remarkable freedom of design, because it allows control over the electronic transitions, gain flatness, optical nonlinearities and dispersion through band structure engineering. The large bandwidth, in combination with independent control over the carrier frequency offset and the mode spacing, opens the way to metrological and sensing applications.

The field of QCLs, in particular broadband QCLs, is a very thrilling one, with a bright future ahead. After almost 20 years have passed since the invention of the QCL, the research is still strong. The demonstration of an optical frequency-comb QCL is particularly interesting for future research and applications. The prospect of realizing an all-solid state dual-comb spectrometer based on two QCL combs is very intriguing. One can dream of small and robust, field deployable broadband chemical sensors, capable of acquiring the entire spectrum nearly instantaneous. On the research side, there is a lot of work to be done to further understand the system. Investigation of the role of the GVD and its sign is necessary. Simulations of these QCL combs featuring a frequency-modulated like output are still needed to better understand the system. The bandwidth of mid-infrared quantum-cascade-laser frequency combs should be improved. A detailed understanding of the phase-locking mechanism and by appropriately engineering the GVD using waveguide and facet coatings will help to realize this. In the future, the mid-infrared quantum-cascade-laser frequency comb could become standard technology for broadband, compact, all-solid-state mid-infrared spectrometers.

Bibliography

- [1] T. R. Karl. „Modern Global Climate Change“. In: *Science* 302.5651 (Dec. 2003), pp. 1719–1723. ISSN: 0036-8075, 1095-9203. DOI: 10.1126/science.1090228.
- [2] David J. Frame and Dáithí A. Stone. „Assessment of the first consensus prediction on climate change“. en. In: *Nature Climate Change* (2012). ISSN: 1758-678X. DOI: 10.1038/nclimate1763.
- [3] Markus W Sigrist. *Air monitoring by spectroscopic techniques*. English. New York: Wiley, 1994. ISBN: 0471558753.
- [4] Frank K. Tittel, Dirk Richter, and Alan Fried. „Mid-Infrared Laser Applications in Spectroscopy“. In: *Solid-State Mid-Infrared Laser Sources*. Ed. by Irina T. Sorokina and Konstantin L. Vodopyanov. Vol. 89. Berlin, Heidelberg: Springer Berlin Heidelberg, 2003, pp. 458–529. ISBN: 978-3-540-00621-3.
- [5] Sumner P Davis, Mark C Abrams, and J. W Brault. *Fourier transform spectrometry*. English. San Diego: Academic Press, 2001. ISBN: 0120425106 9780120425105.
- [6] Robert John Bell. *Introductory Fourier transform spectroscopy*. English. New York: Academic Press, 1972. ISBN: 0120851504 9780120851508.
- [7] Omar Manzardo et al. „Miniaturized time-scanning Fourier transform spectrometer based on silicon technology“. In: *Optics Letters* 24.23 (Dec. 1999), pp. 1705–1707. DOI: 10.1364/OL.24.001705.
- [8] W. Demtröder. *Laser spectroscopy*. 4th ed. Berlin: Springer, 2008. ISBN: 9783540749523.
- [9] Markus W Sigrist. „Trace gas monitoring by laser photoacoustic spectroscopy and related techniques (plenary)“. In: *Review of Scientific Instruments* 74.1 (Jan. 2003), pp. 486–490. ISSN: 00346748. DOI: doi:10.1063/1.1512697.
- [10] „ANNUAL REVIEW AND FORECAST: Economic aftershocks keep laser markets unsettled“. In: *Laser Focus World* (Jan. 2012). ISSN: 1043-8092.
- [11] Jerome Faist et al. „Quantum Cascade Laser“. In: *Science* 264.5158 (Apr. 1994), pp. 553 –556. DOI: 10.1126/science.264.5158.553.
- [12] Richard Maulini. „Broadly tunable mid-infrared quantum cascade lasers for spectroscopic applications“. PhD thesis. Université de Neuchâtel, 2006.

- [13] Hans Sauren et al. „Resonant Stark spectrophone as an enhanced trace level ammonia concentration detector: design and performance at CO₂ laser frequencies“. In: *Applied Optics* 29.18 (June 1990), pp. 2679–2681. DOI: 10.1364/AO.29.002679.
- [14] S.M. Cristescu et al. „Laser-based systems for trace gas detection in life sciences“. In: *Applied Physics B* 92.3 (Aug. 2008), pp. 343–349. ISSN: 0946-2171, 1432-0649. DOI: 10.1007/s00340-008-3127-y.
- [15] D.D. Nelson et al. „Sub-part-per-billion detection of nitric oxide in air using a thermoelectrically cooled mid-infrared quantum cascade laser spectrometer“. In: *Applied Physics B: Lasers and Optics* 75.2-3 (Sept. 2002), pp. 343–350. ISSN: 0946-2171, 1432-0649. DOI: 10.1007/s00340-002-0979-4.
- [16] Raed A Dweik, ed. *Journal of Breath Research Special issue on exhaled breath analysis: from sensors to devices and applications*. Vol. 5. 3. IOP Publishing, Sept. 2011.
- [17] H. Dahnke et al. „Real-time monitoring of ethane in human breath using mid-infrared cavity leak-out spectroscopy“. In: *Applied Physics B: Lasers and Optics* 72.8 (2001), pp. 971–975. ISSN: 0946-2171. DOI: 10.1007/s003400100609.
- [18] K.D. Skeldon et al. „Application of laser spectroscopy for measurement of exhaled ethane in patients with lung cancer“. In: *Respiratory Medicine* 100.2 (Feb. 2006), pp. 300–306. ISSN: 09546111. DOI: 10.1016/j.rmed.2005.05.006.
- [19] Matthew R McCurdy et al. „Recent advances of laser-spectroscopy-based techniques for applications in breath analysis“. In: *Journal of Breath Research* 1.1 (Sept. 2007), p. 014001. ISSN: 1752-7155, 1752-7163. DOI: 10.1088/1752-7155/1/1/014001.
- [20] Chuji Wang and Anand B Surampudi. „An acetone breath analyzer using cavity ringdown spectroscopy: an initial test with human subjects under various situations“. In: *Measurement Science and Technology* 19.10 (Oct. 2008), p. 105604. ISSN: 0957-0233, 1361-6501. DOI: 10.1088/0957-0233/19/10/105604.
- [21] Richard Bartlome and Markus W. Sigrist. „Laser-based human breath analysis: D/H isotope ratio increase following heavy water intake“. In: *Optics Letters* 34.7 (Apr. 2009), pp. 866–868. DOI: 10.1364/OL.34.000866.
- [22] Michael Phillips et al. „Volatile biomarkers in the breath of women with breast cancer“. In: *Journal of Breath Research* 4.2 (June 2010), p. 026003. ISSN: 1752-7155, 1752-7163. DOI: 10.1088/1752-7155/4/2/026003.
- [23] R. Martini et al. „High-speed modulation and free-space optical audio/video transmission using quantum cascade lasers“. English. In: *Electronics Letters* 37.3 (Feb. 2001), pp. 191–193. ISSN: 0013-5194. DOI: 10.1049/el:20010102.
- [24] S. Blaser et al. „Free-space optical data link using Peltier-cooled quantum cascade laser“. In: *Electronics Letters* 37.12 (2001), p. 778. ISSN: 00135194. DOI: 10.1049/el:20010504.

- [25] Christoph Walther et al. „Quantum cascade lasers operating from 1.2 to 1.6 THz“. In: *Applied Physics Letters* 91.13 (Sept. 2007), ISSN: 00036951. DOI: doi: 10.1063/1.2793177.
- [26] G. Scalari et al. „THz and sub-THz quantum cascade lasers“. en. In: *Laser & Photonics Reviews* 3.1-2 (2009), 45–66. ISSN: 1863-8899. DOI: 10.1002/lpor. 200810030.
- [27] Matthias Beck et al. „Continuous Wave Operation of a Mid-Infrared Semiconductor Laser at Room Temperature“. In: *Science* 295.5553 (Jan. 2002), pp. 301–305. DOI: 10.1126/science.1066408.
- [28] Y. Bai et al. „Room temperature continuous wave operation of quantum cascade lasers with 12.5% wall plug efficiency“. In: *Applied Physics Letters* 93.2 (July 2008), ISSN: 00036951. DOI: doi:10.1063/1.2957673.
- [29] A. Lyakh et al. „3 W continuous-wave room temperature single-facet emission from quantum cascade lasers based on nonresonant extraction design approach“. In: *Applied Physics Letters* 95.14 (Oct. 2009), ISSN: 00036951. DOI: doi:10.1063/1.3238263.
- [30] Richard Maulini et al. „High power thermoelectrically cooled and uncooled quantum cascade lasers with optimized reflectivity facet coatings“. In: *Applied Physics Letters* 95.15 (Oct. 2009), ISSN: 00036951. DOI: doi:10.1063/1.3246799.
- [31] Arkadiy Lyakh et al. „Multiwatt long wavelength quantum cascade lasers based on high strain composition with 70% injection efficiency“. In: *Optics Express* 20.22 (Oct. 2012), p. 24272. ISSN: 1094-4087. DOI: 10.1364/OE.20.024272.
- [32] Richard Maulini et al. „7.1 μm quantum cascade lasers with 19% wall-plug efficiency at room temperature“. In: *Optics Express* 19.18 (2011), pp. 17203–17211. DOI: 10.1364/OE.19.017203.
- [33] Y. Bai et al. „Room temperature quantum cascade lasers with 27% wall plug efficiency“. In: *Applied Physics Letters* 98.18 (2011), p. 181102. ISSN: 00036951. DOI: 10.1063/1.3586773.
- [34] Arkadiy Lyakh et al. „Tapered 4.7 μm quantum cascade lasers with highly strained active region composition delivering over 4.5 watts of continuous wave optical power“. In: *Optics Express* 20.4 (Feb. 2012), pp. 4382–4388. DOI: 10.1364/OE.20.004382.
- [35] L. Diehl et al. „High-power quantum cascade lasers grown by low-pressure metal organic vapor-phase epitaxy operating in continuous wave above 400 K“. In: *Applied Physics Letters* 88.20 (May 2006), ISSN: 00036951. DOI: doi:10.1063/1.2203964.
- [36] A. Wittmann et al. „Distributed-Feedback Quantum-Cascade Lasers at 9 μm Operating in Continuous Wave Up to 423 K“. In: *IEEE Photonics Technology Letters* 21.12 (June 2009), pp. 814–816. ISSN: 1041-1135. DOI: 10.1109/LPT.2009.2019117.

- [37] Y. Bai et al. „Optimizing facet coating of quantum cascade lasers for low power consumption“. In: *Journal of Applied Physics* 109.5 (2011), p. 053103. ISSN: 00218979. DOI: 10.1063/1.3553863.
- [38] B. Hinkov et al. „Singlemode quantum cascade lasers with power dissipation below 1W“. In: *Electronics Letters* 48.11 (2012), p. 646. ISSN: 00135194. DOI: 10.1049/el.2012.1204.
- [39] Q. Y. Lu et al. „2.4 W room temperature continuous wave operation of distributed feedback quantum cascade lasers“. In: *Applied Physics Letters* 98.18 (2011), p. 181106. ISSN: 00036951. DOI: 10.1063/1.3588412.
- [40] Mariano Troccoli et al. „Mid-infrared (7.4 μ m) quantum cascade laser amplifier for high power single-mode emission and improved beam quality“. In: *Applied Physics Letters* 80.22 (June 2002), pp. 4103–4105. ISSN: 00036951. DOI: doi: 10.1063/1.1479453.
- [41] Stefan Menzel et al. „Quantum cascade laser master-oscillator power-amplifier with 1.5 W output power at 300 K“. In: *Optics Express* 19.17 (2011), pp. 16229–16235. DOI: 10.1364/OE.19.016229.
- [42] A Bismuto et al. „Sb-free quantum cascade lasers in the 3–4 μ m spectral range“. In: *Semiconductor Science and Technology* 27.4 (Apr. 2012), p. 045013. ISSN: 0268-1242, 1361-6641. DOI: 10.1088/0268-1242/27/4/045013.
- [43] N. Bandyopadhyay et al. „Room temperature continuous wave operation of 3–3.2 μ m quantum cascade lasers“. In: *Applied Physics Letters* 101.24 (Dec. 2012), ISSN: 00036951. DOI: doi:10.1063/1.4769038.
- [44] N. Bandyopadhyay et al. „High power, continuous wave, room temperature operation of 3.4 μ m and 3.55 μ m InP-based quantum cascade lasers“. In: *Applied Physics Letters* 100.21 (May 2012), ISSN: 00036951. DOI: doi: 10.1063/1.4719110.
- [45] John U. White. „Long Optical Paths of Large Aperture“. In: *Journal of the Optical Society of America* 32.5 (May 1942), p. 285. ISSN: 0030-3941. DOI: 10.1364/JOSA.32.000285.
- [46] Donald R. Herriott and Harry J. Schulte. „Folded Optical Delay Lines“. In: *Applied Optics* 4.8 (Aug. 1965), p. 883. ISSN: 0003-6935, 1539-4522. DOI: 10.1364/AO.4.000883.
- [47] J. Barry McManus. „Paraxial matrix description of astigmatic and cylindrical mirror resonators with twisted axes for laser spectroscopy“. In: *Applied Optics* 46.4 (Feb. 2007), pp. 472–482. DOI: 10.1364/AO.46.000472.
- [48] J. B. McManus, P. L. Kebabian, and M. S. Zahniser. „Astigmatic mirror multipass absorption cells for long-path-length spectroscopy“. In: *Applied Optics* 34.18 (June 1995), pp. 3336–3348. DOI: 10.1364/AO.34.003336.

- [49] Mark S. Zahniser et al. „Measurement of Trace Gas Fluxes Using Tunable Diode Laser Spectroscopy [and Discussion]“. In: *Philosophical Transactions: Physical Sciences and Engineering* 351.1696 (May 1995). ArticleType: research-article / Issue Title: The Exchange of Trace Gases between Land and Atmosphere / Full publication date: May 16, 1995 / Copyright © 1995 The Royal Society, pp. 371–382. ISSN: 0962-8428.
- [50] A. A. Kosterev et al. „Quartz-enhanced photoacoustic spectroscopy“. In: *Optics Letters* 27.21 (Nov. 2002), pp. 1902–1904. DOI: 10.1364/OL.27.001902.
- [51] Matthew C. Stowe et al. „Direct frequency comb spectroscopy“. In: *Advances In Atomic, Molecular, and Optical Physics*. Vol. 55. Elsevier, 2008, pp. 1–60. ISBN: 9780123737106.
- [52] Angela Elia et al. „Photoacoustic Techniques for Trace Gas Sensing Based on Semiconductor Laser Sources“. In: *Sensors* 9.12 (Dec. 2009), pp. 9616–9628. ISSN: 1424-8220. DOI: 10.3390/s91209616.
- [53] András Miklós, Peter Hess, and Zoltán Bozóki. „Application of acoustic resonators in photoacoustic trace gas analysis and metrology“. In: *Review of Scientific Instruments* 72.4 (Apr. 2001), pp. 1937–1955. ISSN: 00346748. DOI: doi:10.1063/1.1353198.
- [54] Edwin L. Kerr and John G. Atwood. „The Laser Illuminated Absorptivity Spectrophone: A Method for Measurement of Weak Absorptivity in Gases at Laser Wavelengths“. In: *Applied Optics* 7.5 (May 1968), pp. 915–921. DOI: 10.1364/AO.7.000915.
- [55] L. B Kreuzer. „Ultralow Gas Concentration Infrared Absorption Spectroscopy“. In: *Journal of Applied Physics* 42.7 (June 1971), pp. 2934–2943. ISSN: 00218979. DOI: doi:10.1063/1.1660651.
- [56] Daniel Hofstetter et al. „Photoacoustic spectroscopy with quantum cascade distributed-feedback lasers“. In: *Optics Letters* 26.12 (June 2001), pp. 887–889. DOI: 10.1364/OL.26.000887.
- [57] A.A. Kosterev, Y.A. Bakhirkin, and F.K. Tittel. „Ultrasensitive gas detection by quartz-enhanced photoacoustic spectroscopy in the fundamental molecular absorption bands region“. In: *Applied Physics B* 80.1 (Sept. 2004), pp. 133–138. ISSN: 0946-2171, 1432-0649. DOI: 10.1007/s00340-004-1619-y.
- [58] Anatoliy A Kosterev et al. „Applications of quartz tuning forks in spectroscopic gas sensing“. In: *Review of Scientific Instruments* 76.4 (Mar. 2005), p. 043105. ISSN: 00346748. DOI: doi:10.1063/1.1884196.
- [59] Rafal Lewicki et al. „QEPAS based detection of broadband absorbing molecules using a widely tunable, cw quantum cascade laser at 8.4 μm “. In: *Optics Express* 15.12 (June 2007), pp. 7357–7366. DOI: 10.1364/OE.15.007357.
- [60] Yufei Ma et al. „QEPAS based ppb-level detection of CO and N₂O using a high power CW DFB-QCL“. In: *Optics Express* 21.1 (Jan. 2013), pp. 1008–1019. DOI: 10.1364/OE.21.001008.

- [61] Adela Marian et al. „United Time-Frequency Spectroscopy for Dynamics and Global Structure“. en. In: *Science* 306.5704 (Dec. 2004), pp. 2063–2068. ISSN: 0036-8075, 1095-9203. DOI: 10.1126/science.1105660.
- [62] V. Gerginov et al. „High-resolution spectroscopy with a femtosecond laser frequency comb“. In: *Optics Letters* 30.13 (2005), p. 1734. ISSN: 0146-9592, 1539-4794. DOI: 10.1364/OL.30.001734.
- [63] Michael J. Thorpe et al. „Broadband Cavity Ringdown Spectroscopy for Sensitive and Rapid Molecular Detection“. en. In: *Science* 311.5767 (Mar. 2006), pp. 1595–1599. ISSN: 0036-8075, 1095-9203. DOI: 10.1126/science.1123921.
- [64] Scott A. Diddams, Leo Hollberg, and Vela Mbele. „Molecular fingerprinting with the resolved modes of a femtosecond laser frequency comb“. en. In: *Nature* 445.7128 (Feb. 2007), pp. 627–630. ISSN: 0028-0836. DOI: 10.1038/nature05524.
- [65] Christoph Gohle et al. „Frequency Comb Vernier Spectroscopy for Broadband, High-Resolution, High-Sensitivity Absorption and Dispersion Spectra“. In: *Physical Review Letters* 99.26 (Dec. 2007). ISSN: 0031-9007, 1079-7114. DOI: 10.1103/PhysRevLett.99.263902.
- [66] Th. Udem et al. „Absolute Optical Frequency Measurement of the Cesium D₂-{1} Line with a Mode-Locked Laser“. In: *Physical Review Letters* 82.18 (May 1999), pp. 3568–3571. DOI: 10.1103/PhysRevLett.82.3568.
- [67] Th. Udem et al. „Accurate measurement of large optical frequency differences with a mode-locked laser“. In: *Optics Letters* 24.13 (July 1999), pp. 881–883. DOI: 10.1364/OL.24.000881.
- [68] Scott A. Diddams et al. „Direct Link between Microwave and Optical Frequencies with a 300 THz Femtosecond Laser Comb“. In: *Physical Review Letters* 84.22 (May 2000), pp. 5102–5105. DOI: 10.1103/PhysRevLett.84.5102.
- [69] David J. Jones et al. „Carrier-Envelope Phase Control of Femtosecond Mode-Locked Lasers and Direct Optical Frequency Synthesis“. en. In: *Science* 288.5466 (Apr. 2000), pp. 635–639. ISSN: 0036-8075, 1095-9203. DOI: 10.1126/science.288.5466.635.
- [70] Th. Udem, R. Holzwarth, and T. W. Hänsch. „Optical frequency metrology“. In: *Nature* 416.6877 (2002), pp. 233–237. ISSN: 0028-0836. DOI: 10.1038/416233a.
- [71] Norman Ramsey. *Molecular beams*. English. Oxford; New York: Clarendon Press ; Oxford University Press, 1985. ISBN: 0198520212 9780198520214.
- [72] M. M. Salour and C. Cohen-Tannoudji. „Observation of Ramsey’s Interference Fringes in the Profile of Doppler-Free Two-Photon Resonances“. In: *Physical Review Letters* 38.14 (Apr. 1977), pp. 757–760. DOI: 10.1103/PhysRevLett.38.757.
- [73] R. Teets, J. Eckstein, and T. W. Hänsch. „Coherent Two-Photon Excitation by Multiple Light Pulses“. In: *Physical Review Letters* 38.14 (Apr. 1977), pp. 760–764. DOI: 10.1103/PhysRevLett.38.760.

- [74] J. N. Eckstein, A. I. Ferguson, and T. W. Hänsch. „High-Resolution Two-Photon Spectroscopy with Picosecond Light Pulses“. In: *Physical Review Letters* 40.13 (Mar. 1978), pp. 847–850. DOI: 10.1103/PhysRevLett.40.847.
- [75] A. I. Ferguson, J. N. Eckstein, and T. W. Hänsch. „A subpicosecond dye laser directly pumped by a mode-locked argon laser“. In: *Journal of Applied Physics* 49.11 (Nov. 1978), pp. 5389–5391. ISSN: 00218979. DOI: doi : 10 . 1063 / 1 . 324509.
- [76] S. Harris and O. McDuff. „Theory of FM laser oscillation“. In: *Quantum Electronics, IEEE Journal of* 1.6 (Sept. 1965), pp. 245 –262. ISSN: 0018-9197. DOI: 10.1109/JQE.1965.1072231.
- [77] D. Kuizenga and A. Siegman. „FM-laser operation of the Nd:YAG laser“. In: *Quantum Electronics, IEEE Journal of* 6.11 (Nov. 1970), pp. 673 –677. ISSN: 0018-9197. DOI: 10.1109/JQE.1970.1076348.
- [78] T W Hänsch and N C Wong. „Two-Photon Spectroscopy with an FM Laser“. In: *Metrologia* 16.2 (Apr. 1980), pp. 101–104. ISSN: 0026-1394, 1681-7575. DOI: 10.1088/0026-1394/16/2/006.
- [79] W. Kaiser and C. G. B. Garrett. „Two-Photon Excitation in CaF₂: Eu²⁺“. In: *Physical Review Letters* 7.6 (1961), pp. 229–231. DOI: 10.1103/PhysRevLett.7.229.
- [80] Adela Marian et al. „Direct Frequency Comb Measurements of Absolute Optical Frequencies and Population Transfer Dynamics“. In: *Physical Review Letters* 95.2 (July 2005), p. 023001. DOI: 10.1103/PhysRevLett.95.023001.
- [81] L.S. Vasilenko, V.P. Chebotaev, and A.V. Shishaev. „LINE SHAPE OF TWO-PHOTON ABSORPTION IN A STANDING-WAVE FIELD IN A GAS“. In: *JETP Lett.* 12 (1970), p. 113.
- [82] F. Biraben, B. Cagnac, and G. Grynberg. „Experimental Evidence of Two-Photon Transition without Doppler Broadening“. In: *Physical Review Letters* 32.12 (Mar. 1974), pp. 643–645. DOI: 10.1103/PhysRevLett.32.643.
- [83] T. W. Hänsch et al. „Doppler-Free Two-Photon Spectroscopy of Hydrogen 1S-2S“. In: *Physical Review Letters* 34.6 (Feb. 1975), pp. 307–309. DOI: 10 . 1103/PhysRevLett.34.307.
- [84] F. Herlemont et al. „Doppler-free two-photon spectrum of SF₆ for metrological purposes“. In: *Optics Letters* 23.12 (June 1998), p. 957. ISSN: 0146-9592, 1539-4794. DOI: 10.1364/OL.23.000957.
- [85] A. Amy-Klein et al. „Slow molecule detection or Ramsey fringes in two-photon spectroscopy: which is better for high resolution spectroscopy and metrology ?“. In: *Optics Express* 4.2 (Jan. 1999), p. 67. ISSN: 1094-4087. DOI: 10.1364/OE.4.000067.
- [86] Elisabeth Peters. „Experimental and theoretical investigation of direct frequency comb spectroscopy“. PhD thesis. 2011.

- [87] Florian Adler et al. „Mid-infrared Fourier transform spectroscopy with a broadband frequency comb“. In: *Optics Express* 18.21 (Sept. 2010), p. 21861. ISSN: 1094-4087. DOI: 10.1364/OE.18.021861.
- [88] Florian Adler et al. „Cavity-Enhanced Direct Frequency Comb Spectroscopy: Technology and Applications“. In: *Annual Review of Analytical Chemistry* 3.1 (2010), pp. 175–205. DOI: 10.1146/annurev-anchem-060908-155248.
- [89] B. Bernhardt et al. „Mid-infrared dual-comb spectroscopy with 2.4 m Cr₂+:ZnSe femtosecond lasers“. en. In: *Applied Physics B* 100.1 (July 2010), pp. 3–8. ISSN: 0946-2171, 1432-0649. DOI: 10.1007/s00340-010-4080-0.
- [90] Giorgetta F. R. et al. „Fast high-resolution spectroscopy of dynamic continuous-wave laser sources“. In: *Nat Photon* 4.12 (Dec. 2010), pp. 853–857. ISSN: 1749-4885. DOI: 10.1038/nphoton.2010.228.
- [91] E. Baumann et al. „Spectroscopy of the methane ν_3 band with an accurate midinfrared coherent dual-comb spectrometer“. In: *Physical Review A* 84.6 (Dec. 2011), p. 062513. DOI: 10.1103/PhysRevA.84.062513.
- [92] T. A. Johnson and S. A. Diddams. „Mid-infrared upconversion spectroscopy based on a Yb:fiber femtosecond laser“. In: *Applied Physics B* 107.1 (Oct. 2011), pp. 31–39. ISSN: 0946-2171, 1432-0649. DOI: 10.1007/s00340-011-4748-0.
- [93] Aleksandra Foltynowicz et al. „Quantum-Noise-Limited Optical Frequency Comb Spectroscopy“. In: *Physical Review Letters* 107.23 (Nov. 2011), p. 233002. DOI: 10.1103/PhysRevLett.107.233002.
- [94] Tyler W. Neely et al. „Broadband mid-infrared frequency upconversion and spectroscopy with an aperiodically poled LiNbO₃ waveguide“. In: *Optics Letters* 37.20 (Oct. 2012), pp. 4332–4334. DOI: 10.1364/OL.37.004332.
- [95] Albert Schliesser, Nathalie Picqué, and Theodor W. Hänsch. „Mid-infrared frequency combs“. en. In: *Nature Photonics* 6.7 (2012), pp. 440–449. ISSN: 1749-4885. DOI: 10.1038/nphoton.2012.142.
- [96] Julien Mandon, Guy Guelachvili, and Nathalie Picqué. „Fourier transform spectroscopy with a laser frequency comb“. en. In: *Nature Photonics* 3.2 (Feb. 2009), pp. 99–102. ISSN: 1749-4885. DOI: 10.1038/nphoton.2008.293.
- [97] Thomas Udem. „Spectroscopy: Frequency comb benefits“. en. In: *Nature Photonics* 3.2 (Feb. 2009), pp. 82–84. ISSN: 1749-4885. DOI: 10.1038/nphoton.2008.284.
- [98] D.W. Van der Weide, J. Murakowski, and F. Keilmann. „Gas-absorption spectroscopy with electronic terahertz techniques“. In: *Microwave Theory and Techniques, IEEE Transactions on* 48.4 (Apr. 2000), pp. 740–743. ISSN: 0018-9480. DOI: 10.1109/22.841967.
- [99] S. Schiller. „Spectrometry with frequency combs“. In: *Optics Letters* 27.9 (May 2002), p. 766. ISSN: 0146-9592, 1539-4794. DOI: 10.1364/OL.27.000766.
- [100] Fritz Keilmann, Christoph Gohle, and Ronald Holzwarth. „Time-domain mid-infrared frequency-comb spectrometer“. In: *Optics Letters* 29.13 (July 2004), pp. 1542–1544. DOI: 10.1364/OL.29.001542.

- [101] Albert Schliesser et al. „Frequency-comb infrared spectrometer for rapid, remote chemical sensing“. In: *Optics Express* 13.22 (Oct. 2005), pp. 9029–9038. DOI: 10.1364/OPEX.13.009029.
- [102] Takeshi Yasui et al. „Terahertz frequency comb by multifrequency-heterodyning photoconductive detection for high-accuracy, high-resolution terahertz spectroscopy“. In: *Applied Physics Letters* 88.24 (June 2006), ISSN: 00036951. DOI: doi:10.1063/1.2209718.
- [103] Ian Coddington. „Coherent Multiheterodyne Spectroscopy Using Stabilized Optical Frequency Combs“. In: *Physical Review Letters* 100.1 (2008). DOI: 10.1103/PhysRevLett.100.013902.
- [104] Philippe Giaccari et al. „Active Fourier-transform spectroscopy combining the direct RF beating of two fiber-based mode-locked lasers with a novel referencing method“. In: *Optics Express* 16.6 (Mar. 2008), pp. 4347–4365. DOI: 10.1364/OE.16.004347.
- [105] Ian Coddington, William C. Swann, and Nathan R. Newbury. „Time-domain spectroscopy of molecular free-induction decay in the infrared“. In: *Optics Letters* 35.9 (May 2010), pp. 1395–1397. DOI: 10.1364/OL.35.001395.
- [106] Nathan R. Newbury, Ian Coddington, and William Swann. „Sensitivity of coherent dual-comb spectroscopy“. In: *Optics Express* 18.8 (Apr. 2010), pp. 7929–7945. DOI: 10.1364/OE.18.007929.
- [107] Birgitta Bernhardt et al. „Cavity-enhanced dual-comb spectroscopy“. In: *Nat Photon* 4.1 (Jan. 2010), pp. 55–57. ISSN: 1749-4885. DOI: 10.1038/nphoton.2009.217.
- [108] T. Ideguchi et al. „Adaptive dual-comb spectroscopy in the green region“. In: *Optics Letters* 37.23 (Dec. 2012), pp. 4847–4849. DOI: 10.1364/OL.37.004847.
- [109] Julien Roy et al. „Continuous real-time correction and averaging for frequency comb interferometry“. In: *Optics express* 20.20 (Sept. 2012). PMID: 23037343, pp. 21932–21939. ISSN: 1094-4087.
- [110] Laura Antonucci et al. „Asynchronous optical sampling with arbitrary detuning between laser repetition rates“. In: *Optics Express* 20.16 (July 2012), pp. 17928–17937. DOI: 10.1364/OE.20.017928.
- [111] Naoya Kuse, Akira Ozawa, and Yohei Kobayashi. „Comb-Resolved Dual-Comb Spectroscopy Stabilized by Free-Running Continuous-Wave Lasers“. In: *Applied Physics Express* 5.11 (Oct. 2012), p. 112402. ISSN: 1882-0778, 1882-0786. DOI: 10.1143/APEX.5.112402.
- [112] Jerome Faist. *Quantum cascade lasers*. English. [S.l.]: Oxford University Press, 2013. ISBN: 978-0-19-852824-1.
- [113] Andreas Hugi, Richard Maulini, and Jérôme Faist. „External cavity quantum cascade laser“. In: *Semiconductor Science and Technology* 25 (Aug. 2010), p. 083001. ISSN: 0268-1242, 1361-6641. DOI: 10.1088/0268-1242/25/8/083001.
- [114] R. Kazarinov and R. Suris. „Possibility of the amplification of electromagnetic waves in a semiconductor with a superlattice“. In: 5.4 (1971), pp. 707–709.

- [115] Richard Maulini et al. „Broadband tuning of external cavity bound-to-continuum quantum-cascade lasers“. In: *Applied Physics Letters* 84.10 (Mar. 2004), pp. 1659–1661. ISSN: 00036951. DOI: doi:10.1063/1.1667609.
- [116] Jérôme Faist et al. „Quantum-cascade lasers based on a bound-to-continuum transition“. English. In: *Applied Physics Letters* 78.2 (Jan. 2001), pp. 147–149. ISSN: 0003-6951. DOI: 10.1063/1.1339843.
- [117] Daniel Hofstetter et al. „Continuous wave operation of a 9.3 m quantum cascade laser on a Peltier cooler“. In: *Applied Physics Letters* 78.14 (Apr. 2001), pp. 1964–1966. ISSN: 00036951. DOI: doi:10.1063/1.1360225.
- [118] K. Faist et al. „Bound-to-continuum and two-phonon resonance, quantum-cascade lasers for high duty cycle, high-temperature operation“. English. In: *IEEE Journal of Quantum Electronics* 38.6 (June 2002), pp. 533–546. ISSN: 0018-9197. DOI: 10.1109/JQE.2002.1005404.
- [119] A. Lyakh et al. „1.6W high wall plug efficiency, continuous-wave room temperature quantum cascade laser emitting at 4.6m“. In: *Applied Physics Letters* 92.11 (Mar. 2008), ISSN: 00036951. DOI: doi:10.1063/1.2899630.
- [120] Arkadiy Lyakh et al. „Progress in high-performance quantum cascade lasers“. In: *Optical Engineering* 49.11 (2010), p. 111105. ISSN: 00913286. DOI: 10.1117/1.3506192.
- [121] A. Wittmann et al. „Intersubband linewidths in quantum cascade laser designs“. In: *Applied Physics Letters* 93.14 (Oct. 2008), ISSN: 00036951. DOI: doi:10.1063/1.2993212.
- [122] Yu Yao et al. „High performance “continuum-to-continuum” quantum cascade lasers with a broad gain bandwidth of over 400cm[sup −1]“. In: *Applied Physics Letters* 97.8 (2010), p. 081115. ISSN: 00036951. DOI: 10.1063/1.3484279.
- [123] Kazuue Fujita et al. „High-performance, homogeneous broad-gain quantum cascade lasers based on dual-upper-state design“. In: *Applied Physics Letters* 96.24 (June 2010), ISSN: 00036951. DOI: doi:10.1063/1.3455102.
- [124] Kazuue Fujita et al. „Broad-gain (/0 0.4), temperature-insensitive (T0 510K) quantum cascade lasers“. In: *Optics Express* 19.3 (Jan. 2011), p. 2694. ISSN: 1094-4087. DOI: 10.1364/OE.19.002694.
- [125] Kazuue Fujita et al. „High-performance quantum cascade lasers with wide electroluminescence (600cm−1), operating in continuous-wave above 100°C“. In: *Applied Physics Letters* 98.23 (June 2011), ISSN: 00036951. DOI: doi:10.1063/1.3596706.
- [126] Yu Yao et al. „Broadband quantum cascade laser gain medium based on a “continuum-to-bound” active region design“. In: *Applied Physics Letters* 96.21 (May 2010), ISSN: 00036951. DOI: doi:10.1063/1.3431577.
- [127] Peter Q. Liu et al. „Highly power-efficient quantum cascade lasers“. In: *Nat Photon* 4.2 (Feb. 2010), pp. 95–98. ISSN: 1749-4885. DOI: 10.1038/nphoton.2009.262.

- [128] Sabine Riedi. „Master Thesis: Characterisation of broadband Quantum Cascade Lasers in External Cavity“. PhD thesis. ETH Zurich, 2011.
- [129] Claire Gmachl et al. „Ultra-broadband semiconductor laser“. In: *Nature* 415.6874 (Feb. 2002), pp. 883–887. ISSN: 0028-0836. DOI: 10.1038/415883a.
- [130] Claire Gmachl et al. „Quantum cascade lasers with a heterogeneous cascade: Two-wavelength operation“. In: *Applied Physics Letters* 79.5 (July 2001), pp. 572–574. ISSN: 00036951. DOI: doi:10.1063/1.1383806.
- [131] M. B. Panish. „Molecular Beam Epitaxy“. en. In: *Science* 208.4446 (May 1980), pp. 916–922. ISSN: 0036-8075, 1095-9203. DOI: 10.1126/science.208.4446.916.
- [132] M. Beck et al. „Buried heterostructure quantum cascade lasers with a large optical cavity waveguide“. English. In: *IEEE Photonics Technology Letters* 12.11 (Nov. 2000), pp. 1450–1452. ISSN: 1041-1135. DOI: 10.1109/68.887653.
- [133] Alfredo Bismuto. „Mid-infrared quantum cascade lasers : active medium and waveguide engineering“. PhD thesis. ETH Zurich, 2011.
- [134] Rüdiger Paschotta. *Encyclopedia of laser physics and technology*. Weinheim: Wiley-VCH, 2008. ISBN: 9783527408283.
- [135] Edward D. Palik and Gorachand Ghosh. *Handbook of optical constants of solids*. San Diego: Academic Press, 1998. ISBN: 0125444206.
- [136] Edward D. Palik. *Handbook of optical constants of solids II*. Boston: Academic Press, 1991. ISBN: 0125444222.
- [137] Pochi Yeh. „Guided Waves in Layered Media“. In: *Optical waves in layered media*. Hoboken NJ: Wiley, 2005, pp. 298–374. ISBN: 9780471731924.
- [138] I. Vurgaftman, J. R. Meyer, and L. R. Ram-Mohan. „Band parameters for III–V compound semiconductors and their alloys“. In: *Journal of Applied Physics* 89.11 (June 2001), pp. 5815–5875. ISSN: 00218979. DOI: doi:10.1063/1.1368156.
- [139] C. Sirtori et al. „Low-loss Al-free waveguides for unipolar semiconductor lasers“. In: *Applied Physics Letters* 75.25 (Dec. 1999), pp. 3911–3913. ISSN: 00036951. DOI: doi:10.1063/1.125491.
- [140] Robert W. Boyd. „Quantum-Mechanical Theory of the Nonlinear Optical Susceptibility“. In: *Nonlinear optics*. 3. ed. Elsevier/Academic Press, 2008, pp. 135–206. ISBN: 9780123694706.
- [141] B Saleh. *Fundamentals of photonics (Wiley Series in Pure and Applied Optics)*. New York N.Y.: Wiley, 1991. ISBN: 9780471839651.
- [142] A. L. Schawlow and C. H. Townes. „Infrared and Optical Masers“. In: *Physical Review* 112.6 (Dec. 1958), pp. 1940–1949. DOI: 10.1103/PhysRev.112.1940.
- [143] C. Henry. „Theory of the linewidth of semiconductor lasers“. English. In: *IEEE Journal of Quantum Electronics* 18.2 (Feb. 1982), pp. 259–264. ISSN: 0018-9197. DOI: 10.1109/JQE.1982.1071522.

- [144] S. Bartalini et al. „Observing the Intrinsic Linewidth of a Quantum-Cascade Laser: Beyond the Schawlow-Townes Limit“. In: *Physical Review Letters* 104.8 (Feb. 2010), p. 083904. DOI: 10.1103/PhysRevLett.104.083904.
- [145] Lionel Tombez et al. „Temperature dependence of the frequency noise in a mid-IR DFB quantum cascade laser from cryogenic to room temperature“. In: *Optics express* 20.7 (Mar. 2012). PMID: 22453362, pp. 6851–6859. ISSN: 1094-4087.
- [146] F. Cappelli et al. „Subkilohertz linewidth room-temperature mid-infrared quantum cascade laser using a molecular sub-Doppler reference“. In: *Optics Letters* 37.23 (Dec. 2012), pp. 4811–4813. DOI: 10.1364/OL.37.004811.
- [147] Romain Terazzi. „Transport in quantum cascade lasers“. PhD thesis. ETH Zurich, 2012.
- [148] Romain Terazzi and Jérôme Faist. „A density matrix model of transport and radiation in quantum cascade lasers“. In: *New Journal of Physics* 12.3 (Mar. 2010), p. 033045. ISSN: 1367-2630. DOI: 10.1088/1367-2630/12/3/033045.
- [149] Carlo Sirtori et al. „Observation of large second order susceptibility via inter-subband transitions at 10 m in asymmetric coupled AlInAs/GaInAs quantum wells“. In: *Applied Physics Letters* 59.18 (1991), p. 2302. ISSN: 00036951. DOI: 10.1063/1.106050.
- [150] E. Rosencher et al. „Quantum Engineering of Optical Nonlinearities“. In: *Science* 271.5246 (Jan. 1996), pp. 168–173. DOI: 10.1126/science.271.5246.168.
- [151] Mikhail A. Belkin et al. „Terahertz quantum-cascade-laser source based on intracavity difference-frequency generation“. In: *Nat Photon* 1.5 (May 2007), pp. 288–292. ISSN: 1749-4885. DOI: 10.1038/nphoton.2007.70.
- [152] Q. Y. Lu et al. „High performance terahertz quantum cascade laser sources based on intracavity difference frequency generation“. In: *Optics Express* 21.1 (Jan. 2013), pp. 968–973. DOI: 10.1364/OE.21.000968.
- [153] Nina Owschimikow et al. „Resonant Second-Order Nonlinear Optical Processes in Quantum Cascade Lasers“. In: *Physical Review Letters* 90.4 (Jan. 2003), p. 043902. DOI: 10.1103/PhysRevLett.90.043902.
- [154] C. Gmachl et al. „Optimized second-harmonic generation in quantum cascade lasers“. In: *IEEE Journal of Quantum Electronics* 39 (Nov. 2003), pp. 1345–1355. ISSN: 0018-9197. DOI: 10.1109/JQE.2003.818315.
- [155] Carlo Sirtori et al. „Giant, triply resonant, third-order nonlinear susceptibility χ^3 in coupled quantum wells“. In: *Physical Review Letters* 68.7 (Feb. 1992), p. 1010. DOI: 10.1103/PhysRevLett.68.1010.
- [156] D. Walrod et al. „Observation of third order optical nonlinearity due to inter-subband transitions in AlGaAs/GaAs superlattices“. In: *Applied Physics Letters* 59.23 (1991), p. 2932. ISSN: 00036951. DOI: 10.1063/1.105827.
- [157] Ilan Gravé, Mordechai Segev, and Amnon Yariv. „Observation of phase conjugation at 10.6 m via intersubband third-order nonlinearities in a GaAs/AlGaAs multi-quantum-well structure“. In: *Applied Physics Letters* 60.22 (June 1992), pp. 2717–2719. ISSN: 00036951. DOI: doi:10.1063/1.106854.

- [158] J. B. Khurgin and S. Li. „Two-photon absorption and nonresonant nonlinear index of refraction in the intersubband transitions in the quantum wells“. In: *Applied Physics Letters* 62.2 (Jan. 1993), pp. 126–128. ISSN: 00036951. DOI: doi:10.1063/1.109346.
- [159] Jianwei Ma et al. „Large (3) determined by the degenerate four-wave mixing in a GaAsAlGaAs step multiple quantum well“. In: *Optics Communications* 124.5–6 (Mar. 1996), pp. 457–461. ISSN: 0030-4018. DOI: 10.1016/0030-4018(95)00746-6.
- [160] W. S. Rabinovich, G. Beadie, and D. S. Katzer. „Intersubband 3 in coupled InGaAs-AlGaAs multiple quantum wells“. English. In: *IEEE Journal of Quantum Electronics* 34.6 (June 1998), pp. 975–981. ISSN: 0018-9197. DOI: 10.1109/3.678593.
- [161] Amnon Yariv. *Photonics : optical electronics in modern communications*. 6. ed. New York [u.a.]: Oxford Univ. Press, 2007. ISBN: 9780195179460.
- [162] Robert Boyd. *Nonlinear optics*. 3. ed. Amsterdam [u.a.]: Elsevier/Academic Press, 2008. ISBN: 9780123694706.
- [163] Peter Friedli et al. „Four-wave mixing in a quantum cascade laser amplifier“. In: *Applied Physics Letters* 102.22 (June 2013), ISSN: 00036951. DOI: doi: 10.1063/1.4807662.
- [164] Kyo Inoue, Takaaki Mukai, and Tadashi Saitoh. „Nearly degenerate four-wave mixing in a traveling-wave semiconductor laser amplifier“. English. In: *Applied Physics Letters* 51.14 (Oct. 1987), pp. 1051–1053. ISSN: 0003-6951. DOI: 10.1063/1.99004.
- [165] Govind P. Agrawal. „Highly nondegenerate four-wave mixing in semiconductor lasers due to spectral hole burning“. In: *Applied Physics Letters* 51.5 (1987), p. 302. ISSN: 00036951. DOI: 10.1063/1.98450.
- [166] A. Uskov, J. Mork, and J. Mark. „Wave mixing in semiconductor laser amplifiers due to carrier heating and spectral-hole burning“. English. In: *IEEE Journal of Quantum Electronics* 30.8 (Aug. 1994), pp. 1769–1781. ISSN: 0018-9197. DOI: 10.1109/3.301641.
- [167] Rene Daendliker. „Coupled waves: a powerful concept in modern optics“. In: *Proceedings of SPIE*. Delft, Netherlands, 1997, pp. 279–288. DOI: 10.1117/12.294394.
- [168] Palik and Gosh. *Handbook of optical constants of solids III*. English. San Diego [etc.]: Academic Press, 1998. ISBN: 012544415X 9780125444156 0125444249 9780125444248 0125444206 9780125444200 0125444222 9780125444224 0125444230 9780125444231 0122818555 9780122818554.
- [169] A. Schnellbuegel, Harro Hagedorn, and Rainer Anton. „Ion-assisted deposition of nontoxic coatings for high-power CO₂ laser optics“. In: ed. by Florin Abeles. Nov. 1994, pp. 839–848. DOI: 10.1117/12.192160.

- [170] W. Heitmann and E. Ritter. „Production and Properties of Vacuum Evaporated Films of Thorium Fluoride“. In: *Applied Optics* 7.2 (Feb. 1968), pp. 307–309. DOI: 10.1364/AO.7.000307.
- [171] Martin Fritz and Friedrich Waibel. *Optical Interference Coatings*. 2003. ISBN: 978-3-540-00364-9.
- [172] Manfred Rahe et al. „Absorption calorimetry and laser-induced damage threshold measurements of antireflective-coated ZnSe and metal mirrors at 10.6 m“. In: (June 1991), pp. 113–126. DOI: 10.1117/12.57208.
- [173] Pochi Yeh. *Optical waves in layered media*. Hoboken NJ: Wiley, 2005. ISBN: 9780471731924.
- [174] Sabine S. Riedi et al. „External cavity tuning of broadband quantum cascade laser active region designs around 3.3 μm and 8 μm “. In: *CLEO: Science and Innovations*. OSA Technical Digest (online). Optical Society of America, May 2012, CF1K.2.
- [175] Arun Mohan et al. „Room-temperature continuous-wave operation of an external-cavity quantum cascade laser“. In: *Optics Letters* 32.19 (Oct. 2007), pp. 2792–2794. DOI: 10.1364/OL.32.002792.
- [176] Richard Maulini et al. „External cavity quantum-cascade laser tunable from 8.2 to 10.4 μm using a gain element with a heterogeneous cascade“. In: *Applied Physics Letters* 88.20 (May 2006), ISSN: 00036951. DOI: doi : 10 . 1063 / 1 . 2205183.
- [177] A. Wittmann et al. „Heterogeneous High-Performance Quantum-Cascade Laser Sources for Broad-Band Tuning“. English. In: *IEEE Journal of Quantum Electronics* 44.11 (Nov. 2008), pp. 1083–1088. ISSN: 0018-9197. DOI: 10.1109/JQE.2008.2001928.
- [178] Andreas Hugi et al. „External cavity quantum cascade laser tunable from 7.6 to 11.4 μm “. In: *Applied Physics Letters* 95 (2009), p. 061103. ISSN: 00036951. DOI: 10.1063/1.3193539.
- [179] Jérôme Faist et al. „Distributed feedback quantum cascade lasers“. In: *Applied Physics Letters* 70.20 (May 1997), pp. 2670–2672. ISSN: 00036951. DOI: doi : 10 . 1063 / 1 . 119208.
- [180] C. Gmachl et al. „Complex-coupled quantum cascade distributed-feedback laser“. In: *IEEE Photonics Technology Letters* 9.8 (Aug. 1997), pp. 1090–1092. ISSN: 1041-1135, 1941-0174. DOI: 10.1109/68.605510.
- [181] K. Namjou et al. „Sensitive absorption spectroscopy with a room-temperature distributed-feedback quantum-cascade laser“. In: *Optics Letters* 23.3 (Feb. 1998), p. 219. ISSN: 0146-9592, 1539-4794. DOI: 10.1364/OL.23.000219.
- [182] S. W. Sharpe et al. „High-resolution (Doppler-limited) spectroscopy using quantum-cascade distributed-feedback lasers“. In: *Optics Letters* 23.17 (1998), pp. 1396–1398. DOI: 10.1364/OL.23.001396.

- [183] A.A. Kosterev and F.K. Tittel. „Chemical sensors based on quantum cascade lasers“. In: *IEEE Journal of Quantum Electronics* 38.6 (June 2002), pp. 582–591. ISSN: 0018-9197. DOI: 10.1109/JQE.2002.1005408.
- [184] Benjamin G. Lee et al. „Widely tunable single-mode quantum cascade laser source for mid-infrared spectroscopy“. In: *Applied Physics Letters* 91.23 (Dec. 2007), ISSN: 00036951. DOI: doi:10.1063/1.2816909.
- [185] B.G. Lee et al. „Broadband Distributed-Feedback Quantum Cascade Laser Array Operating From 8.0 to 9.8 μm “. In: *IEEE Photonics Technology Letters* 21.13 (July 2009), pp. 914–916. ISSN: 1041-1135. DOI: 10.1109/LPT.2009.2020440.
- [186] Patrick Rauter et al. „High-power arrays of quantum cascade laser master-oscillator power-amplifiers“. In: *Optics Express* 21.4 (Feb. 2013), pp. 4518–4530. DOI: 10.1364/OE.21.004518.
- [187] S. Slivken et al. „Sampled grating, distributed feedback quantum cascade lasers with broad tunability and continuous operation at room temperature“. In: *Applied Physics Letters* 100.26 (2012), p. 261112. ISSN: 00036951. DOI: 10.1063/1.4732801.
- [188] G. P. Luo et al. „Grating-tuned external-cavity quantum-cascade semiconductor lasers“. In: *Applied Physics Letters* 78.19 (May 2001), pp. 2834–2836. ISSN: 00036951. DOI: doi:10.1063/1.1371524.
- [189] G. Totschnig et al. „Mid-infrared external-cavity quantum-cascade laser“. In: *Optics Letters* 27.20 (Oct. 2002), p. 1788. ISSN: 0146-9592, 1539-4794. DOI: 10.1364/OL.27.001788.
- [190] Guipeng Luo et al. „Broadly wavelength-tunable external cavity, mid-infrared quantum cascade lasers“. In: *IEEE Journal of Quantum Electronics* 38.5 (May 2002), pp. 486–494. ISSN: 0018-9197. DOI: 10.1109/3.998621.
- [191] Chuan Peng, Guipeng Luo, and Han Q. Le. „Broadband, Continuous, and Fine-Tune Properties of External-Cavity Thermoelectric-Stabilized Mid-infrared Quantum-Cascade Lasers“. In: *Applied Optics* 42.24 (2003), p. 4877. ISSN: 0003-6935, 1539-4522. DOI: 10.1364/AO.42.004877.
- [192] F. J Duarte. *Tunable lasers handbook*. English. San Diego: Academic Press, 1995. ISBN: 012222695X 9780122226953.
- [193] Michael G. Littman and Harold J. Metcalf. „Spectrally narrow pulsed dye laser without beam expander“. In: *Applied Optics* 17.14 (July 1978), pp. 2224–2227. DOI: 10.1364/AO.17.002224.
- [194] Guipeng Luo et al. „Broadly wavelength-tunable external cavity, mid-infrared quantum cascade lasers“. English. In: *IEEE Journal of Quantum Electronics* 38.5 (May 2002), pp. 486–494. ISSN: 0018-9197. DOI: 10.1109/3.998621.
- [195] G. Wysocki et al. „Widely tunable mode-hop free external cavity quantum cascade lasers for high resolution spectroscopy and chemical sensing“. In: *Applied Physics B* 92.3 (May 2008), pp. 305–311. ISSN: 0946-2171, 1432-0649. DOI: 10.1007/s00340-008-3047-x.

- [196] Michael Pushkarsky et al. „Sub-parts-per-billion level detection of NO₂ using room-temperature quantum cascade lasers“. In: *Proceedings of the National Academy of Sciences* 103.29 (July 2006), pp. 10846–10849. ISSN: 0027-8424, 1091-6490. DOI: 10.1073/pnas.0604238103.
- [197] Timothy Day et al. „Compact widely tunable ECqL and its applications for gas spectroscopy“. In: (Jan. 2009), 72220G–72220G. DOI: 10.1117/12.814988.
- [198] T. Tsai and G. Wysocki. „Active wavelength control of an external cavity quantum cascade laser“. en. In: *Applied Physics B* (May 2012), pp. 1–7. ISSN: 0946-2171, 1432-0649. DOI: 10.1007/s00340-012-5075-9.
- [199] G. Wysocki et al. „Widely tunable mode-hop free external cavity quantum cascade laser for high resolution spectroscopic applications“. In: *Applied Physics B: Lasers and Optics* 81.6 (2005), pp. 769–777. ISSN: 0946-2171. DOI: 10.1007/s00340-005-1965-4.
- [200] B. Hinkov et al. „Time-resolved spectral characteristics of external-cavity quantum cascade lasers and their application to stand-off detection of explosives“. en. In: *Applied Physics B* 100.2 (Aug. 2010), pp. 253–260. ISSN: 0946-2171, 1432-0649. DOI: 10.1007/s00340-009-3863-7.
- [201] Richard Maulini et al. „Continuous-wave operation of a broadly tunable thermoelectrically cooled external cavity quantum-cascade laser“. In: *Optics Letters* 30.19 (Oct. 2005), pp. 2584–2586. DOI: 10.1364/OL.30.002584.
- [202] A. Bismuto et al. „Electrically tunable, high performance quantum cascade laser“. In: *Applied Physics Letters* 96.14 (2010), p. 141105. ISSN: 00036951. DOI: 10.1063/1.3377008.
- [203] Michael B. Pushkarsky et al. „High-sensitivity detection of TNT“. In: *Proceedings of the National Academy of Sciences* 103.52 (Dec. 2006), pp. 19630–19634. ISSN: 0027-8424, 1091-6490. DOI: 10.1073/pnas.0609789104.
- [204] T. H. Risby and S. F. Solga. „Current status of clinical breath analysis“. en. In: *Applied Physics B* 85.2-3 (Nov. 2006), pp. 421–426. ISSN: 0946-2171, 1432-0649. DOI: 10.1007/s00340-006-2280-4.
- [205] A. Kosterev et al. „Application of quantum cascade lasers to trace gas analysis“. en. In: *Applied Physics B* 90.2 (Feb. 2008), pp. 165–176. ISSN: 0946-2171, 1432-0649. DOI: 10.1007/s00340-007-2846-9.
- [206] Mark C. Phillips et al. „External cavity quantum cascade laser for quartz tuning fork photoacoustic spectroscopy of broad absorption features“. In: *Optics Letters* 32.9 (May 2007), pp. 1177–1179. DOI: 10.1364/OL.32.001177.
- [207] Stefano Barbieri et al. „Gas detection with quantum cascade lasers: An adapted photoacoustic sensor based on Helmholtz resonance“. In: *Review of Scientific Instruments* 73.6 (June 2002), pp. 2458–2461. ISSN: 00346748. DOI: doi:10.1063/1.1480463.
- [208] A. A. Kosterev et al. „QEPAS detector for rapid spectral measurements“. en. In: *Applied Physics B* 100.1 (July 2010), pp. 173–180. ISSN: 0946-2171, 1432-0649. DOI: 10.1007/s00340-010-3975-0.

- [209] Frank K. Tittel et al. „Sensitive detection of nitric oxide using a 5.26 m external cavity quantum cascade laser based QEPAS sensor“. In: ed. by Chun Lei and Kent D. Choquette. Jan. 2012, DOI: 10.1117/12.905621.
- [210] Du'an Stupar et al. „Fully reflective external-cavity setup for quantum-cascade lasers as a local oscillator in mid-infrared wavelength heterodyne spectroscopy“. In: *Applied Optics* 47.16 (June 2008), pp. 2993–2997. DOI: 10.1364/AO.47.002993.
- [211] Damien Weidmann and Gerard Wsocki. „High-resolution broadband (>100 cm $^{-1}$) infrared heterodyne spectro-radiometry using an external cavity quantum cascade laser“. In: *Optics Express* 17.1 (Jan. 2009), pp. 248–259. DOI: 10.1364/OE.17.000248.
- [212] Rafał Lewicki et al. „Ultrasensitive detection of nitric oxide at 5.33 μ m by using external cavity quantum cascade laser-based Faraday rotation spectroscopy“. In: *Proceedings of the National Academy of Sciences* 106.31 (Aug. 2009), pp. 12587–12592. ISSN: 0027-8424, 1091-6490. DOI: 10.1073/pnas.0906291106.
- [213] Timothy Day et al. „Recent advances in compact broadly tunable external-cavity quantum cascade lasers (ECQCL)“. In: (May 2009), 73190F–73190F. DOI: 10.1117/12.818978.
- [214] Kevin Knabe et al. „Frequency characterization of a swept- and fixed-wavelength external-cavity quantum cascade laser by use of a frequency comb“. In: *Optics express* 20.11 (May 2012). PMID: 22714230, pp. 12432–12442. ISSN: 1094-4087.
- [215] Yu Yao et al. „Broadband quantum cascade lasers based on strongly-coupled transitions with an external cavity tuning range over 340 cm $^{-1}$ “. In: *2011 Conference on Lasers and Electro-Optics (CLEO)*. May 2011, pp. 1–2.
- [216] Yu Yao, Anthony J. Hoffman, and Claire F. Gmachl. „Mid-infrared quantum cascade lasers“. en. In: *Nature Photonics* 6.7 (2012), pp. 432–439. ISSN: 1749-4885. DOI: 10.1038/nphoton.2012.143.
- [217] Tatsuo Dougakiuchi et al. „Broadband Tuning of External Cavity Dual-Upper-State Quantum-Cascade Lasers in Continuous Wave Operation“. In: *Applied Physics Express* 4.10 (Sept. 2011), p. 102101. ISSN: 1882-0778, 1882-0786. DOI: 10.1143/APEX.4.102101.
- [218] Andreas Karpf and Gottipaty N. Rao. „Absorption and wavelength modulation spectroscopy of NO $_2$ using a tunable, external cavity continuous wave quantum cascade laser“. In: *Applied Optics* 48.2 (Jan. 2009), pp. 408–413. DOI: 10.1364/AO.48.000408.
- [219] G. Hancock et al. „Direct and wavelength modulation spectroscopy using a cw external cavity quantum cascade laser“. In: *Applied Physics Letters* 94.20 (May 2009), ISSN: 00036951. DOI: doi:10.1063/1.3141521.
- [220] J. H. van Helden et al. „Rapid passage effects in nitrous oxide induced by a chirped external cavity quantum cascade laser“. In: *Applied Physics Letters* 94.5 (Feb. 2009), ISSN: 00036951. DOI: doi:10.1063/1.3079420.

- [221] Yunjie Xu et al. „Application of quantum cascade lasers for infrared spectroscopy of jet-cooled molecules and complexes“. In: (Jan. 2009), pp. 722208–722208. DOI: 10.1117/12.814878.
- [222] C. Young et al. „External cavity widely tunable quantum cascade laser based hollow waveguide gas sensors for multianalyte detection“. In: *Sensors and Actuators B: Chemical* 140.1 (June 2009), pp. 24–28. ISSN: 0925-4005. DOI: 10.1016/j.snb.2009.03.023.
- [223] X. Chao, J. B. Jeffries, and R. K. Hanson. „Wavelength-modulation-spectroscopy for real-time, in situ NO detection in combustion gases with a 5.2 m quantum-cascade laser“. In: *Applied Physics B: Lasers and Optics* 106 (Mar. 2012), pp. 987–997. DOI: 10.1007/s00340-011-4839-y.
- [224] Grant Ritchie. „Applications of QCLs in Studies of Chemical Dynamics“. In: *Lasers, Sources, and Related Photonic Devices*. OSA Technical Digest (CD). Optical Society of America, Jan. 2012, LT1B.3.
- [225] M. Rezaei, K. H. Michaelian, and N. Moazzen-Ahmadi. „Nonpolar nitrous oxide dimer: Observation of combination bands of (14N2O)2 and (15N2O)2 involving the torsion and antigeared bending modes“. In: *The Journal of Chemical Physics* 136.12 (Mar. 2012), ISSN: 00219606. DOI: doi:10.1063/1.3697869.
- [226] R. Maulini et al. „Widely tunable high-power external cavity quantum cascade laser operating in continuous-wave at room temperature“. In: *Electronics Letters* 45.2 (2009), pp. 107–108. ISSN: 0013-5194. DOI: 10.1049/el:20093057.
- [227] *Quantum Cascade Laser and FTIR Spectrometers by Block Engineering*.
- [228] E. Sorokin et al. „Sensitive multiplex spectroscopy in the molecular fingerprint 2.4 μm region with a Cr2+:ZnSe femtosecond laser“. In: *Optics Express* 15.25 (Dec. 2007), pp. 16540–16545. DOI: 10.1364/OE.15.016540.
- [229] Andreas Hugi et al. „Mid-infrared frequency comb based on a quantum cascade laser“. en. In: *Nature* 492.7428 (Dec. 2012), pp. 229–233. ISSN: 0028-0836. DOI: 10.1038/nature11620.
- [230] *Nobelprize.org. The Nobel Prize in Physics 2005*. Feb. 2013.
- [231] Scott A. Diddams. „The evolving optical frequency comb [Invited]“. In: *Journal of the Optical Society of America B* 27.11 (Nov. 2010), B51–B62. DOI: 10.1364/JOSAB.27.000B51.
- [232] W. Sibbett, A. A. Lagatsky, and C. T. A. Brown. „The development and application of femtosecond laser systems“. In: *Optics Express* 20.7 (Mar. 2012), pp. 6989–7001. DOI: 10.1364/OE.20.006989.
- [233] Ariel Gordon et al. „Multimode regimes in quantum cascade lasers: From coherent instabilities to spatial hole burning“. In: *Physical Review A* 77.5 (May 2008), p. 053804. DOI: 10.1103/PhysRevA.77.053804.
- [234] Jrme Faist et al. „Laser action by tuning the oscillator strength“. In: *Nature* 387.6635 (June 1997), pp. 777–782. ISSN: 0028-0836.

- [235] Christine Y. Wang et al. „Mode-locked pulses from mid-infrared Quantum Cascade Lasers“. In: *Optics Express* 17.15 (July 2009), pp. 12929–12943. DOI: 10.1364/OE.17.012929.
- [236] L. E. Hargrove, R. L. Fork, and M. A. Pollack. „LOCKING OF He-Ne LASER MODES INDUCED BY SYNCHRONOUS INTRACAVITY MODULATION“. In: *Applied Physics Letters* 5.1 (July 1964), pp. 4–5. ISSN: 00036951. DOI: doi:10.1063/1.1754025.
- [237] Hermann A Haus. „Theory of mode locking with a fast saturable absorber“. In: *Journal of Applied Physics* 46.7 (July 1975), pp. 3049–3058. ISSN: 00218979. DOI: doi:10.1063/1.321997.
- [238] H. Haus. „Theory of mode locking with a slow saturable absorber“. In: *IEEE Journal of Quantum Electronics* 11.9 (Sept. 1975), pp. 736–746. ISSN: 0018-9197. DOI: 10.1109/JQE.1975.1068922.
- [239] H. A Haus. „Mode-locking of lasers“. English. In: *IEEE Journal of Selected Topics in Quantum Electronics* 6.6 (Dec. 2000), pp. 1173–1185. ISSN: 1077-260X. DOI: 10.1109/2944.902165.
- [240] E. P. Ippen, C. V. Shank, and A. Dienes. „Passive mode locking of the cw dye laser“. In: *Applied Physics Letters* 21.8 (Oct. 1972), pp. 348–350. ISSN: 00036951. DOI: doi:10.1063/1.1654406.
- [241] U. Keller. „Ultrafast solid-state laser oscillators: a success story for the last 20 years with no end in sight“. en. In: *Applied Physics B* 100.1 (July 2010), pp. 15–28. ISSN: 0946-2171, 1432-0649. DOI: 10.1007/s00340-010-4045-3.
- [242] D. E. Spence, P. N. Kean, and W. Sibbett. „60-fsec pulse generation from a self-mode-locked Ti:sapphire laser“. In: *Optics Letters* 16.1 (Jan. 1991), pp. 42–44. DOI: 10.1364/OL.16.000042.
- [243] U. Keller et al. „Semiconductor saturable absorber mirrors (SESAM's) for femtosecond to nanosecond pulse generation in solid-state lasers“. In: *IEEE Journal of Selected Topics in Quantum Electronics* 2.3 (Sept. 1996), pp. 435–453. ISSN: 1077-260X. DOI: 10.1109/2944.571743.
- [244] S. Tsuda et al. „Mode-locking ultrafast solid-state lasers with saturable Bragg reflectors“. In: *IEEE Journal of Selected Topics in Quantum Electronics* 2.3 (Sept. 1996), pp. 454–464. ISSN: 1077-260X. DOI: 10.1109/2944.571744.
- [245] Cyrill Roman Emmanuel Baer et al. „Femtosecond thin-disk laser with 141 W of average power“. In: *Optics Letters* 35.13 (July 2010), pp. 2302–2304. DOI: 10.1364/OL.35.002302.
- [246] Jinendra K. Ranka, Robert S. Windeler, and Andrew J. Stentz. „Visible continuum generation in air-silica microstructure optical fibers with anomalous dispersion at 800 nm“. In: *Optics Letters* 25.1 (Jan. 2000), pp. 25–27. DOI: 10.1364/OL.25.000025.

- [247] H.R. Telle et al. „Carrier-envelope offset phase control: A novel concept for absolute optical frequency measurement and ultrashort pulse generation“. In: *Applied Physics B: Lasers and Optics* 69.4 (Oct. 1999), pp. 327–332. ISSN: 0946-2171, 1432-0649. DOI: 10.1007/s003400050813.
- [248] Albrecht Bartels, Dirk Heinecke, and Scott A. Diddams. „10-GHz Self-Referenced Optical Frequency Comb“. en. In: *Science* 326.5953 (Oct. 2009), pp. 681–681. ISSN: 0036-8075, 1095-9203. DOI: 10.1126/science.1179112.
- [249] Clara J. Saraceno et al. „Self-referenceable frequency comb from an ultrafast thin disk laser“. In: *Optics Express* 20.9 (Apr. 2012), pp. 9650–9656. DOI: 10.1364/OE.20.009650.
- [250] P. Del’Haye et al. „Full Stabilization of a Microresonator-Based Optical Frequency Comb“. In: *Physical Review Letters* 101.5 (July 2008), p. 053903. ISSN: 0031-9007. DOI: 10.1103/PhysRevLett.101.053903.
- [251] Fahmida Ferdous et al. „Spectral line-by-line pulse shaping of on-chip microresonator frequency combs“. In: *Nat Photon* 5.12 (Dec. 2011), pp. 770–776. ISSN: 1749-4885. DOI: 10.1038/nphoton.2011.255.
- [252] L.F. Tiemeijer et al. „Passive FM locking in InGaAsP semiconductor lasers“. In: *IEEE Journal of Quantum Electronics* 25.6 (June 1989), pp. 1385–1392. ISSN: 0018-9197. DOI: 10.1109/3.29273.
- [253] Murray Sargent, Marlan O Scully, and Willis E Lamb. *Laser physics*. English. Reading, Mass.; London: Addison-Wesley, 1977. ISBN: 0201069121 9780201069129 020106913X 9780201069136.
- [254] E. Ammann, B. McMurtry, and M. Oshman. „Detailed experiments on helium-neon FM lasers“. In: *IEEE Journal of Quantum Electronics* 1.6 (Sept. 1965), pp. 263–272. ISSN: 0018-9197. DOI: 10.1109/JQE.1965.1072232.
- [255] T. J. Kippenberg, R. Holzwarth, and S. A. Diddams. „Microresonator-Based Optical Frequency Combs“. en. In: *Science* 332.6029 (Apr. 2011), pp. 555–559. ISSN: 0036-8075, 1095-9203. DOI: 10.1126/science.1193968.
- [256] V. V. Fedorov S. B. Mirov. „Recent Progress in Transition-Metal-Doped II–VI Mid-IR Lasers“. In: *Selected Topics in Quantum Electronics, IEEE Journal of* 3 (2007), pp. 810–822. ISSN: 1077-260X. DOI: 10.1109/JSTQE.2007.896634.
- [257] E. Sorokin, S. Naumov, and I.T. Sorokina. „Ultrabroadband infrared solid-state lasers“. In: *IEEE Journal of Selected Topics in Quantum Electronics* 11.3 (2005), pp. 690–712. ISSN: 1077-260X. DOI: 10.1109/JSTQE.2003.850255.
- [258] I. S. Moskalev, V. V. Fedorov, and S. B. Mirov. „Tunable, Single-Frequency, and Multi-Watt Continuous-Wave Cr²⁺:ZnSe Lasers“. In: *Optics Express* 16.6 (Mar. 2008), pp. 4145–4153. DOI: 10.1364/OE.16.004145.
- [259] Umit Demirbas and Alphan Sennaroglu. „Intracavity-pumped Cr²⁺:ZnSe laser with ultrabroad tuning range between 1880 and 3100 nm“. In: *Optics Letters* 31.15 (Aug. 2006), pp. 2293–2295. DOI: 10.1364/OL.31.002293.
- [260] Timothy J. Carrig et al. „Mode-locked Cr²⁺:ZnSe laser“. In: *Optics Letters* 25.3 (Feb. 2000), pp. 168–170. DOI: 10.1364/OL.25.000168.

- [261] M. Natali Cizmeciyan et al. „Kerr-lens mode-locked femtosecond Cr²⁺:ZnSe laser at 2420 nm“. In: *Optics Letters* 34.20 (Oct. 2009), pp. 3056–3058. DOI: 10.1364/OL.34.003056.
- [262] M. N. Cizmeciyan et al. „Graphene mode-locked femtosecond Cr:ZnSe laser at 2500 nm“. In: *Optics Letters* 38.3 (Feb. 2013), pp. 341–343. DOI: 10.1364/OL.38.000341.
- [263] K. L. Vodopyanov et al. „Mid-IR frequency comb source spanning 4.4–5.4 μm based on subharmonic GaAs optical parametric oscillator“. In: *Optics Letters* 36.12 (June 2011), p. 2275. ISSN: 0146-9592, 1539-4794. DOI: 10.1364/OL.36.002275.
- [264] Nicola Coluccelli et al. „1.6-W self-referenced frequency comb at 2.06 μm using a Ho:YLF multipass amplifier“. In: *Optics Letters* 36.12 (June 2011), pp. 2299–2301. DOI: 10.1364/OL.36.002299.
- [265] M. P. Frolov et al. „Laser radiation tunable within the range of 4.35–5.45 μm in a ZnTe crystal doped with Fe²⁺ ions“. en. In: *Journal of Russian Laser Research* 32.6 (Nov. 2011), pp. 528–536. ISSN: 1071-2836, 1573-8760. DOI: 10.1007/s10946-011-9243-x.
- [266] Vladimir I. Kozlovskii et al. „Pulsed Fe²⁺:ZnS laser continuously tunable in the wavelength range of 3.49 — 4.65 μm“. en. In: *Quantum Electronics* 41.1 (Jan. 2011), p. 1. ISSN: 1063-7818. DOI: 10.1070/QE2011v041n01ABEH014451.
- [267] Chenan Xia et al. „Mid-infrared supercontinuum generation to 4.5 μm in ZBLAN fluoride fibers by nanosecond diode pumping“. In: *Optics Letters* 31.17 (Sept. 2006), pp. 2553–2555. DOI: 10.1364/OL.31.002553.
- [268] Alireza Marandi et al. „Mid-infrared supercontinuum generation in tapered chalcogenide fiber for producing octave-spanning frequency comb around 3 μm“. In: *Optics Express* 20.22 (Oct. 2012), pp. 24218–24225. DOI: 10.1364/OE.20.024218.
- [269] Florian Adler and Scott A. Diddams. „High-power, hybrid Er: fiber/Tm: fiber frequency comb source in the 2 μm wavelength region“. In: *Optics Letters* 37.9 (May 2012), pp. 1400–1402. DOI: 10.1364/OL.37.001400.
- [270] C. R. Phillips et al. „Supercontinuum generation in quasi-phase-matched LiNbO₃ waveguide pumped by a Tm-doped fiber laser system“. In: *Optics Letters* 36.19 (Oct. 2011), pp. 3912–3914. DOI: 10.1364/OL.36.003912.
- [271] P. Maddaloni et al. „Mid-infrared fibre-based optical comb“. en. In: *New Journal of Physics* 8.11 (Nov. 2006), p. 262. ISSN: 1367-2630. DOI: 10.1088/1367-2630/8/11/262.
- [272] C. Erny et al. „Mid-infrared difference-frequency generation of ultrashort pulses tunable between 3.2 and 4.8 μm from a compact fiber source“. In: *Optics Letters* 32.9 (May 2007), pp. 1138–1140. DOI: 10.1364/OL.32.001138.
- [273] R. Huber et al. „Generation and field-resolved detection of femtosecond electromagnetic pulses tunable up to 41 THz“. In: *Applied Physics Letters* 76.22 (May 2000), pp. 3191–3193. ISSN: 00036951. DOI: doi:10.1063/1.126625.

- [274] R. A. Kaindl et al. „Femtosecond infrared pulses tunable from 9 to 18 μm at an 88-MHz repetition rate“. In: *Optics Letters* 23.11 (June 1998), pp. 861–863. DOI: 10.1364/OL.23.000861.
- [275] Fritz Keilmann and Sergiu Amarie. „Mid-infrared Frequency Comb Spanning an Octave Based on an Er Fiber Laser and Difference-Frequency Generation“. In: *Journal of Infrared, Millimeter and Terahertz Waves* 33.5 (2012), pp. 479–484. ISSN: 1866-6892. DOI: 10.1007/s10762-012-9894-x.
- [276] Florian Adler et al. „Phase-stabilized, 1.5 W frequency comb at 2.8-4.8 μm “. In: *Optics Letters* 34.9 (Apr. 2009), pp. 1330–1332. ISSN: 0146-9592, 1539-4794. DOI: 10.1364/OL.34.001330.
- [277] Samuel T. Wong, Konstantin L. Vodopyanov, and Robert L. Byer. „Self-phase-locked divide-by-2 optical parametric oscillator as a broadband frequency comb source“. In: *Journal of the Optical Society of America B* 27.5 (Apr. 2010), p. 876. ISSN: 0740-3224, 1520-8540. DOI: 10.1364/JOSAB.27.000876.
- [278] Nick Leindecker et al. „Broadband degenerate OPO for mid-infrared frequency comb generation“. In: *Optics Express* 19.7 (Mar. 2011), pp. 6296–6302. DOI: 10.1364/OE.19.006296.
- [279] Nick Leindecker et al. „Octave-spanning ultrafast OPO with 2.6-6.1 μm instantaneous bandwidth pumped by femtosecond Tm-fiber laser“. In: *Optics Express* 20.7 (Mar. 2012), p. 7046. ISSN: 1094-4087. DOI: 10.1364/OE.20.007046.
- [280] D. J. Derickson et al. „Short pulse generation using multisegment mode-locked semiconductor lasers“. English. In: *IEEE Journal of Quantum Electronics* 28.10 (Oct. 1992), pp. 2186–2202. ISSN: 0018-9197. DOI: 10.1109/3.159527.
- [281] E.A. Avrutin, J.H. Marsh, and E.L. Portnoi. „Monolithic and multi-GigaHertz mode-locked semiconductor lasers: Constructions, experiments, models and applications“. In: *IEEE Proceedings - Optoelectronics* 147.4 (2000), p. 251. ISSN: 13502433. DOI: 10.1049/ip-opt:20000282.
- [282] A. Akrouf et al. „Error-free transmission of 8 WDM channels at 10 Gbit/s using comb generation in a quantum dash based mode-locked laser“. In: *34th European Conference on Optical Communication, 2008. ECOC 2008*. Sept. 2008, pp. 1–2. DOI: 10.1109/ECOC.2008.4729565.
- [283] Martijn J. R. Heck and John E. Bowers. „Integrated Fourier-Domain Mode-Locked Lasers: Analysis of a Novel Coherent Comb Laser“. In: *IEEE Journal of Selected Topics in Quantum Electronics* 18.1 (Jan. 2012), pp. 201–209. ISSN: 1077-260X, 1558-4542. DOI: 10.1109/JSTQE.2011.2113371.
- [284] E. U. Rafailov, M. A. Cataluna, and W. Sibbett. „Mode-locked quantum-dot lasers“. en. In: *Nature Photonics* 1.7 (July 2007), pp. 395–401. ISSN: 1749-4885. DOI: 10.1038/nphoton.2007.120.
- [285] E. U. Rafailov et al. „High-power picosecond and femtosecond pulse generation from a two-section mode-locked quantum-dot laser“. In: *Applied Physics Letters* 87.8 (Aug. 2005), ISSN: 00036951. DOI: doi:10.1063/1.2032608.

- [286] Ksenia A. Fedorova et al. „Broadly tunable high-power InAs/GaAs quantum-dot external cavity diode lasers“. In: *Optics Express* 18.18 (Aug. 2010), pp. 19438–19443. DOI: 10.1364/OE.18.019438.
- [287] D. I. Nikitichev et al. „Broad wavelength tunability from external cavity quantum-dot mode-locked laser“. In: *Applied Physics Letters* 101.12 (Sept. 2012), ISSN: 00036951. DOI: doi:10.1063/1.4751034.
- [288] Adrian H. Quarterman et al. „A passively mode-locked external-cavity semiconductor laser emitting 60-fs pulses“. In: *Nature Photonics* 3.12 (Nov. 2009), pp. 729–731. ISSN: 1749-4885, 1749-4893. DOI: 10.1038/nphoton.2009.216.
- [289] Martin Hoffmann et al. „Femtosecond high-power quantum dot vertical external cavity surface emitting laser“. In: *Optics Express* 19.9 (Apr. 2011), pp. 8108–8116. DOI: 10.1364/OE.19.008108.
- [290] P. Del’Haye et al. „Optical frequency comb generation from a monolithic microresonator“. In: *Nature* 450.7173 (Dec. 2007), pp. 1214–1217. ISSN: 0028-0836. DOI: 10.1038/nature06401.
- [291] Tal Carmon, Lan Yang, and Kerry Vahala. „Dynamical thermal behavior and thermal self-stability of microcavities“. In: *Optics Express* 12.20 (Oct. 2004), pp. 4742–4750. DOI: 10.1364/OPEX.12.004742.
- [292] T. Herr et al. „Universal formation dynamics and noise of Kerr-frequency combs in microresonators“. en. In: *Nature Photonics* 6.7 (2012), pp. 480–487. ISSN: 1749-4885. DOI: 10.1038/nphoton.2012.127.
- [293] P. Del’Haye et al. „Octave Spanning Tunable Frequency Comb from a Microresonator“. In: *Physical Review Letters* 107.6 (2011), p. 063901. DOI: 10.1103/PhysRevLett.107.063901.
- [294] Yoshitomo Okawachi et al. „Octave-spanning frequency comb generation in a silicon nitride chip“. In: *Optics Letters* 36.17 (Sept. 2011), pp. 3398–3400. DOI: 10.1364/OL.36.003398.
- [295] Anatoliy A. Savchenkov et al. „Tunable Optical Frequency Comb with a Crystalline Whispering Gallery Mode Resonator“. In: *Physical Review Letters* 101.9 (Aug. 2008), p. 093902. DOI: 10.1103/PhysRevLett.101.093902.
- [296] A. A. Savchenkov et al. „Kerr combs with selectable central frequency“. en. In: *Nature Photonics* 5.5 (2011), pp. 293–296. ISSN: 1749-4885. DOI: 10.1038/nphoton.2011.50.
- [297] Imad H. Agha et al. „Four-wave-mixing parametric oscillations in dispersion-compensated high-Q silica microspheres“. In: *Physical Review A* 76.4 (Oct. 2007), p. 043837. DOI: 10.1103/PhysRevA.76.043837.
- [298] Jacob S. Levy et al. „CMOS-compatible multiple-wavelength oscillator for on-chip optical interconnects“. en. In: *Nature Photonics* 4.1 (Jan. 2010), pp. 37–40. ISSN: 1749-4885. DOI: 10.1038/nphoton.2009.259.
- [299] Mark A. Foster et al. „Silicon-based monolithic optical frequency comb source“. In: *Optics Express* 19.15 (July 2011), pp. 14233–14239. DOI: 10.1364/OE.19.014233.

- [300] Danielle Braje, Leo Hollberg, and Scott Diddams. „Brillouin-Enhanced Hyperparametric Generation of an Optical Frequency Comb in a Monolithic Highly Nonlinear Fiber Cavity Pumped by a cw Laser“. In: *Physical Review Letters* 102.19 (May 2009), p. 193902. DOI: 10.1103/PhysRevLett.102.193902.
- [301] C. Y. Wang et al. „Mid-Infrared Optical Frequency Combs based on Crystalline Microresonators“. In: *arXiv:1109.2716* (Mar. 2012).
- [302] R. Trebino. *Frequency-resolved optical gating : the measurement of ultrashort laser pulses*. English. Boston: Kluwer Academic, 2000. ISBN: 1402070667 9781402070662.
- [303] K. Sala, G. Kenney-Wallace, and G. Hall. „CW autocorrelation measurements of picosecond laser pulses“. In: *Quantum Electronics, IEEE Journal of* 16.9 (Sept. 1980), pp. 990–996. ISSN: 0018-9197. DOI: 10.1109/JQE.1980.1070606.
- [304] R. Wyatt and E. Marinero. „Versatile single-shot background-free pulse duration measurement technique, for pulses of subnanosecond to picosecond duration“. In: *Applied Physics A: Materials Science & Processing* 25.3 (1981), pp. 297–301. ISSN: 0947-8396. DOI: 10.1007/BF00902986.
- [305] D. M. Rayner, P. A. Hackett, and C. Willis. „Ultraviolet laser, short pulse-width measurement by multiphoton ionization autocorrelation“. In: *Review of Scientific Instruments* 53.4 (Apr. 1982), pp. 537–538. ISSN: 00346748. DOI: doi : 10.1063/1.1136978.
- [306] Roberto Paiella et al. „Self-Mode-Locking of Quantum Cascade Lasers with Giant Ultrafast Optical Nonlinearities“. In: *Science* 290.5497 (Dec. 2000), pp. 1739–1742. DOI: 10.1126/science.290.5497.1739.
- [307] P. D. Grant et al. „Room-Temperature Heterodyne Detection up to 110 GHz With a Quantum-Well Infrared Photodetector“. English. In: *IEEE Photonics Technology Letters* 18.21 (Nov. 2006), pp. 2218–2220. ISSN: 1041-1135. DOI: 10.1109/LPT.2006.884267.
- [308] I. P. Kaminow. „Balanced Optical Discriminator“. In: *Applied Optics* 3.4 (Apr. 1964), p. 507. ISSN: 0003-6935, 1539-4522. DOI: 10.1364/AO.3.000507.
- [309] Thierry Aellen et al. „Direct measurement of the linewidth enhancement factor by optical heterodyning of an amplitude-modulated quantum cascade laser“. In: *Applied Physics Letters* 89 (2006), p. 091121. ISSN: 00036951. DOI: 10.1063/1.2345035.
- [310] A. Soibel et al. „Active mode locking of broadband quantum cascade lasers“. English. In: *IEEE Journal of Quantum Electronics* 40.7 (July 2004), pp. 844–851. ISSN: 0018-9197. DOI: 10.1109/JQE.2004.830186.

Concerning the copyrighted materials: Readers may view, browse, and/or download material for temporary copying purposes only, provided these uses are for noncommercial personal purposes. Except as provided by law, this material may not be further reproduced, distributed, transmitted, modified, adapted, performed, displayed, published, or sold in whole or part, without prior written permission from the American Physical Society.



Andreas Hugli
Saumackerstrasse 86
8048 Zürich
Switzerland

Mobile: +41 79 778 57 11

E-mail: contact@andreashugi.com

LinkedIn professional profile:

<http://www.linkedin.com/pub/andreas-hugi/59/531/892>

ANDREAS HUGLI

20TH MARCH 1981

ACADEMIC HISTORY

- 2013–present** **PostDoc - ETH Zürich, Switzerland**
Department of Physics, Quantum Optoelectronics Group, Prof. Jérôme Faist
- 2007–2013** **PhD student - ETH Zürich, Switzerland**
Department of Physics, Quantum Optoelectronics Group, Prof. Jérôme Faist
Doctoral thesis: Single-mode and Comb Operation of Broadband Quantum Cascade Lasers
- 2003–2007** **Master of Science in Micro and Nanotechnology - University of Neuchâtel, Switzerland**
Module Electronics & Photonics, Institute of Microtechnology (IMT), Switzerland
Master thesis: High Power, Continuous-Wave Broadband Back-Extraction External Cavity Quantum Cascade Laser (Prof. Jérôme Faist, Institute of Physics)
Semester projects: Tunable External-Cavity Diode Laser (Neuchâtel Observatory & Optics Lab IMT) – Interfacing High-Fill Factor Micro-Mirror Arrays (SAMLAB IMT)

WORK EXPERIENCE

- 04/2013–09/2013** **EMPA – Materials Science & Technology, Dübendorf, Switzerland**
Laboratory for Air Pollution/Environmental Technology
Development of laser based sensing platforms
- 08/2008** **BLOCK engineering, Massachusetts, USA**
Consulting and realization of tuneable single mode external-cavity quantum cascade laser setup
- 04/2006–09/2006** **Sensors, Actuators and Microsystems Laboratory, IMT, University of Neuchâtel, Switzerland**
Research assistant: development of control interface of optical MEMS mirrors
- 07/2006** **Electronics and Signal Processing Laboratory, IMT, University of Neuchâtel, Switzerland**
Research assistant: study to accurately determine the height of the apical constriction of the root canal of a tooth
- 08/2005** **Syderal SA - Electronics and Software, Gals, Switzerland**
Internship: development of an analog to digital converter for space applications

REWARDS

- 2007** **Prix Omega**
For the final grade of 6/6 at the master thesis
- 2005** **Prix Jean Landry**
For the final grade of 5.51/6 at the Bachelor of Science in Micro- and Nanosciences

LANGUAGE SKILLS

German (native speaker), English (excellent), French (excellent)

MOST RELEVANT PUBLICATIONS

Journal papers

- *Mid-infrared frequency comb based on a quantum cascade laser*
Hugi A., Villares G., Blaser S., Liu H. C. & Faist J., *Nature*, **492**, 229–233 (2012)
- *External cavity quantum cascade laser*
Hugi A., Maulini R. & Faist J., *Semiconductor Science and Technology*, **25**, 083001 (2010)
- *External cavity quantum cascade laser tunable from 7.6 to 11.4 μm*
Hugi A. et al., *Applied Physics Letters*, **95**, 061103 (2009)
- *Four-wave mixing in a quantum cascade laser amplifier*
Friedli P., Sigg H., Hinkov B., **Hugi A.**, Riedi S., Beck M. & Faist J., *Applied Physics Letters*, **102**, 222104 (2013)
- *Heterogeneous high-performance quantum-cascade laser sources for broad-band tuning*
Wittmann A., **Hugi A.**, Gini E., Hoyler N. & Faist J., *IEEE Journal of Quantum Electronics*, **44**, 1083–1088 (2008)
- *Room-temperature continuous-wave operation of an external-cavity quantum cascade laser*
Mohan A., Wittmann A., **Hugi A.**, Blaser S., Giovannini M. & Faist J., *Optics Letters*, **32**, 2792 (2007)

Conference presentations

- *Broadband external-cavity quantum cascade laser (invited)*
Hugi A. et al., *IQCLSW, Monte Verita, Switzerland*, September (2008)
- *Broadband external-cavity quantum cascade laser*
Hugi A. et al., *CLEO Europe, Munich, Germany*, June (2009)
- *Broadband external-cavity quantum cascade laser*
Hugi A. et al., *ITQW, Montreal, Canada*, September (2009)
- *Broadband quantum cascade lasers - from white light sources to tunable broadband single mode sources*
Hugi A. et al., *ISLC, Kyoto, Japan*, September (2010)
- *Broadband quantum cascade lasers for mid-infrared white light applications*
Hugi A. et al., *CLEO Europe, Munich, Germany*, May (2011)
- *Multimode instabilities of broadband quantum cascade laser operating in continuous wave*
Hugi A. et al., *ITQW, Sardegna, Italy*, September (2011)
- *Mid-IR broadband quantum cascade laser frequency-comb*
Hugi A. et al., *CLEO US, San Jose, USA*, May (2012)
- *Mid-IR broadband quantum cascade laser frequency-comb*
Hugi A. et al., *ICPS, Zürich, Switzerland*, July (2012)
- *Dual-comb spectrometer based on mid-IR quantum cascade laser frequency combs*
Hugi A. et al., *CLEO US, San Jose, USA*, June (2013)